Photonic entanglement engineering for quantum information applications and fundamental quantum optics

Florian Kaiser

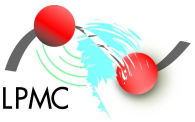

Université de Nice-Sophia Antipolis - UFR Sciences

École Doctorale : Sciences Fondamentales et Appliquées (ED n°364)

Thèse

Pour obtenir le grade de

Docteur en Sciences

de l'Université de Nice-Sophia Antipolis

dans la spécialité : **Physique**

présentée et soutenue par

Florian Kaiser

Photonic entanglement engineering for quantum information applications and fundamental quantum optics

Thèse dirigée par Sébastien Tanzilli et
co-dirigée par Marc De Micheli

préparée au Laboratoire de Physique de la Matière Condensée

soutenue le 12 novembre 2012

à 14 h au Laboratoire de Physique de la Matière Condensée

Président :	Thomas Coudreau	-	Professeur, Université Paris-7 Diderot (France)
Rapporteurs :	Jürgen Eschner	-	Professeur, Universität des Saarlandes (Allemagne)
	Nicolas Treps	-	Professeur, Université Pierre et Marie Curie, Paris (France)
Examinateur :	Vincent Jacques	-	Chargé de Recherche CNRS, ENS de Cachan (France)
Directeur :	Sébastien Tanzilli	-	Chargé de Recherche CNRS, Université de Nice - Sophia Antipolis
Co-directeur :	Marc De Micheli	-	Directeur de Recherche CNRS, Université de Nice - Sophia Antipolis
	Daniel B. Ostrowsky	-	Professeur Émérite, Université de Nice - Sophia Antipolis
	Olivier Alibart	-	Maître de Conférences, Université de Nice - Sophia Antipolis

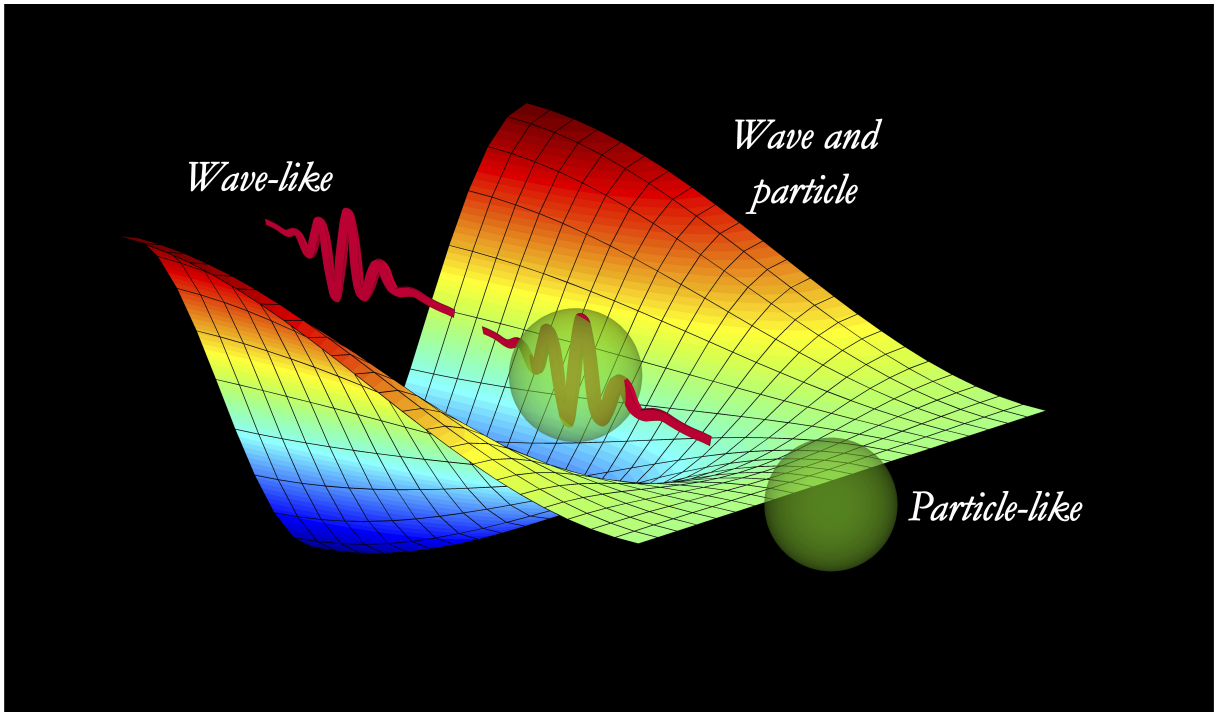

What is a photon, really?

Contents

Acknowledgements

Before describing the work done in this thesis, I would like to thank all the people that contributed to its success and to everyone who made my lab life 'easier'. It is natural that a thesis requires financial support and I would first like to thank the French Ministère de l'Enseignement Supérieur et de la Recherche for financing my work through the bourse ministérielle.

I would like to thank all the external jury members, namely Thomas Coudreau (président), Jürgen Eschner (rapporteur), Nicolas Treps (rapporteur), and Vincent Jacques (examinateur) for taking the time to carefully read the thesis manuscript and giving me advises for improvement. Thank you also for traveling to Nice for the oral thesis defense.

The first lab director during my thesis time was Gérard Monnom, who was also my lab godfather. I learnt a lot from you during our discussions about optical fibres and I would also like to greatly thank you for having a look on my first thesis talk draft and helping me to be more pedagogic.

Briefly after I arrived in Nice, a new lab director was elected, Fabrice Mortessagne whose great humor I appreciated a lot. During summer 2011 our lab experienced an almost never ending series of air conditioning problems, which made it impossible to run our high sensitivity experiments. You were in the front row to fight for improvements and I don't know how we could have made the experiments running without your help.

I would like to express an infinitely big THANK YOU SO MUCH to my thesis director Sébastien Tanzilli whom I generally referred to as *le patron*. During my first visit in your lab, I was quickly impressed by your great passion about quantum optics and your knowledge in this field. This experience made the decision to come to Nice pretty simple and I never regretted it. You were also the first to motivate me and deliver solutions when I questioned myself at the end of my first thesis year as the experiments did not advance at the speed I wished. At this point I realized that you were not only a thesis director but also a good friend. The confidence you provided in me permitted me to reach a new level at which we, together, advanced at an incredible speed with the experiments. You always put me in the spotlight in front of others, which allowed me to accumulate a lot of new contacts and future job offers. I will never forget the great times that we spent on conferences, especially Shanghai and Torino

were simply amazing. We had many vivid discussions about anything and everything which permitted me to become greater in physics and life. I am sure that we continue staying entangled and time will not play a role in this affair.

I express my gratitude to my thesis co-director Marc De Micheli. From you I learned a lot about integrated and non-linear optics concerning everything between production, characterization and optimization. Your waveguide samples were essential for my thesis. You were always open for discussions and I appreciate that you gave me deeper insights into the engineering and troubleshooting part of non-linear optics devices - something which is often forgotten by the quantum optics community.

Somebody who I cannot forget to thank (not only because he is so tall) is Olivier Alibart. He was my first instructor in the lab after I arrived in Nice and I guess he had the most difficult role. Coming from a free-space optics group, I constantly tried to convince him that fibre-optics is disadvantageous. But finally, with almost infinite patience, he got me convinced about the great advantages of guided-wave technologies. You were open for discussions about anything at any time which led to many lively discussions about physics, its interpretation and its possibilities. Thank you also for your great and very valuable inputs you provided on both the thesis manuscript and talk.

I had the great pleasure to meet Dan Ostrowsky during my thesis. You were the starting point of the realization of the type-0 source experiments. A simple *'What are you waiting for? Just do it, Florian!'* did it. Thanks also for your constant help on the delayed choice experiment. We have literally spent weeks and months to understand this experiment, but what shall we conclude? We still don't know, right? Apart from physics, we had the best lunches in the world in your house and I enjoyed a lot to listen to your crazy times in the USA and with your racing car. Finally, the probably most important things that I take from you are your important advices for life, family and career. Thank you very much for that.

Every physics lab has an engineer, and it is discussed whether he failed in life (obviously this is meant as a joke). In our case, this is Florent Doutre, or simply called 'D'. He made a great PhD in Limoges but then decided to become an engineer and nobody knows why. But let's face it: Florent is really a great guy and I would like to thank you for providing me with Raman scattering calculations, last-minute proof reading my thesis manuscript and explaining me the 'théorie de la Belote'. I wish you all the best for your future and your family with your little baby called D....

I thank Laurent Labonté aka Woohoo Goodness, the fibre expert in our team, for providing me with essentially all possible theoretical calculations in optical fibres. You were really a great help. In addition, you are the organizer of the group meetings, which is a tough task! And at the same time, you organized great lab trips such as

the canopy tour during which we came up with our million dollar idea - the paintball carting business! One day the world will be ready for this great idea.

Grazie Virginia D'Auria for repeated advice on Mathematica and cavity calculations. I think I asked you at least 10 times the same questions, but you always took the time and patience to explain everything once more again to me.

Tack Anders Kastberg for your explanations on absorption spectroscopy and laser stabilization. In my shame I have to admit that I failed this lab course experiment during my studies, so your advise were kind of crucial. I remember also very well our stay in Umea, where we disassembled the Cs experiment. On my way back to Nice there was a huge strike of the airline company, so I was a bit lost how to handle all, especially that there were no more free hotels in Stockholm. But thanks to your great travel experience you managed to have a new flight on the next day and a prepaid hotel within less than two minutes. Pretty amazing!

I had the tremendous honour to work during two years with doubtlessly one of the greatest scientists in our field, Anthony Martin, and I cannot say how much I learned from him during this time. Sometimes I had the feeling that you were like my secret french brother. It is characteristic that we had both, at the same time, the ideas for two of our experiments and we pushed ourselves to always go one step further and faster. I could perfectly rely on you not only for physics but also for out-of-the-lab life. We shared many unforgettable moments drinking beers, playing cards and I will never forget your Belote announcement '120 cœur' with a 'neuf sec' just because you didn't want the others to play. I was a bit depressed when you continued working in Geneva, but I hope that our ways in life will cross again. I wish you all the best for your future.

There is a young lady in the lab, who took a maximum of jobs for me, Amandine Issautier. Some of her duties were professional secretary, translator, plotting and 3d drawing program expert, styling expert, lab trip organizer, general consultant for regional food, and many many more. Without your help I would have been completely lost in bureaucracy and missed many important deadlines. Although you are too modest to take this for your achievement, I know that it was only your input that made me understand feedback loops in detail, which is one of the essential parts of my thesis. Another essential part of my thesis were our regular and hilarious beer and cards / volleyball / darts / frisbee evenings which have almost become a tradition! I will always remember our conference trips to Glasgow (or in other words the beer, table football and darts festival), Shanghai (hot orange juice, t-t-ten minutes oke, Rihanna, crazy horse stories and Italians), Paris (best hotel room ever, 'mais, tu travailles dans quelle équipe ?') and Grenoble (burning cars in the streets, rural disco). For your last thesis year and the following future I wish you all the best.

Since 2011 we have a new PhD student in our lab, Lutfi Arif Bin Ngah aka LBANG or 'Mister blindé des jokers'. I thank you very much for your help on most of the experiments in my thesis. Even for the most boring measurements you are highly motivated which is inspiring. I will always remember the many funny moments after working hours that we had, playing cards, you telling funny stories or bringing crazy Malaysian food. For your current highly competitive project I wish you all the best. You'll make it!

Although we shared our office only for half a year, I was very happy to have met Jim Liljekvist aka the Buffalo Soldier. Your crazy humour was hilarious and you contributed a lot to the good ambiance in the office and lab. It is a pity that you went back to Sweden but I think it was the best choice for your personal life.

I thank Valérie Mauroy for being a good friend in the lab, especially after the lunch breaks, when you typically got out of control laughing like crazy. Probably this damaged my ears irreparably but it was definitely worth it! Thanks also for all the good times that we had on the beach and during the canyoning trip. I wish you all the best for your future and I hope you will continue staying in Nice a while.

Without the help of the two computer experts, Bernard Gay-Para and Greg Sauder, most of our experiments would be simply impossible. Bernard is always there to solve any software problem on any operating system and Greg is *the* LabView expert. I am always astonished by your great patience when you try to find a problem during hours. Thank you very much, your help cannot be rated high enough!

In most experimental physics experiments, good mechanics and electronics is crucial. Therefore I would like to thank André Audoly†, Frédéric Lippi, Christophe Pitiot, Frédéric Juan and Jérôme Mauro for providing me with all the necessary parts and information.

I would like to thank the administrative team comprising Christine Chassagneux, Christine Boudard-Morteau and especially Nathalie Koulechoff for their great and uncomplicated help on everything concerning bureaucracy, reimbursements and anything else. Nathalie took also the role of distracting me sometimes during the writing process of the manuscript, which permitted me to refresh my thoughts.

I would like to express my deepest gratitude to Coralie, Carole and Guy† Raedersdorff. You accompanied me during all the time in Nice and you solved all problems that strangers have in a foreign country (apartment, bank account, health insurance, ...). You have been my second family and I could always rely on your great support during my thesis and we spent wonderful times.

I would like to thank my brother Fabian Kaiser for being the best brother in the world and frequently visiting me in Nice and all the good times that we had. I wish you all the best for your future and career and I hope that we will live closer in the near future.

Last but not least I thank my parents Erhard and Sabine Kaiser as well as my wonderful grandma Hedwig Kaiser† who believed all the time in me and economized themselves a lot in order to permit me to study at the university. No matter what happened, I could always rely on you and during my thesis I never felt far away from you, and that is what is the most important in life.

General introduction

In this thesis, the properties of light are studied and manipulated at a single photon level. In this regime, a classical description of many of the observed phenomena fails, such that new theories have been developed, the theories of *quantum physics* and *quantum optics*. In this framework, discussions on the nature of light have a long history. In the 17^{th} century, Huygens introduced the wave-front theory of light [1]. However, at that time, more people believed in Newton's corpuscular theory, in which light is treated as indivisible particles [2]. As Newton's theory could not explain the phenomena of interference, diffraction, and polarization of light, his model was eventually abandoned for Huygens' one. In addition, the wave-like description of light was backed up with Maxwell's theory of electro-magnetism that came up in the 19^{th} century [3]. In the beginning of the 20^{th}, Planck introduced the quantization of energy in order to explain the emission spectrum of a black body [4]. This lead then to the quantization of the light-field by Dirac in 1927, which can be seen as the signature of indivisible particles [5]. Many other quantum physical phenomena have soon been shown to also exhibit a quantized energy spectrum, *e.g.* the photo-electric effect, found by Einstein [6]. Altogether, these contributions led then to the development of the theory of quantum physics.

In the 1930s, the completeness of quantum physics was vividly debated as it predicted phenomena, such as entanglement, for which no classical analogue can be found [7, 8, 9, 10]. However, at that time, no general agreement was found, mainly because neither theoretical, nor experimental tools existed to prove or falsify the completeness of quantum physics.

Concerning the quantum theory of light, or in short *quantum optics*, it was thoroughly refined in the 1960s by applying quantum physics to the electromagnetic field, which led to new insights on the behaviour and statistics of light [11, 12, 13, 14]. With the laser being demonstrated in 1960, a first experimental tool was available permitting to revise the quantum theory of light [15].

In 1964, important theoretical advances have been made towards testing the completeness of quantum physics, including the phenomenon of entanglement [16]. In 1969, an experimental procedure was even described to perform these tests [17], and first experiments confirming the completeness of quantum physics were performed in the early 1970s [18]. Eventually, in the early 1980s, with the experiments of Aspect and collaborators, the existence of entanglement was unambiguously proven using entangled photons [19]. This represents the starting point of an entire new field of physics, namely that of quantum information.

In the 1980s and 1990s, several proposals have been made in the field of quantum

information, exploiting the laws of quantum physics for computational tasks, enabling faster, and more efficient simulations compared to their classical counterparts [20, 21]. In the 1990s, actual quantum algorithms were developed for prime factorizing large numbers [22] and searching an entry in an unsorted database [23]. In the meantime, the notation *qubit* (for quantum bit) was introduced as an analogue to the so-called classical bit [24]. Around the same time, several quantum communication protocols have been proposed [25, 26], offering a new way of establishing secret keys between distant communication parties: this was the birth of quantum key distribution [27, 28, 29].

It was soon found that quantum optics represents an excellent tool for performing these new quantum tasks. Many proof-of-principle quantum communication experiments have been performed in the 1990s using single photons, and now applications (such as QKD) are already commercialized [30, 31, 32, 33, 34, 35, 36]. Simultaneously, theoretical research made progress and showed that the communication distance of quantum networks can be increased using new protocols based on entangled photons [37, 38]. Additionally, in 2001, it was shown how to use single and entangled photons for quantum computational tasks using only linear optics [39].

What is the situation today? Theoretical proposals are still ahead of experimental realizations, but entanglement is frequently used as a fundamental resource for testing the foundations of quantum physics, notably its non-locality via the violation of the Bell's inequalities [40, 41, 42, 43]. However, there is also a growing interest in studying the interaction of single photons with matter, mainly for two reasons. First, this permits improving our deep understanding of, and degree of control on, quantum physics. Second, the storage of entangled photons (qubits) in stationary quantum memories has been shown (in theory) to be an efficient approach for increasing the communication rate and distance of current quantum communication protocols [44]. We now find a variety of single photon sources, based either on faint laser pulses, quantum dots, atoms, ions, colour defects, molecules, non-linear optics crystals, and many more. A good review on such sources is found in reference [45]. In principle, photonic entanglement can be obtained from either one of these single photon sources, however, up to now, non-linear optics crystals have been usually the first choice, due to ease of use (see section 2.1). The list of matter systems being studied at the single photon level is also very long and comprises quantum dots, atoms, ions, colour centres, molecules, bulk crystals, and Josephson junctions [46]. On the photonic side, generation, manipulation, and distribution over tens to hundreds of kilometres of single and entangled photons is well established, especially from the visible to the telecom range of wavelengths [47]. Much of this progress is ascribed to the rapid development of integrated (quantum) optics technologies, especially in the telecom range of wavelengths [48]. Quantum computation tasks and storage of qubits are generally established using the above mentioned matter systems. However, it was only very recently that the compatibility between entangled photons and quantum memories has been shown in proof-of-principle experiments [49, 50, 51].

In order to push quantum information science one step further, we need to develop new systems showing both versatility and compatibility. The aim of this thesis is to establish

high performance and reliable photonic sources for entanglement based quantum communication tasks [26], but also for studying the foundations of quantum physics, such as light-matter interaction [52, 53, 54], and wave-particle complementarity [9, 10]. By extensively employing telecom guided-wave optics, we demonstrate various entanglement transcribing, bandwidth adaptation, and wavelength conversion procedures. One of the long term goals of this thesis work is to study light-matter interactions, *e.g.* storing photonic entanglement (flying qubits) in quantum memories (stationary qubits). The results obtained in this thesis present a good starting point for the future realization of such experiments.

First chapter: Basics of quantum information science

The first chapter recalls briefly classical communication and outlines the security issues. Then, the field of quantum information science is introduced. Systems of one and two qubits are discussed in detail and a quick overview over currently used entanglement observables and their respective analysis procedures is given. Then their application for secret key distribution is outlined, followed by a brief discussion on more complex protocols, such as teleportation and entanglement swapping (without and with quantum memories).

Second chapter: Sources of photonic entanglement

Three different entangled photon pair sources are presented, all of them being based on spontaneous parametric down-conversion in periodically poled lithium niobate waveguides [55, 56, 57, 58]. Such guided-wave structures offer, at the same time, high brightnesses, setup compactness and high stabilities, thus satisfying the current technological demands. All sources operate in the favourable telecom C-band of wavelengths (1530-1565 nm), thus exploiting the lowest optical fibre transmission losses. In addition, all sources are based on standard telecom components making possible the future integration into standard telecom networks.

The first source generates high quality polarization entanglement in a very simple and intuitive manner and offers deterministic photon pair splitting and low losses. High stability is achieved by relying on standard telecom optics only [59].

The second source takes advantage of a polarization to time-bin entanglement transcriber, which permits obtaining the time-bin entangled bi-photon state $|\Psi^-\rangle$ in an astute manner. To our knowledge, such a state has not been generated before. In addition, it is depicted how this state can be utilized for quantum key distribution tasks with passive analysers and only four instead of eight single photon detectors [60].

The third source offers one of the highest entangled photon pair brightnesses reported to date. An advanced energy-time to polarization entanglement transcriber is used to generate polarization entanglement. The high entanglement quality and spectral bandwidth versatility (25 MHz - 4 THz) of this source enables employing it for various

tasks, such as dense wavelength division multiplexed quantum key distribution [61], continuous wave quantum relay, teleportation, and entanglement swapping schemes [58], as well as photon storage in current quantum memory devices [54, 53, 50].

Third chapter: A photonic quantum interface

Current quantum memory devices operate in the visible to near-infrared range of wavelengths (500-900 nm), which is not adapted for long distance photon distribution, due to high optical fibre losses. In this chapter, preliminary results obtained on a coherent wavelength conversion device are shown. It is based on the process of sum frequency generation in periodically poled lithium niobate waveguides [62]. Using such a device, photons at 1560 nm are coherently converted to 795 nm, which matches the absorption wavelength of quantum memories based on rubidium atoms. The conversion wavelength can be conveniently adapted to match other quantum memory absorption wavelengths, *i.e.* Thulium doped crystal quantum memories operating at around 793 nm [63]. Such wavelength conversion allows benefiting from both low propagation losses for telecom wavelength entangled photon pairs, and high efficiency quantum memories at 500-900 nm. For future applications, the noise figures of this converter need to be further reduced and it is depicted how this can be achieved using an optical cavity filter.

Fourth chapter: An entanglement-enabled quantum delayed choice experiment

The versatility of the above mentioned high brightness photon pair source [64] permits revisiting Niels Bohr's so-called wave-particle complementarity notion via employing a quantum beam-splitter in a true superposition of being present or absent. Such an experiment has recently been proposed in theory [65, 66]. The obtained experimental results demonstrate interference between wave and particle behaviour of single photons and underline strikingly the impropriety of using too simple classical models for describing the phenomena of quantum physics [43].

Introduction générale

Dans ce manuscrit, les propriétés de la lumière sont étudiées et manipulées au niveau des photons uniques. Dans ce régime, une description classique ne peut pas expliquer la plupart des phénomènes observés, si bien qu'il est necessaire d'employer la théorie quantique, à savoir la physique quantique. Dans ce cadre, les discussions sur la nature de la lumière ont une longue histoire. Au 17 ème siècle, Huygens a présenté la théorie du front d'onde de la lumière [1]. Pourtant, à cette epoche, la plupart des scientifiques favorisait la théorie corpusculaire de Newton, dans laquelle la lumière est traitée comme des particules indivisibles [2]. Comme la théorie de Newton n'était pas capable d'expliquer les phénomènes d'interférence, de diffraction et encore la polarisation de la lumière, sa théorie a été finalement abandonnée, en faveur de la théorie ondulatoire de Huygens. Plus tard, le traitement de la lumière en tant qu'onde a été appuyé par la théorie électromagnétique développé par Maxwell au 19ème siècle [3]. Au début du 20ème siècle, Planck a présenté la quantification de l'énergie pour expliquer le spectre d'émission du corps noir [4]. Cela aboutît à la quantification du champ lumineux par Dirac en 1927, qui est par ailleurs souvent interprété comme une signature des particules indivisibles [5]. Dans le même temps, plusieurs autres phénomènes quantiques ont été découverts, proposant également des spectres énergétiques discrets, comme par exemple l'effet photoélectrique expliqué par Einstein en 1905 [6]. Notons que c'est bien l'ensemble de ces découvertes qui ont lancé le développement de la théorie quantique.

Dans les années 1930, la complétude de la physique quantique fut intensément discutée. En effet, la théorie prévoit des propriétés, comme l'intrication, pour lesquelles aucune explication classique n'est réellement possible [7, 8, 9, 10]. Toutefois, à cette époque, aucun accord n'a pu être trouvé, principalement en raison d'un cadre théorique trop jeune, mais également en raison de dispositifs expérimentaux limités qui auraient pu permettre de confirmer ou d'infirmer certaines hypothèses, et la complétude, ou non, de la physique quantique.

Concernant la théorie quantique de la lumière, plus connue aujourd'hui sous l'appellation "optique quantique", celle-ci a été proprement élaborée dans des années 1960, en appliquant les déclinaisons de la physique quantique au camp électromagnétique. Ceci permit la compréhension du comportement et des statistiques effectuées sur le camp lumineux sous un jour nouveau [11, 12, 13, 14]. Grâce notamment au développement du laser dans les années 1960, les physiciens expérimentateurs eurent pour la première fois un outil expérimental pertinent pour reconsidérer, voir revisiter, la théorie quantique de la lumière [15].

En 1964, des développements théoriques importants ont été conduits par J. S. Bell

afin de pouvoir tester la complétude de la physique quantique, en incluant la propriété d'intrication [16]. En 1969, un protocole expérimental a même été proposé pour effectuer ces tests [17], et les premières expériences confirmant la validité de la physique quantique ont été faites au début des années 1970 [18]. Finalement, ce n'est qu'au début des années 1980, avec notamment les expériences d'Aspect et ses collaborateurs, que l'existence de la validité de l'intrication a été confirmée sans aucun doute possible, grâce à l'utilisation des paires de photons intriqués [19]. Il est aujourd'hui clair que ces expériences représentent, avec l'ensemble des développements théoriques et expérimentaux conduits dans les années 1980, le point de départ d'une nouvelle discipline connue aujourd'hui sous le nom "d'information quantique".

En effet, au cours des années 1980 et 1990, de nombreuses propositions ont été faites dans le but d'utiliser les lois fondamentales de la physique quantique pour effectuer des tâches de calcul de manière plus rapide, des simulations plus efficaces, en comparaison avec des ordinateurs classiques [20, 21]. Dans les années 1990, des algorithmes quantiques ont été démontrés, allant de la factorisation des grands entiers en leurs facteurs premiers [22], à la recherche d'une entrée dans une base de données [23]. Entre temps, la notion de "qubit" (raccourci pour "bit quantique") fut introduite comme étant l'analogue du bit classique [24]. A peu près à la même période, plusieurs protocoles de communication quantique ont été proposés [25, 26], ce qui autorisa de nouvelles perspectives en matière de cryptographie à clefs privées, aujourd'hui appelée génériquement "cryptographie quantique". L'ensemble des protocoles cités ci-dessus représentent le véritable cœur de ce nouveau camp de recherche qu'est l'information quantique [27, 28, 29].

Peu de temps après, il fut démontré que l'optique quantique représente un cadre pertinent pour la réalisation de ces nouvelles tâches de communication quantique. En effet, beaucoup de preuves de principe expérimentales furent démontrées au cours des années 1990, grâce notamment au développement de nouvelles sources de photons uniques toujours plus pures et efficaces. Les progrès ont été tels que la cryptographie quantique est déjà commercialisée depuis presqu'une décennie [30, 31, 32, 33, 34, 35, 36]. En même temps, la recherche théorique a progressé et a démontré que la distance de communication peut être augmentée en utilisant l'intrication comme une ressource primaire autorisant les protocoles de téléportation d'états [37, 38]. De plus, en 2001, il a été montré comment il est possible d'utiliser des photons uniques et intriqués pour effectuer des tâches de calculs quantiques en se basant uniquement sur de l'optique linéaire [39].

Où en est-on aujourd'hui ? Les développements théoriques sont toujours en avance par rapport aux réalisations expérimentales, mais l'intrication est aujourd'hui abondamment employée comme ressource fondamentale pour tester des fondements de la physique quantique, comme par exemple la non-localité avec la violation des inégalités de Bell [40, 41, 42, 43]. Pourtant il existe aussi un fort intérêt pour étudier les interactions entre des photons uniques et la matière, principalement pour deux raisons. D'une part, cela permet d'acquérir une meilleure compréhension ainsi qu'un niveau de contrôle plus fin sur les applications liées à la physique quantique. D'autre part, le stockage de photons uniques ou intriqués dans des mémoires quantiques stationnaires

s'est avéré être une approche pertinente pour augmenter la distance et le débit de la communication quantique [44]. Aujourd'hui, nous trouvons toute une variété de sources de photons uniques et de paires de photons intriqués basées sur des boîtes quantiques, des ensembles atomiques, des ions uniques piégés, des centres colorés dans le diamant, des molécules, des cristaux non-linéaires, et bien d'autres systèmes encore. Une revue de ces sources de photons est portée en référence [45]. En principe l'intrication photonique peut être obtenue à partir biais de toutes les sources susmentionnées, mais jusqu'à présent, le choix s'est très largement porté sur les cristaux non-linéaires, en raison de leur faible encombrement et de leur simlicité d'utilisation (voir section 2.1). En ce qui concerne la communication quantique, c'est-à-dire à base de qubits photoniques, la génération, la manipulation, et la distribution de l'information quantique sur plusieurs dizaines de kilomètres sont aujourd'hui bien développées, spécialement dans les plages spectrales couvrant le visible et l'infra rouge [47], au sein duquel on trouve les bandes des télécommunications optiques standards. Ce progrès est également en partie dû au développement rapide de l'optique quantique intégrée, opérant notamment aux longueurs d'ondes de télécoms [48]. Par ailleurs, le calcul quantique et le stockage des qubits sont généralement réalisés en utilisant des systèmes matériels, tels les atomes et les ions piégés. Par contre, la compatibilité entre photons intriqués et mémoires quantiques à base d'ensembles d'atomes et d'ions n'a été démontrée que très récemment par le biais d'expériences pionnières faisant foi de preuves de principe [49, 50, 51].

Pour aller plus loin avec l'information quantique, il est nécessaire de développer de nouveaux systèmes versatiles et compatibles les uns avec les autres. Le but de cette thèse est de réaliser des sources photoniques ultra performantes et fiables pour la communication quantique [26], mais également pour des études sur les fondements de la physique quantique, par exemple l'intrication lumière-matière [52, 53, 54] et la dualité onde-corpuscule [9, 10]. En utilisant beaucoup de composants en standard des télécoms, nous montrons plusieurs schémas de conversion de l'intrication, adaptation de la larguer spectrale et de conversion de longueur d'onde. Un des buts à long terme de cette thèse est d'étudier l'interaction lumière-matière, c'est-à-dire le stockage de l'intrication photonique dans des mémoires quantiques. Les résultats obtenus dans cette thèse représentent un très bon point de départ pour réaliser ces expériences dans un avenir proche.

Premier chapitre : les bases de la science de l'information quantique

Le premier chapitre rappelle brièvement les notions relatives à la communication et au traitement classique de l'information et discute les problèmes qui s'y rapportent, notamment en termes de sécurisation des échanges de données effectués à l'aide de moyens conventionnels.

Par la suite, la science de l'information quantique est introduite, via notamment la définition des systèmes quantiques à un et deux qubits. Une brève vue d'ensemble est donnée sur les observables communément utilisées pour coder l'information quantique,

et sur les procédés généralement mis en œuvre pour les manipuler et les analyser. Enfin, l'utilisation des qubits dans des systèmes de distribution quantique de clefs secrètes est présentée. Il s'ensuit une brève discussion sur les protocoles plus complexes liés à la communication quantique, comme par exemple la téléportation d'états, la téléportation de l'intrication, proposés avec ou sans mémoires quantiques.

Deuxième chapitre : sources d'intrication photonique

Ce chapitre est consacré aux réalisations de trois sources différentes de paires de photons intriqués. Toutes trois sont basées sur la conversion paramétrique spontanée dans des guides d'ondes intégrés sur substrat de niobate de lithium polarisé périodiquement [55, 56, 57, 58]. Ce type de structures guidante offre à la fois haute brillance, compacité expérimentale et haute stabilité, satisfaisant ainsi les défis technologiques d'aujourd'hui. Ces sources opèrent toutes dans la bande C des télécommunications optiques (1530-1565 nm) exploitant ainsi les plus faibles pertes de la transmission d'information par fibre optique. De plus, les réalisations expérimentales associées à ces sources sont basées sur l'utilisation massive de composants télécoms standards, rendant possible leur future intégration dans les réseaux télécoms existants.

La première source génère de l'intrication en polarisation de haute qualité, d'une manière simple et intuitive, offrant par ailleurs une séparation déterministe des paires de photons ainsi que de faibles pertes. Aussi, haute stabilité et simplicité de fonctionnement sont rendues possibles grâce à l'utilisation exclusive de composants très performantes issus de l'industrie de télécoms optiques [59].

La seconde source est basée sur l'application d'un convertisseur d'intrication en polarisation vers l'intrication en time-bin. Ceci permet de générer de manière astucieuse, et ce pour la première fois, l'état intriqué en time-bin croisé $|\Psi^-\rangle$. De plus, il est démontré comment cet état peut être utilisé dans des systèmes de distribution quantique de clefs secrètes n'employant que des analyseurs passifs et seulement quatre détecteurs de photons uniques au lieu de huit comme c'est le cas communément [60].

La troisième source offre l'une des plus hautes brillances pour la génération de paires de photons intriqués démontrée à ce jour. Le cœur de la source est constitué d'un convertisseur, dit avancé, d'intrication en énergie-temps vers l'intrication en polarisation. La haute qualité d'intrication et la versatilité de la source obtenue à la fois sur la largeur de bande spectrale (25 MHz - 4 THz) des photons générés, sur la longueur d'onde d'émission, ainsi que sur l'état quantique porté par ces photons, permettent d'employer la source pour de nombreuses tâches associées aux applications de type "reseaux quantiques". En effet, la versatilité de cette source permet de répondre à la fois aux défis de la distribution quantique de clefs au sein de réseaux à multiplexage en longueurs d'ondes [61], aux relais quantiques en régime de pompage continu basés sur la téléportation de l'intrication [58], ainsi qu'au stockage de l'intrication au sein de plusieurs types de mémoires quantiques actuelles [54, 53, 50].

Troisième chapitre : interface quantique photonique

Les mémoires quantiques actuelles opèrent préférentiellement à des longueurs d'ondes appartenant aux bandes du visible et du proche infrarouges (500 - 900 nm). Ces bandes spectrales ne sont malheureusement pas adaptées à la distribution de qubits photoniques sur longue distance, en raison de pertes à la propagation trop importantes dans les fibres optiques dédiées. Il est donc nécessaire d'adapter les longueurs d'ondes de distribution de qubits et de stockage de l'information quantique, tout en préservant l'intégrité quantique des qubits photoniques considérés : on parle alors d'interface quantique pour qubits photoniques. L'expérience que nous avons conduite est basée sur le processus de génération des somme de fréquences dans des guides d'ondes intégrés sur substrat de niobate de lithium périodiquement polarisé [62]. En utilisant un tel dispositif, les photons initialement à la longueur d'onde télécom de 1560 nm sont convertis de manière cohérente vers la longueur d'onde de 795 nm, qui correspond à la ligne central de l'une des raies d'absorption des mémoires quantiques basées sur des atomes de rubidium. Aussi, le processus de conversion peut être rendu, de manière simple, compatible avec des raies d'absorption relatives à d'autres types de supports de stockage, comme c'est le cas par exemple des mémoires quantiques à base de cristaux dopés aux ions thulium opérant autour de 793 nm [63]. Une telle conversion de longueurs d'ondes permet de bénéficier à la fois de faibles pertes de propagation pour les photons intriqués émis dans l'une des bandes des télécommunications, et des mémoires quantiques à haute efficacité, opérant dans la bande 500 - 900 nm. Nous présentons et discutons dans ce chapitre les résultats préliminaires obtenus avec un tel dispositif à conversion cohérente de longueur d'ondes. Afin de rendre ce dispositif opérationnel pour des futures applications, le bruit photonique associé à ce convertisseur, principalement relié à la diffusion Raman dans les cristaux non-linéaires, doit être substantiellement réduit. Nous décrivons comment opérer une telle réduction de bruit grâce à l'utilisation d'un filtre spectral basé sur une cavité optique.

Quatrième chapitre : interface quantique photonique

La versatilité de la source de paires de photons à haute brillance mentionnée plus haut [64] a permis de revisiter la notion de complémentarité onde-corpuscule, ainsi nommée par Niels Bohr, en employant un interféromètre Mach-Zehnder possédant une lame séparatrice de sortie préparée dans une superposition cohérente des deux états, présente et absente. Une telle expérience a été récemment proposée du point de vue théorique [65, 66]. Les résultats expérimentaux obtenus démontrent l'interférence entre des comportements ondulatoires et corpusculaires des photons uniques envoyés dans l'interféromètre, ce qui souligne de manière frappante qu'il est tout à fait inapproprié d'utiliser des modèles classiques trop simples pour décrire les phénomènes observé et prédits par la théorie quantique [43].

Chapter 1.

Basics of quantum information science

Generation and manipulation of entanglement is at the heart of the work of this thesis. Entanglement has passed from being a *spooky action at a distance* [67] to be one of the main resources for testing the foundations of quantum physics. Currently, there is a high interest to study the interaction of matter with entangled light, which might eventually lead to new applications and deeper insights into quantum physics. Today, photonic sources of entanglement are already commercialized [30, 31, 34, 36, 35, 32] and exploited in research laboratories and quantum key distribution (QKD) systems. In this chapter, we discuss the implications of entanglement, how to measure it, and how to use it for QKD applications.

The organization is as follows: after briefly recalling classical communication and its limitations for secure communication, its quantum analogue is described in detail. The notation *qubit* is introduced and extended to particular (entangled) systems of two qubits leading to the observation of strong correlations between the measurements being performed on each individual qubit. Such strong correlations are shown to be a purely quantum effect with no classical analogue. An overview is given about the currently exploited photonic entanglement observables and how the corresponding measurements are made. Finally it is described how to exploit these correlations for quantum cryptography tasks, where photons are the preferred information carriers.

1.1. Classical information

The rapid development of humankind is doubtlessly ascribed to our ability to communicate and process information [68]. In the early days, exchanging information was done *viva voce*, consequently the communication parties had to physically meet. Everything changed with the first written language, Archaic Sumerian (31^{th} - 26^{th} century BC), in which texts were written onto clay tablets enabling a completely new way of exchanging and storing information. The clay tablets were transported from reader to reader, or the reader travelled to the clay tablets, which permitted obtaining information at any desired time. The first mentioning of information exchange over large distances without

involving physical displacement is found in the ancient Greek trilogy 'Oresteia' (1184 BC), where smoke clouds were used to tell the fall of Troy. Ever since then, enormous efforts have been made to exchange information over larger distances, in faster ways, and with higher privacy. Certainly, one of the biggest milestones in the history was achieved in 1858 when businessman Cyrus West Field pushed forward the realization of the first transatlantic telegraph cable, installed between Ireland and Newfoundland. Although the communication speed was only about 0.1 words per minute, exchanging information between two continents did not require physical travel, for the first time. With technology evolving, the communication speed between the continents has been tremendously increased, two of the major breakthroughs being the first transatlantic telephone cable TAT-1 (1956) [69], and the first transatlantic fibre-optic communication cable TAT-8 (1988).

What is the representation form of information today? The big majority of current information systems takes advantage of the binary representation of information. The basic unit is therefore the bit[1], which can have the value of either '0' or '1'. These two values can be physically encoded in many ways, a few examples being the telegraph system in which the temporal length of current pulses denotes the two values, fibre-optic systems use the intensity of light pulses, and on hard-disk drives the magnetization is taken. Using a series of bits allows then to encode characters, *e.g.* when using the ASCII[2] character-encoding system the character 'A' is represented by the seven bit series '1 0 0 0 0 0 1', while for 'Z' it is '1 0 1 1 0 1 0'.

A problem of all (purely) classical schemes is that they cannot guarantee absolute communication privacy [70]. Although enormous efforts have been made to increase privacy by new information encryption and decryption schemes, a potential eavesdropper could, in principle, always decrypt the information, which is most of the times highly undesirable. In the following, it is briefly explained why (purely) classical communication schemes are insecure, and later it is shown how quantum communication protocols overcome this problem.

1.1.1. Encrypting information - a brief history

In this subsection, a quick historical summary of the development of cryptography is given. The interested reader can find a more exhaustive summary in the following books [71], and references [27, 28]. The general strategy for (symmetric) encryption of information requires the use of an algorithm that transforms the original message into an unreadable one. A key might be used to determine the exact use of the algorithm at each instance. The encrypted message is then sent via a public communication channel. The desired communication partner has a precise knowledge on the used algorithm (and the key) and can consequently decrypt the unreadable message towards obtaining the

[1] The term *bit* is actually the contracted version for *binary digit*.
[2] ASCII is an acronym for American Standard Code for Information Interchange.

original one. Cryptography has a long history, *e.g.* a Mesopotamian clay tablet dated to around 1500 BC contains an algorithm for encrypting a recipe for pottery glaze. Since then, many algorithms have been developed, *e.g.* the Caesar's code encrypts a message by shifting each letter by a fixed number of letter positions in the alphabet[3]. Around World War I, the first cryptography machines have been used in order to account for the increased amount of information exchange. Since then, more and more complex machines have been developed, one of the most known examples being the Enigma machine, which was heavily used in World War II. But all these machines have been proven to lack of security. As soon as the key was known by the spy/eavesdropper, it took only several efforts to obtain the algorithm, and consequently to decrypt the messages. This is summarized by Kerckhoffs's assumption stating that 'A cryptosystem should be secure even if everything about the system, except the key, is public knowledge.' [72]. In other words, no complex algorithm is required to secure a message, we need only a secret key. This led to the development of the Vernam cypher, which is described in subsection 1.1.2.

1.1.2. The Vernam cypher, or one time pad method

The Vernam cypher uses the simplest cryptography algorithm, a logic XOR gate (see Table 1.1), in combination with an absolutely random and private key for data encryption and decryption [73]. To date the Vernam cypher is the only information encryption/decryption scheme that has been proven to be absolutely secure, provided that several

[3]For example a shift parameter (key) of 3 would result in A→D, B→E, C→F, ...

Original message m	Key k	Encrypted message $m \oplus k$	Decrypted message $(m \oplus k) \oplus k$
0	0	0	0
0	1	1	0
1	0	1	1
1	1	0	1

Table 1.1.: The Vernam cypher using the simplest algorithm, a logic XOR gate (symbolized mathematically by $\oplus$). The original message m is encrypted using a key k by the operation $m \oplus k$ and sent through a public channel. This message is conveniently retrieved by applying another XOR gate, using the same key, for decryption, $(m \oplus k) \oplus k = m$. Although an extremely simple algorithm is used, this protocol allows for absolutely secure information exchange, provided the facts that a new and random key is used for every bit to be encoded, and that the key is only known by the sender and receiver.

precautions are taken [74].

(a) For every message bit a new key k needs to be used - every key is only used once (this is often called to be a 'one-time-pad' method).

(b) Every key k needs to be generated in a completely random fashion.

(c) At any time, the key is exclusively known by the sender and receiver.

Requirement (a) is straightforward to fulfil. But for (b) there is no classical solution [75]. True randomness requires non-deterministic processes, but the classical world is considered to be deterministic. However, there are several strategies, exploiting non-deterministic processes in quantum physics, allowing for absolutely random key generation using so-called quantum random number generators (QRNG) [76, 77, 78, 79, 80, 81, 82, 30, 31, 34, 36, 35, 32][4]. Nevertheless, a major issue is requirement (c). Even if an absolutely random key has been generated, which process shall be used to faithfully distribute this key only to the sender and receiver, without there being an eavesdropper having access to this information? As for (b), this problem cannot be solved in the classical world of physics. It turns out that, again, quantum physics offers an already commercialized solution for this problem [30, 31, 34, 36, 35, 32]. But before entering into the details of this quantum solution, a brief summary of the working principle of the most used classical cryptography protocol is given and it is highlighted why this protocol is insecure.

1.1.3. The RSA protocol - a brief abstract

One widely used cryptography strategy for internet based communication relies on the RSA[5] algorithm. It was published in 1977 [83] and its (temporal) security is based on the fact that, currently, factorizing large numbers is a difficult (time consuming) task, making it quite impossible for a spy to retrieve the message in a decent time. However, as soon as the large number is factorized, the spy can decrypt the message conveniently. Consequently, Kerckhoffs's assumption is not fulfilled. In the following, a quick example is given to outline how the RSA protocol works.

Assume two communication parties, say Alice and Bob. Alice wants to receive a message from Bob. To do so, the following steps are performed:

(1) Alice chooses randomly two large and distinct prime numbers, p and q.

(2) Alice computes $n = p \cdot q$, where n is referred to be the modulus.

(3) Alice computes Euler's totient function $\Phi(n) = (p-1) \cdot (q-1)$.

[4] This list does not claim completeness.

[5] RSA stands for the designers of this algorithm, Ron Rivest, Adi Shamir and Leonard Adleman.

(4) Alice chooses an integer number e that is coprime to $\Phi(n)$ and $1 < e < \Phi(n)$.

(5) Alice publishes the numbers n and e.

(6) Bob encrypts the message m to be sent by calculating $m^e \bmod n = c$, where c represents the encrypted message, that is sent to Alice via a public channel.

(7) Alice solves (typically by using the extended Euclidean algorithm) the following equation for d and k: $e \cdot d + k \cdot \Phi(n) = 1$ with $d, k \in \mathbb{Z}$.

(8) Alice decrypts the message c conveniently by performing the following operation $c^d \bmod n = m$.

Note that an eavesdropper can decrypt the message, as soon as d is known. However, this requires knowing Euler's totient function $\Phi(n)$ in order to perform step (7). Without knowing p and q (see steps (1) to (3)), this represents a difficult task, requiring very high computational powers. An example is given in the following:

(1) Alice chooses two distinct prime numbers, $p = 29\,611$ and $q = 56\,897$.[6]

(2) Alice computes the modulus $n = p \cdot q = 1\,684\,777\,067$.

(3) Alice computes the Euler's totient function $\Phi(n) = (p-1) \cdot (q-1) = 1\,684\,690\,560$.

(4) Alice chooses an integer number $e = 39\,119$ that is coprime to $\Phi(n)$ and $1 < e < \Phi(n)$.

(5) Alice publishes the numbers n and e.

(6) Bob encrypts the message $m = 7$ to be sent by calculating $m^e \bmod n = c$, where $c = 772\,513\,208$ represents the encrypted message, that is sent to Alice via a public channel.

(7) Alice solves the following equation for d and k: $e \cdot d + k \cdot \Phi(n) = 1$ with $d, k \in \mathbb{Z}$ and obtains $d = 1\,440\,335\,279$ and $k = -33\,445$.

(8) Alice decrypts the message c conveniently by performing the following operation $c^d \bmod n = m = 7$.

As mentioned before, a potential spy would need to solve the following equation:

$$1\,684\,777\,067 = p \cdot q \qquad \text{with } q, p \in \mathbb{N}. \tag{1.1}$$

[6] Note that these prime numbers are considered as *relatively* small for cryptography tasks, thus only minor security is expected. But for this didactic example this is considered as being sufficient.

Solving this equation on an Intel® Core(TM) i7-2677M CPU operating at 1.80 GHz clock frequency in Mathematica 8.0.4.0 (operating system MAC OS X 10.7.4) requires a computational time of ~ 150 ms, meaning that Bob's message would be secure for at least 150 ms. Note that the RSA modulus n in this example is a 10 digit number. Typical internet protocols use RSA modulus' of at least 77 digits length (256 bit encryption). At the time this thesis is written there is no (classical) efficient algorithm to factorize large numbers. This means that the calculation time increases exponentially as a function of the RSA modulus length. For example, the prime factorization of a 768 bit RSA modulus took around half a year using 80 AMD Opteron 2.2 GHz processors in parallel [84, 85]. Although this time seems relatively long, it underlines clearly that this way of message encryption with a public key is inappropriate for long term privacy. This is why in 2007 the American national institute of standards and technologies (NIST) recommended using at least 2048 bit RSA encryption for a ~ 20 year message security and 3072 bits for even longer times [86]. However, these recommendations assume that within this time, we will not find a more efficient algorithm for prime factorization. Note that until today there is no mathematical proof that such a classical efficient factorization algorithm does not exist. In the quantum world, an efficient factorization algorithm exists already, namely Shor's algorithm [22], but unfortunately current quantum computers are not *yet* powerful enough to perform factorizations faster than their classical counterparts.

1.2. Quantum information

In this section the principles of quantum communication are introduced. We will see that this allows establishing absolutely random and secret keys between Alice and Bob, and consequently Kerckhoffs's assumption is fulfilled. It is then possible to use a very simple algorithm to encrypt and to decrypt the message, *i.e.* the one proposed by Vernam (see subsection 1.1.2).

1.2.1. The quantum bit - qubit

The equivalent of the classical bit is the quantum bit, or in short, the qubit [24]. A qubit can be '0' or '1', but thanks to the principles of quantum physics, a qubit can also be in superposition quantum states $|\psi\rangle$ such as

$$|\psi\rangle = \alpha\,|0\rangle + \beta\,|1\rangle\,. \tag{1.2}$$

Here, $\alpha, \beta \in \mathbb{C}$ are the probability amplitudes of the qubits, and for pure states the general normalization, $|\alpha|^2+|\beta|^2 = 1$, is applied. The 2d Hilbert space vectors $|0\rangle \equiv \begin{pmatrix}1\\0\end{pmatrix}$ and $|1\rangle \equiv \begin{pmatrix}0\\1\end{pmatrix}$ denote the qubits '0' and '1', respectively. Note that the state of

equation 1.2 is given in the so-called Dirac notation. For convenience, this state can be rewritten as

$$|\psi\rangle = \cos\frac{\theta}{2}\,|0\rangle + e^{i\,\phi}\sin\frac{\theta}{2}\,|1\rangle\,, \tag{1.3}$$

with θ, $\phi \in \mathbb{R}$. This notation is sometimes more convenient as it gives automatically normalized quantum states. In this notation, the quantum state of the qubit can be represented as a point on the Bloch sphere as shown in Figure 1.1. From the Bloch sphere picture, and with equation 1.3, it is seen that the three Cartesian axes $\hat{x}$, $\hat{y}$, and $\hat{z}$ correspond to 2d Hilbert space vectors, as defined by

$$\hat{x} = \frac{1}{\sqrt{2}}\begin{pmatrix}1\\1\end{pmatrix} \equiv |0_x\rangle\,, \qquad -\hat{x} = \frac{1}{\sqrt{2}}\begin{pmatrix}1\\-1\end{pmatrix} \equiv |1_x\rangle\,, \tag{1.4}$$

$$\hat{y} = \frac{1}{\sqrt{2}}\begin{pmatrix}1\\i\end{pmatrix} \equiv |0_y\rangle\,, \qquad -\hat{y} = \frac{1}{\sqrt{2}}\begin{pmatrix}1\\-i\end{pmatrix} \equiv |1_y\rangle\,, \tag{1.5}$$

$$\hat{z} = \begin{pmatrix}1\\0\end{pmatrix} \equiv |0_z\rangle\,, \qquad -\hat{z} = \begin{pmatrix}0\\1\end{pmatrix} \equiv |1_z\rangle\,. \tag{1.6}$$

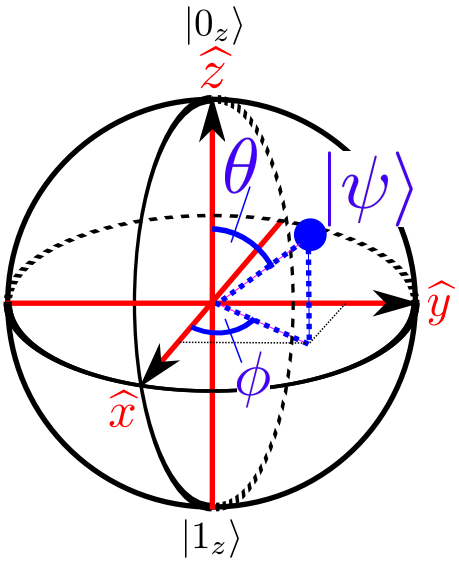

Figure 1.1.: Bloch sphere representation of a qubit. A pure quantum state $|\psi\rangle$ is defined as a vector pointing at the surface on the Bloch sphere characterized by two angles θ and ϕ.

1.2.2. Measuring a qubit

What happens when a measurement is performed on the qubit? One axiom of quantum physics is that:

A measurement projects the quantum state $|\psi\rangle$ onto one of the (orthonormal) eigenstates of the corresponding measurement.

Quantum physics does not tell us why this is, but to date no experiment contradicted this statement. We just have to accept this. The Bloch sphere allows getting an intuitive picture of what happens when a measurement is performed. For a given point (state) at the surface of the Bloch sphere, the corresponding orthonormal point (state) is located at the diametral position on the sphere. As a consequence, a measurement projects the quantum state on one of the two points in a probabilistic manner. Which two diametral points on the Bloch sphere are chosen depends on the measurement that is performed. After the state projection, any repetition of the same measurement results deterministically in the same outcome. The fact that the quantum state is projected means in general that information about the initial quantum state is irreversibly lost.

An example is given: We start with the most general quantum state $|\psi\rangle = \begin{pmatrix} \cos\frac{\theta}{2} \\ e^{i\,\phi}\sin\frac{\theta}{2} \end{pmatrix}$ and we perform a measurement along the Cartesian z-axis. In other words, $|\psi\rangle$ is projected on either $\begin{pmatrix} 1 \\ 0 \end{pmatrix} = |0_z\rangle$ or $\begin{pmatrix} 0 \\ 1 \end{pmatrix} = |1_z\rangle$ (see equation 1.6). The corresponding probabilities are given by the following equations

$$p_{0_z} = |\langle 0_z\,|\psi\rangle|^2 = \cos^2\frac{\theta}{2}, \tag{1.7}$$

$$p_{1_z} = |\langle 1_z\,|\psi\rangle|^2 = \sin^2\frac{\theta}{2}. \tag{1.8}$$

Here, $\langle\ldots|$ denotes the Hermitian conjugate vector $|\ldots\rangle^*$. Although the outcome of each measurement gives us either '0' or '1', a repeated preparation of the state $|\psi\rangle$, followed by the projective measurement, allows determining θ by averaging the obtained results. Note that repeatedly measuring the *single* qubit along the z-axis does not deliver additional information on θ. After the first measurement $|\psi\rangle$ is projected onto $|0_z\rangle$ ($|1_z\rangle$) and all following measurements along the z-direction will then result with unit probability in $|0_z\rangle$ ($|1_z\rangle$). In other words, to obtain a significant sample, the state $|\psi\rangle$ has to be repeatedly prepared and measured. Obviously, we have to trust that this preparation procedure is faithful.

From equations 1.7 and 1.8, it is seen that even a repetitive qubit measurement along the z-axis does not permit obtaining the full information about the quantum state $|\psi\rangle$. The probabilities p_{0_z} and p_{1_z} do not comprise the phase ϕ. Information about ϕ is obtained by projecting the state $|\psi\rangle$ onto the x-axis and y-axis. It is then

$$\frac{p_{0_y}}{p_{0_x}} = \frac{1-p_{1_y}}{1-p_{1_x}} = \tan\phi. \tag{1.9}$$

Consequently, we need to repeatedly prepare the state $|\psi\rangle$ and measure it along all three axis, x, y, z to obtain the full information about a qubit whose initial state is unknown. This procedure is generally called quantum state tomography.

1.2.3. No-cloning theorem

The above made statements about the limited amount of information obtained from measurements performed on a single qubit would not hold if we were able to reproduce (clone) the initial qubit. In this case, we could reproduce the qubit of interest many times, and by performing on each third of the cloned qubits a measurement along the x, y, z-axis, respectively, the full information about the initial single qubit would be obtained. In the following, we show that such a cloning procedure is not possible [87].

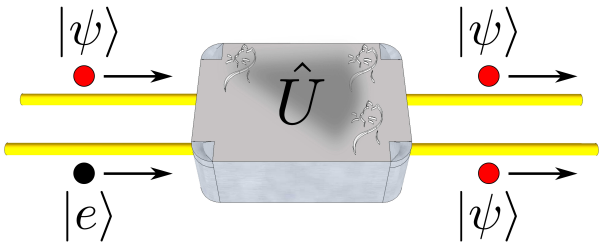

Figure 1.2.: Considered cloning machine. We wish to clone the incoming state $|\psi\rangle$ (top left side, red colour) by writing it onto another state $|e\rangle$ (black). After applying an unitary operation $\hat{U}$ on both input qubits, the state $|\psi\rangle$ shall be duplicated.

Suppose an unknown qubit state $|\psi\rangle$ that we wish to clone and let us consider the following procedure: We take another state $|e\rangle$ onto which we want to write the properties of the state $|\psi\rangle$ using an unitary operation $\hat{U}$. This procedure is also depicted in Figure 1.2 and described by the following equation:

$$\hat{U}(|\psi\rangle\,|e\rangle) = |\psi\rangle\,|\psi\rangle\,. \tag{1.10}$$

In the quantum world, we need to choose a basis in which the state $|\psi\rangle$ is represented by a linear combination of orthonormal basis vectors. As shown before, for a single qubit, $|\psi\rangle$, such an orthonormal basis is defined by two vectors, *e.g.* we can use the two vectors $|0_z\rangle$ and $|1_z\rangle$. We have then

$$|\psi\rangle = \alpha\,|0_z\rangle + \beta\,|1_z\rangle\,, \tag{1.11}$$

where α, $\beta \in \mathbb{C}$ are the probability amplitudes of the basis vectors $|0_z\rangle$ and $|1_z\rangle$, respectively. As the set of basis vectors is orthonormal, one has

$$|\alpha|^2 + |\beta|^2 = 1. \tag{1.12}$$

Inserting equation 1.11 in equation 1.10 results in

$$\hat{U}\Big((\alpha\,|0_z\rangle + \beta\,|1_z\rangle)\,|e\rangle\Big) = \Big(\alpha\,|0_z\rangle + \beta\,|1_z\rangle\Big) \cdot \Big(\alpha\,|0_z\rangle + \beta\,|1_z\rangle\Big). \tag{1.13}$$

Due to the linearity of quantum mechanics, this equation can be rewritten:

$$\alpha\Big(\hat{U}(|0_z\rangle\,|e\rangle)\Big) + \beta\Big(\hat{U}(|1_z\rangle\,|e\rangle)\Big) = \alpha^2\,|0_z\rangle + \beta^2\,|1_z\rangle\,. \tag{1.14}$$

Here we have used the relations $|0_z\rangle \cdot |1_z\rangle = |1_z\rangle \cdot |0_z\rangle = 0$ (the basis vectors are orthonormal). Moreover, if the transformation $\hat{U}$ is capable of cloning arbitrary states $|\psi\rangle$, then it is also capable of cloning all basis vectors onto $|e\rangle$ (meaning that $\hat{U}(|0_z\rangle\,|e\rangle) = |0_z\rangle\,|0_z\rangle$ and $\hat{U}(|1_z\rangle\,|e\rangle) = |1_z\rangle\,|1_z\rangle$), which leads to

$$\alpha\,|0_z\rangle + \beta\,|1_z\rangle = \alpha^2\,|0_z\rangle + \beta^2\,|1_z\rangle\,. \tag{1.15}$$

This equation does generally not hold. It is only true if one of the amplitudes, α or β, is unity and the other is zero. This means that the state $|\psi\rangle$ corresponds to one of the chosen basis vectors, $|0_z\rangle$ or $|1_z\rangle$, which is in general not the case, such that we state that cloning of arbitrary qubits $|\psi\rangle$ is not possible. The no-cloning theorem represents one of the most important results for quantum information applications and we shall see later why.

Although it has been shown that perfect cloning using the general procedure shown in Figure 1.2 is not possible, it is possible to increase the cloning fidelity up to $\frac{5}{6} \approx 83\%$ for copying single qubits. A detailed analysis for cloning of more complex qubit systems is given in references [88, 89, 90].

1.2.4. Systems of two qubits

A classical system of two bits can be in four different states $|0\rangle_a\,|0\rangle_b$, $|0\rangle_a\,|1\rangle_b$, $|1\rangle_a\,|0\rangle_b$, and $|1\rangle_a\,|1\rangle_b$. Here, the subscripts a and b denote the two qubits and we shall see later why this notation is useful. Similar to the single qubit case discussed before, a system of two qubits can be in a superposition of the form

$$|\psi\rangle = \alpha_{00}\,|0\rangle_a\,|0\rangle_b + \alpha_{01}\,|0\rangle_a\,|1\rangle_b + \alpha_{10}\,|1\rangle_a\,|0\rangle_b + \alpha_{11}\,|1\rangle_a\,|1\rangle_b\,, \tag{1.16}$$

where α_{00}, α_{01}, α_{10}, $\alpha_{11} \in \mathbb{C}$ and $|\alpha_{00}|^2 + |\alpha_{01}|^2 + |\alpha_{10}|^2 + |\alpha_{11}|^2 = 1$. For $\alpha_{00} = \alpha_{01} = \alpha_{10} = \alpha_{11} = \frac{1}{2}$ a special case is obtained. The state $|\psi\rangle$ is separable in two independent substates $|\psi\rangle_a$ and $|\psi\rangle_b$:

$$\begin{aligned} |\psi\rangle &= \frac{1}{2}\,|0\rangle_a\,|0\rangle_b + \frac{1}{2}\,|0\rangle_a\,|1\rangle_b + \frac{1}{2}\,|1\rangle_a\,|0\rangle_b + \frac{1}{2}\,|1\rangle_a\,|1\rangle_b && (1.17)\\ &= \frac{1}{\sqrt{2}}\,(|0\rangle_a + |1\rangle_a)\;\frac{1}{\sqrt{2}}\,(|0\rangle_b + |1\rangle_b) && (1.18)\\ &= |\psi\rangle_a\;|\psi\rangle_b\,. && (1.19) \end{aligned}$$

Each qubit state $|\psi\rangle_a$ and $|\psi\rangle_b$ can be seen as an individual, and independent, system that does not influence the other. But in some special cases, such a separation in two subsystems is not possible. To see this, consider the following two-qubit states:

$$|\Phi^+\rangle = \frac{1}{\sqrt{2}}\left(|0\rangle_a|0\rangle_b + |1\rangle_a|1\rangle_b\right), \tag{1.20}$$

$$|\Phi^-\rangle = \frac{1}{\sqrt{2}}\left(|0\rangle_a|0\rangle_b - |1\rangle_a|1\rangle_b\right), \tag{1.21}$$

$$|\Psi^+\rangle = \frac{1}{\sqrt{2}}\left(|0\rangle_a|1\rangle_b + |1\rangle_a|0\rangle_b\right), \tag{1.22}$$

$$|\Psi^-\rangle = \frac{1}{\sqrt{2}}\left(|0\rangle_a|1\rangle_b - |1\rangle_a|0\rangle_b\right). \tag{1.23}$$

They form a complete orthonormal basis in the two-qubit (4d) Hilbert space and permit generating arbitrary two-qubit states of the form given in equation 1.16 using the superposition principle. There is no way to write these states in a separable form of two individual qubit states $|\psi\rangle_a$ and $|\psi\rangle_b$. These four particular states are generally referred to be the four *Bell states*[7], and they show remarkable properties, as we shall demonstrate in the following.

For example, consider the state $|\Phi^+\rangle$. If a measurement is performed on qubit a, one obtains the result '0' respectively '1' with equal probabilities of one half. However, if qubit a is measured to be '0' ('1'), then the quantum state is reduced to be $|0\rangle_a|0\rangle_b$ ($|1\rangle_a|1\rangle_b$). Consequently, a measurement performed on qubit b gives the same result as for qubit a. The same is true when first measuring qubit b and thereafter a. The measurement outcomes are said to be correlated. So far, the observations seem to be not *remarkable* and could be attributed to classical states, for example a statistical mixture of the two-qubit states $|0\rangle_a|0\rangle_b$ and $|1\rangle_a|1\rangle_b$, respectively. What is *remarkable*, is the fact that these correlations are even then observed, when some operations are performed on the qubits before the measurement. For example, consider the operation $\hat{U}_{\theta=\pi/2}$, whose action is described by

$$\hat{U}_{\theta=\pi/2,j}|0\rangle_j = \frac{1}{\sqrt{2}}\left(|0\rangle_j + |1\rangle_j\right), \tag{1.24}$$

$$\hat{U}_{\theta=\pi/2,j}|1\rangle_j = \frac{1}{\sqrt{2}}\left(|1\rangle_j - |0\rangle_j\right). \tag{1.25}$$

Here, the subscript j denotes the qubits a and b. Concerning the Bloch sphere picture (see Figure 1.1), this operation represents a qubit rotation by an angle of $\theta = \frac{\pi}{2}$. Applying this operation to the state given in equation 1.20 results in

$$\hat{U}_{\theta=\pi/2,a}\hat{U}_{\theta=\pi/2,b}|\Phi^+\rangle = \frac{1}{\sqrt{2}}\left(|0\rangle_a|0\rangle_b + |1\rangle_a|1\rangle_b\right) = |\Phi^+\rangle. \tag{1.26}$$

[7]This notation is done in honour to the famous physicist John S. Bell.

Consequently, applying a rotation operation on this Bell state leaves the state unchanged and the same correlations between the measurements on qubits a and b are obtained. When applying the same procedure to the other Bell states, the following results are obtained:

$$\hat{U}_{\theta=\pi/2,a}\hat{U}_{\theta=\pi/2,b}\left|\Phi^-\right\rangle = \left|\Psi^+\right\rangle \tag{1.27}$$

$$\hat{U}_{\theta=\pi/2,a}\hat{U}_{\theta=\pi/2,b}\left|\Psi^+\right\rangle = -\left|\Phi^-\right\rangle \tag{1.28}$$

$$\hat{U}_{\theta=\pi/2,a}\hat{U}_{\theta=\pi/2,b}\left|\Psi^-\right\rangle = \left|\Psi^-\right\rangle . \tag{1.29}$$

We attribute such strong correlations, that are observed even after an operation is performed, to *entangled* states and their rotation invariance. When both qubits of an entangled state are rotated, then another, or the same, entangled state is obtained. In subsection 1.2.5 we show that such strong correlations go beyond the correlation strength obtained in classical physics [16] and that information about the individual qubit states does not exist until a measurement is performed. Moreover, equations 1.20-1.23 are time-independent. This leads to another remarkable property of entangled quantum states. When a measurement on one qubit is performed, then the other is *instantaneously* projected in the corresponding correlated state. This causes strong contradictions when trying to explain this behaviour in terms of classical physics. Nothing prevents us from separating the two qubits by a large (space-like) distance before applying some qubit operations, and finally performing the measurement. Surprisingly, in this case, quantum physics predicts that *exactly nothing* changes. From a classical physics point of view this is astonishing as the theory of relativity predicts that space-like separated events cannot influence each other. As a consequence, we would expect less strong correlations. These contradictory behaviours predicted by classical and quantum physics were already vividly debated in the 1920s and 1930s, and divided the physics community in two groups. Some physicists (N. Bohr, W. Heisenberg, W. Pauli, ...) defended quantum physics and stated that although we do not know how it happens, a measurement on one qubit projects instantaneously the second qubit into a defined state. Others (A. Einstein, B. Podolsky, N. Rosen (EPR [8]), ...) did not share this point of view and they argued that there is an underlying (yet unknown) physical reality pre-defining the measurement outcomes. In either case, enormous changes in our minds are required. But can we find out which of the two statements is correct? Fortunately, thanks to the important works of J. S. Bell, J. Clauser, M. Horne, A. Shimony, and R. Holt [16, 17] we can answer this question with a 'yes' as shown in subsection 1.2.5.

1.2.5. The Bell, Clauser, Horne, Shimony and Holt inequalities

At first glance, the difference in the two views of instantaneous projection and pre-defined measurement outcomes might be not very important, if they were to produce the same experimental results. However, it seems somewhat odd that an experiment in which the information about the measurement outcome is (in principle) known all the time

produces the same results like another experiment in which information is 'generated' or determined only at the time of a measurement. But for almost 30 years it seemed that the theories of Bohr and EPR indeed predict the same measurement outcomes. In the following, a measurement is shown that produces different results for the two theoretical assumptions, which permits determining which of the two theories is the suitable one. An experimental schematic is shown in Figure 1.3.

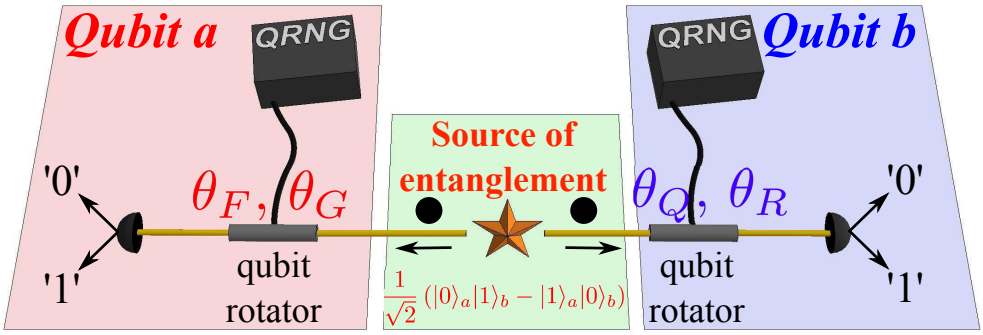

Figure 1.3.: Experimental schematic for testing whether the measurement outcomes for entangled qubit pairs are pre-determined or not. An entanglement source generates repeatedly the state $\frac{1}{\sqrt{2}}(|0\rangle_a|1\rangle_b - |1\rangle_a|0\rangle_b)$ and sends one qubit to each analyser (red and blue). When the qubits arrive, they are randomly rotated by an angle θ_F, θ_G, θ_Q, or θ_R and measured. The choice on the angle is made by a high speed quantum random number generator (QRNG). The apparatus are space-like separated which prohibits classical communication between the qubits.

We perform our analysis on the particular maximally entangled Bell state $|\Psi^-\rangle = \frac{1}{\sqrt{2}}(|0\rangle_a|1\rangle_b - |1\rangle_a|0\rangle_b)$, but either one of the four Bell states would result in the same analysis. If we measure a qubit in the state $|0\rangle$ ($|1\rangle$) we note a value of $+1$ (-1), which is often referred to be a dichotomic measurement. This means in other words, if Alice and Bob multiply their obtained values ± 1, they obtain:

- as a multiplication result $+1$ for identical measurement outcomes and we speak about a correlated measurement;
- as a multiplication result -1 for opposed measurement outcomes and we speak about an anti-correlated measurement;

Before a measurement is performed, each qubit is subjected to an operation $\hat{U}_{\theta,j}$ defined as:

$$\hat{U}_{\theta,j}|0\rangle_j = \cos\theta_j|0\rangle_j + \sin\theta_j|1\rangle_j, \tag{1.30}$$

$$\hat{U}_{\theta,j}|1\rangle_j = \cos\theta_j|1\rangle_j - \sin\theta_j|0\rangle_j. \tag{1.31}$$

Here, the subscript j denotes the qubit (a or b) to which qubit the operation is applied. $\theta \in \mathbb{R}$ is a rotation angle. For the qubit a we choose randomly to measure it after a rotation of θ_F or θ_G. In this case we obtain the measurement outcomes $F = \pm 1$ or $G = \pm 1$. Similarly, qubit b is measured randomly either at θ_Q or θ_R resulting in the outcomes $Q = \pm 1$ or $R = \pm 1$. The measurement apparatus for the two qubits are assumed to be space-like separated and the choice on which angle θ_F, θ_G, θ_Q, and θ_R is used is done in such a fashion that the two apparatus cannot communicate their respective operations in a causal fashion. Consequently, a measurement on qubit a cannot causally influence the measurement outcomes on qubit b and vice versa. In the following, we introduce a new measurement quantity Γ, defined as

$$\Gamma = FQ + GQ + GR - FR = F\,(Q - R) + G\,(Q + R). \tag{1.32}$$

As $F, G, Q, R = \pm 1$, it is obvious that either $Q - R = 0$ or $Q + R = 0$ and consequently $\Gamma = \pm 2$.

EPR picture

We take now the role of EPR and assume that measurement outcomes can be predicted even *before* a measurement is carried out [8]. Let $p(f, g, q, r)$ be the probability that the quantum system is in a state in which $F = f$, $G = g$, $Q = q$, and $R = r$. The variables f, g, q, and r might be hidden such that we do not know how to measure them, but they exist and are an object of physical reality. The mean value of of the quantity Γ is then

$$E(\Gamma) \;=\; \sum_{f,g,q,r} p(f, g, q, r) \cdot \Gamma, \tag{1.33}$$

where E denotes the mean value. As the sum of the probabilities has to equal unity, it follows that

$$-2 \leq E(\Gamma) \leq 2. \tag{1.34}$$

This implies furthermore that

$$-2 \leq E(FQ) + E(GQ) + E(GR) - E(FR) \leq 2, \tag{1.35}$$

which is referred to as the Bell, Clauser, Horne, Shimony, and Holt (B-CHSH) inequality[8] [17]. Remarkably, we have derived this inequality independently of the four angles θ_F, θ_G, θ_Q, and θ_R. In order to experimentally measure the quantities contained in equation 1.35, the experiment needs to be repeated several times. For each measurement configuration (θ_F and θ_Q, θ_G and θ_Q, θ_G and θ_R, θ_F and θ_R) the obtained results (± 1) are multiplied and the corresponding mean value is calculated after several repetitions towards verifying, or violating, equation 1.35.

[8] A set of inequalities was first introduced by Bell, however it was not obvious how to apply them to a real experiment. The equation shown here is the one derived by Clauser, Horne, Shimony, and Bolt, which stands for an extended and simplified version of the Bell's inequalities. In this form it is straightforward to apply it to a real experiment.

Bohr's picture

We now take the role of Bohr and colleagues and consider that the measurement outcomes are not pre-defined. We consider the following particular set of rotation angles:

$$\theta_F = \frac{\pi}{4}, \qquad \theta_G = 0, \qquad \theta_Q = \frac{\pi}{8}, \qquad \theta_R = -\frac{\pi}{8}. \tag{1.36}$$

Then, we proceed to calculate the mean values of FQ, GQ, GR, and FR.

Calculating $E(FQ)$

The initial two-qubit state reads

$$|\Psi^-\rangle = \frac{1}{\sqrt{2}} \left(|0\rangle_a |1\rangle_b - |1\rangle_a |0\rangle_b \right). \tag{1.37}$$

After applying the rotations $\theta_F = \frac{\pi}{4}$ and $\theta_Q = \frac{\pi}{8}$ it comes

$$\begin{aligned} |\Psi^-_{FQ}\rangle \;=\; & \frac{1}{\sqrt{2}} \Bigg(\left[\cos\frac{\pi}{4} |0\rangle_a + \sin\frac{\pi}{4} |1\rangle_a \right] \cdot \left[\cos\frac{\pi}{8} |1\rangle_b - \sin\frac{\pi}{8} |0\rangle_b \right] \\ & - \left[\cos\frac{\pi}{4} |1\rangle_a - \sin\frac{\pi}{4} |0\rangle_a \right] \cdot \left[\cos\frac{\pi}{8} |0\rangle_b + \sin\frac{\pi}{8} |1\rangle_b \right] \Bigg). \end{aligned} \tag{1.38}$$

The corresponding mean value is then given by

$$\begin{aligned} E(FQ) \;=\; & \left| \frac{1}{\sqrt{2}} \right|^2 \Bigg(\underbrace{\frac{\left(\cos\frac{\pi}{8} + \sin\frac{\pi}{8}\right)^2}{2} \cdot (-1)}_{{}_a\langle 0|_b \langle 1||\Psi^-_{FQ}\rangle} + \underbrace{\frac{\left(\cos\frac{\pi}{8} - \sin\frac{\pi}{8}\right)^2}{2} \cdot (+1)}_{{}_a\langle 0|_b \langle 0||\Psi^-_{FQ}\rangle} \\ & + \underbrace{\frac{\left(\cos\frac{\pi}{8} + \sin\frac{\pi}{8}\right)^2}{2} \cdot (-1)}_{{}_a\langle 1|_b \langle 0||\Psi^-_{FQ}\rangle} + \underbrace{\frac{\left(\cos\frac{\pi}{8} - \sin\frac{\pi}{8}\right)^2}{2} \cdot (+1)}_{{}_a\langle 1|_b \langle 1||\Psi^-_{FQ}\rangle} \Bigg) \\ =\; & -\frac{1}{\sqrt{2}}. \end{aligned} \tag{1.39}$$

For easier understanding, the corresponding two-qubit contribution is written under each term.

Calculating $E(GQ)$ and $E(GR)$

The mean values of $E(GQ)$ and $E(GR)$ are performed in the same fashion as outlined above and both of them deliver as a result:

$$E(GQ) = -\frac{1}{\sqrt{2}}, \text{ and} \tag{1.40}$$

$$E(GR) = -\frac{1}{\sqrt{2}}. \tag{1.41}$$

Calculating $E(FR)$

The initial two-qubit state reads

$$|\Psi^-\rangle = \frac{1}{\sqrt{2}} \left(|0\rangle_a |1\rangle_b - |1\rangle_a |0\rangle_b \right). \tag{1.42}$$

After applying the rotations $\theta_F = \frac{\pi}{4}$ and $\theta_R = -\frac{\pi}{8}$, and the trigonometric identities $\cos(x) = \cos(-x)$ respectively $\sin(x) = -\sin(-x)$, it comes

$$\begin{aligned} |\Psi^-_{FR}\rangle &= \frac{1}{\sqrt{2}} \Bigg(\left[\cos\frac{\pi}{4} |0\rangle_a + \sin\frac{\pi}{4} |1\rangle_a \right] \cdot \left[\cos\frac{\pi}{8} |1\rangle_b + \sin\frac{\pi}{8} |0\rangle_b \right] \\ &\quad - \left[\cos\frac{\pi}{4} |1\rangle_a - \sin\frac{\pi}{4} |0\rangle_a \right] \cdot \left[\cos\frac{\pi}{8} |0\rangle_b - \sin\frac{\pi}{8} |1\rangle_b \right] \Bigg). \end{aligned} \tag{1.43}$$

The corresponding mean value is then given by

$$\begin{aligned} E(FR) &= \left| \frac{1}{\sqrt{2}} \right|^2 \Bigg(\underbrace{\frac{\left(\cos\frac{\pi}{8} - \sin\frac{\pi}{8}\right)^2}{2} \cdot (-1)}_{{}_a\langle 0|_b\langle 1||\Psi^-_{FR}\rangle} + \underbrace{\frac{\left(\cos\frac{\pi}{8} + \sin\frac{\pi}{8}\right)^2}{2} \cdot (+1)}_{{}_a\langle 0|_b\langle 0||\Psi^-_{FR}\rangle} \\ &\quad + \underbrace{\frac{\left(\sin\frac{\pi}{8} - \cos\frac{\pi}{8}\right)^2}{2} \cdot (-1)}_{{}_a\langle 1|_b\langle 0||\Psi^-_{FR}\rangle} + \underbrace{\frac{\left(\sin\frac{\pi}{8} + \cos\frac{\pi}{8}\right)^2}{2} \cdot (+1)}_{{}_a\langle 1|_b\langle 1||\Psi^-_{FR}\rangle} \Bigg) \\ &= +\frac{1}{\sqrt{2}}. \end{aligned} \tag{1.44}$$

Back to Bohr's picture

We can now calculate the value of the quantity $E(FQ) + E(GQ) + E(GR) - E(FR)$ and obtain

$$E(FQ) + E(GQ) + E(GR) - E(FR) = -2\sqrt{2} \approx -2.8284 < -2. \tag{1.45}$$

This result is in contrary to the B-CHSH inequality (equation 1.35), predicting for pre-determined measurement outcomes

$$-2 \leq E(FQ) + E(GQ) + E(GR) - E(FR) \leq 2.$$

Consequently, an experimentally accessible measurement quantity was found, that allows us to answer the question whether the measurement outcomes are pre-determined (EPR picture), or whether they are only generated at the time the measurement is performed

(Bohr's picture). For reasons of simplicity we introduce a new notation that is applied for the rest of this thesis:

$$S = E(FQ) + E(GQ) + E(GR) - E(FR). \tag{1.46}$$

In this equation S is generally referred to be the *Bell parameter*, that quantifies how much quantumness (entanglement) the investigated state contains. Many experiments have been performed using various entanglement supports and they all confirmed Bohr's picture by delivering $|S| > 2$. Four of them are found in this thesis, see sections 2.3, 2.4, 2.5 and chapter 4. Consequently, it is likely that there is no pre-existing information and the measurement outcomes are only defined upon a measurement. This means that one qubit is randomly projected onto a given state and the other qubit is instantaneously projected on the corresponding correlated state. Such strong correlations are a purely quantum behaviour and have no classical equivalent.

As a summary, we state that entangled quantum systems are to be considered as a whole, in the precise sense that they cannot be treated as individual (separable) systems.

1.3. Commonly used qubit carriers and observables

1.3.1. Qubit carriers

In classical, as well as in quantum information, we need an *information carrier* of whom some properties are manipulated in order to encode information on it. In the quantum world, the information carrier is referred to as the *qubit carrier*. Information is then coded onto different observables of the respective carrier. All over the world, many different qubit carriers are extensively studied. The choice on the preferred carrier/observable depends strongly on the desired application. Some examples are given in the following:

- When long distance distribution of qubits is desired, photons are the preferred qubit carrier (flying qubit). Their high speed of travel and (almost) decoherence free propagation in free-space and optical fibres makes them an ideal candidate for distribution tasks. Many properties (observables) of photons are suitable for information coding, *e.g.* the polarization, time-bin, and many more [48, 91]. Manipulation of photonic qubits is conveniently achieved by standard optics, such as birefringent plates and/or interferometers.

- Quantum information processing tasks require typically the interaction of two qubits, which is difficult to achieve for photons. This is why for these tasks, one prefers in general stationary qubit systems, in which the qubits can be brought close to each other for sufficiently long interaction times. Some examples are Josephson junctions [92, 93], cold ions [94, 95, 96, 97, 98], cold and ultracold atoms [99, 100, 101, 102], colour centres [103], and many more. Many observables

are exploited for these carriers, such as the spin of an electron or nucleus, energy levels, vibration modes.

- The storage of quantum information requires obviously stationary devices and many different approaches are studied all over the world. They are either based on a solid state [104, 53, 54], hot [105, 106, 107, 108] and cold atoms [109, 110, 111, 112, 113, 114, 115, 116, 117, 118, 119, 120, 121, 122, 123, 124, 125], cold ions [50] and many more. In most of the cases, they use different energy levels as observables. The reader can find a good summary about current quantum memory devices in the following references [126, 46, 127].

The work of this thesis is mainly outlined around the distribution of qubits for quantum communication tasks, such that the preferred qubit carrier is the photon. The qubit properties '0' and '1' are encoded by manipulating various properties of the photon. In the following, we briefly describe the two most exploited strategies to encode information onto a photon, namely via the observable polarization and energy-time. These two strategies are also heavily used in this thesis, and explained in more detail in the corresponding sections. At the end, a quick summary about other photonic entanglement observables is given.

1.3.2. Polarization observable

One of the most exploited photonic entanglement observables is the polarization state of the photon, for which we can define three conjugate bases, as shown in Figure 1.4. Here $|H\rangle$ and $|V\rangle$ define the basis of horizontally and vertically polarized photons. $|D\rangle = \frac{1}{\sqrt{2}}(|H\rangle + |V\rangle)$ and $|A\rangle = \frac{1}{\sqrt{2}}(|H\rangle - |V\rangle)$ define the basis of diagonally and anti-diagonally polarized photons. Finally, $|R\rangle = \frac{1}{\sqrt{2}}(|H\rangle + i\,|V\rangle)$ and $|L\rangle = \frac{1}{\sqrt{2}}(|H\rangle - i\,|V\rangle)$ define the basis of circular right and circular left polarized photons. Polarization encoded photonic qubits are conveniently manipulated using birefringent optics, such as half-wave plates and quarter-wave plates. This way, it is possible to generate any state of the form $\cos\frac{\theta}{2}\,|H\rangle + e^{i\,\phi}\sin\frac{\theta}{2}\,|V\rangle$, with θ, $\phi \in \mathbb{R}$. The polarization state is then analysed using a polarizing beam-splitter (PBS), followed by single photon detectors at each of its outputs. The advantage of polarization encoded qubits is that they are relatively simple to analyse by employing the above mentioned optical components. A drawback is that long distance distribution of polarization entanglement requires several precautions as the photon polarization state is typically rotated in optical fibres and this rotation has to be compensated in a real-time fashion [128, 129, 130, 131].

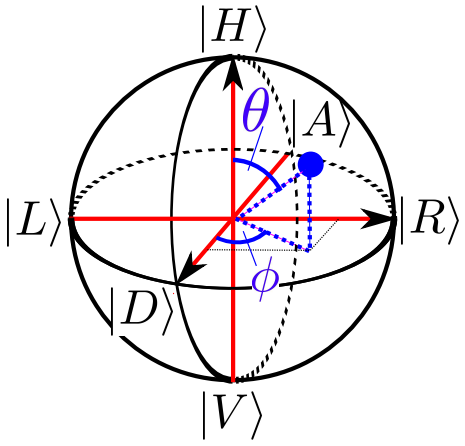

Figure 1.4.: The Bloch sphere representation for polarization qubits. The three orthonormal basis vectors are $|H\rangle$, $|V\rangle$, $|D\rangle$, $|A\rangle$, $|R\rangle$, and $|L\rangle$, standing for horizontal, vertical, diagonal, anti-diagonal, circular-right, and circular-left polarized light, respectively.

1.3.3. Energy-time / time-bin observable

Another possibility to encode information onto a photon is achieved when considering two possible qubit arrival times, say early ($|e\rangle$) and late ($|l\rangle$) [132, 133, 134]. Quantum physics also permits generating a photon being in a superposition of early and late times. An experimental implementation is shown in Figure 1.5.
A photon produced at a given time $t = 0$ is sent though an unbalanced Mach-Zehnder interferometer in which the photon can take both paths (long and short) with the same

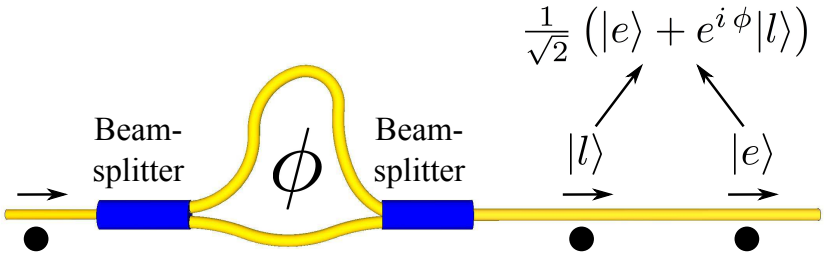

Figure 1.5.: Principle of generating energy-time or time-bin photonic qubits. A photon is sent to an unbalanced Mach-Zehnder interferometer. At the output the photon is in a superposition state of early and late states $\frac{1}{\sqrt{2}}\left(|e\rangle + e^{i\,\phi}\,|l\rangle\right)$ linked by a path length difference dependent phase relation ϕ.

probabilities. At the interferometer output, the quantum state reads

$$|\psi\rangle = \frac{1}{\sqrt{2}} \left(|e\rangle + e^{i\,\phi} \, |l\rangle \right) . \tag{1.47}$$

These two contributions are linked by a phase factor ϕ, that is given by the path length difference between the two arms in the interferometer. Typically, the amplitudes of the vectors $|e\rangle$ and $|l\rangle$ are not adjusted in energy-time protocols, such that one is left with only two complementary bases which are defined by the phase ϕ. One basis is obtained for $\phi = 0$ and $\phi = \pi$, while the other basis is given by $\phi = -\frac{\pi}{2}$ and $\phi = \frac{\pi}{2}$.

Energy-time encoded qubits are manipulated via tuning the phase ϕ, for example by changing the optical path length difference. Qubit analysis is also performed using similar interferometers.

A quick remark is given on the difference between energy-time and time-bin. We typically refer to time-bin qubits when the qubit generation process takes place at regular instants, *i.e.* the qubit is generated at the time t, or $t + \delta t$, or $t + 2\,\delta t$, ..., where δt is a fixed time interval. This offers the advantage that the qubit arrival times are precisely known (modulus δt), which allows synchronizing photonic entanglement sources, as required for entanglement swapping protocols. On the other hand, energy-time qubits are the extended version of time-bin qubits. In this case the qubit generation time remains completely unknown. Typically, energy-time qubits are easier to generate, but synchronization of such energy-time sources for entanglement swapping procedures requires a more elaborate experimental setup [58].

Energy-time and time-bin qubits can be distributed over long distances in optical fibre networks without active polarization state stabilization (the polarization state of the photons is irrelevant in these schemes). A drawback is that highly stabilized interferometers are required in order to achieve a good phase stability.

1.3.4. Other photonic observables

There are various other schemes employed to encode information onto photons. A few of them are listed in the following.

One method is to use frequency-bin encoded qubits. The natural basis is defined by the vectors $|0\rangle_n = |\omega_1\rangle$ and $|1\rangle_n = |\omega_2\rangle$ and the complementary basis by $|0\rangle_c = \frac{1}{\sqrt{2}} (|\omega_1\rangle + |\omega_2\rangle)$ and $|1\rangle_c = \frac{1}{\sqrt{2}} (|\omega_1\rangle - |\omega_2\rangle)$, where, ω_1 and ω_2 denote two angular frequencies of the photon. Manipulation of frequency-bin encoded photons is achieved using acousto-optical modulators or electro-optical modulators in combination with optical filters [135, 136, 137, 138, 139].

Another strategy takes advantage of the orbital angular momentum of the photon as a resource for encoding information. Although this strategy is difficult to apply in fibre-optical networks, as the corresponding optical modes are not guided, a free-space based network might be established using such a strategy [140].

Finally, by combining various of these above mentioned techniques it is possible to encode multiple qubits onto one photon [141, 142, 143, 144, 145, 146], generally referred as the generation of hyper-entanglement.

1.4. Quantum key distribution

In this section, the field of quantum key distribution (QKD) is introduced. Two protocols are introduced, namely the BB84, and Ekert protocol. When being properly used, both protocols offer the generation of absolutely secret and random keys that are shared only between two communication partners. This means that Kerckhoffs's assumption is fulfilled and absolutely secure communication can be established. The section starts with introducing the BB84 protocol (single qubits), followed by a security proof. Then, the Ekert protocol (two qubits) is outlined and limitations of current QKD protocols are discussed.

1.4.1. The BB84 protocol

The first quantum communication protocol towards establishing secret keys between Alice and Bob has been reported by Charles Bennett and Gilles Brassard in 1984 [25][9]. The protocol is meant for single qubit operation and a schematic is shown in Figure 1.6. Suppose that Alice prepares initial qubits in the state

$$|\psi\rangle_{\text{ini}} = |0\rangle\,. \tag{1.48}$$

She performs randomly and with equal probabilities one out of four operations $\hat{U}_{an0,an1,ac0,ac1}$ on this qubit, defined as:

$$\hat{U}_{an0}\,|0\rangle = |0\rangle \tag{1.49}$$
$$\hat{U}_{an1}\,|0\rangle = |1\rangle \tag{1.50}$$
$$\hat{U}_{ac0}\,|0\rangle = \frac{1}{\sqrt{2}}(|0\rangle + |1\rangle) \tag{1.51}$$
$$\hat{U}_{ac1}\,|0\rangle = \frac{1}{\sqrt{2}}(-|0\rangle + |1\rangle). \tag{1.52}$$

The subscripts n and c denote the natural and conjugate bases, respectively. The subscripts 0 (1) means that a '0' ('1') qubit is prepared in the corresponding basis[10]. In order to obtain a *faithful* (and high-speed) randomness we prefer using a quantum random number generator (QRNG) to perform this task. Alice can gain information about

[9] It is debated to whom this communication protocol should be ascribed to. Already in the beginning of the 70s, many years before Bennett and Brassard, a similar protocol was developed by Stephen Wiesner, however only published in 1983 [88].

[10] In the Bloch sphere representation, see Figure 1.1, n and c correspond to the axes z and x.

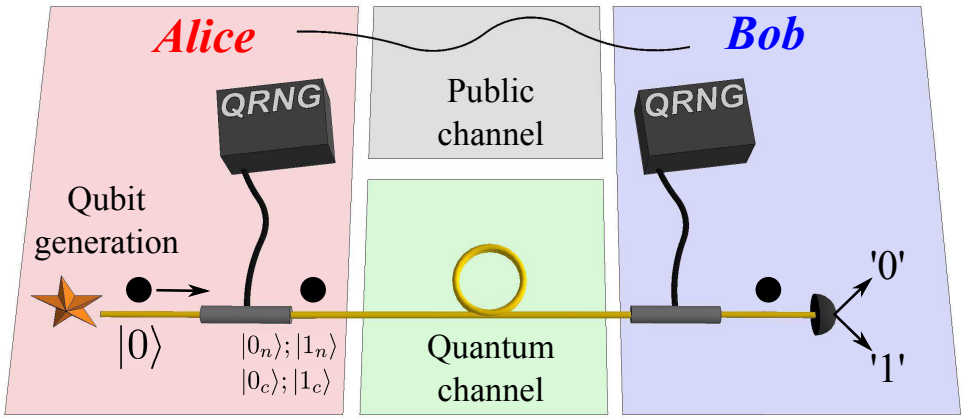

Figure 1.6.: Schematic of the BB84 protocol. On Alice's side qubits in the state $|0\rangle$ are prepared and manipulated to be in one out of four states $|0_n\rangle$, $|1_n\rangle$, $|0_c\rangle$, or $|1_c\rangle$, according to a QRNG. The qubit is sent via a quantum channel to Bob, where it is further manipulated and detected. Alice and Bob compare (some) settings of their respective QRNGs via public channel communication and post-select a correlated string of measurement outcomes, which can be further processed as a secret key.

which operation has been performed by reading out the QRNG, in principle at any time she wants[11]. The manipulated qubit is then sent to Bob via a quantum channel, who chooses randomly (by the help of a QRNG) to perform one out of two operations $\hat{U}_{bn,bc}$, whose actions are described by

$$\hat{U}_{bn}|0\rangle = |0\rangle_b \qquad \hat{U}_{bn}|1\rangle = |1\rangle_b\,, \tag{1.53}$$

$$\hat{U}_{bc}|0\rangle = \frac{1}{\sqrt{2}}(|0\rangle_b - |1\rangle_b) \qquad \hat{U}_{bc}|1\rangle = \frac{1}{\sqrt{2}}(|0\rangle_b + |1\rangle_b). \tag{1.54}$$

In other words, Bob leaves the qubit unchanged ($\hat{U}_{bn}$) or rotates it ($\hat{U}_{bc}$). Having four possible operations at Alice's and two operations at Bob's side results in eight possible

[11] In practice, the QRNG or the device used to perform the operation $\hat{U}_{an0,an1,ac0,ac1}$ reveals this information earlier by changing the environment as a function of which operation is performed.

combinations, that are listed in the following:

$$\begin{aligned}
\hat{U}_{bn}\hat{U}_{an0}\left|0\right\rangle &= \left|0\right\rangle_b \\
\hat{U}_{bc}\hat{U}_{an0}\left|0\right\rangle &= \left(\left|0\right\rangle_b - \left|1\right\rangle_b\right)/\sqrt{2} \\
\hat{U}_{bn}\hat{U}_{an1}\left|0\right\rangle &= \left|1\right\rangle_b \\
\hat{U}_{bc}\hat{U}_{an1}\left|0\right\rangle &= \left(\left|0\right\rangle_b + \left|1\right\rangle_b\right)/\sqrt{2} \\
\hat{U}_{bn}\hat{U}_{ac0}\left|0\right\rangle &= \left(\left|0\right\rangle_b + \left|1\right\rangle_b\right)/\sqrt{2} \\
\hat{U}_{bc}\hat{U}_{ac0}\left|0\right\rangle &= \left|0\right\rangle_b \\
\hat{U}_{bn}\hat{U}_{ac1}\left|0\right\rangle &= \left(-\left|0\right\rangle_b + \left|1\right\rangle_b\right)/\sqrt{2} \\
\hat{U}_{bc}\hat{U}_{ac1}\left|0\right\rangle &= \left|1\right\rangle_b
\end{aligned} \tag{1.55}$$

What do we learn from the equation system 1.55? If Alice and Bob chose different bases for preparation and analysis, then the measurement outcome at Bob's place is random and no correlations with the prepared qubit at Alice are observed. On the other side, if Alice and Bob find that both their QRNGs chose a qubit operation having both the subscript n, or both having c, then the result of a qubit measurement at Bob's side is the results in the same qubit as prepared by Alice. Considering only these cases allows Alice and Bob to establish completely random, *but identical* data streams of 0s and 1s which can be further used as secret keys. This allows to fulfil Kerckhoffs's assumption and consequently to establish a secure communication link. The typical protocol of communication is summarized in the following:

- Alice prepares qubits in $\left|0\right\rangle$.
- The QRNG at Alices side chooses randomly for each qubit to prepare one out of four states $\left|0\right\rangle$, $\left|1\right\rangle$, $\left(\left|0\right\rangle + \left|1\right\rangle\right)/\sqrt{2}$, or $\left(-\left|0\right\rangle + \left|1\right\rangle\right)/\sqrt{2}$ but the information on which state is generated is not revealed.
- The prepared qubits are sent to Bob via a quantum channel.
- The QRNG at Bob's side chooses randomly to leave the qubits unchanged or to rotate them.
- Bob measures the state of the qubits and receives as results '0's or '1's, which he keeps as a secret.
- Alice communicates to Bob via a classical channel in which basis the quantum states have been generated (but she does not tell which states have been prepared).
- Bob tells Alice whether he used the same or the other bases. This process is called basis reconciliation.
- In cases when they used different bases, they drop their measurement outcomes.

- In cases when they used the same bases, then they know that Bob's measurement outcome is identical to the preparation of Alice and they keep this set of data.
- Doing so, Alice and Bob obtain identical data streams of zeros and ones, which can then be used as a private keys for cryptography tasks.

In the following, we demonstrate the security of the BB84 protocol.

1.4.2. The case of an eavesdropper

As we have seen in subsection 1.4.1, Alice and Bob obtain perfectly correlated measurement outcomes when post-selecting cases in which the same bases have been used. In this subsection we show that the presence of a potential eavesdropper, typically named Eve, introduces errors in the measured correlations. This permits Alice and Bob to reveal the presence of Eve. The strategy is then to repeatedly change the quantum channel until one is found where the key is generated with absolute privacy.

For this security proof, we assume two things. The qubit preparation and measurement apparatus on Alice's and Bob's side are secure, meaning that no (unwanted) information is leaking out. In addition, we assume that quantum physics is correct. Now, if Eve wants to gain information about the secret key that is established between the two communication partners, she has essentially two problems. First, she needs to perform some kind of measurement on the qubits that are sent from Alice to Bob, but the amount of information that she can gain is limited, if she does not know in which basis every single qubit has been prepared. Second, her attack needs to be as discreet as possible, such that Alice and Bob do not notice her. In the following, we consider these two problems for a simple intercept-resend attack. There are more complex eavesdropping attacks, however all of them introduce errors, such that Alice and Bob can reveal the presence of the spy [147, 148, 29].

Eve needs to measure the qubits

For reasons of simplicity we assume the case in which Eve measures Alice's qubits in the natural basis, n, *i.e.* she does not rotate the qubits. The measurement outcomes are summarized in Table 1.2. We see that Eve's measurements lead to the right result for all qubits that are prepared in the natural basis (n). However, if Alice prepared a qubit in the complementary basis (c), Eve's measurements are wrong in half of these cases. This means that the amount of information that Eve can gain on the qubits sent by Alice is limited, such that she will never obtain the full key (see also subsection 1.2.2).

Eve needs to resend qubits to Bob

In order to be as discreet as possible, Eve needs to send qubits to Bob, such that the qubit stream is not interrupted. In the intercept-resend attack, Eve prepares new qubits

Alice prepares	$\|0_n\rangle$	$\|1_n\rangle$	$\|0_c\rangle$	$\|0_c\rangle$	$\|1_c\rangle$	$\|1_c\rangle$
Eve measures	'0'	'1'	'0'	'1'	'0'	'1'
Probability	$\frac{1}{4}$	$\frac{1}{4}$	$\frac{1}{8}$	$\frac{1}{8}$	$\frac{1}{8}$	$\frac{1}{8}$
Comment	right outcome	right outcome	right outcome	wrong outcome	wrong outcome	right outcome

Table 1.2.: Eve intercepts the qubits sent by Alice and measures them in the natural basis n. When Alice prepares qubits in the n-basis, Eves measurements are always correct. But in half of the cases when Alice prepares qubits in the c-basis, Eve obtains wrong results.

(ideally identical to the measured ones) and sends them to Bob. As Eve measured all qubits in the n-basis, she will therefore prepare all new qubits also in the n-basis. As shown in Table 1.3, this introduces errors between the measurement outcomes at Alice's and Bob's side. If Alice and Bob compare (a fraction of) their data streams, they find that in 25% of the cases in which they expect identical measurement outcomes, opposed results are actually obtained. This procedure permits revealing the presence of the eavesdropper.

There are more sophisticated eavesdropping strategies, permitting Eve to obtain more information and/or introduce less errors between Alice and Bob. For instance, Eve can increase the obtainable amount of information on the qubits sent by Alice by cloning the qubits, storing them in a suitable memory, and performing a measurement only after Alice and Bob have announced their respective preparation and measurement bases. But it is important to note that no matter how clever Eve might be, she will always introduce some error. Considering all possible attacks, it has been shown that this error rate is at least 7% [149, 150, 151]. Therefore, if Alice and Bob compare a fraction of

Alice prepares	$\|0_n\rangle$	$\|1_n\rangle$	$\|0_c\rangle$	$\|0_c\rangle$	$\|0_c\rangle$	$\|0_c\rangle$	$\|1_c\rangle$	$\|1_c\rangle$	$\|1_c\rangle$	$\|1_c\rangle$
Eve measures	'0'	'1'	'0'	'0'	'1'	'1'	'0'	'0'	'1'	'1'
Eve sends	$\|0_n\rangle$	$\|1_n\rangle$	$\|0_n\rangle$	$\|0_n\rangle$	$\|1_n\rangle$	$\|1_n\rangle$	$\|0_n\rangle$	$\|0_n\rangle$	$\|1_n\rangle$	$\|1_n\rangle$
Bob measures†	'0'	'1'	'0'	'1'	'0'	'1'	'0'	'1'	'0'	'1'
Comment‡	✓	✓	✓	×	✓	×	×	✓	×	✓
Probability	$\frac{1}{4}$	$\frac{1}{4}$	$\frac{1}{16}$	$\frac{1}{16}$	$\frac{1}{16}$	$\frac{1}{16}$	$\frac{1}{16}$	$\frac{1}{16}$	$\frac{1}{16}$	$\frac{1}{16}$

Table 1.3.: Case study for the intercept-resend attack. †: only cases in which Alice and Bob have chosen the same basis, n or c, are considered as the measurement outcomes of other cases are anyway rejected. ‡: the symbol ✓ denotes a right measurement outcome (meaning that Eve's attack was discreet), while × symbolizes an error (indicating to Alice and Bob that there is an eavesdropper).

their data streams and they find an error rate of less than 7%, they are sure that a secret key can be established. This means that the BB84 protocol permits fulfilling Kerckhoffs's assumption. We can then use a simple cryptography algorithm, such as the Vernam cypher, in combination with the secret key, towards establishing absolutely secure and private communication between Alice and Bob. Today, such systems are already commercialized using photons as information carriers [30, 31, 34, 36, 35, 32].

1.4.3. The Ekert protocol for secure quantum key distribution

One of the main difficulties of the BB84 protocol is that the qubit preparation on Alice's side needs to be purely random and Alice has to make sure that no information about the qubit preparation leaks out of her apparatus before Bob has received the qubit. In addition, it is very difficult for Alice and Bob to verify whether the qubit preparation device operates really in a true random fashion. For example, Alice might be unaware that she bought a cryptosystem from Eve. Instead of a purely random qubit preparation, this system could use only a pseudo-random (obviously known to Eve) preparation procedure, which provides Eve with the possibility to infer the key. Such problems are overcome when using another entanglement based QKD protocol, developed by A. Ekert in 1991 [26] and further developed by C. H. Bennett [152]. A schematic of the this QKD scheme is given in Figure 1.7. Assume that a source of entanglement is placed in the middle between Alice and Bob and emits repeatedly the two-qubit entangled Bell state

$$|\Phi^+\rangle = \frac{1}{\sqrt{2}} \left(|0\rangle_a |0\rangle_b + |1\rangle_a |1\rangle_b \right), \tag{1.56}$$

where a and b denote a qubit sent to Alice and Bob, respectively. Although our example is based on the Bell state $|\Phi^+\rangle$, we note that any other Bell state could be used for this protocol. Alice and Bob employ each a QRNG to randomly rotate their respective qubits by either $\theta_n = 0$ or $\theta_c = \frac{\pi}{2}$, as defined by equations 1.24 and 1.25. Here, n and c denote the natural and conjugate bases, respectively. As demonstrated in subsection 1.2.4, performing such a rotation on both qubits does not alter the correlations between Alice and Bob ($\hat{U}_{\theta=\pi/2} |\Phi^+\rangle = |\Phi^+\rangle$). This means, if Alice and Bob do not rotate their qubits (they analyse their qubits in the n-basis), they will measure both either '0's or '1's. But even when they both rotate their qubits by $\frac{\pi}{2}$ (c-basis), nothing changes. As we have demonstrated in subsection 1.2.5, the individual qubit states do not exist until a measurement is performed.

The latter statement has two major implications. First, this ensures automatically a pure randomness on the measurement outcome of the *first* qubit (the outcomes '0' and '1' are equally probable), that projects the *second* qubit instantaneously into the

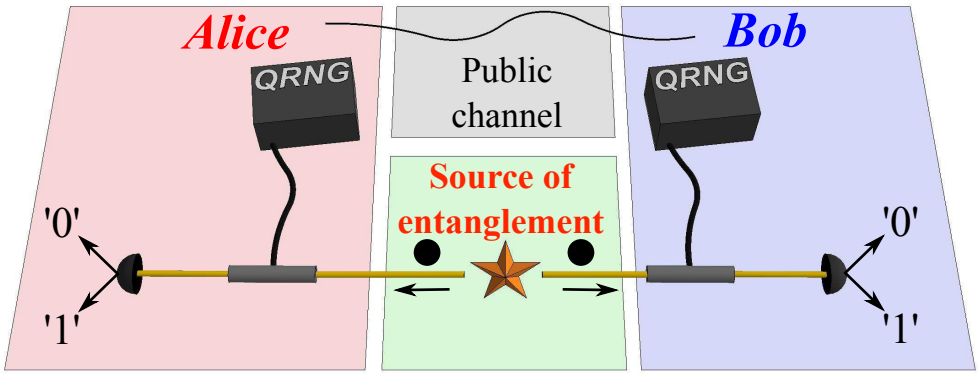

Figure 1.7.: Schematic of the Ekert protocol for QKD. A source of two-qubit entanglement is placed in the middle of the quantum channel shared by Alice and Bob. Both receive a qubit and perform randomly (with the help of a QRNG) a rotation on their respective qubits. Then they measure both their qubits and note down their results. After the measurement they communicate which rotation they have used on each qubit. If they find that they used the same rotations, the rotation invariance of entangled states ensures that they observe strong correlations between their measurement outcomes, *i.e.* they measure both either a '0' or a '1', see subsection 1.2.4. The obtained data streams can then be further processed for secure information encryption and decryption. A spy needs to perform some kind of measurement which projects the entangled state onto one of its two contributions. This reduces the correlation strength which gives Alice and Bob the means to reveal the presence of a spy by simply comparing a fraction of their data streams.

corresponding correlated state[12]. Second, as the individual qubits of the entangled quantum state are not defined until being measured, this permits revealing the presence of a spy in a relatively simple manner. A spy needs to perform some kind of measurement on the qubits being sent to Alice and Bob to obtain information. Such a measurement forces the qubit state to become determined, a qubit '0' or '1' is measured. If Eve resends then a qubits in a defined state, she reduces the correlation strengths observed between Alice and Bob, as demonstrated in subsection 1.2.5. Consequently, Alice and Bob only need to measure the correlation strength between (some of) their measurements to reveal the spy. As the computation of qubit error rates, introduced by the presence of a spy, is very similar to the one shown in subsection 1.4.2 for the BB84 protocol, we do not repeat

[12]The terms *first* and *second* qubit are somewhat misleading as they imply a causal connection between the measurements. However, such classical models do always lead to contradictions. For example when both qubits are measured simultaneously, which qubit shall be the *first* and *second*? This is why such a description should be avoided as much as possible in quantum physics (see also chapter 4). However, for this particular example, we prefer using a classical notation as it renders the reading easier.

this exercise here again. We just note that for an intercept-resend attack the error rate would also be of 25%, the same as for the implementation of the BB84 protocol using single qubits.

In the following, we summarize the steps of the Ekert QKD protocol, with entangled qubits.

- A source of entanglement sends the two-qubit entangled Bell state $|\Phi^+\rangle = \frac{1}{\sqrt{2}}(|0\rangle_a |0\rangle_b + |1\rangle_a |1\rangle_b)$ via a quantum channel to Alice and Bob.
- Alice and Bob receive the qubits and perform randomly qubit rotations by an angle $\theta_n = 0$ or $\theta_c = \frac{\pi}{2}$.
- Both label their measurement outcomes '0' and '1'.
- Alice and Bob communicate via a public channel which angle (or basis) they used for each measurement.
- They drop events in which they did not use the same rotation angles (bases).
- Cases in which both used the same angle (basis) lead to the observation of perfect measurement outcome correlations, meaning that both measured either a '0' or '1'. Such correlations are stronger than any correlations that could be obtained with classical means (see subsection 1.2.5).
- By continuously repeating this procedure, Alice and Bob obtain identical data streams of zeros and ones. This data stream can then be used as a private key for cryptography tasks.
- In order to reveal a spy, Alice and Bob compare a fraction of their data streams. A spy needs to perform some kind of measurement on the qubits, meaning that entanglement is broken. This reduces the correlation strength and consequently introduces errors between the recorded data streams.

Note that in reality the BB84 and Ekert protocols require the use of various sophisticated additional techniques in order to ensure the secure establishment of a key. Some examples are communication partner authentication, error correction and privacy amplification [27, 29], however it is not in the scope of this manuscript to list and detail all of them.

1.4.4. Limitations of QKD

The BB84 and Ekert protocols have shown that it is possible to establish, for the first time in human history, absolutely secret keys between distant partners. However, when it comes to practical implementations of QKD, there are some limiting factors. As cloning or amplification of qubits is forbidden (see subsection 1.2.3), and all qubit channels have some losses, severe problems are observed for long distance distribution of secret keys. As an example we consider the most widely used qubit carrier, the photon. Long distance distribution of photons is conveniently achieved using optical fibre networks. Although such fibre systems are extremely advanced, especially for photons in the telecom bands (wavelengths of 1300 - 1600 nm), they exhibit still a small loss figure of typically $\sim 0.2\,\mathrm{dB/km}$ (transmission of $\sim 95.5\%/\mathrm{km}$) at 1550 nm. Consequently, after a fibre transmission length of 100 km, only 1% of the generated qubits arrive. As qubits cannot be cloned or amplified, this means that they are irreversibly lost, which reduces drastically the communication bit rate. The problems are even more severe than that.

In order to detect a single photonic qubit, single photon detection devices are required, showing the highest possible quantum detection efficiency and the lowest possible dark count level (noise probability). The latter feature means that a detector will therefore announce, sometimes, the measurement of a qubit even if there was never a qubit. This introduces errors in the data streams at Alice and Bob. If the detector dark count rate becomes comparable to the real qubit rate (or to the expected error rate introduced by a potential spy), then it is not possible any more to establish a communication link. A solution might be to increase the generation rate of real qubits, such that even after a lossy fibre line, there are more qubits than dark counts. But also here we are limited. In order to distinguish between the individual qubits, the maximum initial qubit rate is ultimately limited by the spectral bandwidth of the qubit carrier. For example when using standard telecom networks, the photon spectral bandwidth is limited to 100 GHz, which corresponds to the bandwidth of typical channels in the widely used telecom C-band (wavelengths of 1530 nm - 1565 nm). This means that the initial qubit rate is also limited to maximally 100 Gqubits per second. In practice the limit is much lower ($\sim 1\,\mathrm{GHz}$) due to the limited timing resolution of current single photon detectors and probabilistic qubit generation processes. It seems that long distance QKD is currently limited by technological constraints that are hard to overcome. Concerning the fibre transmission losses, it seems difficult to further reduce them. The dark count rate of single photon detectors can be strongly reduced and their timing resolution can be improved by employing superconducting devices [153, 154]. However, these devices are not practical to use for real life QKD, as they require the use of liquid Helium, which is expensive and requires serious security precautions. In addition, such superconducting devices show in general a limited single photon detection efficiency.

In Figure 1.8 a plot of the maximum achievable secret key rate as a function of the distance between Alice and Bob is shown for typical experimental values, when the qubit carrier is a 1550 nm photon, *i.e.* fibre transmission losses of 0.2 dB/km, a single photon

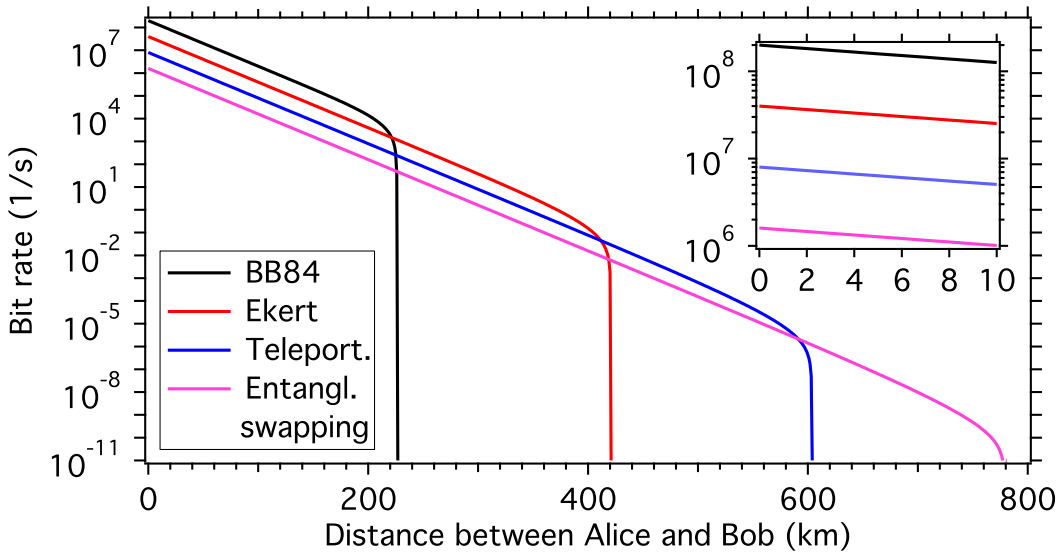

Figure 1.8.: Secret key bit rate as a function of the distance between Alice and Bob for different protocols. The used parameters are a qubit production rate of 10^9/s, photon detection efficiency of 20%, dark count probability of 10^{-6}/ns and fibre transmission losses of 0.2 dB/km, corresponding to the typical values for a 1550 nm photon as a qubit carrier. The maximum tolerable QBER is set to 15% in this case. The BB84 protocol (one detector required) offers the highest absolute bit rate for short distances, but the Ekert protocol (two detectors required) allows for longer absolute communication distances at reduced bit rates for short distances. More complex protocols such as teleportation (three detectors), and entanglement swapping (four detectors) allow for even longer communication distances, however at strongly reduced bit rates. The reduction in communication bit rate is visualized in the inset where the maximum secret key bit rates for all four protocols at short distances are shown.

detection efficiency of 20%, a dark count probability of 10^{-6}/ns[13] and a qubit production rate of 10^9/s[14]. We see that the bit rate is reduced as a function of the distance due to losses in the employed optical fibres. At a certain distance, the communication rate drops down rapidly. This is the distance at which the detector dark count rate becomes comparable to the qubit rate. The key rate at zero distance is given by the detection efficiency. A remarkable property is seen from these graphs. The maximum achievable communication distance for the Ekert protocol is strongly increased compared to the BB84 protocol. Why is this? For the BB84 protocol, the qubit error rate (QBER) is

[13]These are standard values for new generation InGaAs single photon detectors, for example the ones from Id Quantique [30].

[14]The formulae to calculate the secret key rate as a function of the communication distance are taken from reference [155].

directly given by the dark count rate in the detector. In order to observe a false qubit for the Ekert protocol, one needs to have a *simultaneous* dark count on Alice's and Bob's side. The probability for this to happen is very low, such that higher distances are achieved. The other side of the coin is that the secret key rate is reduced compared to the BB84 protocol for the same reason. Alice and Bob need also to simultaneously measure their respective qubits. What is learnt from these graphs is that we can increase the communication distance not only by technological advances, but also by changing the communication protocol. The more detectors are involved in the protocol, the higher is the maximum achievable distance.

1.5. Enabling protocols for long distance QKD

In subsection 1.4.4 it was seen that QKD based on the BB84 and Ekert protocol is limited to maximum communication distances of $\sim 200\,\mathrm{km}$, and $\sim 400\,\mathrm{km}$, respectively. In order to release the dependence on technological advances for longer distribution lengths, new QKD protocols have been developed, of which we introduce in the following the two most known ones, single qubit teleportation (three qubits and detectors required) and entanglement swapping (four qubits and detectors required).

1.5.1. Teleportation

The teleportation protocol was first proposed by C. H. Bennett and collaborators and it allows to transfer the state of a single qubit onto another qubit, that initially belonged to a two-qubit entangled state [37]. The schematic for the teleporation protocol is shown in Figure 1.9. The idea is the following: Alice prepares a qubit in the most general state

$$|\psi\rangle_1 = \alpha\,|0\rangle_1 + \beta\,|1\rangle_1\,, \tag{1.57}$$

where $|\alpha|^2 + |\beta|^2 = 1$. The subscript 1 denotes the path (see Figure 1.9). This qubit is sent to a Bell state measurement (BSM) station, whose function will be described later. A source of entanglement, located between the BSM station and Bob, prepares the two-qubit entangled state

$$|\psi\rangle_{23} = \frac{1}{\sqrt{2}}\left(|0\rangle_2\,|0\rangle_3 + |1\rangle_2\,|1\rangle_3\right). \tag{1.58}$$

One qubit is sent to the BSM (subscript 2) and the other goes to Bob (subscript 3). The full state, comprising the three qubits, reads

$$|\psi\rangle_{123} = |\psi\rangle_1 \otimes |\psi\rangle_{23}\,, \tag{1.59}$$

where the tensor product ($\otimes$) indicates that the systems 1 and 23 are independent. Developing equation 1.59 delivers

$$|\psi\rangle_{123} = \frac{1}{\sqrt{2}}\left(\alpha\,|0\rangle_1\,|0\rangle_2\,|0\rangle_3 + \alpha\,|0\rangle_1\,|1\rangle_2\,|1\rangle_3 + \beta\,|1\rangle_1\,|0\rangle_2\,|0\rangle_3 + \beta\,|1\rangle_1\,|1\rangle_2\,|1\rangle_3\right). \tag{1.60}$$

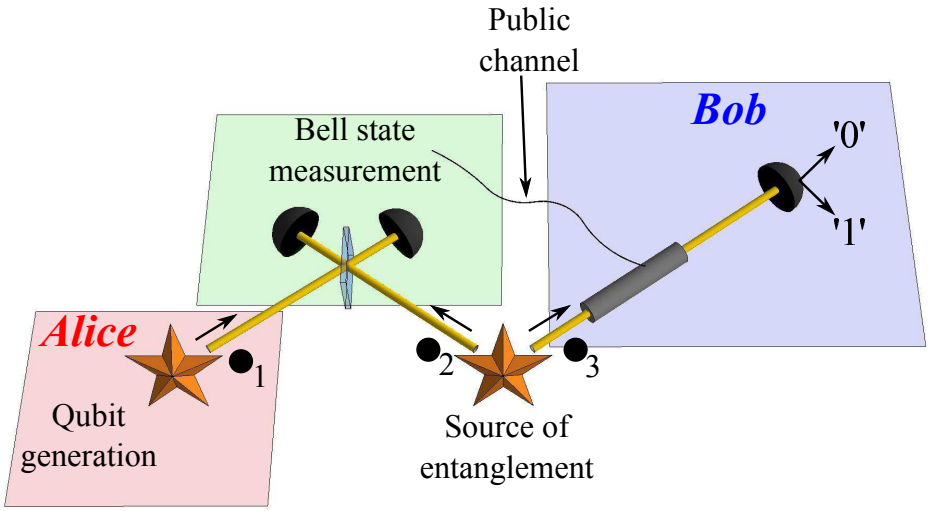

Figure 1.9.: Experimental setup for qubit teleportation. Alice comprises a qubit source generating an unknown qubit $|\psi\rangle_1$. This qubit, together with another qubit coming from an entanglement source, is projected at a Bell state measurement apparatus. The outcome of this measurement defines the operation that has to be applied to the second qubit of the initially entangled qubit pair, in order to successfully teleport Alice's qubit to Bob.

Note that here we have dropped the tensor product $\otimes$ for reasons of simplicity. We can rewrite then:

$$\begin{aligned} |\psi\rangle_{123} \;=\; & \frac{1}{2}\Big(|\Phi^+\rangle_{12}\,(\alpha\,|0\rangle_3 + \beta\,|1\rangle_3) + |\Phi^-\rangle_{12}\,(\alpha\,|0\rangle_3 - \beta\,|1\rangle_3) \\ & + |\Psi^+\rangle_{12}\,(\beta\,|0\rangle_3 + \alpha\,|1\rangle_3) + |\Psi^-\rangle_{12}\,(-\beta\,|0\rangle_3 + \alpha\,|1\rangle_3)\Big). \end{aligned} \tag{1.61}$$

The four Bell states have been here introduced as they form a complete basis for two-qubit states (see subsection 1.2.4). Let us have a closer look on the state described by equation 1.61. When the BSM measures the state $|\Phi^+\rangle_{12}$, then qubit 3 (going to Bob) is in the same state as initially qubit 1, prepared by Alice. If the BSM apparatus measures one of the three other Bell states, *i.e.* $|\Phi^-\rangle_{12}$, $|\Psi^+\rangle_{12}$, or $|\Psi^-\rangle_{12}$, then a simple unitary operation on qubit 3 is sufficient to retrieve the same quantum properties as the initial qubit $|\psi\rangle_1$. Which state measured at the BSM apparatus is completely random, each of them is measured with a probability of $\frac{1}{4}$. This is why this teleportation protocol needs a public channel in which the result of the BSM is forwarded to Bob, giving him the possibility to apply the correct qubit rotation. It is important to notice that this protocol does not clone the qubit 1. Qubit 1 is entangled with qubit 2, projected, measured and consequently lost at the BSM. The quality of teleportation experiments is generally measured by the fidelity, giving the overlap between qubit 1 and qubit 3. As

shown in Figure 1.8, an ideal teleportation device with unit fidelity allows increasing the maximum communication distance between Alice and Bob. The experimental realization of this teleportation protocol is shown in references [156, 135, 157, 158, 159, 160].

1.5.2. Entanglement swapping

An extension of the single qubit teleportation protocol is the entanglement swapping protocol, or in other words the teleportation of entanglement [161]. A schematic of this protocol is shown in Figure 1.10. Two sources of two-qubit entanglement are used, one of them generates the two-qubit state

$$|\Psi^+\rangle_{12} = \frac{1}{\sqrt{2}} \left(|0\rangle_1 |1\rangle_2 + |1\rangle_1 |0\rangle_2 \right), \tag{1.62}$$

and the other source generates

$$|\Psi^+\rangle_{34} = \frac{1}{\sqrt{2}} \left(|0\rangle_3 |1\rangle_4 + |1\rangle_3 |0\rangle_4 \right). \tag{1.63}$$

Although we have chosen here particular Bell states, any other would lead to a similar analysis. The qubits 2 and 3 are sent to a BSM apparatus, while qubits 1 and 4 are sent to Alice and Bob. The full state, comprising the four qubits, is then

$$|\psi\rangle_{1234} = |\Psi^+\rangle_{12} |\Psi^+\rangle_{34}. \tag{1.64}$$

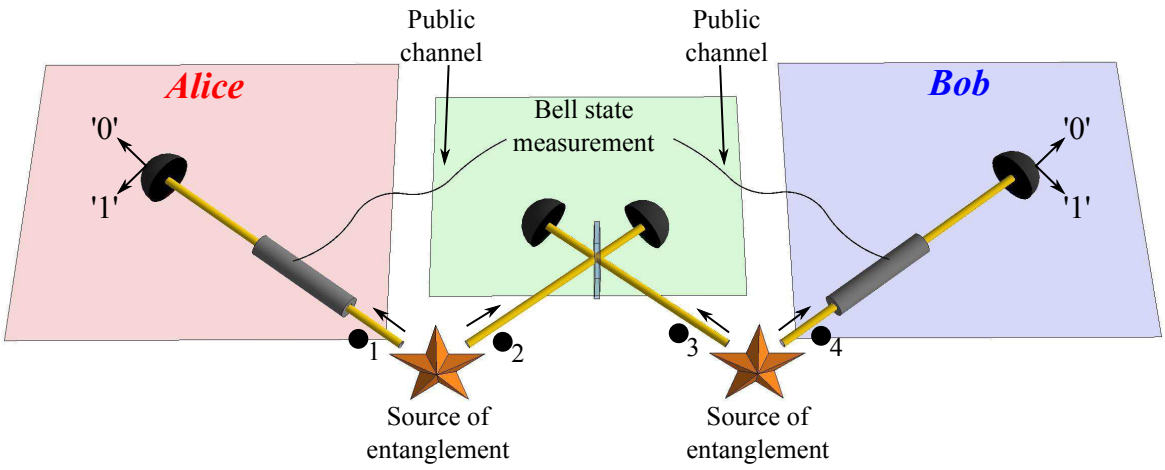

Figure 1.10.: Schematic of the entanglement swapping protocol. Two sources of entanglement are employed between Alice and Bob. The two inner qubits (labelled 2 and 3) are projected at a Bell state measurement apparatus. This entangles the two outer qubits (1 and 4).

This equation can be rewritten as

$$|\psi\rangle_{1234} = \frac{1}{2}\Big(|\Phi^+\rangle_{14}\,|\Phi^+\rangle_{23} - |\Phi^-\rangle_{14}\,|\Phi^-\rangle_{23} + |\Psi^+\rangle_{14}\,|\Psi^+\rangle_{23} - |\Psi^-\rangle_{14}\,|\Psi^-\rangle_{23}\Big). \quad (1.65)$$

Similar to the teleportation protocol, if the BSM apparatus measures one of the four Bell states, then qubits 1 and 4 are projected onto the same Bell state (up to a multiplication of ± 1). The principle is then very similar to the teleporation protocol. The result of the BSM is forwarded through a public channels to Alice and Bob, who apply the necessary qubit operations to obtain the desired correlations.

Experimental entanglement swapping has been realized in various groups [38, 162, 58, 41].

1.5.3. Entanglement swapping with quantum memories

One drawback of the teleporation and entanglement swapping protocols is that a good synchronization between the various qubit sources is required. To perform the BSM, one needs typically that the corresponding qubits arrive simultaneously at the measurement station, which is not a simple task, especially when the qubit sources are separated by long distances, and photons are used as qubit carriers. Another problem is that due to lossy qubit channels, it is very unlikely that all qubits (three qubits for teleportation, four qubits for entanglement swapping), arrive successfully at their respective measurement stations. If only one qubit is lost, we need to repeat the full procedure again, which renders these protocols somewhat inefficient. A big improvement can be achieved when employing quantum memories, as shown schematically in Figure 1.11 for the entanglement swapping protocol. In front of each measurement station, a quantum memory is employed for storing the respective qubit for a certain (controlled) time. We start our analysis with the standard entanglement swapping protocol, in which both entanglement sources generate repeatedly the two-qubit entangled states $|\Psi^+\rangle_{12}$ and $|\Psi^+\rangle_{34}$, respectively, and send them along the corresponding paths. Let μ be the probability that a both qubits of an entangled pair, (1,2) or (3,4), arrives at the corresponding measurement stations. The probability p_{stand} that both entangled qubit pairs succeed to arrive at their respective stations, after $N \in \mathbb{N}$ repetitions, is then given by

$$p_{\text{stand}} = 1 - (1 - \mu^2)^N. \quad (1.66)$$

Here, the exponent of two comes from the fact that two pairs of entangled qubits need to arrive successfully.

With quantum memories the protocol is improved. Both sources send again repeatedly the corresponding entangled qubit pairs to the stations. However, if now a pair of quantum memories (either (1,2) or (3,4)) announces the successful storage of both qubits of a pair, then we stop the qubit distribution on this channel. The entangled qubit transmission procedure is only repeated on the other channels until also here both

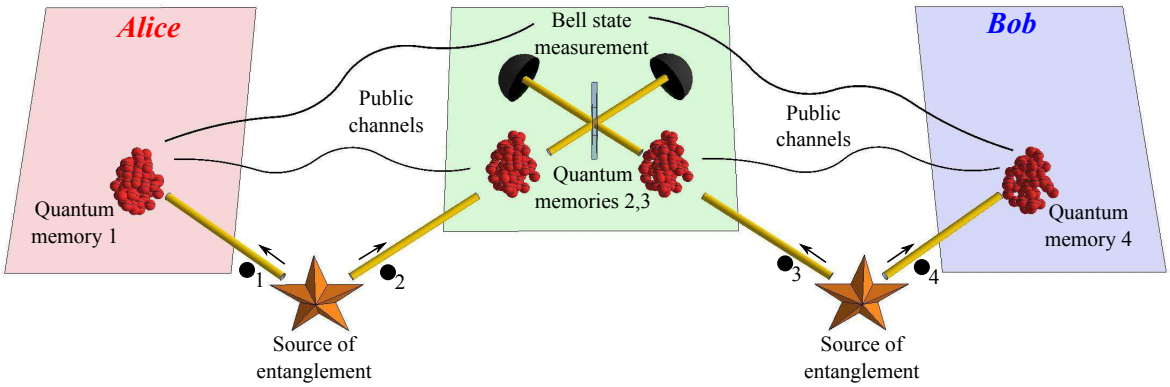

Figure 1.11.: Entanglement swapping protocol with quantum memories. Before each measurement apparatus, quantum memories are employed to store the qubits. Each source of entanglement generates repeatedly entangled qubits until the corresponding quantum memories are loaded. The two sublinks are therefore (initially) independent. When all memories are loaded, one performs a Bell state measurement on the qubits 2 and 3, which entangles then the qubits in the quantum memories 1 and 4.

memories announce that a qubit pair has been successfully stored. For reasons of simplicity we assume that ideal quantum memories are used, *i.e.* an arriving qubit is stored with unit fidelity and efficiency. The probability p_{mem} that all four quantum memories are loaded is then after N repetitions:

$$p_{\text{mem}} = \left(1 - (1-\mu)^N\right)^2 . \tag{1.67}$$

If now a BSM is performed on the qubits stored in the memories 2 and 3, then the qubits in the memories 1 and 4 are projected onto an entangled state, as described in subsection 1.5.2, and entanglement is successfully swapped. In Figure 1.12 we show the successful entanglement swapping probabilities as a function of the number of repetitions for both protocols, the standard entanglement swapping protocol, and the advanced protocol using quantum memories. For this graph, we set $\mu = \frac{1}{6}$, thus the equivalent of successful entanglement swapping would be the probability of throwing a double six with two dices. In this case, the standard entanglement swapping protocol corresponds to the strategy of trying to get a double six by repeatedly throwing both dices. For the quantum memory strategy, we stop throwing a dice as soon as it fell once onto the six and we continue only with the other. The graph shows clearly that the quantum memory strategy allows for much higher success probabilities. For example, obtaining 90% success probability requires in average 82 repetitions for the standard protocol, while the quantum memory based protocol requires only 16 repetitions, corresponding to a five times improvement. This advantage becomes bigger for smaller μ. For example, consider $\mu = 0.01$, corresponding to a 200 km separation between Alice and Bob in a

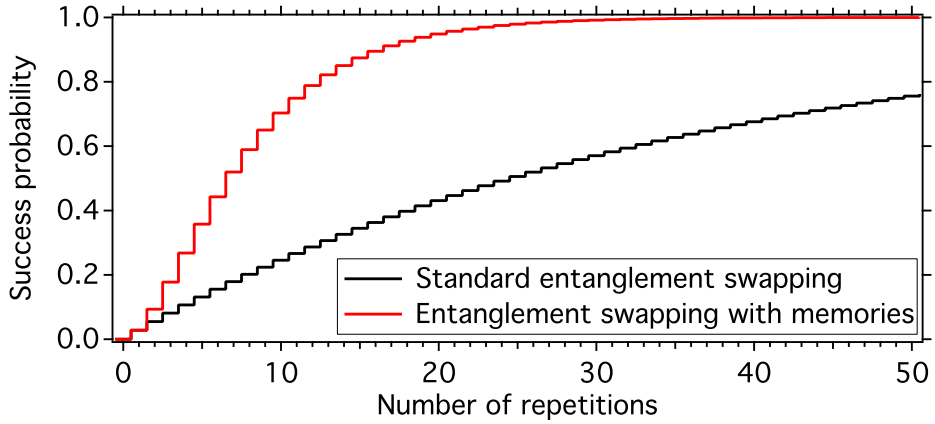

Figure 1.12.: Entanglement swapping probability without and with quantum memories. For this graph, we set $\mu = \frac{1}{6}$, such that the probabilities equivalent to the probabilities of throwing a double six with two dices by repeatedly throwing both dices (standard entanglement swapping) and by stopping to throw a dice as soon as it fell onto a six (entanglement swapping with memories). A clear advantage of the memory strategy is demonstrated.

fibre network. The standard protocol requires an average of 23 025 repetitions for 90% success probability, while the memory based protocol needs only 296. This means that the quantum memory strategy improves the situation by 78 times.

This clearly underlines that the rate of long distance QKD can be strongly improved when using quantum memories. A typical quantum network would therefore take advantage of photons as flying qubits and quantum memories as stationary qubits. There are various possibilities to implement such quantum memories, for example using hot [105, 106, 107, 108] or cold [109, 110] atomic ensembles, ions [50], solid state crystals [104, 53, 54] and many others. Currently, the above mentioned memories do not provide a signal that announce successful qubit storage, which is why they cannot be used advantageously in entanglement swapping protocols. But such storage announcing quantum memories exist already [111, 112, 113, 114, 115, 116, 117, 118, 119, 120, 121, 122, 123, 124, 125], and promising research is going on. A summary on the current qunatum memory research can be found in references [126, 46, 127].

Chapter 2.

Sources of photonic entanglement

2.1. Development of photonic entanglement sources

Already at the end of the 1920's and mid of the 1930's, Niels Bohr and Albert Einstein discussed about systems of entangled quantum objects and their non-intuitive implications [7, 9, 10]. Especially, the stronger than classical and non-local correlations of entangled quantum systems led to important debates about physical reality and the completeness of quantum mechanics. However, even after many discussions, Bohr and Einstein never came to a satisfactory agreement and thus Bohr maintained his conviction that quantum mechanics gives a complete description of physics, while Einstein and collaborators (Boris Podolski and Nathan Rosen) believed that a two-particle enanipultangled quantum state can be treated as two individual particles with pre-defined measurement outcomes for each individual particle [8].

The work of John S. Bell in 1964 marked a major breakthrough for the deeper understanding of quantum mechanics [16]. For the first time, a theoretical procedure was proposed towards determining whether local hidden variables are suitable for describing the strong and faster than speed of light correlations of entanglement or not. In 1969, John Clauser, Michael Horne, Abner Shimony, and Richard Holt (CHSH) developed an experimental procedure to actually produce the desired entangled state and showed how to perform the above mentioned test on the existence of local hidden variables [17]. The proposed idea takes advantage of polarization entangled photons, being emitted by single calcium ions via a two-photon cascade process (see Figure 2.1). As the initial and final quantum state of the calcium atom have zero angular momentum and the same parity, counter-propagating photons coming from the cascade process need to show cross-correlated polarizations to obey the laws of conservation of angular momentum and parity. This way, a polarization entangled state of the form $|\psi\rangle = \frac{1}{\sqrt{2}} (|R\rangle_1 |L\rangle_2 + |L\rangle_1 |R\rangle_2)$ is generated. Here, $|R\rangle$ and $|L\rangle$ denote the polarization states circular right and circular left of the photon, and the subscripts 1 and 2 indicate their wavelengths, which are, in this case, 422.7 nm and 551.3 nm, respectively.

Using such a correlated photon pair source, several experiments indicated that quantum theory is indeed correct [18, 164]. Another approach based on the cascade emission from Hg-atoms confirmed the results of the Ca-experiments [165]. As well did an exper-

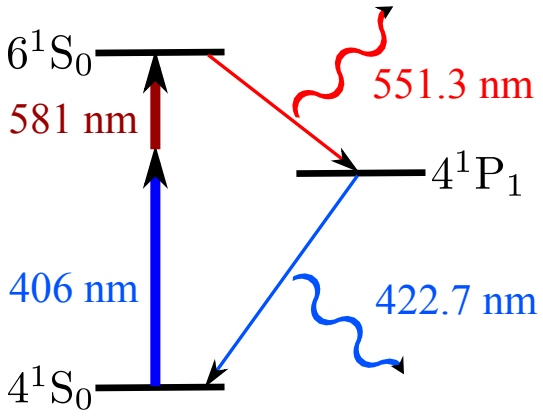

Figure 2.1.: Working principle of the first polarization entangled photon pair source emitting in the visible range of wavelengths (another source of x-ray entangled photon pairs has been demonstrated before [163]). Pump lasers at 406 nm and 581 nm are used to excite calcium atoms from the ground state (4^1S_0) to the excited state (6^1S_0) via two-photon absorption. The atoms can decay back to the ground state via the intermediate state 4^1P_1, which results in photon emission in 4π steradian. When analysing only photons propagating in opposite directions, polarization entangled photons are post-selected in the state $|\psi\rangle = \frac{1}{\sqrt{2}}(|R\rangle_1 |L\rangle_2 + |L\rangle_1 |R\rangle_2)$, where the subscripts 1 and 2 denote the wavelengths.

iment where spin entangled protons have been used [166]. However for all these experiments only a few standard deviations from the classical boundary have been demonstrated. In 1981, Alain Aspect and collaborators performed the experiment proposed by CHSH using a strongly improved experimental apparatus. Thanks to the tremendous efforts on the experimental side, a violation of the Bell-CHSH inequalities by more than 40 standard deviations was shown [19, 167]. These observations clearly ruled out local hidden variable theories as a model for describing entanglement and confirmed the correctness of quantum mechanics.

Ever since these source of polarization entangled photons have been demonstrated, tremendous efforts have been made to realize more compact and practical sources of correlated photon pairs. Especially solid state sources promise much higher applicability.

The first bulk crystal polarization entanglement source has been demonstrated by Paul G. Kwiat and collaborators [168, 169]. The general working principle of this bulk crystal polarization entanglement source is briefly depicted in Figure 2.2. A pump laser is incident on a sample of beta Barium Borate (BBO) and generates, via the non-linear process of spontaneous parametric down-conversion (SPDC), cross-polarized pairs of photons, that are emitted in two distinct emission cones. When properly choosing the pump laser's incident angle, the two cones can be made to overlap in two directions, say a and b. When collecting photons propagating along these two directions, it is

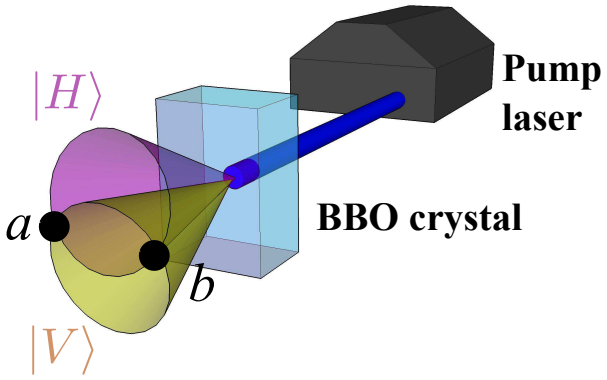

Figure 2.2.: Schematic of the Kwiat bulk crystal polarization entangled photon pair source. A 351 nm pump laser is incident on a BBO crystal and generates cross-polarized photon pairs. Two polarization dependent emission cones are obtained at 702 nm. When collecting only the emission around the two points a and b, where both cones overlap, polarization entangled photon pairs are post-selected.

impossible to predict the individual polarization state of the corresponding photons, thus an entangled state of the form $|\psi\rangle = \frac{1}{\sqrt{2}}\left(|H\rangle_a |V\rangle_b + |V\rangle_a |H\rangle_b\right)$ is generated. This new experiment allowed generating entanglement in a much simpler fashion than before, and it was quickly adapted in many other laboratories.

A new class of experiments was born thanks to the work of James D. Franson [132], who introduced a new entanglement observable, namely energy-time[1]. Here, entanglement is analysed using unbalanced interferometers instead of polarisers. Many groups observed this new kind of entanglement, mainly using SPDC in a bulk crystal towards photon pair generation [170, 171, 172, 173]. The non-local character was unambiguously proven by Kwiat and collaborators using two independent analysis interferometers [174]. It was then shown, that even after several kilometres of photon distribution in optical fibres, entanglement was still preserved [175, 176, 177, 178].

Around the beginning of the 1990's, several proposals have been made towards using photonic entanglement to enable absolute secure communication thanks to secret key exchange [26, 152]. The main quest was then to increase the entangled pair rate of such bulk sources. Employing waveguide structures on these crystals, resulting in stronger light field confinement, promises much higher photon pair generation efficiencies. Note that, compared to the source used by Kwiat, such waveguide structures do not allow to chose the pump laser and photon pair directions after the waveguide is employed. This makes it very hard to observe SPDC. But applying a periodic poling of the crystals susceptibility solves this problem in waveguide structures thanks to quasi phase matching (QPM) [14]. Such periodically poled waveguide crystals have first been implemented

[1] At that time, the used term was position-momentum entanglement.

towards generation of energy-time entangled photons [55, 56, 57, 58]. Lately, Titanium in-diffused waveguide structures on periodically poled lithium niobate (PPLN) enabled high efficiency and quality polarization entanglement generation from a solid state device [179, 180, 181, 182, 59].

The importance of good polarization entanglement sources for future applications is also seen in the fact that there is a vast variety of *hybrid* polarization entanglement sources. Typically, these sources show *a priori* no polarization entangled emission, but a clever arrangement of the experimental apparatus is used for achieving the desired correlations. The main claim for such kind of sources is to exploit much higher efficient non-linear processes compared to the natural polarization entanglement sources. In addition, a better versatility and tunability is often achieved with such sources. Some examples are given in [183, 184, 185, 186, 187, 64].

There are also other strategies for generating entangled photon pairs in a guided-wave fashion. For instance, using the third-order non-linearity process called four-wave mixing (FWM) in special optical fibres (dispersion shifted, polarization maintaining or micro-structured), has shown to be a novel and simple way of generating photonic entanglement [188, 189, 190, 191, 192, 193, 194]. However, such fibre-approaches come with relatively high noise figures due to Raman scattering. The noise can be tremendously reduced when cooling the fibres to cryogenic temperatures, which is somewhat impractical for real applications [195, 190, 196]. Recently, a new strategy based on AlGaAs waveguides showed photonic entanglement from a semiconductor device where the two photons are propagating in opposite directions [197].

Although entangled photon pair sources based on non-linear interactions typically offer both ease of use and high wavelength tunability, they suffer intrinsically from probabilistic multi-pair emission, which potentially reduces the measured entanglement quality. This is why the average pair creation rate needs to be kept low in order to avoid too high multi-pair contributions. However, in this case, photon pairs are only probabilistically available (*i.e.* their creation times cannot be predicted with certainty). To circumvent this problem, new experiments based on deterministic single (double) photon sources have been carried out. To date, deterministic photon pair generation has been obtained from pairs of single atoms [99], ions [198], nitrogen-vacancy color centres in diamond [199, 200] and quantum dots [201, 202, 203, 204]. However, for these realizations, photonic entanglement has not been demonstrated unambiguously, or the entanglement quality was rather low.

At the beginning of the millennium, when Lu Ming Duan, Mikhail Lukin, Ignacio Cirac and Peter Zoller (DLCZ) published their famous paper entitled *Long-distance quantum communication with atomic ensembles and linear optics* [205], polarization entanglement attracted a whole new class of experiments. In their paper, the authors propose a method to entangle two atomic ensembles via a projective measurement on the emitted single photons. In this case, entanglement is correctly generated when the photons are projected onto a polarization entangled state. The beauty of this protocol is that it offers (in theory) to increase the distance of secure quantum key distribution

compared to previously existing protocols. Note that this protocol can also be inverted, such that a pair of entangled photons is absorbed in two distinct atomic ensembles and causes quantum jumps (the atom changes its energy levels) [44]. The photon pair correlations are then stored in the atoms and thus both ensembles become entangled. As the entanglement is stored, the atomic ensembles act as quantum memory devices. Note that similar protocols have also been proposed for other quantum memories, especially solid state devices [46, 206, 207]. For all these protocols to work, the photon pair spectral bandwidth needs to be comparable to the absorption of the desired quantum memory, which is on the order of 1 MHz - 1 GHz [126, 46]. While such bandwidths are emitted intrinsically by deterministic photon pair sources such as atoms, ions and quantum dots [208, 209, 203], non-linear entanglement sources show typically emission bandwidths on the order of a few THz. Thus, certain efforts are required to achieve the desired emission bandwidth. Basically there are two filtering techniques. Either placing the photon pair generator in an optical cavity (this configuration is generally called optical parametric oscillator (OPO)) to restrict the emission bandwidth to the transmission modes of the cavity [210, 211, 212, 213, 214] or applying a suitable filtering stage after the photon pair generator, to attenuate the emission at unwanted wavelengths [58, 215, 52, 64]. Using such sources, preliminary experiments have already shown the storage of photonic entanglement in bulk crystals [53, 54]. Furthermore, heralded single photon absorption has been demonstrated with ions [50]. However, application of the DLCZ protocol could not yet be demonstrated in these experiments. Consequently, promising research in this field is going on, with the ultimate goal being a large scale quantum network.

Aside from the technical application part, photonic entanglement is still used as a main resource for examining and understanding the foundations of quantum physics. For instance, some delayed choice experiments have been carried out for improving our comprehension about various complementarity notations [41, 216, 43, 42].

In the following sections, photon pair generation via the SPDC is first briefly recalled. Then, three different entanglement sources are presented. All sources operate at favourable telecom wavelengths to take advantage of low-loss fibre optical components, and for potential implementation into existing fibre optical networks.
For the first source, the main motivation is the realization of an as-simple-as-possible polarization entanglement source, offering near-perfect entanglement quality and high applicability and reliability.
For the second source, a novel strategy of converting entanglement (polarization $\rightarrow$ cross-time-bin entanglement) is studied and applied, resulting in a simple way of quantum key distribution using passive quantum state analysers and only four instead of eight single photon detectors.
The third source uses an energy-time to polarization entanglement transcribing procedure to realize a source of polarization entangled photons showing a high brightness and spectral bandwidth versatility over five orders of magnitude. The source is suitable for experiments with quantum memories and offers high reliability. The quality of

this source permits to revisit Bohr's so-called complementarity notation using a Mach-Zehnder interferometer in a true superposition of states "closed" and "open".

2.2. Photon pair generation via SPDC - quickly explained

One of the most convenient and exploited ways for generating photon pairs is the so-called spontaneous parametric down-conversion (SPDC) process. This second order optical non-linearity can be exploited in non-centrosymmetric crystals.

In this section, a quick introduction about SPDC is given. A detailed theoretical description is found in Appendix A.

When observing the process of SPDC, a high energy pump photon (p) propagating in a suitable crystal is converted, with a certain probability, to a pair of low energy photons, typically referred to as signal (s) and idler (i). This three wave mixing process obeys the laws of conservation of momentum and energy

$$\omega_\mathrm{p} = \omega_\mathrm{s} + \omega_\mathrm{i}. \tag{2.1}$$
$$\vec{k}_\mathrm{p} = \vec{k}_\mathrm{s} + \vec{k}_\mathrm{i} \tag{2.2}$$

Here, ω denotes the photons' angular frequencies. $\vec{k} = \frac{2\pi n}{\lambda}\vec{u}$ is the photon momentum, with λ being the photon vacuum wavelength, $\vec{u}$ a normalized vector along the light propagation axis and n is the refractive index. Equation 2.2 is typically called the *phase matching condition*. Note that equation 2.2 comprises the wavelength dependent refractive indices for the three photons of interest. Thus, fulfilling this equation is only possible under certain circumstances, *i.e.* for certain photon wavelengths, propagation directions and polarization modes (birefringent phase matching).

The SPDC efficiency of such bulk crystals is typically very weak, on the order of 10^{-10} generated pairs per pump photon and centimetre of crystal length. In the following, two technological steps are explained towards increasing the SPDC efficiency by several orders of magnitude. A schematic is given in Figure 2.3. One main reason for low SPDC efficiency in bulk crystals is that high light field energy densities are difficult maintain over lengths of more than a few mm. Employing a waveguide structure on/in the crystal of interest overcomes this problem conveniently as light can be strongly confined (typical waveguide cross section $10\,\mu\mathrm{m}^2$) over much longer lengths (typically a few centimetres). This clearly gives the potential for much higher SPDC efficiencies. But natural birefringent phase matching is difficult to achieve using such a waveguide structure. The waveguide implies a fixed photon propagation direction. In addition, depending on the waveguide fabrication procedure, only certain polarization modes are guided in the structure. For example, when implementing waveguides on PPLN using the soft proton exchange procedure on a Z-cut lithium niobate wafer, a refractive index modulation is achieved only in one direction. This is why only vertical light polarization modes are guided. Although the waveguide width has some influence on the effective refractive index, only small adjustments can be made, because a too narrow waveguide does not allow for efficient light coupling and a too wide waveguide leads to multi-mode

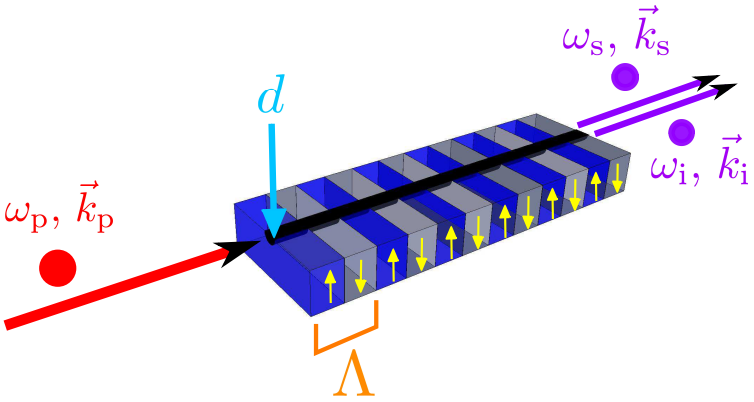

Figure 2.3.: Schematic of a periodically poled lithium niobate waveguide (PPLN/W) operating in the SPDC regime. An incoming pump photon, characterized by an angular frequency ω_p and a momentum $\vec{k}_p$ is converted into a pair of signal (ω_s, $\vec{k}_s$) and idler (ω_i, $\vec{k}_i$) photons. In order to increase the efficiency of this process, a waveguide is employed, which maintains high light field energy densities over a few cm of distance. In order to permit finding the phase matching condition for the three photon process of interest, the ferroelectric polarization of the crystal is repeatedly inverted (poling period Λ) along the light propagation axis. This results in the so-called quasi phase matching (QPM). The QPM is mainly influenced by the poling period while the waveguide width (d) and the crystal temperature allow for further fine adjustment.

behaviour, which reduces the SPDC efficiency. Thus, fulfilling equation 2.2 becomes relatively difficult, as only wavelength and temperature dependency of the refractive index are left as adjustable parameters. However, for most experiments, a certain wavelength combination of pump, signal and idler photons is desired. Then finding the desired phase matching leads quickly to required crystal temperatures beyond practically reachable limits.

To circumvent this problem, while still keeping the efficiency advantage of a waveguide structure, a commonly used solution is to employ the so-called quasi phase matching (QPM). Here, the ferroelectric polarization of the crystal is periodically inverted along the light propagation axis. The adapted phase matching condition is then

$$\vec{k}_p = \vec{k}_s + \vec{k}_i + \frac{2\pi}{\Lambda} \cdot \vec{u}. \tag{2.3}$$

Here, Λ is the poling period and $\vec{u}$ is the normalized light propagation vector. By choosing the poling period, one can essentially phase-match any desired combination of pump, signal and idler wavelengths while still fulfilling equation 2.1. Practically speaking, one is generally limited to wavelengths within the transparency window of the used crystal, *e.g.* the usable window of lithium niobate is 350 - 5200 nm. Moreover, as far

as it concerns SPDC in lithium niobate samples, such a periodic poling allows exploiting the highest non-linear coefficient $d_{33} \approx 30\,\mathrm{pm/V}$. This is approximately six times higher than the d_{31} coefficient, typically used for birefringent phase matching in bulk crystals. Periodically poled lithium niobate waveguide (PPLN/W) samples exploiting the d_{33} coefficient for photon pair generation, are nowadays widely used in research laboratories all over the world for efficient photon pair generation due to their high efficiency, and ease of use. Describing the fabrication techniques for such samples is beyond the scope of this thesis, but the interested reader finds pertinent information in the following references [217, 218, 219, 220, 221, 155], and the references therein.

Until here, only the photons' energies and momenta have been considered. However, depending on the chosen experimental configuration, different relations between the photons' polarizations are demanded. Today's experiments exploit basically three main interaction types (type-0, type-I and type-II), which relate the polarization states vertical ($|V\rangle$) and horizontal ($|H\rangle$) of the three photons involved in the SPDC process. A short summary is given in Table 2.1.

The non-linear devices used for this thesis are all based on waveguide structures on PPLN. The exploited interaction types are type-II ($|H\rangle_\mathrm{p} \rightarrow |H\rangle_\mathrm{s} |V\rangle_\mathrm{i}$) as well as type-0 ($|V\rangle_\mathrm{p} \rightarrow |V\rangle_\mathrm{s} |V\rangle_\mathrm{i}$). In the following, the related experiments are outlined in more details.

Interaction type	**type-0**	**type-I**	**type-II**
Polarizations	$\|V\rangle_\mathrm{p} \rightarrow \|V\rangle_\mathrm{s} \|V\rangle_\mathrm{i}$	$\|V\rangle_\mathrm{p} \rightarrow \|H\rangle_\mathrm{s} \|H\rangle_\mathrm{i}$	$\|H\rangle_\mathrm{p} \rightarrow \|H\rangle_\mathrm{s} \|V\rangle_\mathrm{i}$
Non-linear coefficient of lithium niobate	$d_{33} \sim 30\,\mathrm{pm/V}$	$d_{31} \sim -5\,\mathrm{pm/V}$	$d_{24} = d_{33}/3$ $\sim 10\,\mathrm{pm/V}$
Conversion efficiency in a PPLN/W	$10^{-6} - 10^{-5}$	$\sim 10^{-7}$	$\sim 10^{-9}$
Emission bandwidth at 1550 nm	$20 - 100\,\mathrm{nm}$ 2.5 - 12.5 THz	$20 - 100\,\mathrm{nm}$ 2.5 - 12.5 THz	$0.8 - 3\,\mathrm{nm}$ 0.1 - 0.375 THz
Natural entanglement observable	Energy-time	Energy-time	Polarization
See section	2.5	—	2.3, 2.4

Table 2.1.: Key properties of waveguide based SPDC photon pair generators. The three main interaction types are considered. Note that the SPDC efficiency of the type-II interaction is much smaller than for the type-0 and type-I counterparts. However, the emission bandwidth of the type-II interaction is much narrower. Consequently, when photon pairs with a narrow spectral bandwidth are required, the type-II interaction might be sometimes favourable.

2.3. A polarization entanglement source based on a type-II PPLN/W

In this section, a practical and simple telecom wavelength polarization entanglement source is discussed. The main objectives for this source are:

- Generation of polarization entangled photons in the quantum state $|\Psi^+\rangle = \frac{1}{\sqrt{2}}(|H\rangle_1 |V\rangle_2 + |V\rangle_1 |H\rangle_2)$.
- Photon pair wavelength in the telecom C-band.
- Very high entanglement quality.
- Low losses from the output of the photon pair generator to the output of the source, *i.e.* until the photons are coupled into a single mode fibre directing them towards Alice, respectively Bob.
- Entanglement generation using a fully guided-wave approach to combine applicability and reliability, compared to previous realizations [181, 182].

This section is organized as follows: first, the basic principle of polarization entanglement formation using a non-linear crystal in the type-II configuration is explained. Then, the particular photon pair generator, a periodically poled lithium niobate waveguide (PPLN/W), is described and characterized towards generating entanglement. Thereafter, the performance of the source is tested, especially a high entanglement quality is demonstrated. Then, some possibilities for further improvements are discussed and a conclusion is given. Finally, a more detailed discussion about the formation of entanglement and its manipulation is described.

This section is restricted to the use of a type-II photon pair generator based on a periodically poled lithium niobate waveguide (PPLN/W)[2]. The waveguide structure is made using the titanium in-diffusion technique [222], that allows propagation of arbitrary polarization modes, as opposed to waveguide fabrication procedures based on proton-exchange [219]. The choice for this type-II sample has mainly practical reasons, as it offers one of the easiest and most convenient ways of generating polarization entanglement. The basic idea is outlined in Figure 2.4. A horizontally polarized pump laser is coupled to the PPLN/W sample and generates pairs of cross polarized photons $|H\rangle_{\mathrm{p}} \rightarrow |H\rangle_{\mathrm{s}} |V\rangle_{\mathrm{i}}$, as outlined in Table 2.1. If the two photons are identical in all aspects (but the polarization), then one can drop the subscripts s and i and it is $|H\rangle_{\mathrm{p}} \rightarrow |H\rangle |V\rangle$.

The paired photons are then sent to a 50/50 beam-splitter, having one output sending photons towards Alice (a), while the other output directs the photons to Bob (b). After

[2]The type-II PPLN/W sample has been fabricated at the University of Paderborn (Germany) by the group of Prof. W. Sohler. The reported studies are carried out within the framework of the ERA-SPOT program "WASPS".

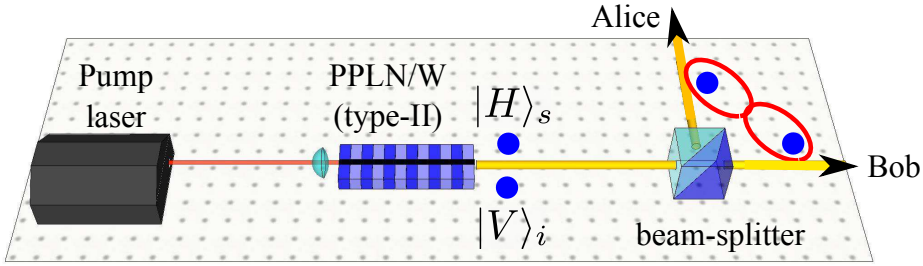

Figure 2.4.: Typical working principle of type-II polarization entanglement waveguide sources. A pump laser is sent to a type-II PPLN/W. The SPDC process generates cross polarized paired photons $|H\rangle_s |V\rangle_i$. If the two photons are identical in all aspects (but the polarization), then one can drop the subscripts s and i and the state is $|H\rangle |V\rangle$. The photons are sent to a 50/50 beam-splitter, which probabilistically splits up the pairs. In the cases when Alice and Bob detect each one single photon, a polarization entangled state of the form $|\psi\rangle_{post} = \frac{1}{\sqrt{2}} (|H\rangle_a |V\rangle_b + |V\rangle_a |H\rangle_b)$ is post-selected. Cases in which both photons go to Alice or to Bob are discarded.

the beam-splitter, the quantum state comprises four contributions

$$|\psi\rangle_{BS} = \frac{1}{2} (|H\rangle_a |V\rangle_a + |H\rangle_a |V\rangle_b + |V\rangle_a |H\rangle_b + |H\rangle_b |V\rangle_b) . \tag{2.4}$$

When post-selecting events in which a photon pair has been split up at the beam-splitter, *i.e.* one photon is sent to Alice and one to Bob, then a maximally polarization entangled state is generated

$$|\psi\rangle_{post} = \frac{1}{\sqrt{2}} (|H\rangle_a |V\rangle_b + |V\rangle_a |H\rangle_b) . \tag{2.5}$$

Note that such an event post-selection is typically very conveniently achieved by counting only events in which Alice and Bob detect a photon simultaneously (we call this a coincidence event).

As outlined above, observation of entanglement requires that the two photon contributions leading to the entangled state are labelled by another observable that does not reveal the polarization state. In the case of the beam-splitter, this labelling is done by the two different output spatial modes, a and b, after the beam-splitter. But this procedure is probabilistic with a success rate of only 50%. In the following, a new strategy is demonstrated towards achieving deterministic photon pair separation by wavelength labelling. Although this strategy is not new for energy-time entanglement sources [215], it has so far never been applied to polarization entanglement sources, as much higher care has to be taken for correct implementation.

A key point towards achieving high entanglement quality is that the horizontal and vertical photon contributions are not labelled by another observable. For example, when

exploiting polarization entanglement, the only way to measure a photon's polarization must be a polarization measurement. For real experiments, and from the experimentalists side of view, the main concerns are typically photon labelling by different emission wavelengths of $|H\rangle$ and $|V\rangle$ modes and time labelling due to waveguide birefringence which causes a temporal walk-off between the two modes. In the first case, a spectrometer would be sufficient to determine the polarization. In the second case, a simple arrival time measurement reveals the polarization state. Note that the principal possibility of performing such a measurement is enough to destroy entanglement. Neither does the experiment have to be actually performed, nor does the corresponding apparatus need to exist.

2.3.1. Optical sample characterization

In the following, three experiments are described towards optical characterization of the waveguide sample, with the main goal being to find the quasi phase matching (QPM) condition permitting to generate polarization entangled photon pairs at 1540 nm coming from a pump laser at 770 nm. In addition, we need to ensure that all aforementioned sources of entanglement degradation are erased/compensated.

- The first characterization is outlined to find the desired QPM. Therefore, a second harmonic generation experiment is carried out, in which a tunable telecom laser is frequency doubled, allowing to roughly find the appropriate quasi phase matching condition, in a short time period.
- Second, fine tuning of the QPM is achieved in a SPDC characterization experiment. This experiment permits exploring the residual degree of parasitic wavelength labelling, which is an important information for deterministic photon pair separation.
- Eventually, the birefringence of the waveguide structure is measured using an advanced interferometer setup, and compensated using a polarization maintaining fibre. This is necessary to improve the entanglement quality via erasing the temporal walk-off.

Second harmonic generation

As a first experiment, the non-linear spectral characteristics of the waveguide sample are examined using the experimental setup depicted in Figure 2.5. The light of a wavelength tunable (1490-1650 nm) fibre telecom laser[3] is sent through a fibre polarization controller and coupled into the waveguide sample. The polarization controller is used to rotate the laser light polarization to be diagonal at the input of the waveguide. This way horizontal and vertical light contributions are simultaneously available in the sample and the type-II

[3]Model: Photonetics Tunics-PRI.

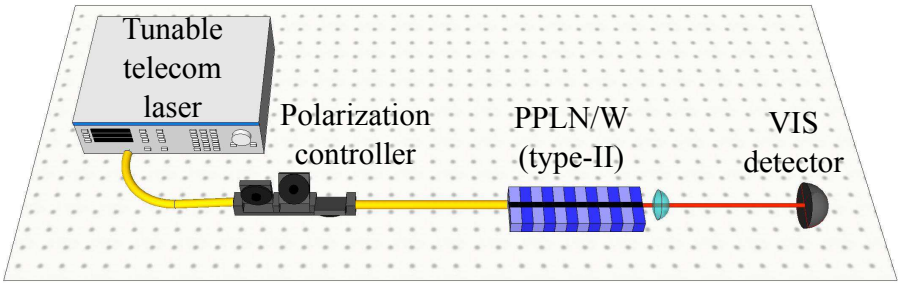

Figure 2.5.: Experimental setup for optical sample characterization via second harmonic generation. A wavelength tunable telecom laser is sent through a polarization controller to orient its polarization to be diagonal at the waveguide input. When the quasi phase matching condition is achieved, the laser light is frequency doubled. Light at the waveguide output is collected using a lens and sent to a power meter.

second harmonic generation process $|H\rangle_{1540}\,|V\rangle_{1540} \rightarrow |H\rangle_{770}$ can be observed. Here, the subscripts denote the photons' wavelength. Note that this process is the inverse process of the one given in Table 2.1. When the laser is operated at the right wavelength, *i.e.* the quasi phase matching condition is achieved, two telecom laser photons can be combined to produce a second harmonic generated photon, *i.e.* a photon at half of the original wavelength (twice the frequency). The converted photons are then detected using an optical power meter being only sensitive to light below 1000 nm, thus no additional filtering of infrared light is required[4]. The key point of this experiment is that when the phase matching condition is achieved for the process $2 \times 1540\,\text{nm} \rightarrow 1 \times 770\,\text{nm}$, the inverse process (SPDC, which is the desired one) is obtained for the same conditions. The particular type-II sample offers a vast variety of different poling periods and waveguide diameters, thus the choice on the used waveguide allows to choose a nearly appropriate QPM via the opto-geometrical parameters. In addition, the sample is placed in a home-made oven, to precisely achieve the good quasi phase matching condition via temperature control. As shown in Figure 2.6, the desired interaction $2 \times 1540\,\text{nm} \rightarrow 1 \times 770\,\text{nm}$ is obtained for a $6\,\mu\text{m}$ diameter waveguide, having a $9.0\,\mu\text{m}$ poling period and at a temperature of 110 °C.

Consequently, this characterization permits finding good starting parameters. In the following, a second experiment is shown for fine tuning of the QPM.

[4]Coherent FieldMax II.

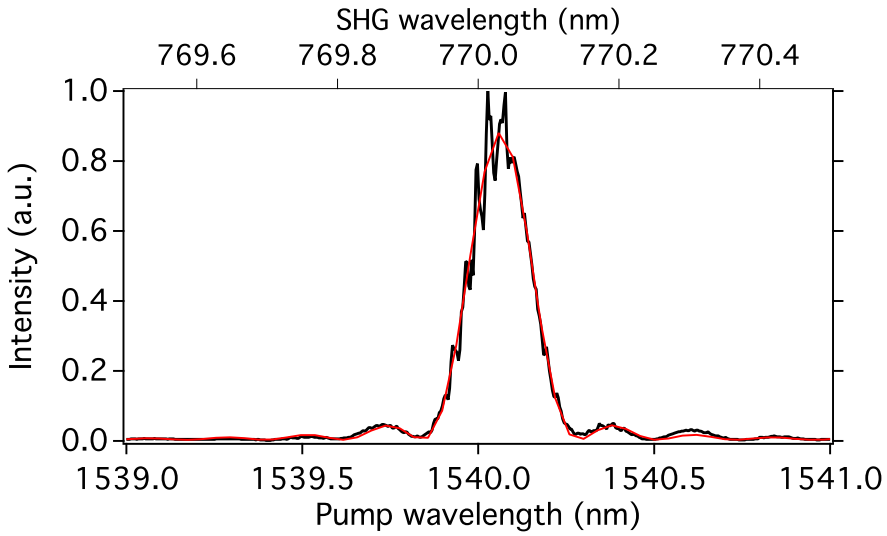

Figure 2.6.: Second harmonic generation (SHG) spectrum at the output of the type-II PPLN/W. The SHG intensity at around 770 nm is measured as a function of the telecom pump laser wavelength. The temperature is adjusted to 110°C. The black curve represents measured data, and the fit using a sinc^2 function (red curve) delivers a full width half maximum acceptance bandwidth of 0.19 nm. The sample's SHG efficiency is calculated to be $\sim 30\%\,\mathrm{W}^{-1}$.

Spontaneous parametric down-conversion

Now, the actual desired experimental configuration is tested. The experimental setup is outlined in Figure 2.7. A continuous wave pump laser is set up[5], operated at a wavelength of 770 nm wavelength controlled using a wavemeter. To avoid spurious infrared emission being coupled in the waveguide sample, the laser output is filtered using a prism. Then the laser is coupled to the PPLN/W to generate the paired photons $1 \times 770\,\mathrm{nm} \rightarrow 2 \times 1540\,\mathrm{nm}$. Note that for the type-II interaction, this process is only possible when the pump laser is horizontally polarized $|H\rangle_\mathrm{p} \rightarrow |H\rangle_\mathrm{s}|V\rangle_\mathrm{i}$, as outlined in Table 2.1. The emission at the waveguide output is collected using a single-mode fibre. After a polarization controller, the photons are sent to a tunable optical filter[6], showing a transmission bandwidth of about 80 pm. As this is much narrower than the expected emission bandwidth, a good resolution is obtained. After the filter, the photons are subjected to a fibre polarizing beam-splitter (f-PBS). The f-PBS reflects (transmits) vertically (horizontally) polarized photons, which are then detected using avalanche photodiodes operated in the Geiger regime[7]. A typical emission spectrum for the $|H\rangle$

[5] Coherent Verdi V18 in combination with Coherent MBR110.
[6] Yenista XTM-50.
[7] Id quantique id220, operated at 20% detection efficiency and 5 μs dead time.

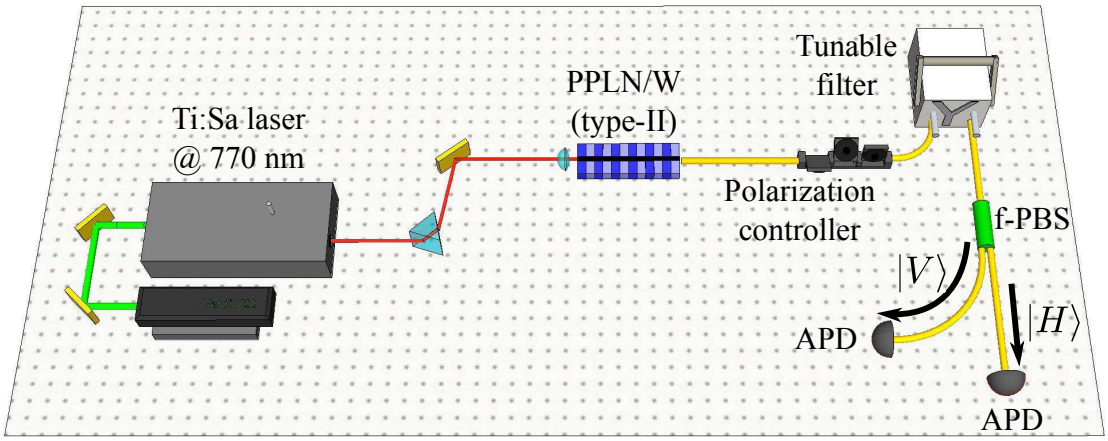

Figure 2.7.: Experimental setup for measuring the SPDC emission at the output of the PPLN/W sample. A Ti:Sa ring cavity laser system is operated at 770 nm, the light is horizontally polarized, and pumps the type-II PPLN/W. The emission of the sample is collected using a single mode fibre and sent through a polarization controller. Then the photons pass a tunable filter and the two emission modes, $|H\rangle$ and $|V\rangle$ are split on a fibre polarizing beam-splitter (f-PBS) and are directed to two avalanche photodiodes (APD).

and $|V\rangle$ modes is shown in Figure 2.8. The emission bandwidth is on the order of 0.85 nm. As shown in Figure 2.10, the emission wavelengths of the two polarization modes can be shifted as a function of the waveguide temperature and diameter. For the following, a waveguide diameter of 6 μm is chosen and the sample temperature is set to 110.2°C, at which both emission modes overlap almost perfectly at 1540 nm. The non-perfect overlap in the side peak regions represents a major issue, as the polarization modes are partially wavelength labelled [181]. This labelling can be circumvented by spectral filtering photons only around the degeneracy point and rejecting photons in the side peaks. In Figure 2.9, the transmission spectrum of a 100 GHz ($\leftrightarrow$ 0.8 nm) fibre Bragg grating (FBG) filter is shown. Employing this filter rejects unwanted photon pairs emitted in the side peak regions. This way wavelength labelling is erased, which is a necessary requirement towards achieving a good entanglement quality.

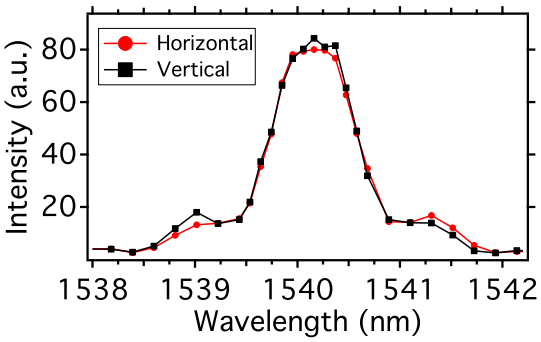

Figure 2.8.: Typical wavelength and polarization dependent emission spectrum of the type-II photon pair generator. The bandwidth of both emission modes is on the order of 0.85 nm. The waveguide diameter is 6 μm and at a temperature of 110.2°C the $|H\rangle$ and $|V\rangle$ modes overlap nearly perfectly at 1540 nm, which is the desired configuration. The non-perfect overlap in the side peak regions comes from sample imperfections and reduces the observed entanglement quality [181].

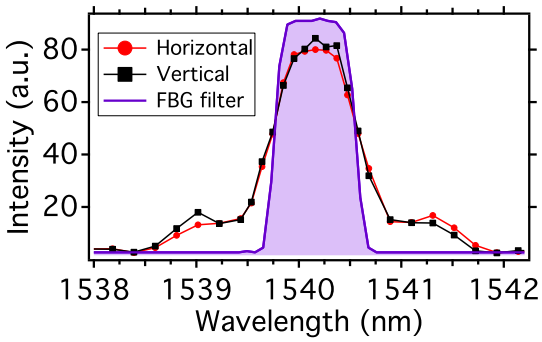

Figure 2.9.: Polarization dependent emission spectrum of the type-II sample in combination with the employed 0.8 nm filter towards removing the emission regions in which a non-perfect overlap between $|H\rangle$ and $|V\rangle$ modes is achieved (in the side peak region). Within the filtering region, the emission peaks overlap almost perfectly, which is one of the necessary requirements towards high quality entanglement formation.

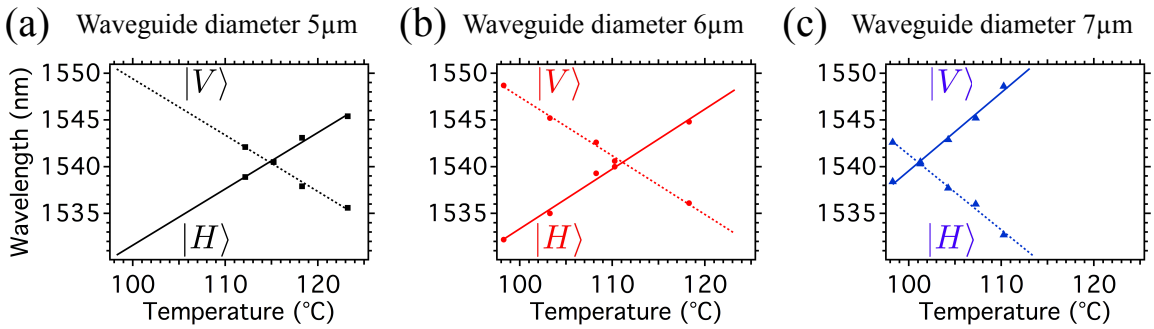

Figure 2.10.: Temperature dependent QPM curves for a waveguide diameter of 5 μm (a), 6 μm (b), and 7 μm (c). In all of the cases, the poling period is 9.0 μm and the pump laser wavelength is fixed at 770 nm. Plotted here are the centres of the $|H\rangle$ and $|V\rangle$ emission peaks. Lines represent linear fits. For the work in this thesis, the PPLN/W having a diameter of 6 μm is used and operated at wavelength degeneracy.

Waveguide birefringence / Temporal walk-off compensation

Typically, non-linear crystal photon pair generators are birefringent, which potentially causes entanglement degradation. Due to the waveguide birefringence, the $|H\rangle$ and $|V\rangle$ modes exit the photon pair generator with a temporal walk-off. This means, that a photon arrival time measurement reveals, in principle, it's polarization state. This circumstance can cause entanglement degradation. For the used PPLN/W, the temporal walk-off is on the order of a few picoseconds and can be calculated via the polarization dependent refractive indices. For lithium niobate, the ordinary (o) and extraordinary (e) refractive indices are $n_\mathrm{o} = 2.21145$ and $n_\mathrm{e} = 2.13785$ as outlined in Appendix D. The expected delay δt is then given by

$$\delta t = \frac{l\,(n_\mathrm{o} - n_\mathrm{e})}{2\,c}. \tag{2.6}$$

Here l is the sample length and $c = 299\,792\,458\,\frac{\mathrm{m}}{\mathrm{s}}$ is the speed of light in vacuum. The denominator of 2 comes from the fact that the photon pairs are generated, in average, at half the length of the sample. For a sample length of 3.6 cm it is predicted $\delta t = 4.42\,\mathrm{ps}$, which is comparable to the emission coherence time of the PPLN/W sample and thus arrival time labelling cannot be considered as negligible. There are two ways to circumvent this problem. Either strongly reducing the photon pair spectral bandwidth, thus increasing the photons' coherence time to a value that is much higher than the temporal walk-off [52]. This way the emission time difference is hidden behind the photon coherence time as shown in Figure 2.11. The second possibility is to get to the root of the problem and compensate the birefringence by an appropriate experimental configuration. In earlier realizations this has been done using bulk optical stages, based on polarization dependent Michelson interferometer like configurations [181]. The artificial delay introduced by the interferometer configuration is chosen such that at the output the two polarization modes overlap perfectly in the temporal domain, as depicted in Figure 2.12.

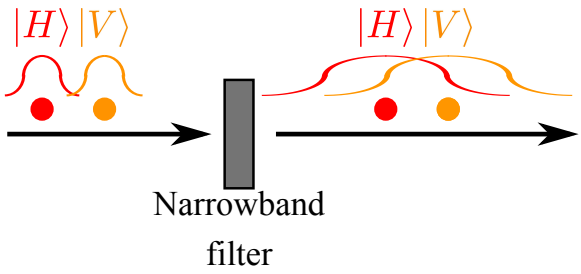

Figure 2.11.: Erasing the temporal walk-off induced by the waveguide birefringence via narrowband filtering. Initially, after the birefringent photon pair generator, the $|H\rangle$ and $|V\rangle$ contributions are temporally distinguishable, as their temporal separation is greater than the single photons' coherence times (indicated by the curves on top of the points). Employing a narrowband filter increases the single photon coherence time of the individual photons and consequently increases the temporal overlap of the two contributions. If the filter is narrow enough, *i.e.* the photons' coherence times are much greater than the temporal delay, temporal photon contribution labelling can be considered as negligible [52].

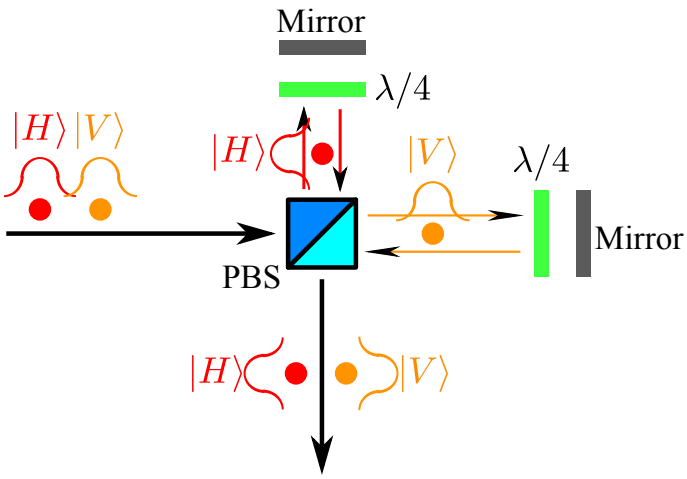

Figure 2.12.: Erasing the temporal walk-off induced by the waveguide birefringence using a Michelson interferometer like configuration. The two polarization modes $|H\rangle$ and $|V\rangle$ of the incoming photons are separated using a polarizing beam-splitter (PBS). Both contributions are reflected back to the PBS by mirrors. The path of the $|V\rangle$ photon is longer than that of the $|H\rangle$ photon, such that both photons come back simultaneously to the PBS. A quarter wave plate in each arm (symbolized by $\lambda/4$) ensures that both photons leave the interferometer through the bottom output port of the PBS. Choosing the path length difference suitably erases the temporal labelling, no matter what the photon coherence time is. Such a setup introduces additional propagation losses, which is generally undesirable [181].

However these two strategies typically exhibit additional propagation losses, which is generally undesirable. Thus, for this work, an essentially loss-free birefringence compensation stage is chosen, namely a polarization maintaining (PM) fibre, in which the sign of the birefringence is inverted compared to that of the PPLN/W. In order to estimate the correct fibre compensation length, three essential measurements have to be carried out.

(a) A polarization dependent delay scanning apparatus has to be calibrated using a femtosecond pulsed laser in a first order interference experiment. This delay scanning apparatus allows to introduce a precisely determined artificial delay between the horizontal and vertical polarization modes of incoming photons.
(b) With the help of this delay apparatus, the natural waveguide birefringence is measured using a second order interference experiment.
(c) Finally, the specific delay compensation of the PM fibre is examined when performing another second order interference experiment. This allows cutting the PM fibre at the optimal length.

To this end, the experimental setup depicted in Figure 2.13 is used. One out of three possible input sources can be chosen at will:
(a) diagonally polarized femtosecond pulsed laser[8], $|\psi_{\mathrm{fs}}\rangle = \frac{1}{\sqrt{2}}(|H\rangle + |V\rangle)$;
(b) PPLN/W with single mode fibre as light collector, $|\psi_{\mathrm{SM}}\rangle = |H,0\rangle\,|V,\delta t_{\mathrm{SM}}\rangle$;
(c) PPLN/W with 6 m PM fibre[9] as light collector, $|\psi_{\mathrm{PM}}\rangle = |H,0\rangle\,|V,\delta t_{\mathrm{PM}}\rangle$.

Here, δt_{SM} and δt_{PM} stand for the temporal delay of the $|V\rangle$ mode compared to the $|H\rangle$ counterpart in front of the polarization dependent Michelson interferometer. Note that δt_{SM} is directly related to the PPLN/W birefringence. δt_{PM} is the combined birefringence of both the waveguide and the PM fibre. The longitudinal position of one mirror can be adjusted with a precision of 50 nm[10], thus allowing for fine tuning of the artificial delay introduced between $|H\rangle$ and $|V\rangle$ modes. After the Michelson interferometer, photons are fibre coupled and the quantum states for the three configurations are given by

$$\text{(a)} \qquad |\psi_{\mathrm{fs}}\rangle = \frac{1}{\sqrt{2}}\left(|H,0\rangle + e^{i\,\phi_{\mathrm{M}}}\,|V,\delta t_{\mathrm{M}}\rangle\right), \tag{2.7}$$

$$\text{(b)} \qquad |\psi_{\mathrm{SM}}\rangle = e^{i\,\phi_{\mathrm{M}}}\,|H,0\rangle\,|V,\delta t_{\mathrm{SM}} + \delta t_{\mathrm{M}}\rangle\,, \tag{2.8}$$

$$\text{(c)} \qquad |\psi_{\mathrm{PM}}\rangle = e^{i\,\phi_{\mathrm{M}}}\,|H,0\rangle\,|V,\delta t_{\mathrm{PM}} + \delta t_{\mathrm{M}}\rangle\,. \tag{2.9}$$

Here, δt_{M} is the delay introduced by the movable mirror in the Michelson interferometer and $\phi_{\mathrm{M}} = \omega_{\mathrm{phot}}\,\delta t_{\mathrm{M}}$ is a phase factor. The photons angular frequency is denoted by

[8] Calmar Optcom, model FPL-R3TFUNC22.
[9] 3 x Thorlabs P1-1550PM-FC-2.
[10] Thorlabs Z825B.

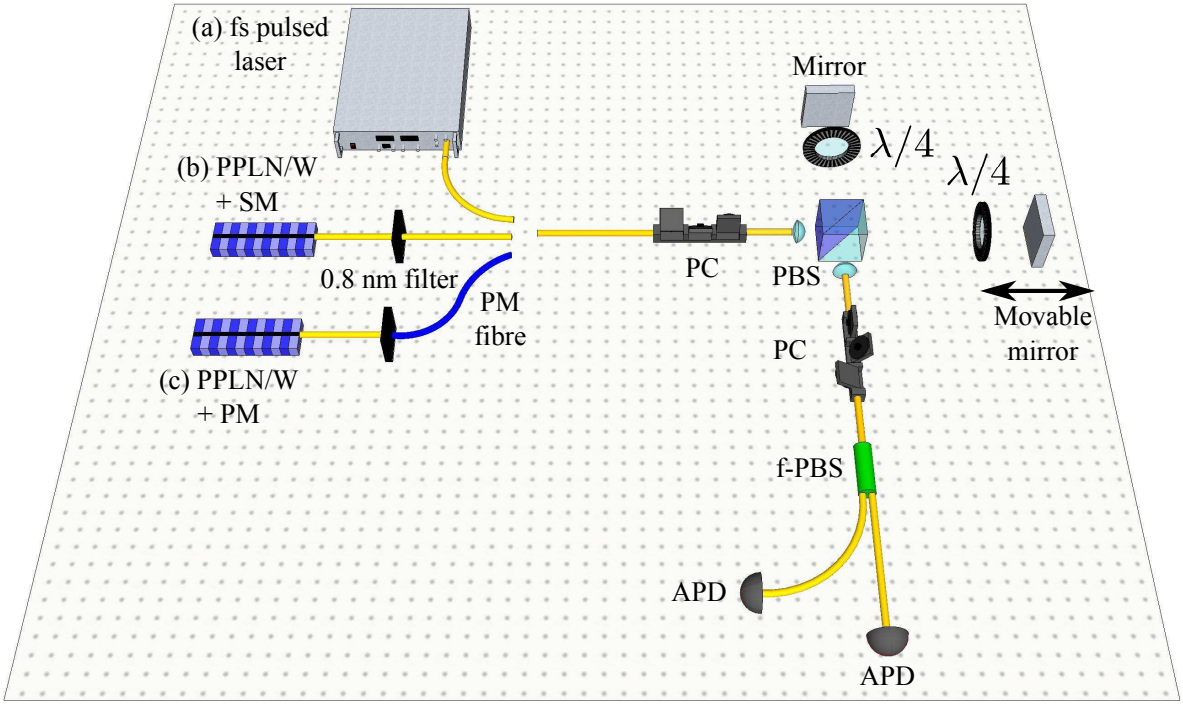

Figure 2.13.: Experimental setup towards measuring the PPLN/W birefringence. One out of three input sources can be chosen at will: (a) a fs pulsed laser, (b) the PPLN/W emission collected by a single mode fibre (yellow line), (c) the PPLN/W emission after passing through a 6 m polarization maintaining (PM) fibre. For the two configurations in which a PPLN/W photon pair generator is employed, a 0.8 nm filter is added towards removing wavelength labelling, as discussed before. Light is then sent to a polarizing beam-splitter (PBS), that separates the $|H\rangle$ and $|V\rangle$ modes. Both photons are reflected back to the PBS by mirrors. One mirror is movable to adjust the delay of the $|V\rangle$ mode. Two quarter wave plates ($\lambda/4$) are employed to guarantee that both photons exit the Michelson interferometer like setup towards the bottom output port. The two polarization modes are then rotated by 45° using a polarization controller (PC) and projected on a fibre-PBS (f-PBS). Finally, two InGaAs APDs are employed as single photon detectors. Configuration (a) serves to find the zero position of the Michelson arrangement (meaning that the two arms are perfectly balanced). In configuration (b) and (c) HOM dip measurements are performed, delivering the birefringence induced by the PPLN/W and the PPLN/W combined with the PM fibre, respectively.

ω_{phot}. Current single photon detectors show a typical timing resolution of $\sim$ 100 ps and are consequently not capable of detecting the small arrival time differences (4.42 ps expected) between the $|H\rangle$ and $|V\rangle$ modes. This is why several interference experiments are performed. In such interference experiments, the time observable is translated to the position, which is often much easier to control (1 ps $\leftrightarrow$ 300 μm). After the Michelson interferometer the photons are rotated by 45° using a fibre polarization controller and sent to a fibre polarizing beam-splitter (f-PBS) at whose outputs two InGaAs single photon avalanche photodiodes (APD) are employed. In this configuration, which is often referred to be a polarization Hong, Ou, and Mandel (HOM) like setup [223], the respective quantum states after the f-PBS read

$$\text{(a)} \quad |\psi_{\text{fs}}\rangle = \frac{1}{2}\left(|H,0\rangle_a + |V,0\rangle_b + e^{i\,\phi_{\text{M}}}\,|V,\delta t_{\text{M}}\rangle_b - e^{i\,\phi_{\text{M}}}\,|H,\delta t_{\text{M}}\rangle_a\right), \tag{2.10}$$

$$\begin{aligned}\text{(b)} \quad |\psi_{\text{SM}}\rangle = \frac{1}{2}e^{i\,\phi_{\text{M}}}\Big(&|H,0\rangle_a\,|V,\delta t_{\text{SM}}+\delta t_{\text{M}}\rangle_b - |H,0\rangle_a\,|H,\delta t_{\text{SM}}+\delta t_{\text{M}}\rangle_a \\ &+|V,0\rangle_b\,|V,\delta t_{\text{SM}}+\delta t_{\text{M}}\rangle_b - |V,0\rangle_b\,|H,\delta t_{\text{SM}}+\delta t_{\text{M}}\rangle_a\Big),\end{aligned} \tag{2.11}$$

$$\begin{aligned}\text{(c)} \quad |\psi_{\text{PM}}\rangle = \frac{1}{2}e^{i\,\phi_{\text{M}}}\Big(&|H,0\rangle_a\,|V,\delta t_{\text{PM}}+\delta t_{\text{M}}\rangle_b - |H,0\rangle_a\,|H,\delta t_{\text{PM}}+\delta t_{\text{M}}\rangle_a \\ &+|V,0\rangle_b\,|V,\delta t_{\text{PM}}+\delta t_{\text{M}}\rangle_b - |V,0\rangle_b\,|H,\delta t_{\text{PM}}+\delta t_{\text{M}}\rangle_a\Big).\end{aligned} \tag{2.12}$$

Here a and b denote the paths towards the two employed APDs. Note that horizontally polarized photons always travel along path a whereas vertically polarized photons along path b. Finally, the detection probabilities on detectors D_a and D_b are evaluated [224]. It comes

$$\text{(a)} \quad p_{a,\,\text{fs}} = \frac{1}{2}\left(1 + e^{-\frac{4\,\ln(2)\,(\delta t_{\text{M}})^2}{\tau_{\text{fs}}^2}}\,\sin^2\frac{\phi_{\text{M}}}{2}\right); \qquad p_{b,\,\text{fs}} = 1 - p_{a,\,\text{fs}} \tag{2.13}$$

$$\text{(b)} \quad p_{a,\,\text{SM}} = p_{b,\,\text{SM}} = \frac{1}{2} \tag{2.14}$$

$$\text{(c)} \quad p_{a,\,\text{PM}} = p_{b,\,\text{PM}} = \frac{1}{2}. \tag{2.15}$$

In equations 2.13, τ_{fs} denotes the coherence time of the femtosecond laser. From these equations it is derived that intensity oscillations are obtained as a function of the phase ϕ_{M}. The oscillation amplitude is maximal when $\delta t_{\text{M}} = 0$. In other words, this amplitude is maximal when the artificial delay introduced by the Michelson interferometer is zero. Thus this first order interference measurement permits finding the zero position of the interferometer. The corresponding measurement is shown in Figure 2.14. The zero position of the interferometer is found with a precision of about 2 μm. From the width of the obtained curve, a laser coherence time of around τ_{fs} =200 fs is deduced. Unfortunately, equations 2.14 and 2.15 are completely parameter independent. Thus a second order interference measurement is considered. Now the probability of detecting a

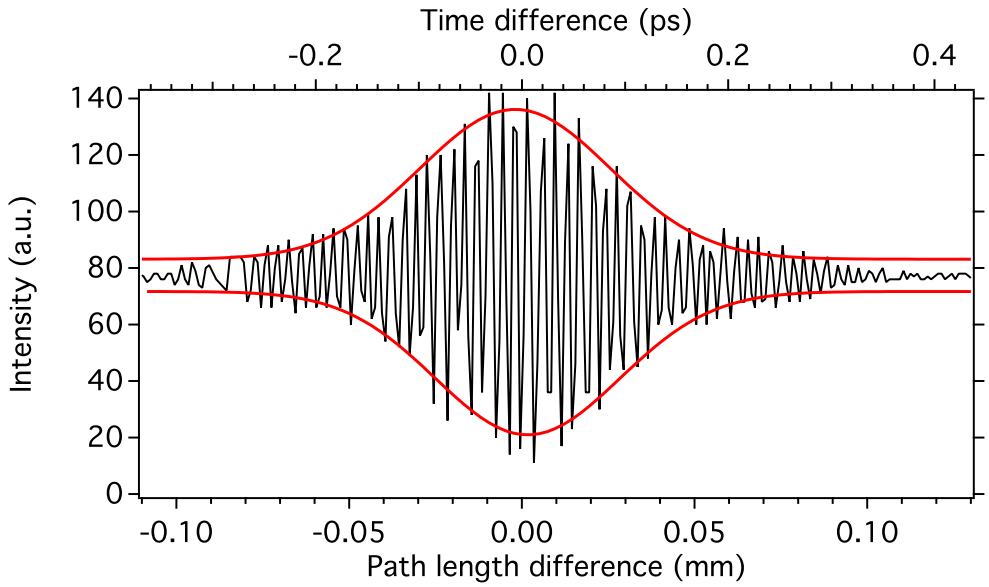

Figure 2.14.: Measurement towards finding the zero position of the Michelson interferometer like apparatus. Plotted here is the intensity at detector D_a as a function of the mirror position, as described by equations 2.13. Represented in black are experimental data, while red curves represent fits using a Gaussian function. The zero position of the interferometer is found with a precision of about $2\,\mu$m. In addition, the laser pulse coherence time is deduced from the width of the fits, delivering $\tau_{\text{fs}} \approx 200\,\text{fs}$.

coincidence between detectors D_a and D_b is considered. To obtain such an event, a pair of photons needs to be split up by the f-PBS. From equations 2.11 and 2.12 it is seen, that this probability drops down to zero for $\delta t_{\text{SM}} + \delta t_{\text{M}} = 0$, respectively $\delta t_{\text{PM}} + \delta t_{\text{M}} = 0$, which is often referred to as the optimal HOM dip position. The general coincidence probabilities are

$$\text{(b)} \qquad p_{ab,\,\text{SM}} = \frac{1}{2}\left(1 - e^{-\frac{4\,\ln(2)\,(\delta t_{\text{SM}}+\delta t_{\text{M}})^2}{\tau_{\text{phot}}^2}}\right), \tag{2.16}$$

$$\text{(c)} \qquad p_{ab,\,\text{PM}} = \frac{1}{2}\left(1 - e^{-\frac{4\,\ln(2)\,(\delta t_{\text{PM}}+\delta t_{\text{M}})^2}{\tau_{\text{phot}}^2}}\right). \tag{2.17}$$

In these equations, τ_{phot} represents the coherence time of the photons, which in this case is determined by the 0.8 nm filter that is employed after the PPLN/W. The reader finds a description of the coincidence measurement apparatus in Appendix B.3. In Figure 2.15, the measured coincidence probability as a function of the delay δt_{M} is shown. The experiment is performed for two configurations: (b) when the paired photons propagate through a single mode (SM) fibre towards the Michelson interferometer, and (c) when

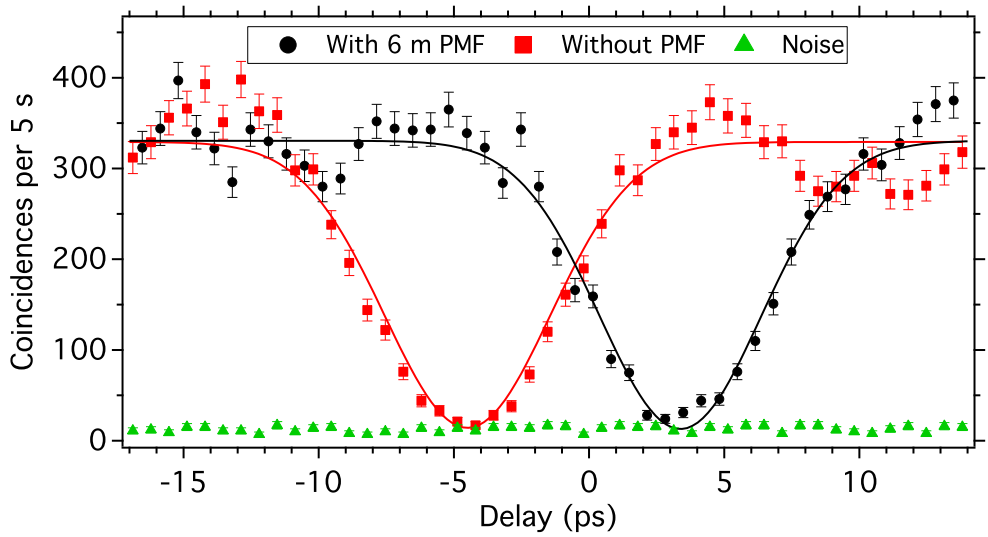

Figure 2.15.: Coincidence rate as a function of the delay introduced by the movable mirror, in configuration (b), *i.e.* when no PM fibre is connected to the PPLN/W output (red points). The dip position is found at a delay position of -4.40 ps, which agrees well with the theoretical predictions. For configuration (c), *i.e.* a 6 m PM fibre is connected (black points), the dip position is shifted to 3.38 ps, thus the 6 m PM fibre overcompensates the birefringence. Lines represent the best fits using a Gaussian function. Starting at this point in the thesis, the error bars denote one standard deviation of error assuming a Poissonian photon distribution, unless specified different.

a 6 m polarization maintaining (PM) fibre is employed in front of the interferometer. The polarization of the photons is chosen such that the slow (fast) axis of the PM fibre coincides with the $|H\rangle$ ($|V\rangle$) polarization of the paired photons. With the SM fibre, the HOM dip position is at $\delta t_{\mathrm{M}} = -4.40$ ps, which agrees well with the theoretical prediction. Using a 6 m PM fibre shifts the HOM dip position to $\delta t_{\mathrm{M}} = 3.38$ ps. Thus the specific birefringence compensation of the PM fibre at 1540 nm is 1.38 ps/m. Therefore a PM fibre length of 3.2 m should shift the HOM dip position to $\delta t_{\mathrm{M}} = 0$ ps, which should render the use of a Michelson interferometer configuration for birefringence compensation obsolete. A 3.2 m PM fibre was obtained by combining a 2 m patch cord PM fibre with another PM fibre cut at a length of 1.2 m and spliced to a standard single mode fibre. In Figure 2.16 the corresponding HOM dip measurements are shown. With the 3.2 m PM fibre, the HOM dip position is shifted to the delay position of 0.03 ps, which means that the birefringence induced delay between the $|H\rangle$ and $|V\rangle$ modes is nearly perfectly compensated. The degree of compensation can be estimated when comparing the residual delay to the coherence time of the paired photons (100 GHz $\leftrightarrow$

0.8 nm ↔ 4.4 ps). The ratio exceeds a factor of 100, thus the residual delay can now be considered as negligible. Moreover, this delay compensation strategy can be considered as essentially loss-free and highly reliable, as no realignment is required after a one-time proper alignment.

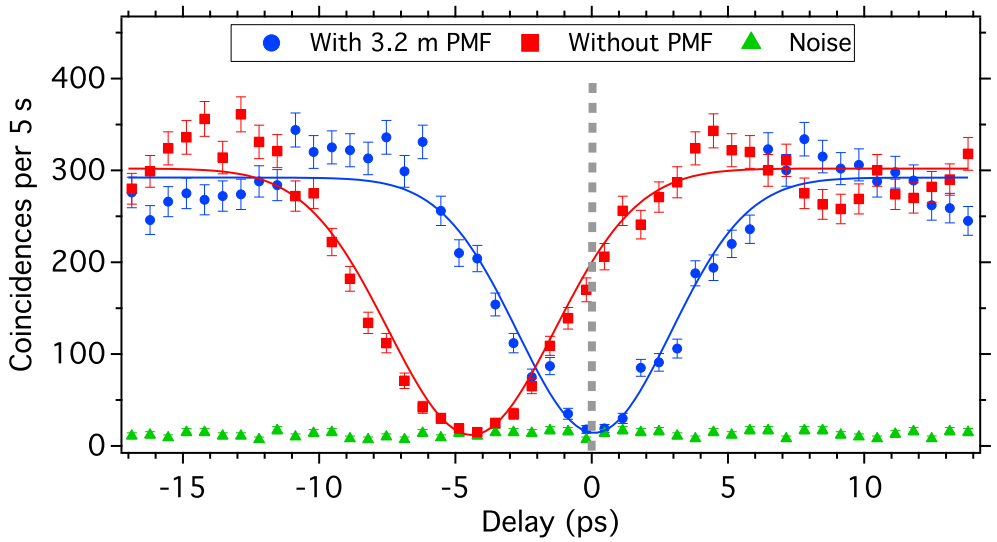

Figure 2.16.: Coincidence rate as a function of the delay introduced by the movable mirror, without PM fibre and with a purpose-cut 3.2 m PM fibre. With the PM fibre in place the HOM dip position is shifted to 0.03 ps, which means that the birefringence is nearly perfectly compensated. Lines are fits to the data using a Gaussian function. The dashed vertical line represents zero delay.

2.3.2. Deterministic photon pair separation

One of the main loss-sources for type-II waveguide based polarization entanglement sources is that entanglement is successfully generated only after pair separation at a beam-splitter (see Figure 2.4). However, this separation procedure is probabilistic with a success rate of only 50%. Consequently, half of the generated photon pairs are lost which is undesirable for two reasons: first, longer integration times are required to acquire the same amount of data, and secondly, the signal to noise ratio is decreased, which is, especially for out-of-the-lab applications, highly undesirable. We employ here a new strategy to deterministically separate the paired photons from a type-II source without reducing the entanglement quality. The general photon pair deterministic separation idea is outlined in Figure 2.17. The emission spectrum of the type-II PPLN/W is divided in two regions, one high and one low wavelength region, labelled + and −,

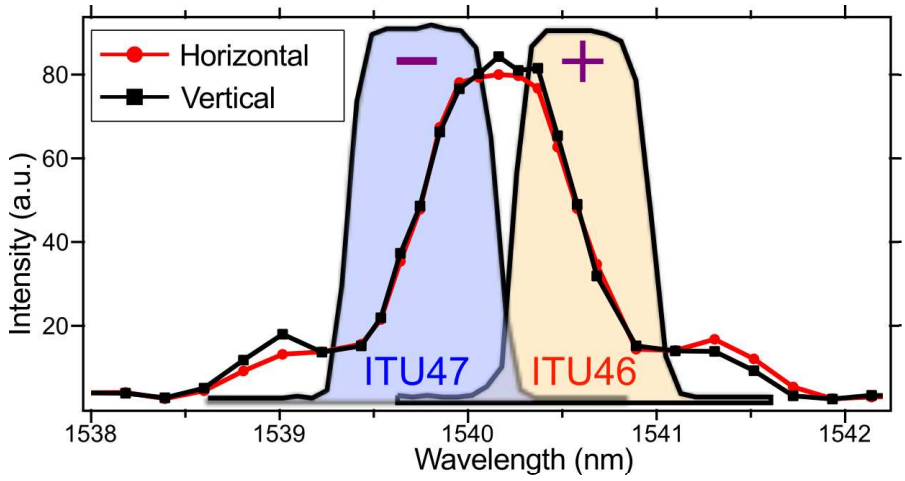

Figure 2.17.: Underlying idea for deterministic photon pair separation. The deterministic wavelength separation can be achieved using a set of two DWDMs. Photons in ITU46 are sent to Alice, while photons in ITU47 are directed to Bob. Due to the conservation of the energy, an existing photon in ITU47 implies that the other photon is in ITU46. Moreover the emission regions in which a non-perfect spectral overlap between $|H\rangle$ and $|V\rangle$ modes is achieved (in the side peak regions) are rejected by both DWDMs. This means that within the two DWDM channels, the wavelength does not reveal the polarization state, thus the formation of high quality entanglement is possible.

respectively. Due to our choice of the QPM these two regions correspond to the reflection spectrum of standard 100 GHz telecom dense wavelength division multiplexers (DWDM) lying in the ITU channels 46 and 47. Photons in the + region are always sent to Alice while photons in the − region go to Bob. Because of conservation of energy for the SPDC process, a photon in the + region implies that the partner photon is in the − region, such that the photon pair is deterministically separated. Experimentally, this is made possible using standard telecom fibre components, namely dense wavelength division multiplexers (DWDM), that show very low loss figures. Note that such DWDMs can be seen as the fibre equivalents of bulk optics dichroic mirrors. From the experimental side, deterministic pair separation is achieved with the following strategy (see also Figure 2.18):

- The PPLN/W emission is directed to an ITU46 DWDM, reflecting the spectrum shown in Figure 2.17 (orange), which is sent to Alice.
- The transmission of the ITU46 DWDM is the complement of its reflection (*i.e.* all the rest) and is further filtered using an ITU47 DWDM.
- The reflection of the ITU47 DWDM, shown in Figure 2.17 (blue), is sent to Bob.

- The transmission of the ITU47 DWDM is discarded.

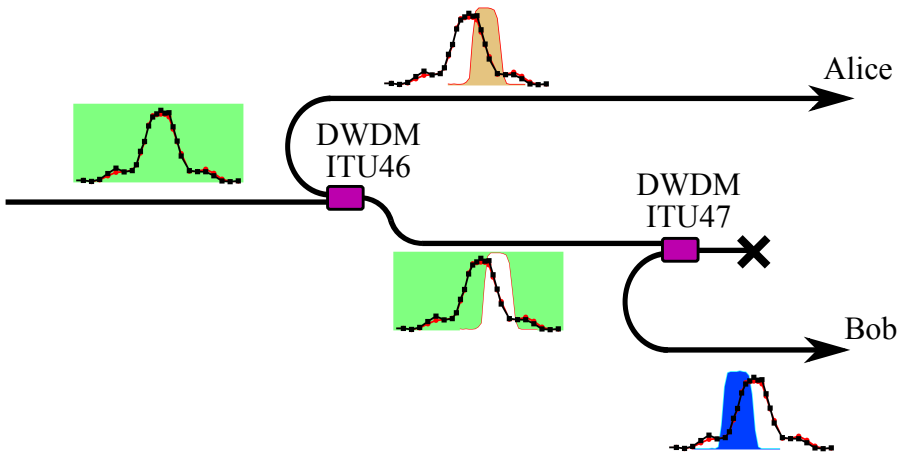

Figure 2.18.: Experimental implementation for deterministic photon pair separation. At the input the full spectrum is present (indicated by the green graph background). After the first DWDM in the channel ITU46, the spectrum sent to Alice is strongly reduced and indicated by the orange area. However, the transmission of the ITU46 DWDM is the complement of its reflection and relatively broadband (indicated by the residual green background). Another DWDM filter (ITU47) is used in reflection, and the corresponding spectrum is sent to Bob (indicated by the blue area in the lower right graph). This way, the photon pairs are deterministically separated between Alice and Bob and, in addition, the undesirable emission in the side peaks are removed.

Using this strategy, every pair (that is emitted within the DWDM filtering region) is deterministically split up between Alice and Bob, thus increasing the entanglement formation efficiency by a factor of two. Note that with this filtering strategy, the wavelength of the photon on Alice's (Bob's) side does not reveal information about the polarization state. Thus both contributions, *i.e.* $|H\rangle_+ |V\rangle_-$ and $|V\rangle_+ |H\rangle_-$, have to be taken into account in a coherent manner. Therefore, one expects the generation of the maximally polarization entangled Bell state $|\Psi^+\rangle$. In this configuration, this state is written as

$$|\Psi^+\rangle = \frac{1}{\sqrt{2}} \left(|H\rangle_+ |V\rangle_- + |V\rangle_+ |H\rangle_- \right). \tag{2.18}$$

2.3.3. Measurement of entanglement quality

The produced entanglement quality is measured using the experimental setup outlined in Figure 2.19. We send 2.5 mW from a 770 nm tapered amplifier laser diode system[11] to the PPLN/W towards generating wavelength degenerate cross-polarized photon pairs at 1540 nm in the state $|H, 0\rangle\,|V, -4.40\,\mathrm{ps}\rangle$. Here, -4.40 ps refers to the fact that the $|V\rangle$ mode exits the PPLN/W delayed, compared to the $|H\rangle$ mode, due to the waveguide birefringence. At the waveguide output, the photon pairs are collected using a single mode fibre. A polarization controller (PC_1) is used to adjust the polarization modes such that the $|H\rangle$ ($|V\rangle$) mode is oriented parallel to the slow (fast) axis of a 3.2 m long polarization maintaining (PM) fibre, which is used to compensate the delay between the contributions to better than 0.03 ps. The PM fibre is enclosed in a temperature stabilized box for better stability. After the PM fibre, the deterministic photon pair separation strategy as outlined in Figure 2.18 is applied. Then, the photons are sent to Alice and Bob at whose locations standard polarization state analysers are employed. To this end, each of them comprises a polarization controller (PC_2 and PC_3), a half-

[11] Toptica TA pro.

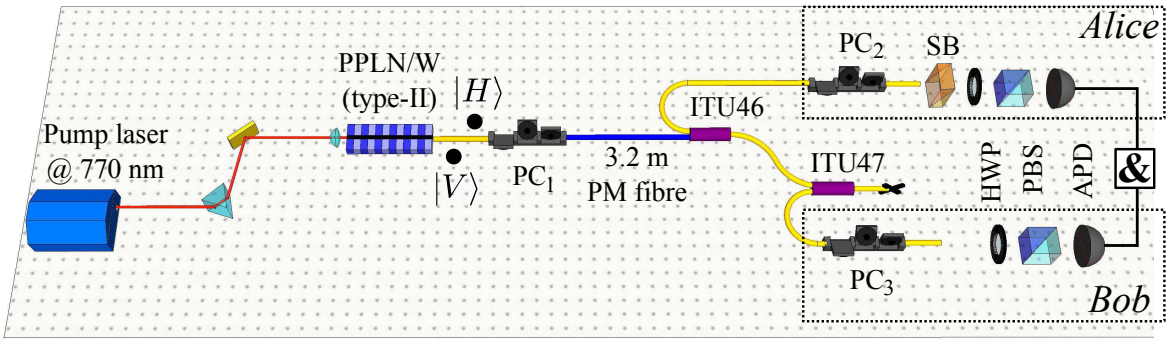

Figure 2.19.: Experimental setup to measure the entanglement quality provided by the type-II PPLN/W in combination with the polarization maintaining (PM) fibre birefringence compensator. 2.5 mW of a tapered amplifier diode laser system are sent to the PPLN/W towards generation of cross polarized photon pairs $|H\rangle\,|V\rangle$ at 1540 nm. A 3.2 m PM fibre compensates the PPLN/W birefringence and thus erases the temporal walk-off induced by the waveguide birefringence. A set of two DWDM filters in the channels ITU46 and ITU47 is used to deterministically separate the paired photons and removes also the wavelength labelling. Finally, Alice and Bob use each a polarization state analyser comprising a polarization controller (PC), a half-wave plate (HWP), a polarizing beam-splitter (PBS) and an InGaAs avalanche photodiode (APD). Alice uses in addition a Soleil-Babinet phase compensator (SB). Coincidences between the two APDs are recorded using an AND-gate (&).

wave plate (HWP) and a polarizing beam-splitter (PBS). Finally, the paired photons are detected using InGaAs single photon detectors in the free running regime[12], featuring 20% detection efficiency at 1540 nm and a probability of dark count as low as $10^{-6}\,\mathrm{ns}^{-1}$. The detectors are placed after the PBS transmission path and coincidence events between these detectors are recorded using a logic AND gate (&). Alice comprises an additional Soleil-Babinet (SB) phase compensator to correct for potential birefringence introduced by the single mode fibres after the DWDMs.

Phase measurement

As a first measurement, the potential birefringence induced by the single mode fibres has to be evaluated. This birefringence can possibly turn a maximally entangled 'Bell state' towards being a more general maximally entangled state of the form

$$|\Psi(\phi)\rangle = \frac{1}{\sqrt{2}}\left(|H\rangle_+ |V\rangle_- + e^{i\,\phi}\,|V\rangle_+ |H\rangle_-\right), \tag{2.19}$$

where ϕ is the birefringence induced phase. To measure the entanglement quality via the violation of the Bell's inequalities in the standard settings, a phase $\phi = 0$ or $\phi = \pi$ is required [225]. The strategy to measure and compensate for ϕ is the following: Alice's and Bob's HWPs are turned to 22.5° to project the quantum state $|\Psi(\phi)\rangle$ into the phase sensitive diagonal basis. The state develops then as follows

$$\begin{aligned} |\Psi(\phi)\rangle_{22.5} &= \frac{1}{2}\left((|H\rangle_+ + |V\rangle_+)(|V\rangle_- - |H\rangle_-) + e^{i\,\phi}(|V\rangle_+ - |H\rangle_+)(|H\rangle_- + |V\rangle_-)\right) \\ &= \frac{1+e^{i\,\phi}}{2}\left(|V\rangle_+ |V\rangle_- - |H\rangle_+ |H\rangle_-\right) + \frac{1-e^{i\,\phi}}{2}\left(|H\rangle_+ |V\rangle_- - |V\rangle_+ |H\rangle_-\right). \end{aligned} \tag{2.20}$$

It is interesting to note that only the contributions $|V\rangle_+ |V\rangle_-$ and $|H\rangle_+ |H\rangle_-$ lead to the observation of coincidence events (*i.e.* both photons are transmitted/reflected at the PBS at Alice's and Bob's side). On the other side, the contributions $|H\rangle_+ |V\rangle_-$ and $|V\rangle_+ |H\rangle_-$ lead to the observation of anti-coincidence events (*i.e.* one photon is reflected at Alice's PBS, while the other is transmitted at Bob's and vice versa). Thus we can rewrite equation 2.20 as

$$|\Psi(\phi)\rangle_{22.5} = \frac{1+e^{i\,\phi}}{2}[\mathrm{coincidence}] + \frac{1-e^{i\,\phi}}{2}[\mathrm{anti}-\mathrm{coincidence}], \tag{2.21}$$

where $[\mathrm{coincidence}] = |V\rangle_+ |V\rangle_- - |H\rangle_+ |H\rangle_-$ and $[\mathrm{anti}-\mathrm{coincidence}] = |H\rangle_+ |V\rangle_- - |V\rangle_+ |H\rangle_-$. Considering now the probabilities of coincidence (p_{coinc}) and anti-coincidence

[12] Id Quantique id220.

(p_{anti}) gives

$$p_{\text{coinc}} = \cos^2 \frac{\phi}{2} \tag{2.22}$$

$$p_{\text{anti}} = \sin^2 \frac{\phi}{2}. \tag{2.23}$$

Consequently, information on the phase ϕ is accessible via measuring the probability of a coincidence or anti-coincidence. In Figure 2.20, we show the observed coincidence rate as a function of the artificial phase introduced by the Soleil-Babinet phase compensator. The coincidence rate follows nearly perfectly the law given by equation 2.22. The tops and bottoms of this curve correspond to $\phi = 0$ and $\phi = \pi$. At these two points, the maximally entangled Bell states $|\Psi^+\rangle = |\Psi(0)\rangle$, respectively $|\Psi^-\rangle = |\Psi(\pi)\rangle$, are properly distributed between Alice and Bob, which is a necessary requirement towards violating the Bell's inequalities using the standard analysis settings. For the following, the phase is set to $\phi = 0$ and the polarization entanglement quality is analysed.

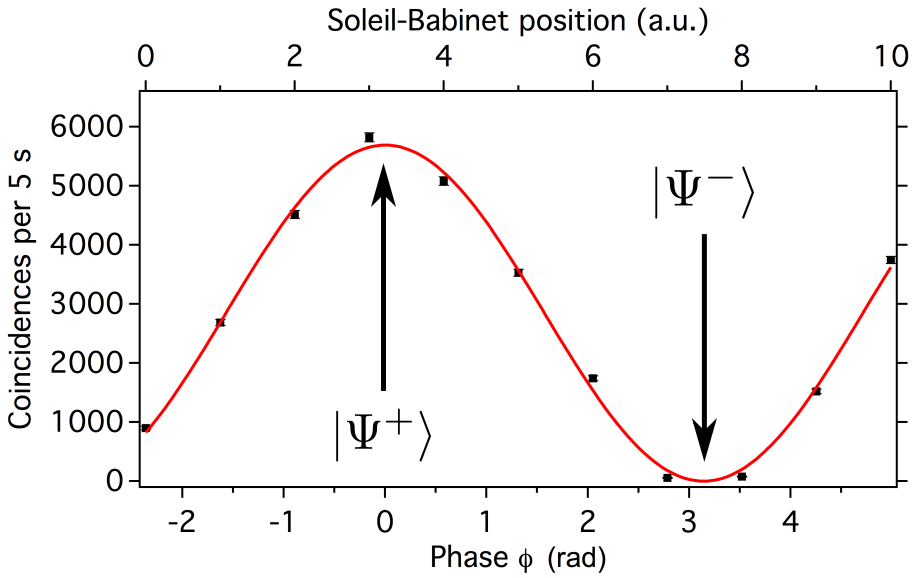

Figure 2.20.: Coincidence rate as a function of the phase introduced by the Soleil-Babinet phase compensator. Alice and Bob set their respective analysers to project the quantum state into the phase sensitive diagonal basis. A sinusoidal coincidence rate modulation is obtained, which is fitted by the red curve. The tops and bottoms of the coincidence rate correspond to the generation of the maximally entangled Bell states $|\Psi^+\rangle$ and $|\Psi^-\rangle$, respectively.

Polarization entanglement analysis

The optimal analyser settings for violation of the Bell's inequalities are derived in subsection 1.2.5. However the underlying idea is briefly repeated in the following:

- The state $|\Psi^+\rangle$ (and also all other maximally entangled states) is rotation invariant.
- This means, when Alice and Bob rotate their respective half-wave plates by the same angle, the coincidence (and anti-coincidence) rates do not change.
- Bell and later Clauser, Horne, Shimony and Holt (B-CHSH) showed that such a behaviour cannot be obtained for classical states, for all possible half-wave plate angles [16, 17].
- In fact, measuring the coincidence probability for four different angles at Alice and Bob is already sufficient, to distinguish between entangled and classical states [16, 17].

In the following, we fix the half-wave plate at Alice's side at the four standard settings $0° \equiv |H\rangle$, $22.5° \equiv |D\rangle$, $45° \equiv |V\rangle$ and $-22.5° \equiv |A\rangle$. For these four settings, the coincidence probability between Alice and Bob is measured as a function of the rotation angle of Bob's half-wave plate. As shown in Figure 2.21, sinusoidal coincidence rate

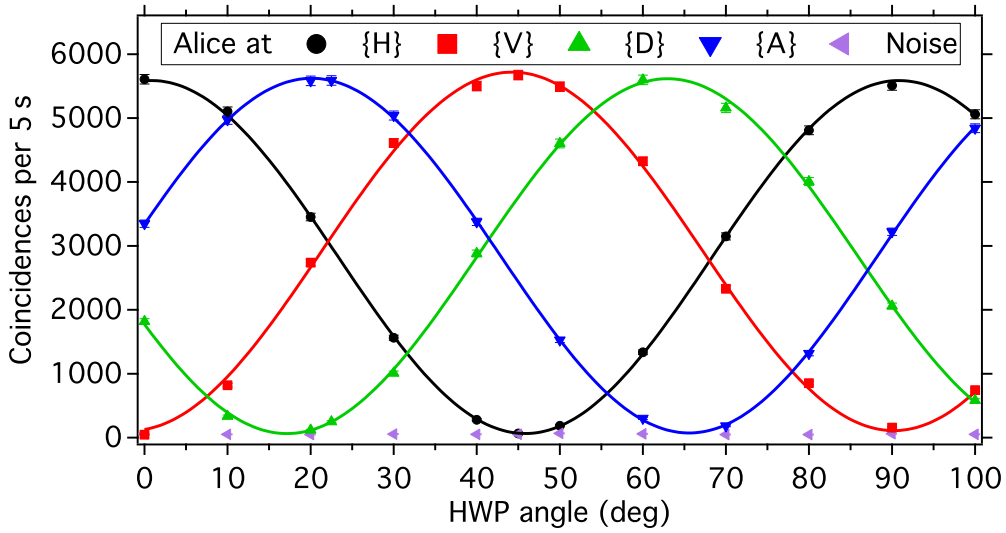

Figure 2.21.: Coincidence rate between Alice and Bob as a function of Bob's half-wave plate (HWP) angle. For all settings on Alice's side, sinusoidal coincidence rate modulations are obtained and fitted by the solid curves. The fact, that for all four settings the same high visibility oscillations are obtained, is a proof of entanglement.

modulations are obtained for all four settings at Alice's side, *i.e.* the coincidence rate behaviour between Alice and Bob is the same for all four settings at Alice's side, which cannot be mimicked when considering a classically (or non-entangled) state, according to B-CHSH [16, 17]. Thus, this measurement proves that a maximally entangled Bell state has been generated. The quality of entanglement can be measured using various techniques. One is to compute the visibility V of the oscillations, given by

$$V = \frac{\text{Max} - \text{Min}}{\text{Max} + \text{Min}}, \tag{2.24}$$

where Max and Min correspond to the maximum and minimum count rates, respectively. The more V approaches unity, the higher is the entanglement quality. Note that the quantum threshold is $V = \sqrt{\frac{1}{2}} \approx 0.71$, when averaging over all four measurements. The average visibility observed in Figure 2.21 is $V_{\text{raw}} = 0.973 \pm 0.006$, which is relatively close to unity. Note that the main deviation from unity comes from accidental dark counts in the employed detectors. Subtracting the detector noise delivers an average visibility of $V_{\text{net}} = 0.995 \pm 0.008$. Note that the net visibility describes the actual entanglement quality of the source as it would be measured using ideal (*i.e.* noise-free) detectors. The raw visibility gives the observed entanglement quality using current state of the art InGaAs detectors.

Another related entanglement criterion is the so-called Bell parameter S. Classical states cannot exceed $S = 2$, while perfectly entangled states reach $S = 2\sqrt{2}$, thus allowing to quantify the quantumness of the generated state (see subsection 1.2.5). Extracting the corresponding points in Figure 2.21, it is calculated $S_{\text{raw}} = 2.806 \pm 0.005$ and $S_{\text{net}} = 2.824 \pm 0.007$, which means that the obtained entanglement quality is more than 100 standard deviations above the classical limit, thus the probability that a classical state has lead to the observed results is essentially zero. Finally, a last criterion is the entangled state fidelity to the closest maximally entangled state, in this case defined by

$$\mathcal{F} = \frac{1 + V}{2}. \tag{2.25}$$

In other words, this quantity describes the successful probability of generating the desired entangled state. The computed fidelities for this experiment are $\mathcal{F}_{\text{raw}} = 0.987$ and $\mathcal{F}_{\text{net}} = 0.998$. In the next subsection a brief performance analysis of this source is given.

2.3.4. Performance analysis

In the performance analysis, three main parameters are given, which are of interest for implementing networking applications. These parameters are the photon pair generator brightness, the internal PPLN/W SPDC efficiency and the photon propagation losses until successful photon pair separation.

Photon pair generator brightness

One main criterion is the efficiency of the photon pair generator, generally referred to as *brightness*. The brightness B of a source is defined as

$$B = \frac{\text{generated pairs}}{(\text{mW of pump power}) \cdot (\text{second}) \cdot (\text{GHz of spectral bandwidth})}. \tag{2.26}$$

While the three quantities in the denominator are easily accessible, the number of generated pairs is sometimes difficult to estimate. In the following, a strategy to estimate the number of generated pairs per time interval (here 1 s) is given, as described in reference [57]. Therefore we first consider the average single photon counting rates S_1 and S_2 on both detectors at Alice (D_1) and Bob (D_2). It is

$$S_1 = \frac{1}{2}\mu_1\eta_1\, N_{\text{pair}} \tag{2.27}$$

$$S_2 = \frac{1}{2}\mu_2\eta_2\, N_{\text{pair}}. \tag{2.28}$$

Here, μ_1 and μ_2 denote the propagation losses from the waveguide to the detectors, η_1 and η_2 are the detection efficiencies of the two detectors and N_{pair} is the number of generated pairs per second. The factor of $\frac{1}{2}$ comes from the fact that half of the photons are lost on the polarizing beam-splitters in Alice's and Bob's measurement apparatuses. The maximum coincidence rate C (*i.e.* when Alice at $\{H\}$ and Bob at $\{V\}$, and vice versa) is then given by

$$C = \frac{1}{2}\mu_1\eta_1\,\mu_2\eta_2\, N_{\text{pair}}. \tag{2.29}$$

Combining equations 2.27, 2.28 and 2.29 delivers

$$N_{\text{pair}} = \frac{2\, S_1\, S_2}{C}. \tag{2.30}$$

Note that equation 2.30 contains only quantities that are directly accessible in an experiment. The equation is independent on more difficult to access quantities, such as detection efficiencies and propagation losses. The measured single photon rates at Alice's and Bob's detector are $S_1 = 28 \cdot 10^3\,\text{s}^{-1}$ and $S_2 = 25 \cdot 10^3\,\text{s}^{-1}$, respectively. As shown in Figure 2.21, the maximum coincidence rate is $C = 1100\,\text{s}^{-1}$, leading to $N_{\text{pair}} = 1.25 \cdot 10^6\,\text{s}^{-1}$. The waveguide coupled pump power was measured to be $\sim$1 mW at 770 nm. In addition, the single photon's spectral bandwidth is 100 GHz, such that the calculated brightness is

$$B = 1.27 \cdot 10^4\, \frac{\text{pairs}}{\text{mW} \cdot \text{s} \cdot \text{GHz}}. \tag{2.31}$$

Total internal SPDC efficiency

The SPDC efficiency η_{SPDC} is strongly related to the brightness [55, 57]. It is defined as the probability to generate a photon pair originating from a single pump photon, within the full emission bandwidth of the PPLN/W. This can thus be rewritten as

$$\eta_{\mathrm{SPDC}} = \frac{N_{\mathrm{pair}}}{N_{\mathrm{pump}}}. \tag{2.32}$$

Here, N_{pump} is the number of pump photons per second coupled in the waveguide. Note that the spectral emission bandwidth is not considered in this case. For some applications that do not require spectral filtering, such a definition might be more suitable. Starting from the source brightness, the SPDC efficiency is calculated as follows

$$\eta_{\mathrm{SPDC}} = \underbrace{\left(B \cdot P_{\mathrm{pump}} \cdot \Delta\nu \cdot 10^3\right)}_{N_{\mathrm{pair}}} \underbrace{\left(\frac{h \cdot c}{P_{\mathrm{pump}} \cdot \lambda_{\mathrm{pump}}}\right)}_{1/N_{\mathrm{pump}}}. \tag{2.33}$$

Here, P_{pump} is the waveguide coupled pump power in W and $\Delta\nu$ is the PPLN/W natural emission bandwidth in GHz (in this case 0.85 nm $\leftrightarrow$ 107 GHz). The factor 10^3 comes from the fact that the brightness is measured per mW of pump power (instead of W). $h = 6.62607 \cdot 10^{-34}\,\mathrm{J \cdot s}$ is the Planck constant, $c = 299\,792\,458\,\mathrm{m \cdot s^{-1}}$ is the vacuum speed of light, and λ_{pump} is the wavelength of the pump laser in m, in this case $770 \cdot 10^{-9}$ m. Inserting all these parameters leads to

$$\eta_{\mathrm{SPDC}} = 3.5 \cdot 10^{-10}\,\frac{\mathrm{pairs}}{\mathrm{pump\ photon}}. \tag{2.34}$$

As shown in Table 2.2, compared to previous sources, this SPDC efficiency belongs to the highest ever measured for type-II polarization entanglement generators. It is mainly ascribed to the waveguide structure, which enables to exploit the non-linear SPDC interaction over long distances combined with a tight light confinement.

Propagation losses until photon pair separation

For applications, the propagation losses experienced by the paired photons until the source output, *i.e.* after birefringence compensation, filtering and successful pair separation, is an important information. This information can be, in principle, deduced from equations 2.27, 2.28 and 2.29 via

$$\frac{C}{S_1} = \mu_2\,\eta_2 \tag{2.35}$$

$$\frac{C}{S_2} = \mu_1\,\eta_1, \tag{2.36}$$

Ref.	Configuration	SPDC efficiency	Net visibility	Coincidence rate
K. F. Lee *et al.* [190]	DSF	3.2×10^{-32}	98.3%	$80\,\mathrm{s}^{-1}$
M. Medic *et al.* [194]	DSF	NA	$99.4 \pm 1.2\%$	$5\,\mathrm{s}^{-1}$
T. Suhara *et al.* [226]	type-II PPLN/W	5.3×10^{-10}	90%	NA
N. Piro *et al.* [52]	type-II PPKTP	2.8×10^{-10}	$98 \pm 1\%$	$5\,\mathrm{s}^{-1}$
A. Martin *et al.* [181]	type-II PPLN/W	1.1×10^{-9}	$99 \pm 2\%$	$800\,\mathrm{s}^{-1}$
This thesis [59]	type-II PPLN/W	3.5×10^{-10}	$99.5 \pm 0.8\%$	$1100\,\mathrm{s}^{-1}$

Table 2.2.: Comparison of different type-II photon pair generators sorted by configuration, SPDC efficiency, and obtained net entanglement visibilities. DSF: Dispersion shifted fibre, PPKTP: Periodically poled potassium titanyl phosphate. The configuration used in this thesis represents one of the most efficient in combination with high entanglement visibilities. Note that it is generally hard to compare DSF sources with the other sources based on PPKTP and PPLN/W crystals, as a different process for photon pair generation is used, namely four wave mixing.

which corresponds to the coincidence to single photon rate ratio. However such a strategy requires precise knowledge on the employed detectors' efficiencies, which often leads to loss underestimation as the detection efficiency is overestimated. Especially InGaAs avalanche photodiodes show a non-negligible detection efficiency decrease when counting high photon rates. This is because an electronic process is started after every photon detection event to stop the avalanche. During this process, which can take up to several tens of μs, the detector is *dead*, meaning that the detection efficiency is reduced to zero and thus no photons can be detected during this time interval.

To avoid such errors, the losses are measured via a telecom laser that is injected in the PPLN/W to simulate the single photons paths. The waveguide coupled power is measured directly at the output using a power meter which allows obtaining a reference power. Then the laser power after the DWDMs is measured. For the path of Alice a loss figure of $-3.0\,\mathrm{dB}$ (50% transmission) is measured, while for Bob we obtain $-3.5\,\mathrm{dB}$ (45% transmission) . The reason for the slightly increased losses towards Bob are explained by the second DWDM filter that is placed on this path (see Figure 2.19). Note that such noise figures are rather low, and mainly ascribed to the fact that standard low-loss telecom components have been used wherever possible.

Some possibilities to further reduce the loss-figures are given in the next subsection.

2.3.5. Possible improvements

As this source was outlined to be as efficient as possible, the list of potential improvements is relatively short. However, as always, there are still possibilities for improvements.

- The experimental setup could be strongly compacted and rendered more stable when using a fully guided-wave approach. Therefore a 770 nm fibre pump laser could be used, with the laser output being fibre pigtailed[13] to the waveguide input, thus requiring no re-alignment after a one-time alignment procedure. In addition, the output of the PPLN/W could be fibre-pigtailed (in this realization the output fibre was not fixed to the waveguide). Such a configuration could give a better stability and reliability for future applications. However, precautions have to be made, as the glue needs to withstand, over long times, high pump powers, and high temperatures to obtain the desired QPM.

- The light coupling efficiency between the integrated waveguide and the collection fibre is currently on the order of 70-80%. Deviations from unit coupling efficiency come from mode mismatch between the two structures. The coupling could be strongly improved using a segmented tapered waveguide structure, that handles the mode adaptation [227, 228].

- Selecting ultra low loss DWDM filters could also reduce the losses to a certain amount ($\sim 0.1 - 0.2\,\mathrm{dB}$). Especially high-power DWDM filters show generally somewhat reduced loss figures.

- The polarization state analysers at Alice's and Bob's place have been used in a free-space configuration, which adds additional losses (typically 1 dB of loss). Using fully fibred polarization state analysers, comprising piezo-driven fibre polarization controllers and fibre polarizing beam-splitters would practically eliminate these losses.

Applying all these improvements could lead to a near perfect source of polarization entangled photons pairs, in the precise sense that as many as possible generated entangled photon pairs arrive at the users, Alice and Bob. Note that ultra low losses from generation to distribution are not only required for quantum communication tasks such as quantum cryptography, but also for quantum information protocols, *e.g.* linear optical quantum computing [39, 229]. In all these applications the highest possible signal to noise ratio is desired for optimum performance.

[13] A fibre-pigtail means that a fibre is connected to the waveguide using a transparent glue, that adapts the refractive indices of the fibre to that of the PPLN/W.

2.3.6. Manipulation of the entangled state symmetry

In subsection 2.3.1, two-photon interference experiments were described for measuring and compensating the birefringence induced temporal walk-off between the horizontal and vertical photon modes. This subsection is outlined to demonstrate that these observations are attributed to an entangled state, available in a natural fashion directly after the PM fibre. In addition, it is shown how to manipulate the symmetry of the entangled state, *i.e.* how to obtain the maximally entangled Bell states $|\Psi^+\rangle$ and $|\Psi^-\rangle$. This then leads to the possibility of observing interference between two photons that do not see each other at the f-PBS.

Consider the experimental apparatus shown in Figure 2.22. This configuration is very similar to that of Figure 2.13. However, before the paired photons are sent to the projecting f-PBS, an additional stage is employed. After the polarization dependent

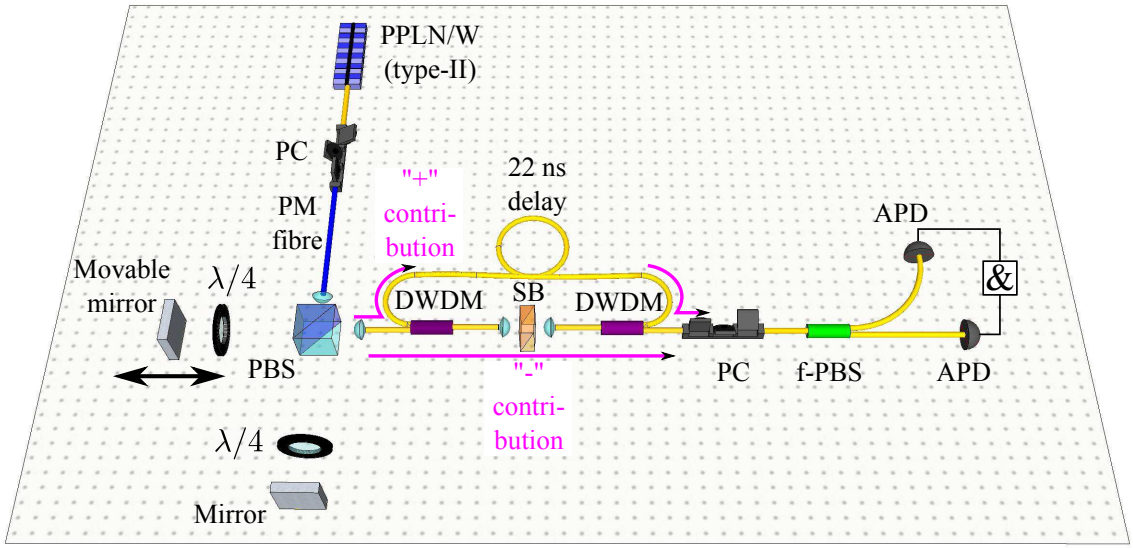

Figure 2.22.: Experimental setup for manipulating the quantum state symmetry. The emission of the type-II PPLN/W is sent through a PM fibre to compensate the waveguide birefringence. Then a Michelson interferometer like configuration is employed to introduce a polarization dependent delay δt_{M}. The photons are then split up into high (+) and low (−) wavelength regions using a DWDM (ITU46). Photons in the + region are 22 ns delayed in a fibre loop. Photons in the − region are sent through a SB that introduces a phase shift ϕ between the contributions $|H\rangle_-$ and $|V\rangle_-$. Both paths are then recombined using another DWDM (ITU47), rotated by 45° using a PC and sent to a f-PBS having two detectors (APDs) at its outputs. The detectors record coincidences (symbolized by &). In the end, interference between photons is observed that have different wavelengths and different arrival times at the f-PBS.

Michelson like interferometer, required to perform the HOM interference experiments, an ITU46 DWDM filter is used to split up the paired photons deterministically. The photons in the (−) region are sent to a variable fibre delay line, while photons in the (+) region are sent to an SB phase compensator. Then the two paths are recombined using an ITU47 DWDM. Thereafter the paired photons are rotated by 45° and projected using an f-PBS in combination with two single photon detectors at its outputs. The detectors are connected by an AND gate towards recording coincidences.

Concerning the state development, we get after the photons have been split up at the first DWDM (ITU46):

$$|\psi\rangle_{\text{split}} = \frac{1}{\sqrt{2}}\left(|H\rangle_+ |V\rangle_- + |V\rangle_+ |H\rangle_-\right). \tag{2.37}$$

After recombination in the ITU47 DWDM, we have

$$|\psi\rangle_{\text{recombine}} = \frac{1}{\sqrt{2}}\left(|H,d\rangle_+ |V,0\rangle_- + e^{i\,\phi}\,|V,d\rangle_+ |H,0\rangle_-\right). \tag{2.38}$$

Here, d is the delay introduced between the (+) and (-) contributions (not to be confused with the delay δt_{M} coming from the Michelson interferometer), while ϕ is the phase shift introduced by the SB between the contributions $|H,0\rangle_-$ and $|V,0\rangle_-$. It is remarkable that equation 2.38 represents a two-photon entangled state. For $d = 0$ and $\phi = 0$, the quantum state remains unchanged. Consequently, one might be tempted to state that there is one $|H\rangle$ and one $|V\rangle$ photon, resulting in $|\psi\rangle_{\text{recombine}}(d = 0, \phi = 0) = |H\rangle\,|V\rangle$ [181, 182]. However, in general, for $d \neq 0$ and/or $\phi \neq 0$, $|\psi\rangle_{\text{recombine}}$ needs to be written as an entangled state as shown in equation 2.38. Obviously, in the particular case $d = 0$ and $\phi = 0$, all experiments deliver the same experimental results, no matter whether the state is described as entangled or separable. But it is almost impudent to reduce an entangled state to be a separable one, just because the same experimental results are obtained. This is why we shall consider also for $\phi = 0$ and $\phi = \pi$ that the two-photon state is a maximally entangled Bell state of the form

$$|\Psi^+\rangle = \frac{1}{\sqrt{2}}\left(|H,d\rangle_+ |V,0\rangle_- + |V,d\rangle_+ |H,0\rangle_-\right), \tag{2.39}$$

and

$$|\Psi^-\rangle = \frac{1}{\sqrt{2}}\left(|H,d\rangle_+ |V,0\rangle_- - |V,d\rangle_+ |H,0\rangle_-\right), \tag{2.40}$$

respectively. Remarkably, these two states show different symmetries. The state $|\Psi^+\rangle$ has an even wave function symmetry, while the symmetry of the $|\Psi^-\rangle$ state is odd.

In addition, a polarization controller permits rotating $|\psi\rangle_{\text{recombine}}$ by 45°, resulting in

$$\begin{aligned} |\psi\rangle_{\text{PC}} \;=\; & \frac{1+e^{i\,\phi}}{2\sqrt{2}}\left(|V,d\rangle_+ |V,0\rangle_- - |H,d\rangle_+ |H,0\rangle_-\right) \\ & + \frac{1-e^{i\,\phi}}{2\sqrt{2}}\left(|H,d\rangle_+ |V,0\rangle_- - |V,d\rangle_+ |H,0\rangle_-\right). \end{aligned} \tag{2.41}$$

After the f-PBS, having the outputs a and b for vertically and horizontally polarized photons, respectively, we have

$$|\psi\rangle_{\mathrm{f-PBS}} = \frac{1+e^{i\,\phi}}{2}[\mathrm{anti-coincidence}] + \frac{1-e^{i\,\phi}}{2}[\mathrm{coincidence}], \tag{2.42}$$

with

$$[\mathrm{anti-coincidence}] = \frac{1}{\sqrt{2}}\left(|V,d\rangle_{+,a}\,|V,0\rangle_{-,a} - |H,d\rangle_{+,b}\,|H,0\rangle_{-,b}\right), \tag{2.43}$$

$$[\mathrm{coincidence}] = \frac{1}{\sqrt{2}}\left(|H,d\rangle_{+,b}\,|V,0\rangle_{-,a} - |V,d\rangle_{+,a}\,|H,0\rangle_{-,b}\right). \tag{2.44}$$

Obviously, [anti−coincidence] corresponds to cases in which both photons travel towards one detector and [coincidence] to cases in which the photon pairs are split up at the f-PBS. The contributions [anti − coincidence] and [coincidence] show an even and odd spatial distribution symmetry, respectively. Subsequently, the observation of [anti − coincidence] and [coincidence] corresponds to the generation of the maximally entangled Bell states $|\Psi^+\rangle$ and $|\Psi^-\rangle$, respectively.

This result can be understood as follows. Photons are bosons and thus require a bosonic (*i.e.* even) total wave function symmetry. This can be achieved in two ways in this experiment. Either combining an even wave function with an even spatial distribution (*i.e.* $|\Psi^+\rangle$ with [anti − coincidence]) or combining an odd wave function with an odd spatial distribution (*i.e.* $|\Psi^-\rangle$ with [coincidence]). The probabilities of having a coincidence, p_{c}, or anti-coincidence, p_{ac}, are

$$p_{\mathrm{c}} = \sin^2\frac{\phi}{2}, \tag{2.45}$$

$$p_{\mathrm{ac}} = \cos^2\frac{\phi}{2}. \tag{2.46}$$

These probabilities are independent of the time delay d. Moreover, as can be understood from equations 2.42, 2.43 and 2.44, these correlations are observed for photons having different wavelengths (there is always one (−) and one (+) photon).

In Figure 2.23, the experimental HOM-dip (peak) results are shown for $\phi = 0$ ($\phi = \pi$). To do so, the delay in the Michelson interferometer δt_{M} is scanned and the coincidence rates between the APDs at the outputs a and b are recorded. The delay d is not scanned and set to 22 ns using a 5 m long single mode fibre. This delay is much greater than the single photon coherence time of about 5 ps, such that any temporal overlap between the two individual photon contributions at the f-PBS is avoided. Thus, observation of interference (HOM-dip/peak) cannot be attributed to be the interference of two (independent) photons. What is actually observed in this experiment is the interference of a two-photon wave function with itself. The state described in equation 2.38 comprises two contributions $|H,d\rangle_+\,|V,0\rangle_-$ and $|V,d\rangle_+\,|H,0\rangle_-$. After the PC and the f-PBS, the

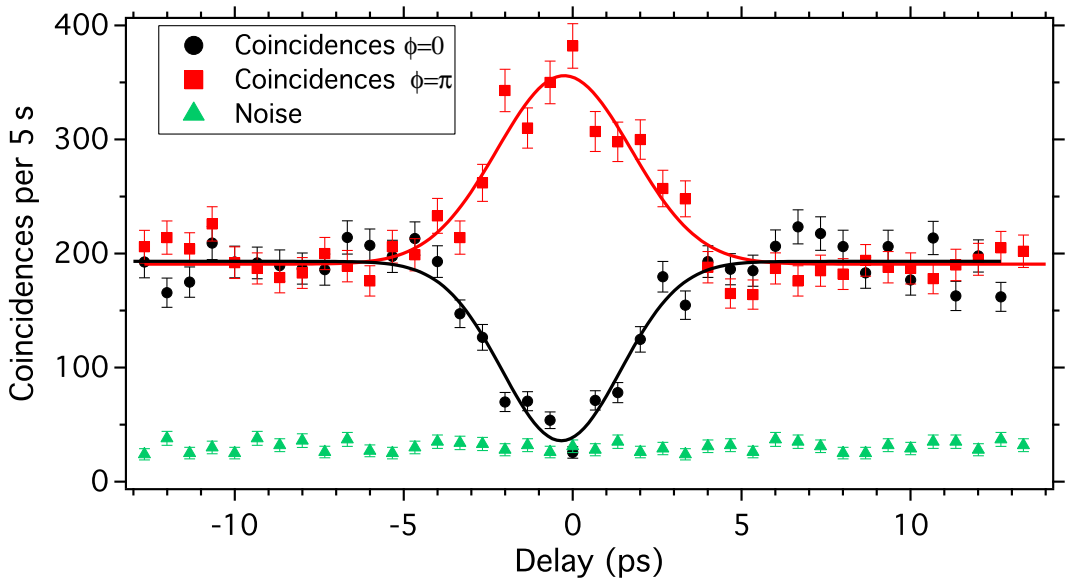

Figure 2.23.: HOM-dip and peak measurements. For $\phi = 0$, the generation of the maximally entangled state $|\Psi^+\rangle$ is expected which has an even wave function symmetry. This is why the spatial symmetry needs also to be even, meaning that both photons of each pair take always one f-PBS output port together. This results in the absence of coincidences as observed for the black data points (the solid line is a fit using a Gaussian function). When $\phi = \pi$, the entangled state $|\Psi^-\rangle$ is generated, which has an odd wave function symmetry. Consequently, the spatial distribution needs also to be odd, *i.e.* all photon pairs are split up at the f-PBS which results in an increased coincidence rate. Red dots are data points and the solid line represents a fit using a Gaussian function.

quantum state is rotated to the diagonal basis. After photon detection, the information about which polarization mode took which optical path is completely erased. Neither the delay (detection time), nor the photon wavelength reveal this information. The two contributions are *indistinguishable*, which means quantum mechanically speaking that all possible contributions have to be taken into account (including the corresponding phase relations). Thanks to their indistinguishability, the two contributions can then interfere, and for particular settings ($\phi = 0$ and $\phi = \pi$) maximum constructive (destructive) interference is obtained, which is expressed by the observation of anti-coincidences (coincidences).

The raw and net interference visibilities of the two obtained curves are $86 \pm 5\%$ and $94 \pm 6\%$, respectively. The relatively low raw visibilities are explained by additional propagation losses in the delay line and the SB phase compensator. In addition, for this experiment, the experimental setup was not optimized. Non-unit net visibilities are

explained by both non-perfect phase adjustment and a small polarization mode mismatch in front of the f-PBS. However, the obtained results demonstrate in a clear manner that the symmetry of the generated quantum states can indeed be manipulated, and the states $|\Psi^+\rangle$ and $|\Psi^-\rangle$ are generated. In addition, the observation of interference between two photons that do not see each other on the projecting f-PBS clearly underlines that a quantum state is observed having (at least) two indistinguishable contributions [230]. The fact that HOM-dips and peaks are observed underlines, additionally, that the phase relation between both contributions is constant (a non-constant phase relation would lead to flat curves), which is a requirement for observing entanglement and underlines our assumption that the two-photon entangled state $|\Psi^+\rangle$ is naturally available after the PM fibre. The experimentalist only needs to properly (post-)select this state using an appropriate setup, in this case DWDM filters.

A remark is given how to interpret this experiment in a different fashion. The experiment performed here is very similar to the phase tuning test shown in subsection 2.3.3. Here, the photon in the + region was always sent to Alice, while Bob obtained the photon in the − region. Then each of them uses a PBS to project the state in the diagonal basis. In the experiment shown in this subsection, Alice and Bob share one single f-PBS and measure their photons are different times. Bob corresponds now to the early photon and Alice to the late (having a temporal delay of d). When seeing this experiment this way, the reader might probably conclude that the obtained results are not surprising. However, the goal of this experiment is to convince the reader about the natural availability of the polarization entangled state $|\Psi^+\rangle$ directly after the PM fibre, which is in contrary to what is often stated in the literature, where only particular two-photon cases are studied [181, 182].

2.3.7. Conclusion

We demonstrated a high quality polarization entanglement source based on the type-II interaction in a PPLN/W. We first introduced the principle of photon pair generation via spontaneous parametric down conversion. Then, optical sample characterization was demonstrated with the main goals being to remove wavelength and temporal labelling of the two photon polarization modes. To do so, the sample was characterized in both the second harmonic generation, and spontaneous parametric down conversion regime. Several HOM-dip experiments have been performed to measure and compensate birefringence. Thereafter a new strategy for deterministic photon pair separation was introduced and applied. Birefringence compensation and photon pair separation have been achieved in a fully fibre configuration, namely using a polarization maintaining fibre and DWDM filters, respectively. This permitted reducing the losses and increasing the reliability and applicability. Then the source entanglement quality was examined via the violation of the Bell's inequalities. Near perfect entanglement was observed, underlining the relevance of our approach. Possible improvements towards further loss reduction have been proposed. Finally, the manipulation of the quantum state sym-

metry was shown and a discussion was given at which stage in the experimental setup polarization entanglement is available.

The work of this section is found summarized in reference [59]

2.4. A cross time-bin entanglement source based on a type-II PPLN/W

In this section, a new time-bin entanglement source is demonstrated, that allows generating the time-bin entangled state $|\Psi^-\rangle$, which has never been reported to date. Using this state, an adapted entanglement analysis system is utilized, that allows, in principle, implementing secure quantum key distribution (QKD) with passive analysers and only four instead of eight single photon detectors.

This section is organized as follows. First, a quick reminder is given on how current QKD systems are made to be secure via introducing randomness. To do so, several efforts on the resource and technology sides are required. Then the new time-bin entanglement source is introduced, that allows implementing secure QKD using a passive setup that requires less resources. Entanglement quality measurements are shown and it is depicted how to use this source for QKD. Then some possible improvements are discussed and a conclusion is given.

2.4.1. Recalling secure quantum key distribution

In secure QKD systems, where Alice and Bob share the entangled photons coming from an appropriate source, they need to choose two complementary quantum state analysis basis, between which they randomly switch [26, 27, 29]. To clarify this point, a quick example is given in the following.

Assume that Alice and Bob believe to share a maximally polarization entangled Bell state $|\Phi^+_{\text{polar}}\rangle = \frac{1}{\sqrt{2}}(|H\rangle_a |H\rangle_b + |V\rangle_a |V\rangle_b)$, where a and b denote Alice and Bob, respectively. As shown in Figure 2.24, if both fix their analysers (in this case polarizing beam-splitters (PBS)) at 0°, they expect to observe only coincidence events between the detectors labelled either "0" or "1". Thus, recording coincidence events results in identical data streams at Alice and Bob. However, this strategy lacks of security. As Alice and Bob do not change the analysis basis, a potential spy, named Eve, knowing the analysis basis, has now the possibility to force the measurement outcomes. Therefore Eve only needs to send pairs of horizontally or vertically polarized photons to Alice and Bob. If Eve sends the state $|H\rangle_a |H\rangle_b$, then the measurements at Alice and Bob deliver both a "0" as output. Sending a $|V\rangle_a |V\rangle_b$ photon pair results in "1" on both sides. Via comparing their data streams, Alice and Bob can convince themselves that they obtained correct results. However, the established key is not secure, as it is shared not only between Alice and Bob, but also with the spy. To circumvent this problem, Alice and Bob need to take advantage of the rotation invariance of maximally entangled states, as stated in subsection 1.4.3. Therefore, they need to randomly change

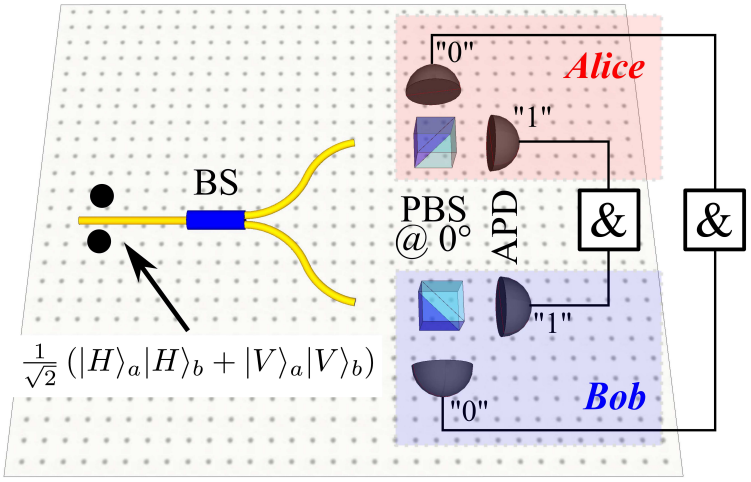

Figure 2.24.: Alice and Bob analyse the polarization entangled state $|\Phi^+\rangle = \frac{1}{\sqrt{2}}(|H\rangle_a|H\rangle_b + |V\rangle_a|V\rangle_b)$ in the $\{H, V\}$ basis only. Alice and Bob can convince themselves that they record only coincidences between both detectors labelled either "0" or "1". Thus, identical data streams are obtained. However, in this situation, a potential spy, Eve, could replace the photon pair source by a controlled source, emitting deterministically either $|H\rangle_a|H\rangle_b$ or $|V\rangle_a|V\rangle_b$. This way, the spy determines the measurement outcomes. Alice and Bob obtain still good measurement results and cannot notice the presence of a spy.

the analysis basis, *i.e.* by rotating the angle of the PBS[14]. To maximize the security, they generally choose two complementary analysis settings, *i.e.* they randomly switch between the PBS rotation angles 0° and 45°. The rotation invariance of entanglement takes care of the fact that both still analyse coincidence between the same detectors, when post-selecting only cases in which both utilized the same analyser settings. In this case, Eve loses her ability to force the measurement outcomes. This is because she does not know how to properly prepare the polarization state of her photons for them to be both deterministically transmitted of reflected at Alice's and Bob's PBS in all cases. Consequently, a potential spy introduces errors in the data streams, which give Alice and Bob the possibility to reveal the presence of a spy, by simply comparing a fraction of the obtained data.

Although this strategy gives the possibility of secure QKD, it requires several efforts on

[14]The term *randomly* implies in this case two things. First, a true randomness is required, which cannot be obtained by classical means. A quantum random number generator has to be used in this case, offering true and independent randomness. Second, Alice and Bob have to make sure, that nobody can know in advance, which setting is used for a particular measurement. Thus, data buffering of a random number stream should be avoided or, at least, be as short as possible to avoid that a spy knows the applied settings before the photons have been detected.

the resource and technological sides. Choosing randomly the analysis basis can be done using two main strategies that are outlined in Figure 2.25. One is to randomly rotate the analysers, as outlined above. This requires both a quantum random number generator, as well as fast switching electronics and optics[15] [231, 232]. Another possibility is that

[15]Note that it is generally not the PBS that is physically rotated, but rather the photon's polarization state is turned, using high-speed electro-optical modulators, in front of the PBS. For energy-time implementations, such modulators can also be used to modify the phase of the analysis interferometers to choose between complementary analysis basis.

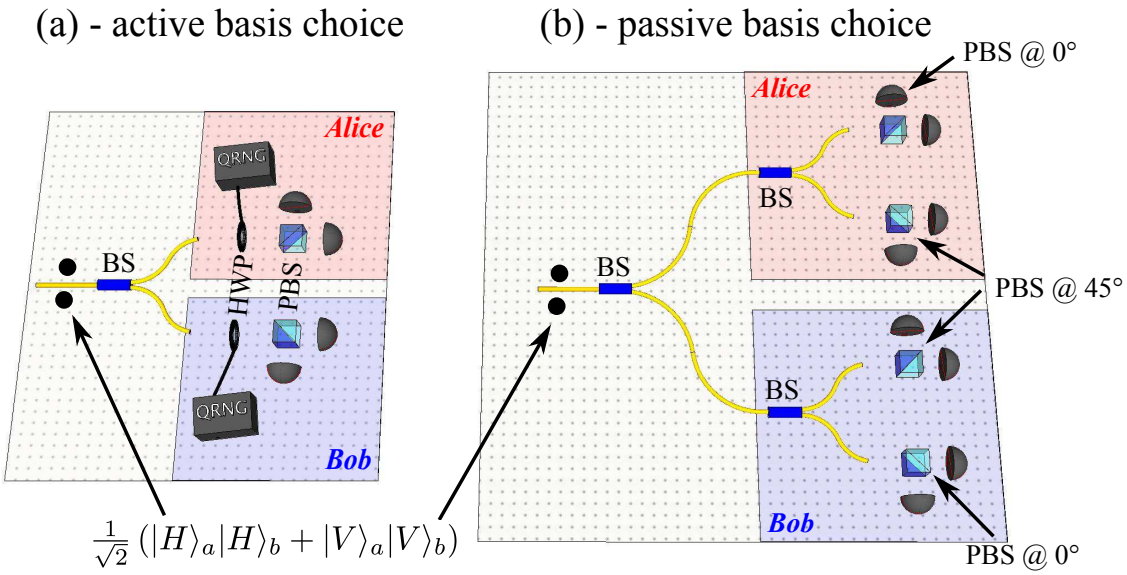

Figure 2.25.: Two generally employed strategies for random analysis basis choice. (a) In the active choice scheme, Alice and Bob employ each a quantum random number generator (QRNG), that chooses one out of two rotation angles for a half-wave plate (HWP), typically 0° and 22.5° for obtaining complementary analysis basis. Sometimes the HWP is also replaced by an electro-optical modulator. This rotates the photons' polarization state and results in the fact that the photons are analysed in different basis at the polarizing beam-splitters (PBS), after which two single photon detectors are employed. If Alice's and Bob's systems are fast enough, a spy cannot know in advance the analysis angles which allows implementing secure QKD. (b) In the passive basis choice scheme, Alice and Bob employ each two analysers, one for each basis, *i.e.* in this case a PBS at 0° and another at 45°. An ordinary beam-splitter (BS) is used to choose in which basis the photons are analysed. Note that in this configuration, eight instead of four detectors are required. Note moreover that the required AND gates between Alice's and Bob's detectors are not represented in this figure for reasons of simplicity.

Alice and Bob employ, each, two analyser setups, one for each basis. A 50/50 beam-splitter in front of the two analysis systems chooses then randomly to which analyser the photon is sent [233, 234]. Note in this case that the number of required single-photon detectors is increased from four to eight. Both strategies require serious demands on the technological side and thus increase the resource overhead.

In the following we employ a new strategy that allows implementing secure QKD using only four detectors and a single passive analyser on both Alice's and Bob's side. Thus, the resource overhead is minimized compared to current protocols. The randomness in this case is introduced in a passive way, via different photon arrival times (time-bins).

2.4.2. Description of the source

The goal for this source is to generate a time-bin entangled bi-photon state

$$|\Psi^-\rangle = \frac{1}{\sqrt{2}} \left(|0\rangle_a |1\rangle_b - |1\rangle_a |0\rangle_b \right). \tag{2.47}$$

Here, a and b denote Alice and Bob, and 0 and 1 are early and late time-bins. As discussed in the following, the generation of such a state is advantageous.

To generate such a state, the experimental setup depicted in Figure 2.26 is employed. As a photon pair generator, we take advantage of the same type-II PPLN/W as described in subsection 2.3. The operation conditions are the same, *i.e.* a horizontally polarized 770 nm pump laser generates cross-polarized paired of photons $|H\rangle |V\rangle$ at the degenerate wavelength of 1540 nm. The photons are collected by a single mode fibre. A 0.2 nm ($\leftrightarrow$ 25 GHz) fibre Bragg grating filter is used to reduce the photons' spectral bandwidth and consequently increases the photons coherence times to 17 ps ($\leftrightarrow$ 5 mm coherence length). Thereafter the photon pairs are sent to an unbalanced polarization dependent Michelson interferometer like configuration [181]. Compared to the similar apparatus employed in subsection 2.3, this time the $|H\rangle$ and $|V\rangle$ photons are temporally separated at the interferometer output. The separation in this case is $\sim$ 2 ns, which is much greater than the photons' coherence time (17 ps) and also much greater than the timing resolution of standard InGaAs single photon detectors ($\sim 100 - 400$ ps). This way, the two photons can be distinguished in their arrival times early and late which is actually the used measurement observable. From the technical side, for this particular realization, the Michelson interferometer is made of a fibre-pigtailed PBS and the two interferometer arms are made of a short and long single mode fibre with Faraday-mirrors at the end. These Faraday mirrors are the equivalent of the combination of a bulk quarter-wave plate and a mirror and guarantee that both photons exit the interferometer through the bottom output port.

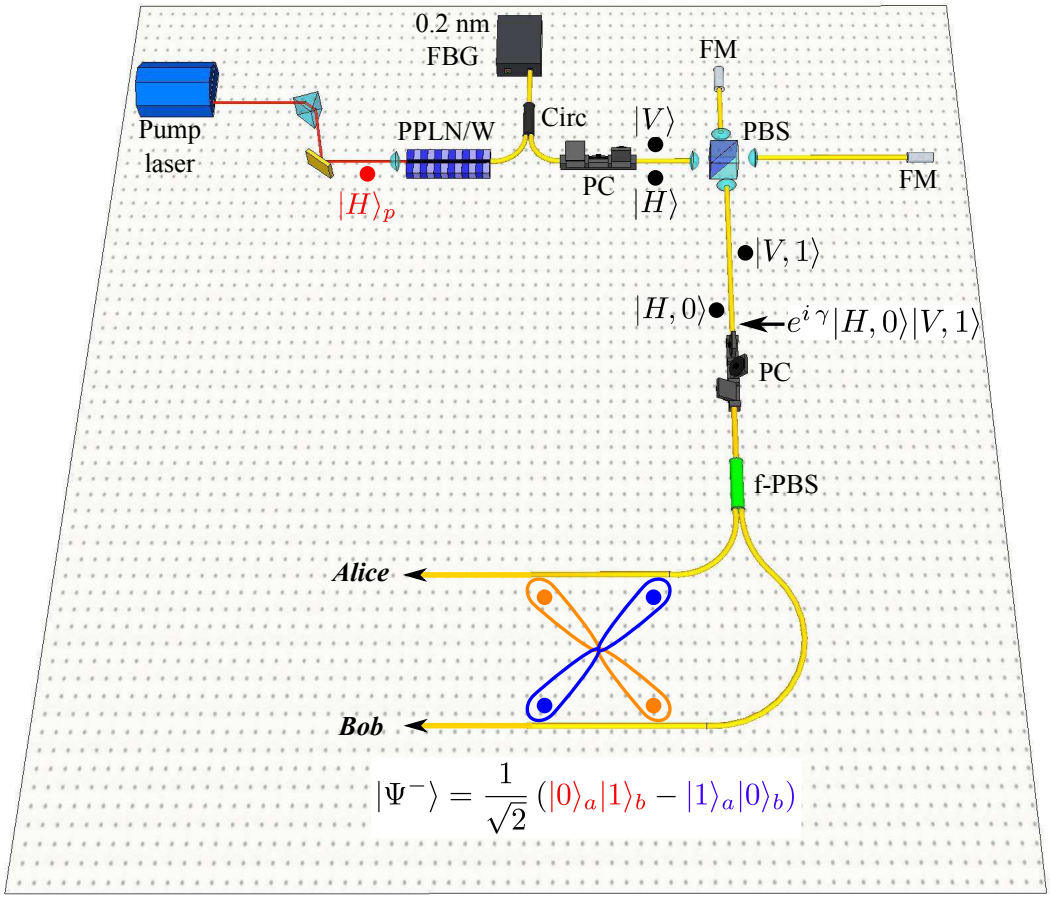

Figure 2.26.: Experimental setup towards generating the time-bin entangled state $|\Psi^-\rangle = \frac{1}{\sqrt{2}}(|0\rangle_a|1\rangle_b - |1\rangle_a|0\rangle_b)$. A horizontally polarized pump laser at 770 nm generates 1540 nm photon pairs $|H\rangle|V\rangle$ in a type-II PPLN/W. After the PPLN/W, the photons are collected using a single mode fibre, filtered down to 0.2 nm spectral bandwidth using a circulator (Circ) and a fibre Bragg grating (FBG). Thereafter they are sent to a polarization dependent Michelson like interferometer having a fibre-pigtailed polarizing beam-splitter (PBS) in the center. Faraday mirrors (FM) serve to reflect the photons back to the PBS. In addition, employing these mirrors compensates for fibre birefringence and guarantees that both photons leave the interferometer towards the bottom output. This introduces deterministically a delay between two photons, such that the state is $|\psi\rangle_{\text{out}} = e^{i\gamma}|H,0\rangle|V,1\rangle$, where 0 and 1 denote the time-bins. The photons are then rotated by 45° using a polarization controller (PC) and sent to a fibre polarizing beam-splitter (f-PBS). Successfully separated photon pairs are projected on the desired maximally time-bin entangled state $|\Psi^-\rangle$.

As the polarization modes are associated with the photon time-bins, the quantum state at the interferometer output reads

$$|\psi\rangle_{\text{out}} = e^{i\gamma}\,|H,0\rangle\,|V,1\rangle\,, \tag{2.48}$$

where $|0\rangle$ and $|1\rangle$ denote early and late time-bins, respectively. Note that for reasons of simplicity, we neglect in the following the global phase factor $e^{i\gamma}$ introduced by the path length difference for the two photon contributions.

Then, the photons are rotated by 45° using a polarization controller (PC), resulting in

$$|\psi\rangle_{\text{PC}} = \frac{1}{2}\left(-\,|H,0\rangle\,|H,1\rangle + |V,0\rangle\,|V,1\rangle + |H,0\rangle\,|V,1\rangle - |V,0\rangle\,|H,1\rangle\right). \tag{2.49}$$

Thereafter, the photons are sent to a polarizing beam-splitter having one output towards Alice (labelled a) and another towards Bob (b). The quantum state after the PBS therefore reads

$$|\psi\rangle_{\text{PBS}} = \frac{1}{2}\left(-\,|H,0\rangle_a\,|H,1\rangle_a + |V,0\rangle_b\,|V,1\rangle_b + |H,0\rangle_a\,|V,1\rangle_b - |V,0\rangle_b\,|H,1\rangle_a\right). \tag{2.50}$$

As the polarization modes $|H\rangle$ and $|V\rangle$ are always connected to the outputs towards Alice (a) and Bob (b), respectively, they are dropped, such the state of equation 2.50 is simplified as

$$|\psi\rangle_{\text{PBS}} = \frac{1}{2}\left(-\,|0\rangle_a\,|1\rangle_a + |0\rangle_b\,|1\rangle_b + |0\rangle_a\,|1\rangle_b - |0\rangle_b\,|1\rangle_a\right). \tag{2.51}$$

Finally, post-selecting only coincidence events, *i.e.* cases in which Alice and Bob obtain each one single photon, results in the desired state

$$|\Psi^-\rangle = \frac{1}{\sqrt{2}}\left(|0\rangle_a\,|1\rangle_b - |1\rangle_a\,|0\rangle_b\right). \tag{2.52}$$

Note that the phase relation between the two contributions $|0\rangle_a\,|1\rangle_b$ and $|1\rangle_a\,|0\rangle_b$ is intrinsically stable, *i.e.* the preparation Michelson like interferometer does not need to be stabilized. Especially for entanglement distribution over long time scales, this is an important advantage compared to previous time-bin realizations, that require an actively stabilized preparation interferometer on the pump laser side [235]. It is noteworthy that, to our knowledge, the generation of such a state has never been reported to date. In the following, we proceed to the analysis of such a state, and show how this state can be advantageously used for quantum key distribution using passive analysers.

2.4.3. Entanglement analysis strategy

Analysing entanglement of the state $|\Psi^-\rangle$ requires the use of unbalanced Mach-Zehnder like interferometers, as proposed for the first time by Franson [132] and experimentally

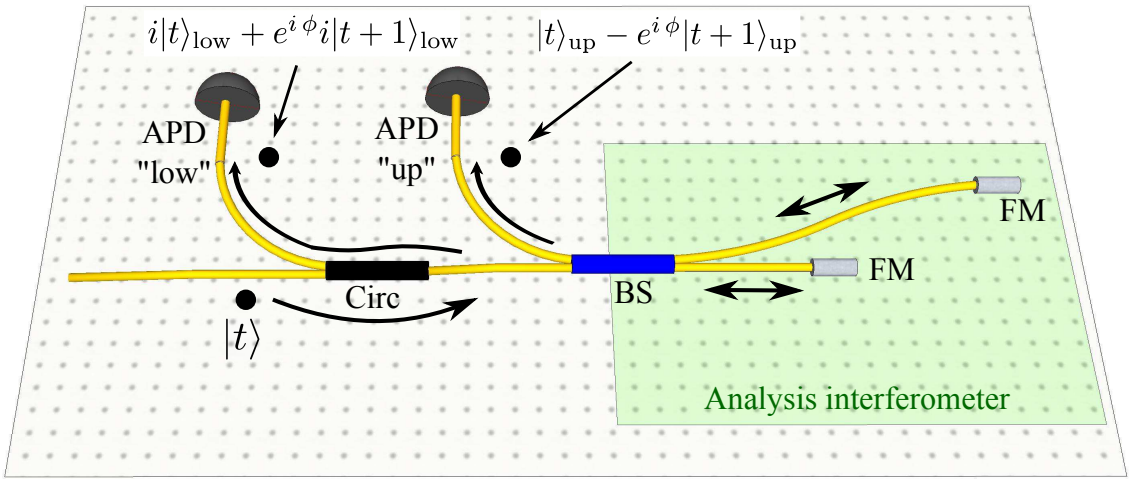

Figure 2.27.: Standard time-bin entanglement analysis interferometers as used in references [236, 237, 176, 233]. An incoming photon in the time-bin $|t\rangle$ passes an optical circulator (Circ), is incident on a fibre beam-splitter (BS), and sent along a short or long path. Faraday mirrors (FM) reflect the photon back to the BS. The path length difference imposes a relative phase ϕ between the single photon contributions. If a photon exits towards the upper BS output, it is projected on the state $\frac{1}{\sqrt{2}}\left(|t\rangle_{\text{up}} - e^{i\phi}|t+1\rangle_{\text{up}}\right)$ and detected on the avalanche photodiode (APD) labelled "up". Photons leaving towards the lower output of the interferometer are sent via a circulator towards APD "low" and are projected onto $\frac{1}{\sqrt{2}}\left(i|t\rangle_{\text{low}} + e^{i\phi} i|t+1\rangle_{\text{low}}\right)$. However, this output is often not utilized for proof-of-principle experiments.

demonstrated by many groups using bulk optics interferometers [170, 171, 172, 173, 174]. Later, fibre interferometers have been employed for better ease of use [157, 235]. In this particular experiment, Alice and Bob employ each a unbalanced fibre interferometer, as shown in Figure 2.27 and used in references [236, 237, 176, 233]. The path length difference of these interferometers is chosen to match the time-bin separation of the source, described in subsection 2.4.2. A photon can then exit the interferometer via the upper BS output towards detector "up". But it can also exit the interferometer back through the input port. In this case the photon is sent to a fibre optical circulator and goes to detector "low". The action U_{int} of this interferometer is given by

$$U_{\text{int}}|t\rangle_i = \frac{1}{2}\left(|t\rangle_{i,\text{up}} + i\,|t\rangle_{i,\text{low}} + e^{i\phi_i}\,i\,|t+1\rangle_{i,\text{low}} - e^{i\phi_i}\,|t+1\rangle_{i,\text{up}}\right). \tag{2.53}$$

Here, t denotes the time-bin of the photons, the subscript $i = \{a, b\}$ represent Alice and Bob and ϕ_i the phase difference introduced by the two respective interferometer arms. The subscripts up and low denote towards which of the two detectors the photon is sent.

In the following, only detection events on the detector labelled up are considered. This is a valid approach for proof-of-principle experiments. The reduced unitary interferometer operation, $U_{\text{int,red}}$, taking into account only the detector labelled "up", is

$$U_{\text{int,red}} \left|t\right\rangle_i = \frac{1}{\sqrt{2}} \left(\left|t\right\rangle_i - e^{i\,\phi_i} \left|t+1\right\rangle_i \right). \tag{2.54}$$

Applying this transformation on the source output state $|\Psi^-\rangle$, results in

$$\begin{aligned} U_{\text{int,red}} \left|\Psi^-\right\rangle \;=\; & \frac{1}{2\sqrt{2}} \Big(\left|0\right\rangle_a \left|1\right\rangle_b - e^{i\,\phi_a} \left|1\right\rangle_a \left|1\right\rangle_b - e^{i\,\phi_b} \left|0\right\rangle_a \left|2\right\rangle_b + e^{i\,(\phi_a+\phi_b)} \left|1\right\rangle_a \left|2\right\rangle_b \\ & - \left|1\right\rangle_a \left|0\right\rangle_b + e^{i\,\phi_a} \left|2\right\rangle_a \left|0\right\rangle_b + e^{i\,\phi_b} \left|1\right\rangle_a \left|1\right\rangle_b - e^{i\,(\phi_a+\phi_b)} \left|2\right\rangle_a \left|1\right\rangle_b \Big). \end{aligned} \tag{2.55}$$

As can be understood from equation 2.55, one needs to consider five relative arrival times between Alice's and Bob's detector. The different arrival time differences are illustrated in Figure 2.28. For this measurement, Alice and Bob employ each an InGaAs single photon detector and measure coincidence events as a function of the detection time difference. For more details on the coincidence measurements, see appendix B.3. The five peaks are labelled T_{-2}, T_{-1}, T_0, T_{+1} and T_{+2}, respectively.

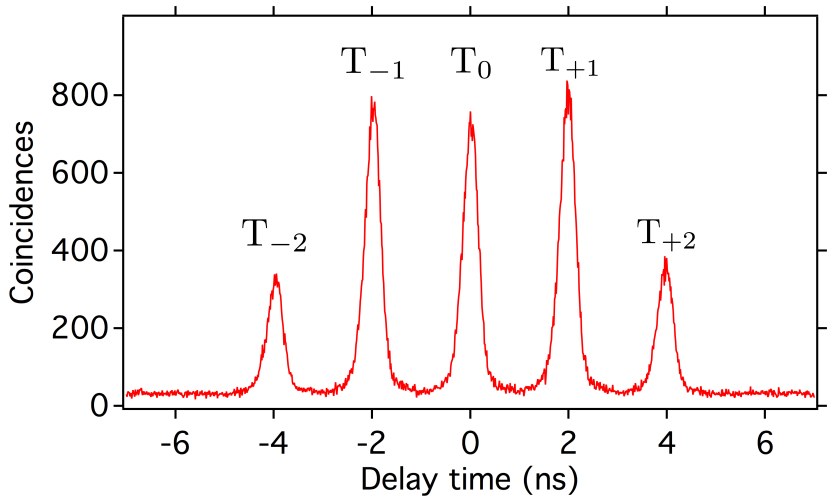

Figure 2.28.: Arrival time difference measurement for the paired photons after Alice's and Bob's analyser. Five coincidence peaks are obtained as predicted by equation 2.55. The peak separation corresponds to one time-bin, *i.e.* 2 ns. The peaks are labelled T_{-2}, T_{-1}, T_0, T_{+1}, and T_{+2}.

They contain the following quantum state contributions

- T_{-2}: $e^{i\,\phi_a}\,|2\rangle_a\,|0\rangle_b\,/\sqrt{8}$,
- T_{-1}: $\left(-\,|1\rangle_a\,|0\rangle_b - e^{i\,(\phi_a+\phi_b)}\,|2\rangle_a\,|1\rangle_b\right)/\sqrt{8}$,
- T_0: $\left(-e^{i\,\phi_a}\,|1\rangle_a\,|1\rangle_b + e^{i\,\phi_b}\,|1\rangle_a\,|1\rangle_b\right)/\sqrt{8}$,
- T_{+1}: $\left(|0\rangle_a\,|1\rangle_b + e^{i\,(\phi_a+\phi_b)}\,|1\rangle_a\,|2\rangle_b\right)/\sqrt{8}$,
- T_{+2}: $-e^{i\,\phi_b}\,|0\rangle_a\,|2\rangle_b\,/\sqrt{8}$.

The coincidence peaks $T_{\pm1}$ and T_0 exhibit the possibility to lead to interference, as they contain two contributions, coherently connected by a phase relation. The central peak, labelled as T_0, contains the two contributions associated with photon-pairs in the state $|1\rangle_a\,|1\rangle_b$. The temporal indistinguishability of these two contributions results in entanglement [132, 175] for which the probability of coincidence between Alice's and Bob's detectors follows

$$p_c^{T_0} \propto \cos^2\frac{\phi_a-\phi_b}{2}. \tag{2.56}$$

Interference in the peaks $T_{\pm1}$ is obtained for the following reason. A continuous wave pump laser is used to generate the photon pairs via SPDC. This results in the fact that the photon pair creation time remains unknown within the laser coherence time ($\sim 400\,\text{ns}$). This time is significantly greater that the time-bin separation (2 ns). As a result, the contributions $|0\rangle_a\,|1\rangle_b$ and $|1\rangle_a\,|2\rangle_b$, as well as $|1\rangle_a\,|0\rangle_b$ and $|2\rangle_a\,|1\rangle_b$, are also temporally indistinguishable and entanglement is observed. The expected coincidence probability follows

$$p_c^{T_{\pm1}} \propto \cos^2\frac{\phi_a+\phi_b}{2}. \tag{2.57}$$

Consequently, entanglement can be proven by observation of phase dependent coincidence rates in the peaks $T_{\pm1}$ and T_0 as described by equations 2.56 and 2.57.

The observed entanglement quality strongly depends on the path length mismatch of the three employed interferometers. We now describe first the performed path length mismatch measurements on the interferometers which allows estimating the maximal attainable entanglement quality. Thereafter, the corresponding entanglement measurements are shown.

2.4.4. Testing the quality of the analysis interferometers

The path length differences between the three employed interferometers (1 x preparation, 2 x analysis) need to be accurately matched for obtaining good entanglement qualities. The term *accurately* means in this case that the residual path length difference mismatch needs to be small compared to the single photon coherence length ($\sim 5\,\text{mm}$). In the following, a procedure towards measuring the path length difference is shown.

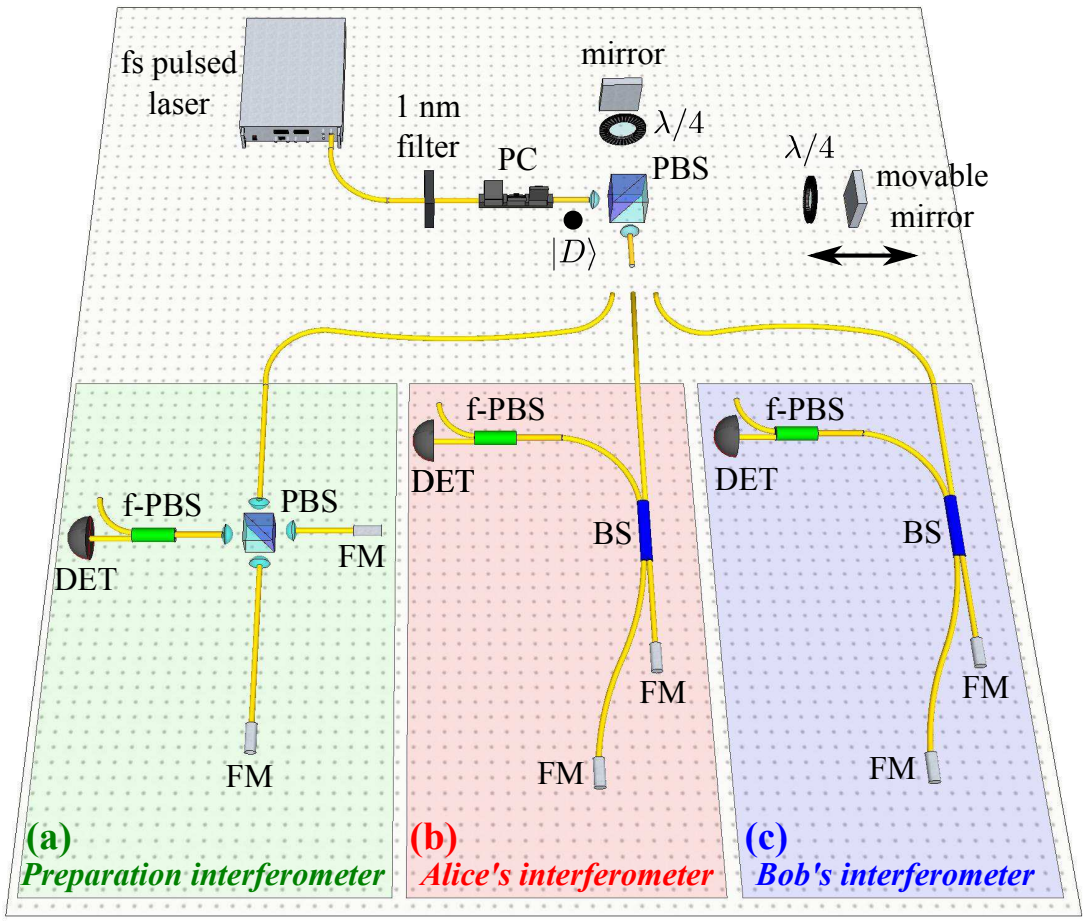

Figure 2.29.: Experimental setup towards measuring the path length differences of the three employed interferometers. The emission of a telecom femtosecond pulsed laser is filtered down to 1 nm and the polarization state is rotated to the diagonal state ($|D\rangle$) at the input of the polarization dependent Michelson interferometer like configuration. A movable mirror introduces a tunable artificial delay between the $|H\rangle$ and $|V\rangle$ modes. Thereafter, the photons are sent to one out of three interferometers. If the path length difference between the Michelson interferometer and the interferometer under test is matched, then maximum interference visibility is observed. Each interferometer output is connected to a fibre polarizing beam-splitter (f-PBS) to erase path labelling via the photons' polarization states. Light is detected using a fast photodiode (DET). (a) time-bin preparation interferometer made of a fibre-pigtailed polarizing beam-splitter (PBS) and two Faraday mirrors (FM). (b) and (c), time-bin analysis interferometers of Alice and Bob, respectively. Each interferometer is made of a beam-splitter (BS) and of two Faraday mirrors.

The experimental setup shown in Figure 2.29 is employed. A femtosecond pulsed laser is filtered down to a spectral bandwidth of about 1 nm and sent to a polarization dependent Michelson like interfereometer in a bulk optics configuration. The interferometer is made of a polarizing beam-splitter (PBS), two quarter-wave plates and two mirrors. One of the mirrors can be moved to introduce a tunable artificial delay between the $|H\rangle$ and $|V\rangle$ modes. The laser is diagonally polarized at the PBS input and consequently, the state at the Michelson interferometer output reads

$$|\psi\rangle = \frac{1}{\sqrt{2}} \left(|H, 0\rangle + e^{i\,\phi} \, |V, \delta l\rangle \right). \tag{2.58}$$

Here, δl symbolizes the path length difference between the two contributions, and ϕ is a phase factor, originating from the path length difference between the two polarization modes.

The laser light is then sent to each of three interferometers. The idea is the following: when the path length of the two interferometers (Michelson interferometer and one out of the three interferometers under test) is matched, maximum interference visibility is observed. If for all three interferometers interference is observed at the same mirror position, it is concluded that they have all the same path length difference.

In order to observe interference for all cases, the interferometer outputs are connected to a fibre-PBS oriented at 45° compared to the orientation of the one in the Michelson interferometer. This erases path labelling via the photon polarization state. After the fibre-PBS, a fast photodiode[16] is used to record the optical output power. In Figure 2.30, the resulting power response is shown as a function of the position of the moveable mirror. The two curves represent the measurements obtained for Alice's and Bob's analysis interferometers. The interference maxima for these two curves are obtained within 0.3 mm. The path length difference of the preparation interferometer (with the fibre-PBS) is measured to be in-between the two analysis interferometers. This means that the path length difference mismatch can be considered as small compared to the photon coherence length of ∼5 mm. The expected entanglement degradation in this case is ∼ 2%, which is small enough. In the following, we proceed to the entanglement analysis using these three interferometers.

[16] Thorlabs DET10C.

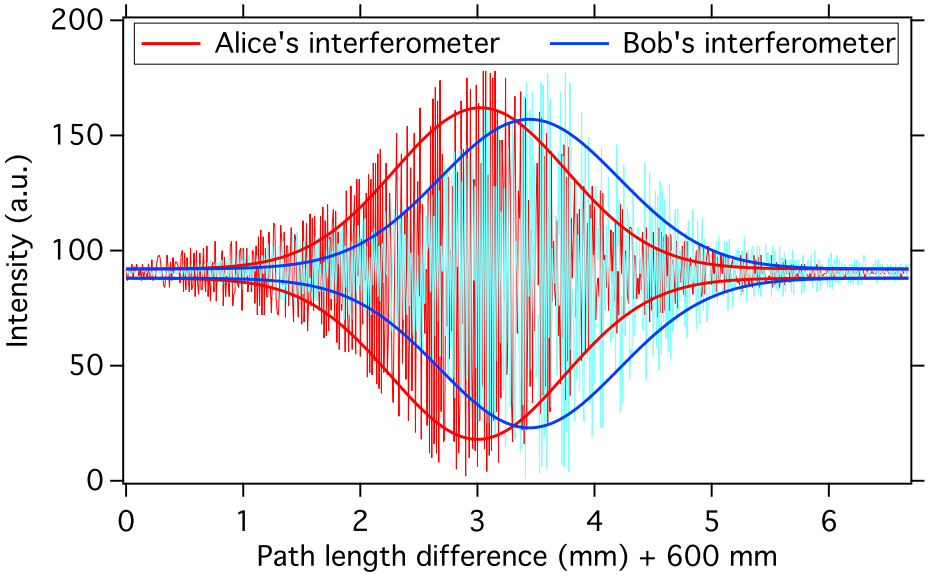

Figure 2.30.: Detected optical power after Alice's (Bob's) analyser as a function of the artificial delay introduced by the Michelson like interferometer. Thick solid lines represent fits using a Gaussian function. Maximum interference visibility is obtained at positions 603.0 mm and 603.3 mm for Alice's and Bob's interferometer, respectively. Note that the mismatch of 0.3 mm is small compared to the single photons' coherence length of ~ 5 mm. The curve width does not represent the single photon coherence length, but the coherence length of the pulsed laser of ~ 1.5 mm. Maximum interference for the preparation interferometer is obtained at position 603.2 mm (curve not represented).

2.4.5. Entanglement analysis

The full experimental setup is outlined in Figure 2.31. The photon pair generator, filtering stage, and time-bin entanglement preparation are explained in the subsections above. In addition, Alice and Bob employ each an analysis interferometer. The phases ϕ_a and ϕ_b in their interferometers can be tuned via temperature control[17]. Photons are detected using an InGaAs APD at Alice and Bob. Both use free running APDs, featuring 20% detection efficiency and 10^{-6}/ns dark count probability[18]. Figure 2.32 shows the three coincidence rates in the peaks T_1 and T_0 as a function of ϕ_a for $\phi_b = 0$. All three curves are oscillating in phase, as it is predicted by equations 2.56 and 2.57. For $\phi_b = \frac{\pi}{2}$,

[17]Note that Alice's and Bob's interferometers are enclosed in a temperature stabilized box for better stability. Via applying a temperature scanning ramp, the phase can be tuned. Real-life quantum key distribution would probably require an active phase stabilization scheme with a fast response time, as it is used in section 2.5.

[18]Id Quantique id220.

the experimental results are shown in Figure 2.33. Here, the curves $T_{\pm 1}$ show a π phase shift compared to the curve T_0, as predicted by theory. The average raw visibility of these oscillations is $V_{\text{raw}} = 95 \pm 2\%$, while subtracting coincidence events associated with detector dark counts leads to $V_{\text{net}} = 97 \pm 2\%$. Note that deviations from unit visibilities

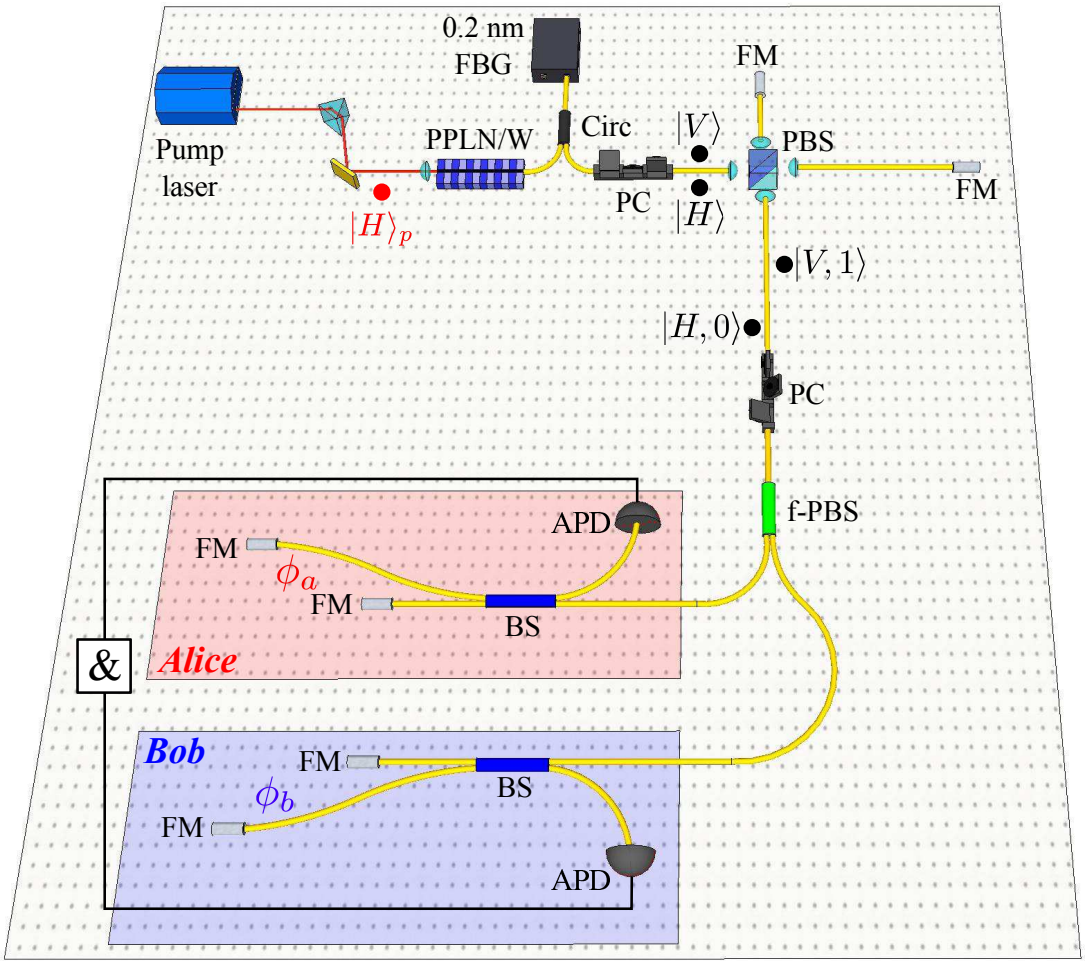

Figure 2.31.: Full experimental setup for generating and analysing the time-bin entangled state $|\Psi^-\rangle$. Cross polarized photon pairs at 1540 nm are generated in a type-II PPLN/W. A fibred polarization dependent Michelson interferometer like configuration (polarizing beam-splitter (PBS), Faraday mirror (FM)) projects deterministically the $|H\rangle$ ($|V\rangle$) modes into the 0 (1) time-bin. Photon pairs are separated using a fibre polarizing beam-splitter (f-PBS) and sent to Alice and Bob. Both users employ standard time-bin analysis interferometers in the Franson configuration for state analysis (beam-splitter (BS) and FM). Coincidences between two avalanche photodiodes (APD) are recorded.

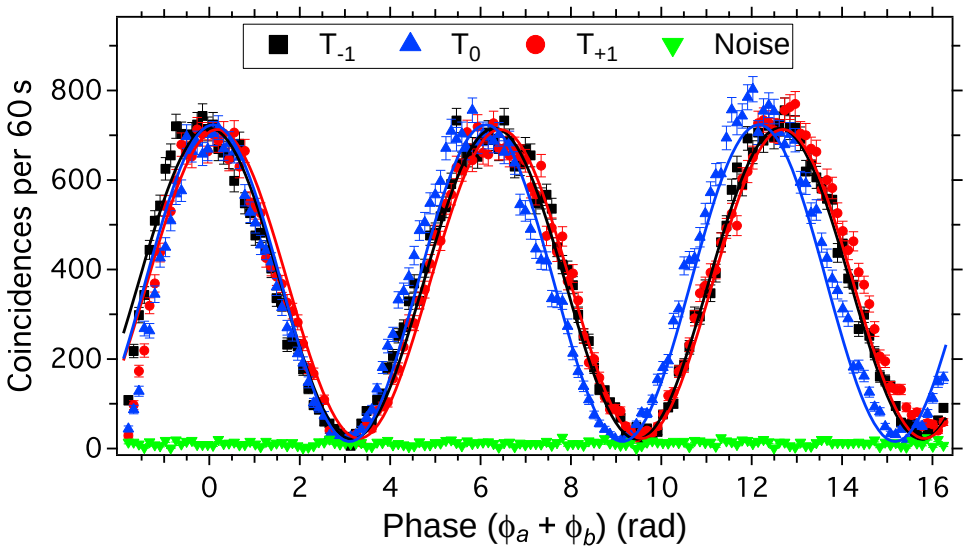

Figure 2.32.: Time-bin entanglement for $\phi_b = 0$. The coincidence rates for the three curves T_0 and $T_{\pm 1}$ are oscillating in phase, when the phase ϕ_a is scanned. This behaviour is predicted by equations 2.56 and 2.57. Lines in the graph represent sinusoidal fits. Note that the phase relation between the curves T_0 and $T_{\pm 1}$ is lost to the end of the measurement as ϕ_b is slowly drifting due to non-perfect interferometer temperature stability. The measurement time is about three hours.

come mainly from path length mismatches of the employed interferometers ($\sim 2\%$). These mismatches could be further reduced, *e.g.* by employing piezoelectric transducer fibre stretchers in the long interferometer arms, to optimize the path length differences.

So far, it has been demonstrated that the employed source generates the maximally entangled time-bin state $|\Psi^-\rangle$. It has also been demonstrated that the employed interferometers at Alice and Bob are suitable for entanglement analysis with a reasonable high quality. In the following, a brief description is given on how to implement secure QKD with this source.

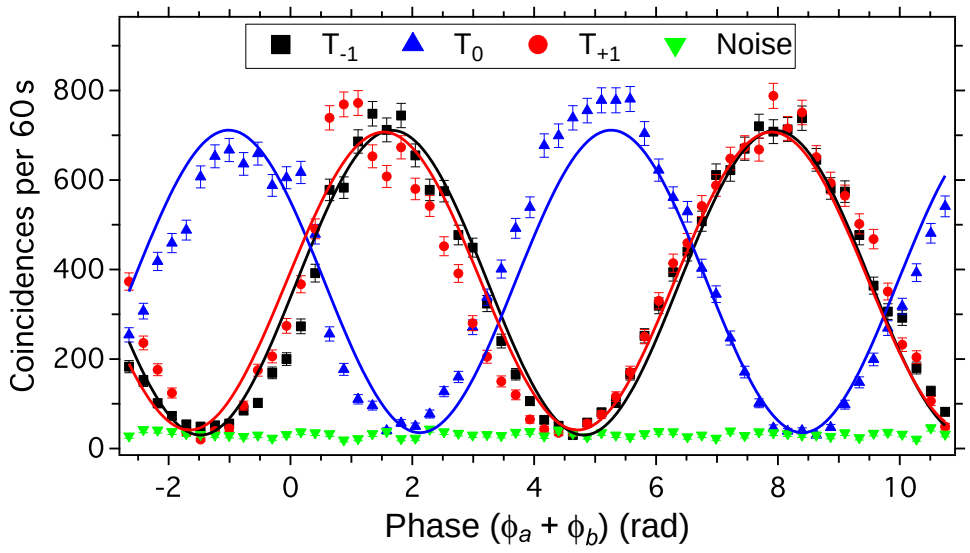

Figure 2.33.: Time-bin entanglement for $\phi_b \approx \frac{\pi}{2}$. The coincidence rates for the three curves T_0 and $T_{\pm 1}$ show a (near) π phase shift, when the phase ϕ_a is scanned. This behaviour is predicted by equations 2.56 and 2.57. Lines in the graph represent sinusoidal fits. The non-perfect π phase shift is explained by non-perfect adjustment of ϕ_b. This measurement is performed in about one hour.

2.4.6. Proposed quantum key distribution protocol

The advantage of the above described entanglement generation and analysis system is that it allows naturally secure QKD using a passive setup with only four detectors. This section explains how this can be implemented. Note that for secure QKD, Alice and Bob need to analyse the quantum state in two complementary basis, chosen in a random fashion, as described in subsection 2.4.1. This makes it impossible for a spy, Eve, to force the measurement outcomes at Alice's and Bob's place. In this particular realization the two complementary basis are

- photon pair detected in T_0,
- photon pair detected in $T_{\pm 1}$.

The choice in which coincidence peak the paired photons are measured is done in a pure random (and passive) way. In particular, the choice is made at the 50/50 fibre beam-splitters in Alice's and Bob's analysers. Thus, a single interferometer at Alice and at Bob is sufficient to randomly choose two complementary analysis basis. No active action is required, reducing the resource overhead in the case of real applications. In this particular proof-of-principle experiment, only two detectors are employed, thus only recording coincidence events. However, QKD protocols require also to analyse

anti-coincidences such that four detectors are needed. The two additional detectors can be connected using an optical circulator at the interferometer input, as outlined in Figure 2.27. To our knowledge such a passive implementation, where only four detectors are needed, has never been shown before. In addition, note that in this case 75% of all *detected photon pairs* are *useful*, in the precise sense that they lead to the observation of entanglement (see Figure 2.28). Typically, in energy-time entanglement experiments, 50% of the detected photon pairs are lost as they are projected into the wrong time-bin slots [238, 239, 133]. In addition, for QKD implementations, 50% of the detected photon pairs are lost as the random basis choice projects only half of the photon pairs on identical analyser settings at Alice and Bob [234].

To demonstrate the security of this implementation, a spy, Eve, is assumed and tries to attack Alice and Bob. Obviously, as Alice and Bob employ analysis interferometers, Eve cannot predict the photon measurement times. We now consider three possible attacks by Eve:

(a) Eve sends a pair of photons in the state $|0\rangle_a |0\rangle_b$. In this case, Alice and Bob obtain a pair of photons in T_0 with probability $p_0 = \frac{1}{2}$. The side peak probabilities are $p_{\pm 1} = \frac{1}{4}$ and $p_{\pm 2} = 0$. Alice and Bob will observe entanglement in T_0, however the expected correlations in $\mathrm{T}_{\pm 1}$ are not found. In addition, they never observe a coincidence in $T_{\pm 2}$.

(b) Eve sends a statistical (but controlled) mixture of photon pairs in the states $|0\rangle_a |1\rangle_b$ and $|1\rangle_a |0\rangle_b$. In this case, Alice and Bob obtain a pair of photons in T_0 with probability $p_0 = \frac{1}{4}$. The side peak probabilities are $p_{\pm 1} = \frac{1}{4}$ and $p_{\pm 2} = \frac{1}{8}$. Consequently, all probabilities of coincidence are correct. However, Alice and Bob can observe entanglement only in $\mathrm{T}_{\pm 1}$. In T_0 no correlations are found.

(c) Eve sends a statistical (but controlled) mixture of photon pairs in the states $|0\rangle_a |2\rangle_b$ and $|2\rangle_a |0\rangle_b$. In this case, Alice and Bob obtain a pair of photons in T_0 with probability $p_0 = 0$. The side peak probabilities are $p_{\pm 1} = \frac{1}{8}$ and $p_{\pm 2} = \frac{1}{4}$. However, Alice and Bob will also observe coincidence events at $\mathrm{T}_{\pm 3}$ with probability $p_{\pm 3} = \frac{1}{8}$. Note that for the original protocol, Alice and Bob do not expect coincidences in $\mathrm{T}_{\pm 3}$.

As we see, if Alice and Bob monitor the probabilities of coincidence in the time-bins T_0, $\mathrm{T}_{\pm 1}$, $\mathrm{T}_{\pm 2}$ and $\mathrm{T}_{\pm 3}$ they reveal the presence of a spy in the cases (a) and (c). Revealing a spy for case (b) requires to check additionally for entanglement in T_0. Alternatively, one could also just check for entanglement in T_0 and $\mathrm{T}_{\pm 1}$ simultaneously.

To be as general as possible, the presence of a spy can be revealed by measuring a simple linear function like

$$S = \sum_{x=0,\pm 1} p_x \, |E_{\mathrm{T}_x}| \; + \; 2 \sum_{x=\pm 2} p_x \, (1 - |E_{\mathrm{T}_x}|) - \sum_{x=\pm 3} p_x . \tag{2.59}$$

Here, E_{T_x} symbolizes the correlation strength, *i.e.* for perfect coincidence behaviour $E_{T_x} = 1$ and for perfect anti-coincidence behaviour $E_{T_x} = -1$. All classical (non-entangled) strategies cannot exceed $S = 1$, while perfect entanglement results in $S = \frac{5}{4}$. We calculate now S for our source, when both phases are fixed $\phi_a = \phi_b = 0$, as shown in Figure 2.32. Our recorded data lead to $S_{raw} = 1.20 \pm 0.02$, using one fixed interferometer setting. This is ten standard deviations above the classical boundary. Consequently, the presence of entanglement in a passive implementation is proven. A similar high value for S_{raw} is obtained for $\phi_a = -\frac{\pi}{2}$ and $\phi_b = \frac{\pi}{2}$, as shown in Figure 2.33. Practical secure QKD requires in general more security checks than only proving the probability of a coincidence and measuring the parameter S_{raw}. For example, a somewhat careless spy could possibly change the photon arrival time statistics, the signal-to-noise-ratio, or the photon coherence time. These errors could be, for instance, monitored using the lateral coincidence peaks $T_{\pm 2}$. A deviation from a Poissonian arrival time statistics would indicate a spy using a deterministic photon pair source. A change in the signal-to-noise-ratio could indicate that there is a spy using a strongly attenuated pulsed laser source. A change in the coincidence peak width could indicate that a spy uses a source with a coherence time that does not match the original source's one.

Note that the list of security checks is far from being exhaustive. However listing them all goes beyond the scope of this thesis. The interested reader can find additional information about secure QKD in the references [27, 29].

2.4.7. Possible improvements

- Probably the most intuitive possible improvement can be achieved when reducing the preparation and analysis interferometer path length mismatches to a minimum. Therefore the interferometers can be cut and re-spliced until success. Another possibility is to employ fibre stretchers in all interferometers towards finding an optimal configuration. Note that optical fibres can typically be extended by at least 1% compared to their original length, without introducing damage [240]. Such an extension should typically be sufficient to find the good settings.

- As outlined before, real QKD schemes require a high phase stability in Alice's and Bob's analysis interferometers. This is currently done using temperature control. However, the obtained experimental results show that the achieved phase stability is not sufficient for applications. An active stabilization scheme can be employed to circumvent this problem (see also section 2.5).

- The phase stabilization problem can be strongly released when using a shorter time-bin separation (currently 2 ns $\leftrightarrow$ 60 cm optical path length). This requires detectors with a better timing resolution. Currently, standard InGaAs detectors achieve timing resolutions of 100 - 400 ps, which requires the 2 ns time-bin separation to properly distinguish between the time-bins. Super conducting detectors

reach timing resolutions down to 30 ps, thus allowing time-bin separations down to 0.2 ns. In this case, the interferometer path length differences can be strongly reduced such that the requirements on temperature stability are released.

- The loss figures of the current setup are relatively high ($\sim 5-6$ dB). This is mainly due to the preparation Michelson like interferometer where a fibre-pigtailed PBS is used, having 1 dB of loss per passage. Employing a ~ 1.5 km long polarization maintaining fibre would also separate the $|H\rangle$ and $|V\rangle$ modes by one time-bin of 2 ns, however in a nearly loss-free fashion [59]. This would then lead to increased coincidence rates between Alice and Bob.
- Currently the paired photons are separated in a probabilistic manner at the f-PBS and consequently only half of the generated pairs are properly distributed between Alice and Bob. This problem could be conveniently circumvented, *i.e.* deterministic pair separation could be reached, by using the same strategy as shown in subsection 2.3.6, thus allowing to increase the quantum key distribution rate by a factor of two.

2.4.8. Conclusion

In this section a new cross time-bin entanglement source has been shown, that can be advantageously used for reliable QKD networking in a passive configuration and with less resource overhead than current time-bin schemes. In addition, 75% of the detected photon pairs lead to the observation of entanglement, compared to 50% in previous realizations [238, 239, 133, 234]. The source takes advantage of a type-II PPLN/W emitting cross polarized photon pairs. A Michelson interferometer like configuration is used to perform the transformation to associate the orthogonal polarization modes ($|H\rangle\,|V\rangle$) with a time-bin (0 and 1). After photon pair separation in a fibre polarizing beam-splitter, the maximally time-bin entangled state $|\Psi^-\rangle = \frac{1}{\sqrt{2}}\left(|0\rangle_a\,|1\rangle_b - |1\rangle_a\,|0\rangle_b\right)$ is generated. Formation of entanglement in this scheme is independent of the phase of the preparation interferometer, thus leading to better stability. Compared to the source described in section 2.3, no polarization state stabilization in the fibres towards Alice and Bob is required, as the entanglement observable is the time-bin. High entanglement quality is measured using a single passive analyser on Alice's and Bob's sides. Deviations from unit visibilities are almost exclusively attributed to path length difference mismatches between the three employed interferometers. Note that for these measurements the choice of the analysis basis is made in a pure random way and no further action from the users is required. An outlook has been given on how to employ this source for future quantum key distribution tasks using passive analysers and only four detectors instead of eight. A security proof, as well as strategies towards revealing a spy, have been briefly discussed. Finally, some rather easy to implement improvements have been outlined which could lead to improved entanglement qualities and higher detected photon pair rates.

The work of this section is found summarized in reference [60].

Note added. We became recently aware of a preprint paper in which a similar experiment has been performed [241].

2.5. Versatile polarization entanglement source based on a type-0 PPLN/W

The entanglement sources introduced in the previous two sections offer a simple way of generating photonic entanglement. Both sources rely on the generation of cross-polarized paired photons. This is enabled by exploiting the type-II SPDC interaction in appropriate PPLN/Ws. However, as the related non-linear coefficient d_{24} is relatively small, only low SPDC efficiencies are obtained. This means that too narrowband photon filtering ($\lesssim 10\,\mathrm{GHz}$ spectral bandwidth) should be avoided to obtain still reasonable high counting rates for reasonable low pump powers.

However, currently, there is an increased interest in narrow bandwidth entangled photon pair sources. There are many reasons for that. Distribution of broadband photons using optical fibres causes problems due to chromatic dispersion (CD). For photons in the telecom C-band of wavelengths (1530 - 1565 nm), this causes a temporal wave packet broadening of $\sim 18\,\mathrm{ps}$ per nm of photon spectral bandwidth and per km of fibre length. If the broadening becomes comparable to the initial wave packet coherence time, then the fidelity for quantum relay and entanglement swapping schemes is drastically reduced, as the photons lose their Fourier-transform limited time-bandwidth relation. Note that CD can, in principle, be compensated using so-called dispersion shifted fibres [242, 162]. Another problem is polarization mode dispersion (PMD), which introduces a random walk-off between the two orthogonal polarization modes $|H\rangle$ and $|V\rangle$. Due to the randomness of this effect, PMD is difficult to overcome. This effect is bandwidth independent and causes a wave packet broadening of $\sim 0.1\,\mathrm{ps}/\sqrt{\mathrm{km}}$. This means that after 200 km of fibre distribution the PMD induced wave packet broadening is about 1.4 ps, which corresponds to a photon spectral bandwidth of $\sim 300\,\mathrm{GHz}$ or $\sim 2.5\,\mathrm{nm}$ at a wavelength of 1550 nm. In order to achieve high quality entanglement, the spectral bandwidth should be one to two orders of magnitudes below that limit. Consequently, entangled photons having a bandwidth of $< 3\,\mathrm{GHz}$ (coherence time of more than 140 ps) are required to observe interference, which drastically reduces the applicability of entanglement swapping and relay protocols. Note that both dispersion effects can be conveniently circumvented using narrowband photons. As far as it concerns CD, a narrower photon bandwidth reduces the speed of the wave packet broadening. For PMD, narrowband photons exhibit longer coherence times, such that the PMD induced wave packet broadening remains small when compared to the initial wave packet coherence time.

In addition, today there is a high interest in developing so-called quantum memories in order to store photonic entanglement in a stationary device [44, 126, 127]. This leads to the possibility to exploit entanglement at a desired time, *e.g.* when the measurement apparatus at Alice and Bob are well synchronized. Studying such kind of light-matter interaction requires spectral bandwidth matching. Solid state and hot atomic vapour quantum memories have reported spectral absorption bandwidths up to 5 GHz [104, 53, 54, 107], while their atom and ion based counterparts exhibit absorption bandwidths up

to a few tens of MHz [109, 110, 50, 111, 112, 113, 114, 115, 116, 117, 118, 119, 120, 121, 122, 123, 124, 125]. This is in complete contrary to the natural emission bandwidth of PPLN/W based photon pair generators (100 GHz - 12.5 THz).

The goal of this section is to develop a high efficiency polarization entanglement source. To do so, a type-0 PPLN/W is chosen as photon pair generator, showing an almost four orders of magnitude higher conversion efficiency than the type-II PPLN/Ws reported in the previous sections. This then permits obtaining high photon pair rates even when applying ultra narrowband filtering. In this realization, the paired photon spectral bandwidth can be chosen over more than five orders of magnitude (25 MHz - 4 THz), which permits achieving bandwidths comparable to hot and cold atom, ion and solid state quantum memories. But the bandwidth can also be adapted to current telecommunication networks, where typically 50 GHz, 100 GHz or 200 GHz channel spacing is used. For all bandwidths, high counting rates are achieved thanks to the use of a high efficiency type-0 PPLN/W photon pair generator combined with a low-loss experimental setup. The source generates photon pairs in the favourable telecom C-band of wavelengths, thus permitting long distance distribution. In order to generate polarization entanglement, a remarkably versatile advanced energy-time to polarization entanglement transcriber apparatus is used. Near perfect entanglement qualities are demonstrated, with the capability of generating any superposition of maximally entangled Bell states $|\Phi^+\rangle$ and $|\Phi^-\rangle$, respectively $|\Psi^+\rangle$ and $|\Psi^-\rangle$, on demand and in a fast manner (< 1 ms). The choice for polarization entanglement is mainly motivated by the fact that heralded quantum memory schemes are naturally designed for the photon polarization observable [205, 243]. The source is built around high performance standard telecommunication components for better stability and reliability.

The section organization is a step-by-step guideline through the experimental apparatus. Therefore, see also the schematic of the full experimental apparatus in Figure 2.34.

- First, a type-0 PPLN/W is used as a photon pair generator. The first part of this section is outlined towards finding the desired QPM condition where a vertically polarized pump photon at 780.24 nm is converted to a pair of vertically polarized photons at 1560.48 nm: $|V\rangle_{780.24} \rightarrow |V\rangle_{1560.48} |V\rangle_{1560.48}$.

- Second, the type-0 interaction shows a relatively broadband emission spectrum of a few THz bandwidth. The employed filtering techniques towards achieving paired photon bandwidths of 25 MHz to 80 GHz are quickly outlined. A more detailed filter analysis is found in Appendix C.

- The type-0 interaction does not permit obtaining polarization entangled photon pairs in a natural fashion. The desired entanglement is engineered using an advanced entanglement transcriber apparatus, whose working principle is briefly explained. A more detailed analysis of the entanglement transcriber is given in Appendix F.

- Thereafter, the produced entanglement quality is examined via the violation of the Bell's inequalities.
- Eventually, a performance analysis is given and the source is compared to other existing narrowband entanglement sources.

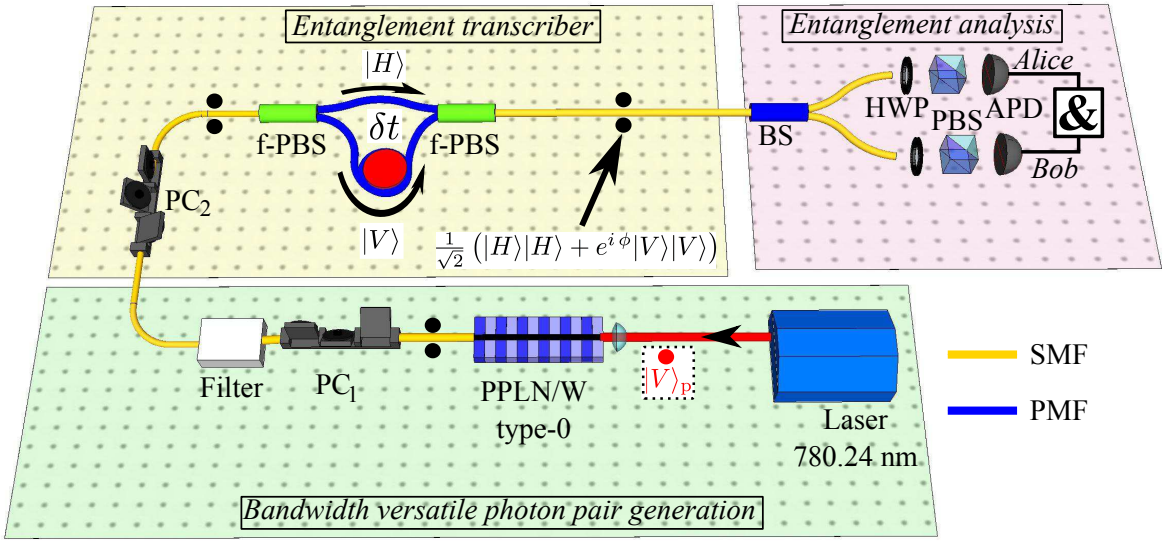

Figure 2.34.: Schematic of the full experimental setup. A 780.24 nm laser generates vertically polarized photon pairs at 1560.48 nm thanks to the SPDC interaction exploited in a type-0 PPLN/W. The pairs are collected using a single mode fibre (SMF) and filtered down to spectral bandwidths ranging from 25 MHz to 80 GHz. Polarization entanglement of the form $\frac{1}{\sqrt{2}}\left(|H\rangle\,|H\rangle + e^{i\,\phi}\,|V\rangle\,|V\rangle\right)$ is created thanks to an entanglement transcriber apparatus. This is made of two fibre polarizing beam-splitters (f-PBS) connected by a short and long polarization maintaining fibre (PMF). Photon pairs are then separated at a beam-splitter (BS) and sent to Alice and Bob. Both of them have a standard polarization state analyser, comprising a half-wave plate (HWP), a polarizing beam-splitter (PBS) and an avalanche photodiode (APD). The coincidence rates as a function of the HWP rotation angles are then measured using an AND-gate (symbolized by the & sign).

2.5.1. Optical sample characterization

To characterize the non-linear optical properties of the PPLN/W, a similar approach is used as the one described in section 2.3. However, there are some subtleness's for the type-0 interaction, which strongly reduce the required efforts towards finding the desired

quasi phase matching. For the type-0 interaction, we typically have

$$|V\rangle_{\mathrm{p}} \rightarrow |V\rangle_{\mathrm{s}} |V\rangle_{\mathrm{i}} \,. \tag{2.60}$$

In other words, a vertically polarized pump photon $|V\rangle_{\mathrm{p}}$ is converted to a pair of vertically polarized signal and idler photons $|V\rangle_{\mathrm{s}} |V\rangle_{\mathrm{i}}$. From this equation it is already clear that birefringence does not have to be considered as an issue. Only one polarization mode is present, such that signal and idler photons can be considered to exit the PPLN/W simultaneously. For the same reason there is also no polarization mode labelling via the photon wavelength. The strategy for characterizing the type-0 PPLN/W is then:

- The desired QPM $|V\rangle_{780.24} \rightarrow |V\rangle_{1560.48} |V\rangle_{1560.48}$ shall be obtained. This particular wavelength choice has mainly practical reasons. At 780.24 nm, powerful diode lasers exist, and active laser wavelength stabilization on a hyperfine transition of rubidium is possible[19]. In addition, the generated paired photons at 1560.48 nm experience very low fibre transmission losses, thus permitting long distribution distances.

- A second harmonic generation (SHG) measurement is performed towards approximately finding the desired QPM.

- Then, spontaneous parametric down-conversion (SPDC) spectra are taken for further fine tuning of the QPM.

- The SPDC efficiency is estimated using a simple coincidence counting experiment.

Second harmonic generation

The second harmonic generation (SHG) characterization is very similar to the procedure described in subsection 2.3.1. The experimental setup is shown in Figure 2.35. A wavelength tunable telecom laser is sent through a polarization controller and the laser light polarization is adjusted to be vertical at the input of a 4.5 cm long home-made type-0 PPLN/W. When QPM is achieved, two vertically polarized photons at the telecom laser wavelength can be merged to generate a frequency doubled vertically polarized photon, *i.e.* a photon at half the wavelength. At the PPLN/W output an optical power meter is used to measure the optical power of the SHG light. The power meter is only sensitive to light below 1000 nm, thus no further filtering of telecom light is required. When all parameters (waveguide diameter, poling period and temperature) are set right, the desired process $|V\rangle_{1560.48} |V\rangle_{1560.48} \rightarrow |V\rangle_{780.24}$ shows a maximum efficiency. As shown in Figure 2.36, at a PPLN/W temperature of 384 K, the desired quasi phase matching is obtained and SHG light is generated at 780.24 nm with an efficiency of $\sim 700\%\cdot\mathrm{W}^{-1}$.

[19] It is explained later why this point is crucial.

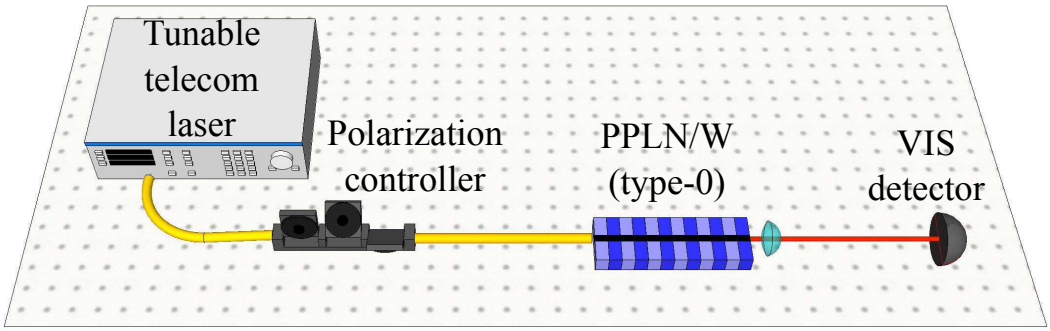

Figure 2.35.: Experimental setup for optical sample characterization via second harmonic generation. A wavelength tunable telecom laser is sent through a polarization controller to orient its polarization to be vertical at the waveguide input. When QPM is achieved, the laser light is frequency doubled. Light at the waveguide output is collected using a lens and sent to a power meter.

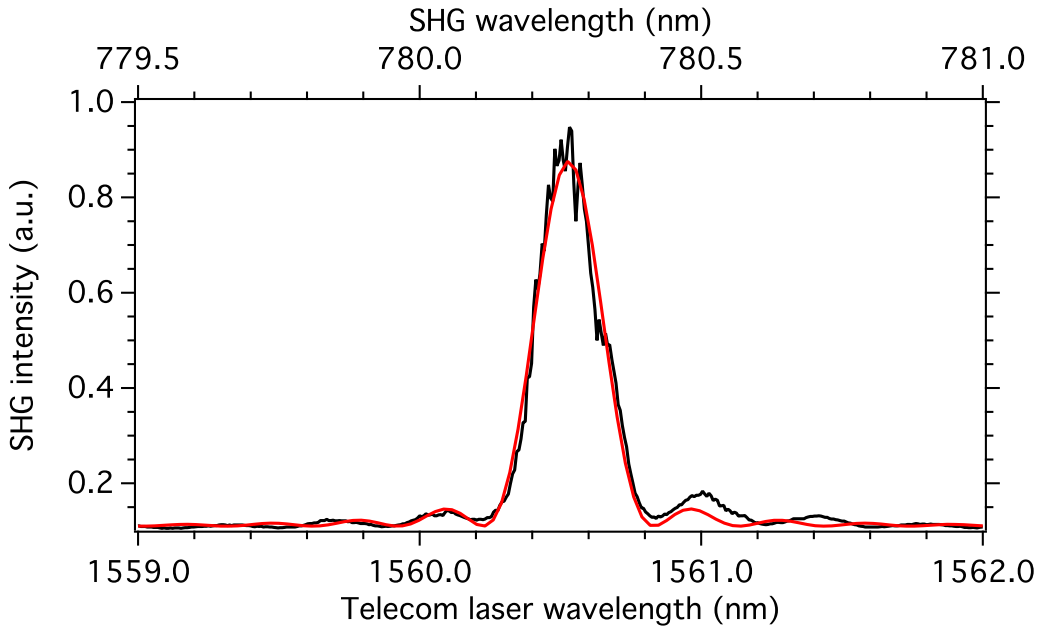

Figure 2.36.: Second harmonic generation signal. The type-0 PPLN/W is heated to the temperature of 384 K to obtain the desired QPM condition, *i.e.* light at 1560.48 nm is converted to 780.24 nm. The black curve represents measured data and the red curve is a fit using a sinc^2 function. The SHG acceptance bandwidth is 0.25 nm at 1560.48 nm. The SHG efficiency is calculated to be $700\%{\cdot}\mathrm{W}^{-1}$.

Spontaneous parametric down-conversion

The spontaneous parametric down-conversion (SPDC) characterization is very similar to the procedure described in subsection 2.3.1. However, as the SPDC emission comprises only vertically polarized photons, the procedure is somewhat simplified. The experimental setup is shown in Figure 2.37. The emission of a 780.24 nm tapered amplifier laser diode system[20] is sent through a prism for removing spurious infrared emission. The laser light is vertically polarized and sent to the type-0 PPLN/W. Via SPDC, vertically polarized paired photons, $|V\rangle_s |V\rangle_i$, are generated and collected using a single mode fibre. The photons are then sent to a wavelength tunable filter having a transmission bandwidth of 0.8 nm. This is much narrower than the expected emission bandwidth of some tens of nm, such that a good resolution is achieved. After the filter, an InGaAs single photon avalanche photodiode (APD)[21] is used to register the down-converted photons. Figure 2.38 depicts the waveguide temperature dependent SPDC emission spectrum. The horizontal line corresponds to the wavelength degeneracy at 1560.48 nm. Without loss of generality, signal (idler) photons have been assigned to be at longer (shorter) wavelengths compared to degeneracy. Note that conservation of energy implies that there is always one photon above and another below the degeneracy line. The SPDC emission wavelength can be tuned by more than 100 nm when changing the waveguide temperature by 3 K. Below the degeneracy temperature of about 387.0 K, the SPDC efficiency drops quickly down to zero. As shown in the graph, between 387.0 K and 388.5 K,

[20] Toptica TA pro.
[21] Id Quantique id201 operated at 10% detection efficiency.

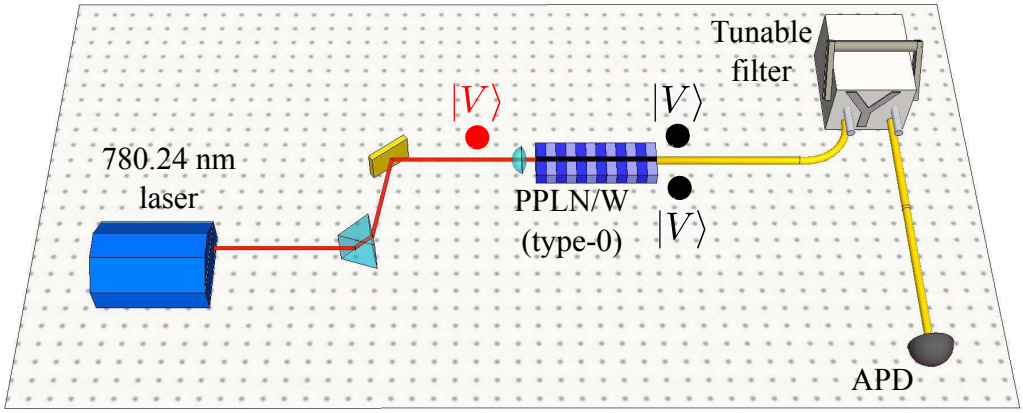

Figure 2.37.: Experimental setup towards SPDC characterization. A vertically polarized 780.24 nm laser is coupled in the type-0 PPLN/W. Vertically polarized paired photons around 1560.48 nm are generated and sent through a wavelength tunable filter, followed by an avalanche photodiode (APD).

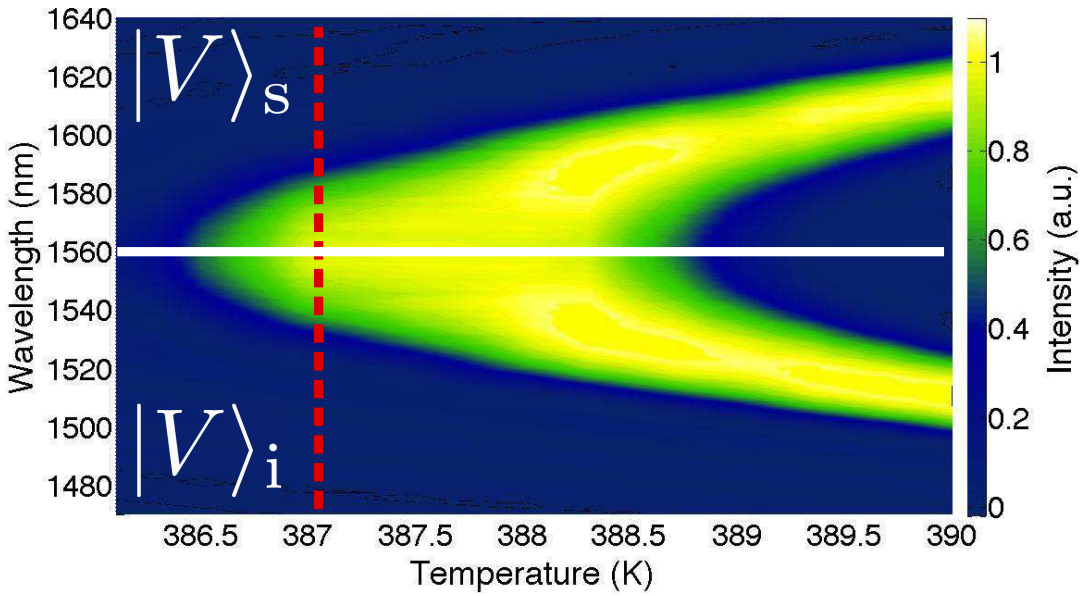

Figure 2.38.: Temperature dependent SPDC emission spectrum of the type-0 PPLN/W. The emission intensity is colour coded, as indicated by the colour scale at the right hand side of the graph. The sample is pumped by a 780.24 nm laser, thus the degeneracy wavelength is at 1560.48 nm as indicated by the horizontal line. Signal (idler) photons are assigned to be at longer (shorter) wavelengths compared to degeneracy. Wavelength degenerate photon pairs are obtained with good efficiency over the temperature range of 387.0 K to 388.5 K. Experiments are carried out at 387.0 K as indicated by the vertical dashed line. The intensities shown in the graph are corrected for the wavelength dependent detection efficiency of the employed APD.

wavelength degenerate photon pairs at 1560.48 nm are obtained with good efficiencies. This relatively broad temperature window in which wavelength degenerate photon pairs are obtained, is a major advantage compared to type-II photon pair generators, where typically temperature stabilities of $\ll 50$ mK are required for proper entanglement generation at wavelength degeneracy. The experiments described in the following are carried out at a PPLN/W temperature of 387.0 K, as indicated by the vertical dashed line in the graph. At this point, the spectral emission bandwidth is about 32 nm ($\leftrightarrow$ 4 THz).

At this stage, wavelength degenerate photon pairs at 1560.48 nm are conveniently generated. In the following, the efficiency of this process is estimated.

PPLN/W SPDC efficiency

In order to characterize the SPDC efficiency, one of the simplest methods is now introduced. Consider the experimental setup outlined in Figure 2.39. The type-0 PPLN/W is pumped by a 780.24 nm laser and 2 μW at this wavelength are coupled into the waveguide. At the waveguide output, the generated photon pairs are collected using a single mode fibre. A standard telecom 100 GHz dense wavelength division multiplexer (DWDM) is used to filter the photons down to a spectral bandwidth of about 80 GHz. The DWDM transmission spectrum is given in Figure 2.40 and shows a near rectangular shaped transmission spectrum. As the DWDM is centred at the degenerate wavelength of $\sim$ 1560.5 nm, the rectangular shape implies that for almost every transmitted signal photon, the corresponding idler photon is also transmitted with a high probability. Note that this is not the case for filters showing Lorentzian or Gaussian shaped transmissions. After the DWDM, photons are sent to a fibre beam-splitter (BS) followed by two free running InGaAs APDs[22]. The APDs are used to record single photon events and a logic AND gate is used for measuring coincidence events. This procedure allows obtaining the SPDC efficiency of the PPLN/W, similarly as the one described in subsection 2.3.4. As in this configuration photon pairs are only probabilistically separated at the BS, equations 2.27, 2.28 and 2.29 need to be reconciled [57]. For the single photon rates S_1 and S_2 on detectors APD_1 and APD_2, respectively, one has

$$S_1 = \mu_1 \eta_1 N \tag{2.61}$$
$$S_2 = \mu_2 \eta_2 N. \tag{2.62}$$

[22]Id Quantique id220 operated at 10% detection efficiency and 5 μs dead time.

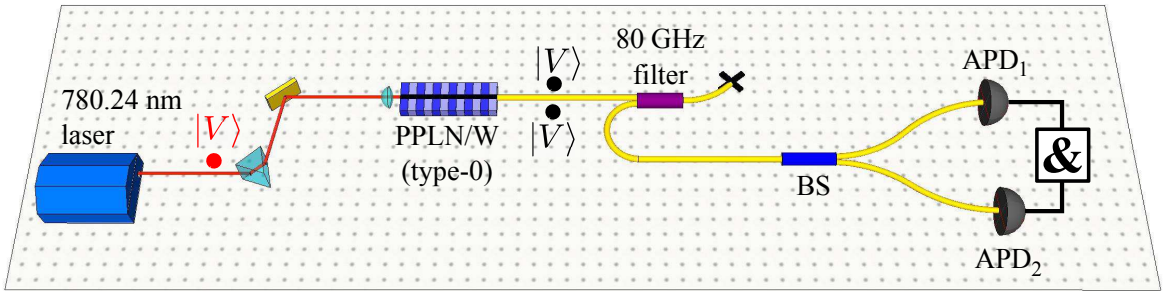

Figure 2.39.: Experimental setup towards SPDC efficiency characterization. The 780.24 nm laser is coupled to the type-0 PPLN/W and photon pairs at the degeneracy wavelength of 1560.48 nm are obtained. Light at the waveguide output is collected using a single mode fibre and filtered down to a spectral bandwidth of 80 GHz using a DWDM. The paired photons are then split up at a beam-splitter (BS) and sent to two avalanche photodiodes, that record coincidence events using a logic AND gate (symbolized by &).

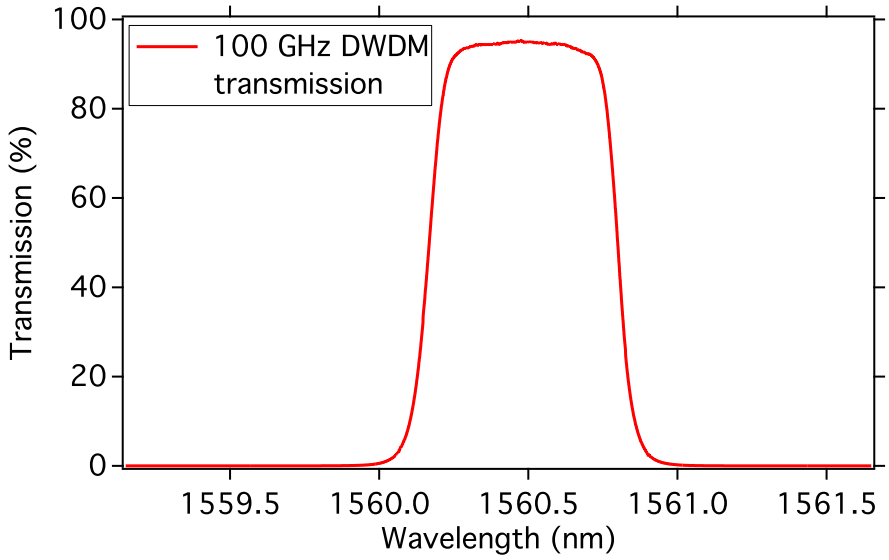

Figure 2.40.: Transmission spectrum of a 100 GHz DWDM filter. Note that the specification 100 GHz does not correspond to the transmission bandwidth, but rather the telecommunication channel separation. The transmission bandwidth of this DWDM is measured to be 80 GHz at full width half maximum. The device shows a good transmission of $> 95\%$ (losses of -0.2 dB) and a near rectangular transmission profile.

Here, μ_1 and μ_2 describe the transmission from photon pair generation to the detectors, η_1 and η_2 are the detectors respective detection efficiencies, and N is the number of generated pairs of photons per second. These formulae take into account that the APDs are not photon number resolving, and the detection efficiency is small compared to unity. This means that cases in which both photons go simultaneously to one APD, result in a two times higher detection event probability, compared to the case when only a single photon arrives on the APD. The coincidence rate C in this configuration is given by

$$C = \frac{1}{2}\mu_1\mu_2\eta_1\eta_2 N. \tag{2.63}$$

The factor of one half comes from the fact that only half of the pairs are split up at the BS. Combining equations 2.61, 2.62 and 2.63 leads to

$$N = \frac{S_1\, S_2}{2\, C}. \tag{2.64}$$

The beauty of this equation is that all parameters μ_1, μ_2, η_1 and η_2, that are difficult to measure, are not present anymore. Only simply accessible quantities, such as the single photon counting rates S_1 and S_2, as well as the coincidence rate C need to be measured to infer N. For a PPLN/W coupled pump power of 1 μW at 780.24 nm, the following

figures are obtained: $S_1 = 11.0 \cdot 10^3\,\mathrm{s}^{-1}$, $S_2 = 11.3 \cdot 10^3\,\mathrm{s}^{-1}$ and $C = 165\,\mathrm{s}^{-1}$. Inserting this in equation 2.64 delivers $N = 377 \cdot 10^3\,\mathrm{s}^{-1}$. The brightness B, defined as the number of photon pairs generated per mW of pump power, per second, and per GHz of spectral emission bandwidth, is then calculated to be

$$B = 4.6 \cdot 10^6 \frac{\text{pairs}}{\text{mW} \cdot \text{s} \cdot \text{GHz}}. \tag{2.65}$$

This brightness is two orders of magnitude higher than the brightness measured for the type-II PPLN/W and stands for one of the highest ever reported, as summarized in Table 2.4 at the end of this section. The SPDC efficiency η_{SPDC} within the full emission bandwidth of the PPLN/W, *i.e.* the probability that a pump photon is converted to a photon pair, is calculated according to equation 2.33, and gives

$$\eta_{\mathrm{SPDC}} = 4.8 \cdot 10^{-6} \frac{\text{pairs}}{\text{pump photon}}. \tag{2.66}$$

Note that this is almost four orders of magnitude higher than the SPDC efficiency reported for the type-II PPLN/W.

Although the efficiency for the type-0 interaction is much higher than the one for for type-II, two inconveniences have to be overcome. The natural emission spectrum is much broader for the type-0 interaction, and in addition, no polarization entanglement is available in a natural fashion. A solution to these two issues is outlined in the following.

2.5.2. Spectral filtering stages

The PPLN/W natural emission bandwidth of $\sim 4\,\mathrm{THz}$ at wavelength degeneracy does not match with current applications. *E.g.* dense wavelength division multiplexed quantum key distribution (DWDM-QKD) requires using the corresponding DWDM filter bandwidths. For quantum relay, long distance teleportation, solid state and hot atomic vapour quantum memory applications, spectral bandwidths of a few 100 MHz are desired. Finally, quantum memories based on cold atomic ensembles or on ions require photon spectral bandwidths of a few tens of MHz. In order to achieve these bandwidths, the following three filters are employed:

- A DWDM-QKD compatible bandwidth is achieved using a DWDM filter after the PPLN/W. We use the same filter as for the SPDC efficiency characterization (transmission spectrum shown in Figure 2.40).
- A photon spectral bandwidth of 540 MHz is conveniently achieved using a phase shifted fibre Bragg grating (PS-FBG) from AOS GmbH. This fully fibred device shows a little residual birefringence, implying that the polarization in front of the filter needs to be properly adjusted using a polarization controller (see Figure 2.41). A detailed characterization of this filter is given in Appendix C.3.

- An ultra narrow spectral bandwidth of 25 MHz is achieved using a PS-FBG from Teraxion corporation. Birefringence is also observed for this filter (see Figure 2.42). A detailed characterization of this filter is given in Appendix C.4.

Note that such PS-FBG filters can be considered as the fibre optical counterpart of standard bulk optical cavities. However, typically such PS-FBGs are much more convenient to use compared to their bulk optics counterparts. No mode-matching procedure is required as the device is fully fibred and thus intrinsically single mode at the design wavelength. In addition, adapted PS-FBG fabrication procedures allow to obtain a nearly temperature independent transmission spectrum. Consequently, aside from basic temperature stabilization, no active wavelength stabilization system is required to obtain absolute frequency stabilities of ~ 1 MHz.

A drawback of the employed devices is the residual PS-FBG birefringence, preventing them from being applied directly to polarization entangled photons[23]. The filter would associate each polarization mode with a transmitted wavelength, which would degrade entanglement. For that reason, the filters in this experiment are all applied directly after the PPLN/W photon pair generator, where both photons are co-polarized ($|V\rangle_s |V\rangle_i$) and experience the same filtering behaviour.

[23] Note that this birefringence is not an intrinsic feature and can be circumvented by adapted PS-FBG fabrication procedures. However, for most applications, birefringence is not an issue, such that the additional efforts towards birefringence cancellation can be avoided.

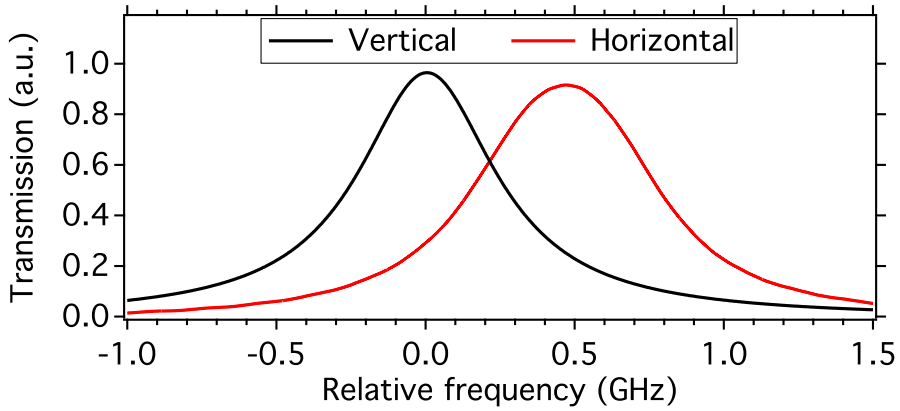

Figure 2.41.: Transmission spectrum of the 540 MHz PS-FBG. Due to a small residual filter birefringence, a polarization dependent transmission spectrum is observed. In order to obtain a maximum transmission, the polarization state of the photons at the filter input is adjusted to be vertical, $|V\rangle_1 |V\rangle_2$. The PS-FBG specifications are: Lorentzian shaped transmission profile with a bandwidth of 540 MHz (580 MHz) for vertically (horizontally) polarized photons. The peak transmission is measured to be 58% (52%).

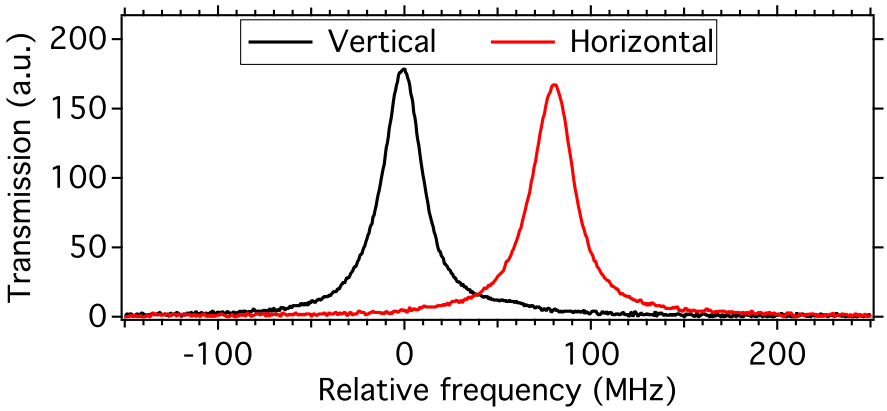

Figure 2.42.: Transmission spectrum of the 25 MHz PS-FBG. A polarization dependent transmission spectrum is observed also for this filter. This is why the polarization state of the photons at the filter input is adjusted to be vertical, $|V\rangle|V\rangle$. The PS-FBG specifications are: Lorentzian shaped transmission profile with a bandwidth of 25 MHz (28 MHz) for vertically (horizontally) polarized photons. The peak transmission is measured to be 71% (63%).

2.5.3. An advanced energy-time to polarization entanglement transcriber

In the previous subsections, high efficiency photon pair generation and filtering towards interesting spectral bandwidths was shown. However, up to now, the paired photons do not show polarization entanglement, as the quantum state after filtering remains $|V\rangle_s|V\rangle_i$. In this subsection, formation of polarization entanglement from such a bi-photon state is shown. To do so, a fibre-optical energy-time to polarization entanglement transcriber apparatus is employed, in an advanced configuration compared to previous realizations [244, 185]. The action of this device is outlined in the following.

First a didactic example is given on how to generate a maximally polarization entangled bi-photon state, reading as:

$$|\Phi(\phi)\rangle = \frac{1}{\sqrt{2}}\left(|H\rangle_a|H\rangle_b + e^{i\phi}|V\rangle_a|V\rangle_b\right). \tag{2.67}$$

The phase relation between the two contributions to the entangled state is described by ϕ. The subscripts a and b denote Alice and Bob, respectively.

After this example, the generalization of the transcriber scheme is described. It is shown how non-degenerate pairs of photons with arbitrary (but known polarizations) are converted to generate any polarization entangled state, such as:

$$|\Phi(\phi,\alpha,\beta)\rangle = \alpha|H\rangle_a|H\rangle_b + e^{i\phi}\beta|V\rangle_a|V\rangle_b \tag{2.68}$$

and

$$|\Psi(\phi,\alpha,\beta)\rangle = \alpha\,|H\rangle_a\,|V\rangle_b + e^{i\,\phi}\beta\,|V\rangle_a\,|H\rangle_b\,. \tag{2.69}$$

Here, the usual normalization is applied, $|\alpha|^2 + |\beta|^2 = 1$.

Entanglement transcriber for generating maximally polarization entangled bi-photon states

The basic idea towards generating polarization entanglement from a $|V\rangle_{\rm s}\,|V\rangle_{\rm i}$ bi-photon state is outlined in Figure 2.43. First of all, assume for reasons of simplicity, that the paired photons are identical in all aspects. In this case the subscripts s and i can be dropped, such that the initial state is

$$|\psi\rangle_{\rm ini} = |V\rangle\,|V\rangle\,. \tag{2.70}$$

The pair is then sent through a polarization controller (PC) and rotated to the diagonal polarization state

$$|\psi\rangle_{\rm PC} = |D\rangle\,|D\rangle \equiv \frac{1}{\sqrt{2}}\left(|V\rangle - |H\rangle\right)\,\frac{1}{\sqrt{2}}\left(|V\rangle - |H\rangle\right). \tag{2.71}$$

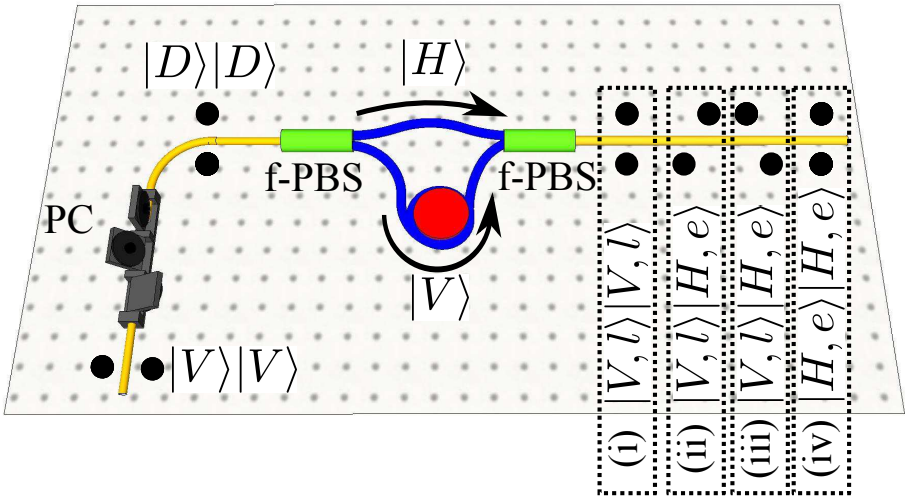

Figure 2.43.: Principle of the entanglement transcriber. Incoming photons, prepared in the state $|V\rangle\,|V\rangle$ are rotated by 45° using a polarization controller (PC), thus being in the state $|D\rangle\,|D\rangle \equiv \frac{1}{\sqrt{2}}\left(|V\rangle - |H\rangle\right)\,\frac{1}{\sqrt{2}}\left(|V\rangle - |H\rangle\right)$. The photons are sent to a fibre polarizing beam-splitter (f-PBS) and the $|H\rangle$ ($|V\rangle$) contribution is sent along a short (long) path made of polarization maintaining fibres. The paths are recombined at another f-PBS. At the output, four contributions are obtained. Post-selecting only contributions (i) and (iv) allows generating polarization entangled bi-photon states.

Then, the photons are incident on a fibre polarizing beam-splitter (f-PBS) that sends the horizontally (vertically) polarized photon state components along a short (long) fibre path. The two paths are recombined using another f-PBS at whose output the quantum state reads

$$\begin{aligned} |\psi\rangle_{\mathrm{f-PBS}} &= \frac{1}{2}\Big(|H,e\rangle\,|H,e\rangle + e^{i\,\phi}\,|V,l\rangle\,|V,l\rangle \\ &\quad -e^{i\,\phi/2}\,|H,e\rangle\,|V,l\rangle - e^{i\,\phi/2}\,|V,l\rangle\,|H,e\rangle\Big). \end{aligned} \tag{2.72}$$

Here, e and l denote the early and late arrival times for the $|H\rangle$ and $|V\rangle$ contributions, respectively. The phase factor ϕ is accumulated due to the path length difference as discussed later in more detail. Sending the paired photons to a fibre beam-splitter (BS) having one output towards Alice (labelled a) and another towards Bob (b), results in

$$\begin{aligned} |\psi\rangle_{\mathrm{BS}} &= \frac{1}{4}\Big(\big[\,|H,e\rangle_a\,|H,e\rangle_a + |H,e\rangle_b\,|H,e\rangle_b + 2\;|H,e\rangle_a\,|H,e\rangle_b\,\big] \\ &\quad +e^{i\,\phi}\big[\,|V,l\rangle_a\,|V,l\rangle_a + |V,l\rangle_b\,|V,l\rangle_b + 2\;|V,l\rangle_a\,|V,l\rangle_b\,\big] \\ &\quad -2\,e^{i\,\phi/2}\big[\,|H,e\rangle_a\,|V,l\rangle_a + |H,e\rangle_b\,|V,l\rangle_b + |H,e\rangle_a\,|V,l\rangle_b + |H,e\rangle_b\,|V,l\rangle_a\,\big]\Big), \end{aligned} \tag{2.73}$$

since each of the contributions of equation 2.72 is split up in four by the BS. If Alice and Bob post-select only coincidence events, *i.e.* when each of them gets one single photon, then the post-selected state reads

$$\begin{aligned} |\psi\rangle_{\mathrm{post}} &= \frac{1}{2}\Big(|H,e\rangle_a\,|H,e\rangle_b + e^{i\,\phi}\,|V,l\rangle_a\,|V,l\rangle_b \\ &\quad -e^{i\,\phi/2}\,|H,e\rangle_a\,|V,l\rangle_b - e^{i\,\phi/2}\,|V,l\rangle_a\,|H,e\rangle_b\Big). \end{aligned} \tag{2.74}$$

As can be understood from equation 2.74, one needs to consider three relative arrival times between the photons impinging at Alice's and Bob's detector. They are illustrated in Figure 2.44. Photon pairs with zero arrival time difference are obtained for the two contributions $|H,e\rangle_a\,|H,e\rangle_b$ and $e^{i\,\phi}\,|V,l\rangle_a\,|V,l\rangle_b$. Positive and negative delays are obtained for the contributions $-e^{i\,\phi}\,|H,e\rangle_a\,|V,l\rangle_b$ and $-e^{i\,\phi}\,|V,l\rangle_a\,|H,e\rangle_b$, respectively. If Alice and Bob further post-select only simultaneously arriving photons, then the quantum state is reduced to

$$|\psi\rangle_{\mathrm{red}} = \frac{1}{\sqrt{2}}\Big(|H,e\rangle_a\,|H,e\rangle_b + e^{i\,\phi}\,|V,l\rangle_a\,|V,l\rangle_b\Big). \tag{2.75}$$

Note that such a post-selection procedure is only possible if the detector's timing jitter τ_{j} as well as the single photon coherence time τ_{s} are short compared to the temporal separation of early and late arrivals, δt, as outlined in Figure 2.44 and reference [57]. Regarding equation 2.75, let us have a closer look on the contributions early-early and late-late. In reality it is not possible to discriminate between these two contributions

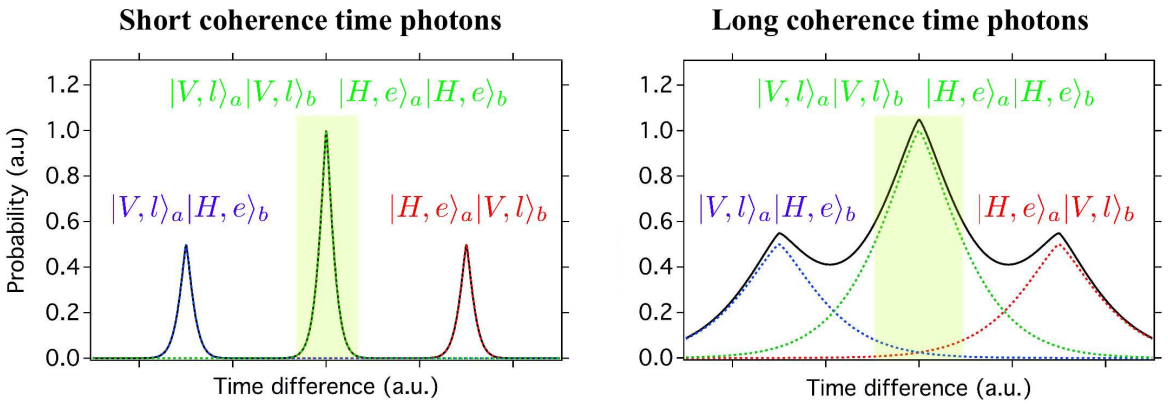

Figure 2.44.: Expected different relative arrival times between the photons at Alice and Bob for short and long coherence time photons (left and right). The central coincidence peak contains the desired contributions $|H,e\rangle_a|H,e\rangle_b$ and $|V,l\rangle_a|V,l\rangle_b$. Alice and Bob need to post-select only the contributions in this peak for entanglement formation (indicated by the filled light green box). For long coherence time photons (or single photon detectors with a long timing jitter) the peaks are broader. When the three peaks start to overlap temporally, a proper post-selection of the desired contributions to the entangled state is no longer possible. In this case, the entanglement transcriber path length difference needs to be further increased.

as a continuous wave pump laser is used and the photon pairs are generated using a spontaneous process. This means that the pair creation time is unknown, and early-early and late-late contributions cannot be distinguished by a simple arrival time measurement (they can only be distinguished by measuring the photons' polarizations). Consequently, the labels e and l become obsolete [132, 170, 133, 174]. As stated for the previous two entanglement sources, in order to observe entanglement, the phase relation between the contributions leading to the entangled state needs to be stable. The phase relation ϕ for this particular source is given by the energy of the two photons and the temporal path length difference in the transcriber apparatus:

$$\phi = 2\,\omega_{\text{phot}}\,\delta t = \omega_{\text{l}}\,\delta t. \tag{2.76}$$

Here, ω_{phot} is the angular frequency of the photons at 1560.48 nm and ω_{l} the pump laser angular frequency. Consequently this means that a stable phase relation ϕ requires a frequency stabilized pump laser. In order to keep the phase fluctuations low, the following relation needs to be fulfilled:

$$\Delta\omega_{\text{l}} \cdot \delta t \ll 1. \tag{2.77}$$

Instead of giving the laser angular frequency stability $\Delta\omega_\mathrm{l}$, we prefer here to refer to the laser coherence time τ_l, defined as

$$\tau_\mathrm{l} = \frac{2\,\pi \cdot 0.44}{\Delta\omega_\mathrm{l}}. \tag{2.78}$$

In this case, the factor 0.44 is the time-to-frequency Fourier-transform factor for Gaussian shapes. This then means that if $\tau_\mathrm{l} \gg \delta t$, the phase relation ϕ is stable and the observation of entanglement is expected. The generated state is then

$$|\psi\rangle_\mathrm{ent} \;=\; \frac{1}{\sqrt{2}}\Big(|H\rangle_a |H\rangle_b + e^{i\,\phi} |V\rangle_a |V\rangle_b \Big). \tag{2.79}$$

As a summary, if the condition

$$\tau_\mathrm{l} \gg \delta t \gg \tau_\mathrm{s} + \tau_\mathrm{j} \tag{2.80}$$

is fulfilled, the above described strategy for generating and observing entanglement is successful.

Before describing how to fulfil equation 2.80 in a real experiment, it is briefly depicted how the entanglement transcriber apparatus can be used to generate any pure polarization entangled bi-photon state.

Generalization of the entanglement transcriber for generating arbitrary pure polarization entangled bi-photon states

To generalize the transcriber scheme, the two input photons might be different in their polarization states and their wavelength, which is denoted by the subscripts 1 and 2, so that it is

$$\begin{aligned} |\psi\rangle_\mathrm{in} &= (\alpha_1 |H\rangle_1 + \beta_1 |V\rangle_1)(\alpha_2 |H\rangle_2 + \beta_2 |V\rangle_2) \\ &= \alpha_1\alpha_2 |H\rangle_1 |H\rangle_2 + \beta_1\beta_2 |V\rangle_1 |V\rangle_2 \\ &\quad + \alpha_1\beta_2 |H\rangle_1 |V\rangle_2 + \beta_1\alpha_2 |V\rangle_1 |H\rangle_2 . \end{aligned} \tag{2.81}$$

Here, $\alpha_j, \beta_j \in \mathbb{C}$ $(j = 1, 2)$ and $|\alpha_j|^2 + |\beta_j|^2 = 1$. The amplitudes α_j, β_j are considered to be fixed and known at all times of the experiment. Alice and Bob post-select simultaneously arriving photons, meaning that only contributions that show parallel polarizations are selected. For reasons of simplicity, we apply this post-selection procedure now, which does not affect the generality of these calculations. Consequently the initial state is reduced to

$$|\psi\rangle_\mathrm{in,post} = \alpha_1\alpha_2 |H\rangle_1 |H\rangle_2 + \beta_1\beta_2 |V\rangle_1 |V\rangle_2 . \tag{2.82}$$

Note that this state is not normalized. The polarization controller turns now the photon polarizations by an angle ξ, so that it is

$$\begin{aligned} |\psi(\xi)\rangle_{\mathrm{PC}} &= \alpha_1\alpha_2\left(\cos^2\xi\,|H\rangle_1\,|H\rangle_2 + \sin^2\xi\,|V\rangle_1\,|V\rangle_2\right) \\ &\quad \beta_1\beta_2\left(\cos^2\xi\,|V\rangle_1\,|V\rangle_2 - \sin^2\xi\,|H\rangle_1\,|H\rangle_2\right). \qquad (2.83) \\ &= (\alpha_1\alpha_2\cos^2\xi - \beta_1\beta_2\sin^2\xi)\,|H\rangle_1\,|H\rangle_2 \\ &\quad +(\beta_1\beta_2\cos^2\xi + \alpha_1\alpha_2\sin^2\xi)\,|V\rangle_1\,|V\rangle_2\,. \qquad (2.84) \end{aligned}$$

We define

$$\alpha(\xi) \equiv \alpha_1\alpha_2\cos^2\xi - \beta_1\beta_2\sin^2\xi \qquad \text{and} \qquad \beta(\xi) \equiv \beta_1\beta_2\cos^2\xi + \alpha_1\alpha_2\sin^2\xi.$$

As α_j, β_j are fixed, we consider that only the ξ-dependence of the functions $\alpha(\xi)$ and $\beta(\xi)$. This leads to the state

$$|\psi(\xi)\rangle_{\mathrm{PC}} = \alpha(\xi)\,|H\rangle_1\,|H\rangle_2 + \beta(\xi)\,|V\rangle_1\,|V\rangle_2\,. \qquad (2.85)$$

Sending these photon pairs through the transcriber interferometer adds a phase shift ϕ on the $|V\rangle_1\,|V\rangle_2$ contribution (and allows to perform the post-selection procedure of only parallel polarized bi-photon contributions). The state after the interferometer is then

$$|\psi(\xi)\rangle_{\mathrm{ent}}\,(\xi,\phi) = \alpha(\xi)\,|H\rangle_1\,|H\rangle_2 + e^{i\,\phi}\beta(\xi)\,|V\rangle_1\,|V\rangle_2\,. \qquad (2.86)$$

which is the desired (fully adjustable) entangled state. In this configuration, all relevant parameters towards generating any pure bi-photon entangled state, are accessible. The amplitudes $\alpha(\xi)$ and $\beta(\xi)$ of the contributions $|H\rangle_1\,|H\rangle_2$ and $|V\rangle_1\,|V\rangle_2$, respectively, can be adjusted via input state polarization control. The phase relation ϕ can be adjusted via fine tuning of the path length difference, which is explained later in more detail. This means that this scheme permits obtaining arbitrary superpositions of the maximally entangled Bell states $|\Phi^{\pm}\rangle = \frac{1}{\sqrt{2}}\,(|H\rangle_1\,|H\rangle_2 \pm |V\rangle_1\,|V\rangle_2)$. In addition, the scheme can be conveniently extended to superpositions of the Bell states $|\Psi^{\pm}\rangle = \frac{1}{\sqrt{2}}\,(|H\rangle_1\,|V\rangle_2 \pm |V\rangle_1\,|H\rangle_2)$ by rotating the polarization of one photon after successful pair separation on a BS. The possibility of achieving any desired Bell state with a single setup underlines the fact that all four Bell states are in principle equivalent.

Fulfilling $\tau_{\mathrm{l}} \gg \delta t \gg \tau_{\mathrm{s}} + \tau_{\mathrm{j}}$ in a real experiment

In order to generate entanglement with the strategy described above, one needs to fulfil $\tau_{\mathrm{l}} \gg \delta t \gg \tau_{\mathrm{s}} + \tau_{\mathrm{j}}$, as outlined in equation 2.80. For this work, photons down to a spectral bandwidth of 25 MHz are used, which implies a single photon coherence time of $\tau_{\mathrm{s}} \approx 18$ ns. Note that timing jitter of typical InGaAs APDs is much smaller ($\tau_{\mathrm{j}} \approx 100{-}400$ ps), such that τ_{j} is neglected from now on. To fulfil $\delta t \gg \tau_{\mathrm{s}}$, the path length difference of the two arms in the entanglement transcriber is chosen to be 18 m of polarization maintaining

fibre, resulting in $\delta t \approx 76\,\text{ns}$. Such a path length difference represents an almost two orders of magnitude improvement compared to previous realizations [233, 244, 215, 213]. A detailed analysis on the optimum path length difference as a function of the single photon spectral bandwidth is given in Appendix F.

Guaranteeing $\tau_l \gg \delta t$ requires some efforts. Non-stabilized diode laser sources hardly meet coherence times of $\tau_l > 100\,\text{ns}$, especially for long time measurements. Consequently, an active laser stabilization system is required towards increasing τ_l. At this point, the choice for a 780.24 nm pump laser becomes clear. Lasers at this wavelength can be conveniently wavelength stabilized on a hyperfine transition in the D_2 line of rubidium. A standard Doppler free saturated absorption spectroscopy setup is employed to resolve the rubidium hyperfine structure [245]. The obtained signal for the transition $F = 2 \rightarrow F'$ of ^{87}Rb is shown in Figure 2.45. For this measurement, the wavelength of the pump laser is scanned. Six narrow lines are obtained, three of them being direct optical transitions, and three being crossover transitions. All lines show a width of $\sim 6\,\text{MHz}$ and are therefore narrow enough for laser stabilization. For all the following experiments carried out in this section, the pump laser is frequency stabilized on the $F = 2 \rightarrow F' = 2 \times 3$ crossover transition of ^{87}Rb. The strategy is the following: The modulation output (20 kHz) of a commercial Lock-In amplifier is sent to a magnetic coil that is wrapped around a Rb spectroscopy cell. This results in an oscillating magnetic

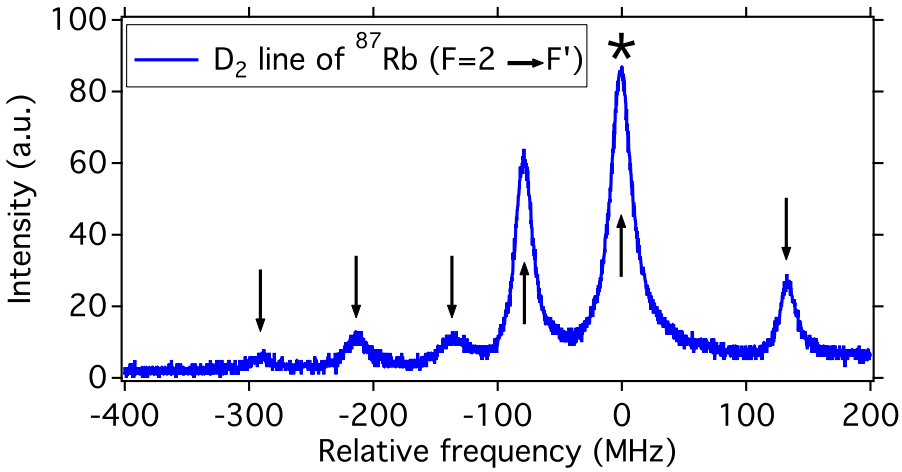

Figure 2.45.: Doppler free saturated absorption spectroscopy signal for the D_2 line of ^{87}Rb. Six peaks are obtained (indicated by small arrows), three of them being optical hyperfine transitions and three being crossover transitions. For all the experiments carried out in this section the 780.24 nm pump laser is locked against the $F = 2 \rightarrow F' = 2 \times 3$ crossover transition (indicated by an asterisk). This results in a pump laser coherence time of $\tau_l \approx 3\,\mu\text{s}$, which allows for the observation of entanglement.

field inside the cell, which periodically shifts the absorption wavelength of the different transitions. The modified saturation absorption spectroscopy signal is then mixed with the modulation signal and an electronic low-pass is applied. The resulting signal is referred as the error signal, and it is proportional to the first derivative of the unmodified saturation absorption signal. Note that the error signal shows a zero-crossing at the peak positions of the saturation absorption signal. The aim is now, that the pump laser frequency is stabilized so as to always be on top of a saturation absorption peak. This implies that the error signal is always zero. Experimentally, this is achieved by integrating the error signal using a home-made electronic circuit and forwarding the resulting signal to the laser current input. If the laser wavelength starts to drift away from the desired saturation absorption peak, the error signal becomes non-zero. Consequently, the current in the laser diode is modified, which shifts back the laser wavelength to the desired value. Using this system, a laser coherence time of $\tau_{\mathrm{l}} \approx 3\,\mu\mathrm{s}$ is achieved, permitting to fulfil equation 2.80. The desired maximally polarization entangled state $|\psi\rangle_{\mathrm{ent}} = \frac{1}{\sqrt{2}}\Big(|H\rangle_a |H\rangle_b + e^{i\,\phi} |V\rangle_a |V\rangle_b \Big)$ is generated.

Stabilizing the phase relation ϕ in the transcriber

Although a maximally polarization entangled state $|\psi\rangle_{\mathrm{ent}}$ is generated at this stage, for most applications, a mandatory requirement towards proper analysis of entanglement is that the phase relation ϕ is kept constant during the full measurement time. Essentially, this means that the entanglement transcriber optical path length difference needs to be kept constant within a small fraction of the photon wavelength λ_{pair}. As a rule of thumb, demonstrating entanglement with a Bell inequality test showing a visibility of more than 99% requires a stability of $< \frac{\lambda_{\mathrm{pair}}}{100} \leftrightarrow \Delta\phi < \frac{2\,\pi}{50}$ [225]. Previous experiments relied (at most) on temperature stabilization of the employed interferometers to guarantee a constant phase relation. However, the used path length differences in these experiments were on the order of a few tens of cm [57, 244, 185, 213]. Our 18 m unbalanced entanglement transcriber apparatus shows an almost two orders of magnitude longer path length difference, such that achieving the desired phase stability via temperature control requires sub-mK stabilities. As such temperature stabilities are very difficult to obtain, an advanced phase stabilization system is employed. A full description, including theoretical considerations, of our phase stabilization system is found in Appendix F. Nevertheless, the basic idea of this system is outlined in Figure 2.46. A wavelength stabilized telecom reference laser is sent in the counter-propagative direction into the transcriber apparatus and accumulates a path length difference dependent phase ϕ_{r}. The subscript r denotes the reference laser. Multiplexing and de-multiplexing the wavelengths of the reference laser and the single photons is conveniently achieved using standard telecom DWDMs. After de-multiplexing, the phase accumulated by the reference laser is measured. Via a piezo-electric fibre stretcher in the long transcriber arm the fibre length can be quickly adjusted in order to correct for unwanted phase drifts, and to adjust the phase to any desired value within sub-ms time scales. The

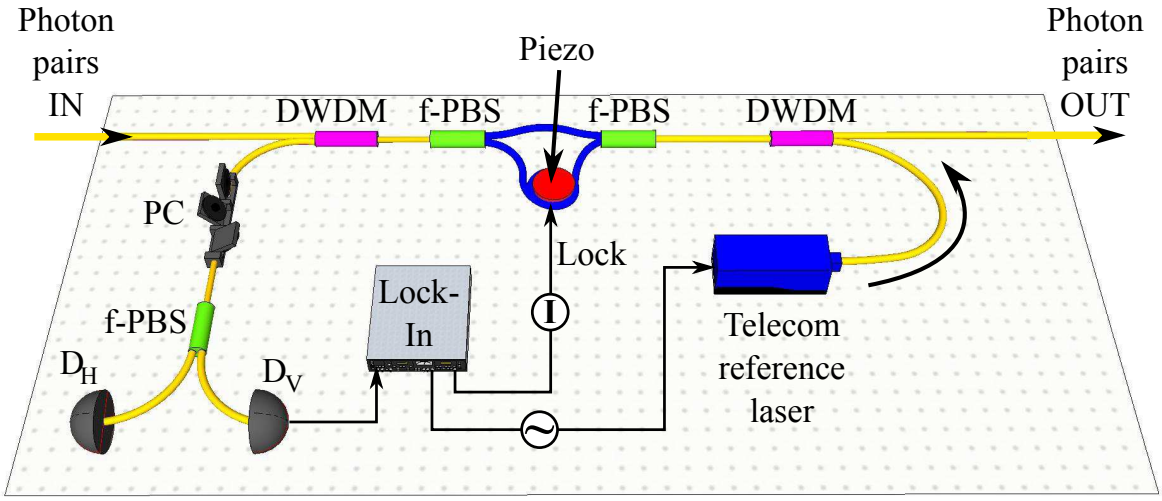

Figure 2.46.: Entanglement transcriber phase stabilization setup. A diagonally polarized telecom reference laser is coupled via a DWDM in the backward direction into the transcriber apparatus in which the light accumulates a phase ϕ_r. Another DWDM is used to separate the reference laser and the photon pairs. Via a polarization controller (PC), the laser light polarization is turned by 45° and sent to a fibre polarizing beam-splitter (f-PBS). Two fast photodiodes are used to measure the phase dependent intensities I_H and I_V. A Lock-In amplifier is used to wavelength modulate the reference laser, to measure the signal I_V, and gives the error signal after appropriate mixing and filtering procedures. The error signal is integrated and sent to a piezoelectric fibre stretcher to compensate phase fluctuations. Superior long term phase stabilities of $\Delta\phi < \frac{2\pi}{200}$ are achieved.

system achieves a superior stability ($\Delta\phi < \frac{2\pi}{200}$) over more than one day of measurement time, which allows generating and analysing high quality polarization entanglement.

2.5.4. Association of filter and entanglement transcriber

In the following, the association of the transcriber interferometer in combination with the three above explained filtering stages is examined. In particular it is shown that the path length difference in the transcriber is long enough for proper post-selection of polarization entangled photon pairs. The corresponding experimental setup is shown in Figure 2.47. The wavelength stabilized 780.24 nm pump laser is coupled into the type-0 PPLN/W towards generating vertically polarized photon pairs at the degenerate wavelength of 1560.48 nm. The photons are collected using a single mode fibre at the PPLN/W output and sent through a polarization controller (PC) towards one out of three filters of interest. PC_1 is used to adjust the polarization state of the incoming

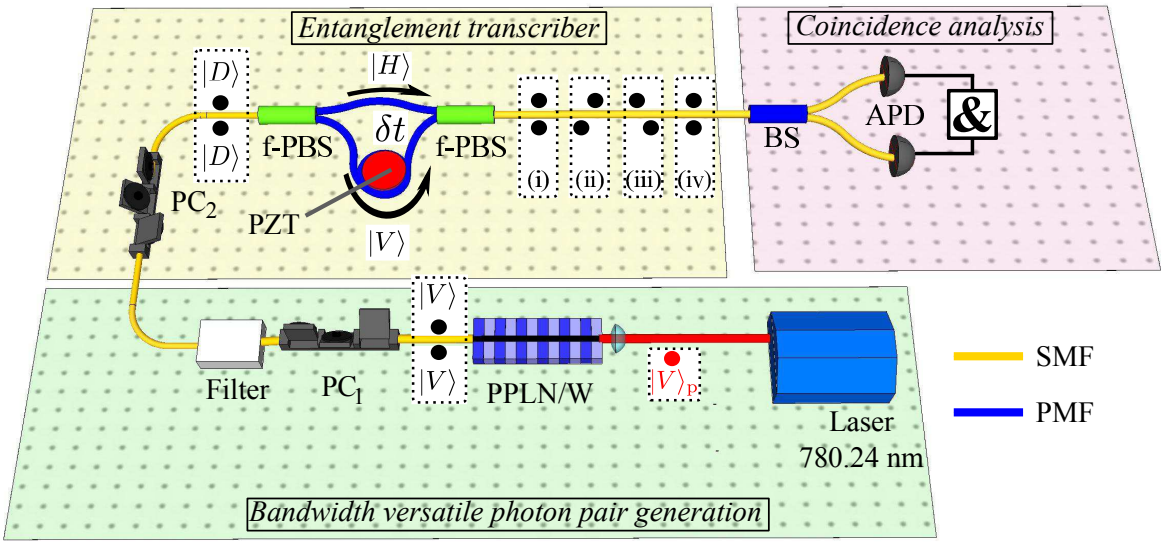

Figure 2.47.: Setup for evaluating whether the delay introduced by the transcriber apparatus is long enough for proper entanglement post-selection. A wavelength stabilized 780.24 nm laser pumps a PPLN/W towards generating photon pairs at 1560.48 nm. The vertically polarized photons are filtered down to bandwidths ranging from 25 MHz to 80 GHz. A polarization controller (PC_1) ensures that possible filter birefringence is avoided by properly aligning the polarization state of the photons. PC_2 rotates the polarization states to diagonal in front of the transcriber apparatus. The temporal distribution of the four possible outcomes after the transcriber are analysed using a beam-splitter (BS) followed by two avalanche photodiodes (APD) connected by a AND-gate (&). SMF and PMF stand for single mode fibre and polarization maintaining fibre, respectively.

photons such that they arrive polarized along the vertical axis of the PS-FBG filters. After the filtering stage, the entanglement transcriber apparatus is employed. PC_2 rotates the photons to the diagonal polarization state $|D\rangle|D\rangle$, followed by the 18 m unbalanced polarization dependent interferometer. After the transcriber, the pairs are then split up at a fibre beam-splitter (BS) and sent to two single photon avalanche photodiodes (APD)[24] towards recoding coincidence events as a function of the detection time delay between the APDs. As shown in Figure 2.48, for all the three filters, three well separated coincidence peaks are obtained. The two outer peaks at ±76 ns correspond to photon pairs that have been split up by the transcriber. The central peak at zero relative delay comprises the two contributions $|H\rangle|H\rangle$ and $|V\rangle|V\rangle$, that lead to the desired entangled state. Note that at this stage the central to side-peak ratio of two indicates that the polarization state at the input of the 18 m unbalanced interferometer

[24]Id Quantique id220 operated at 20% detection efficiency and 7 μs dead time.

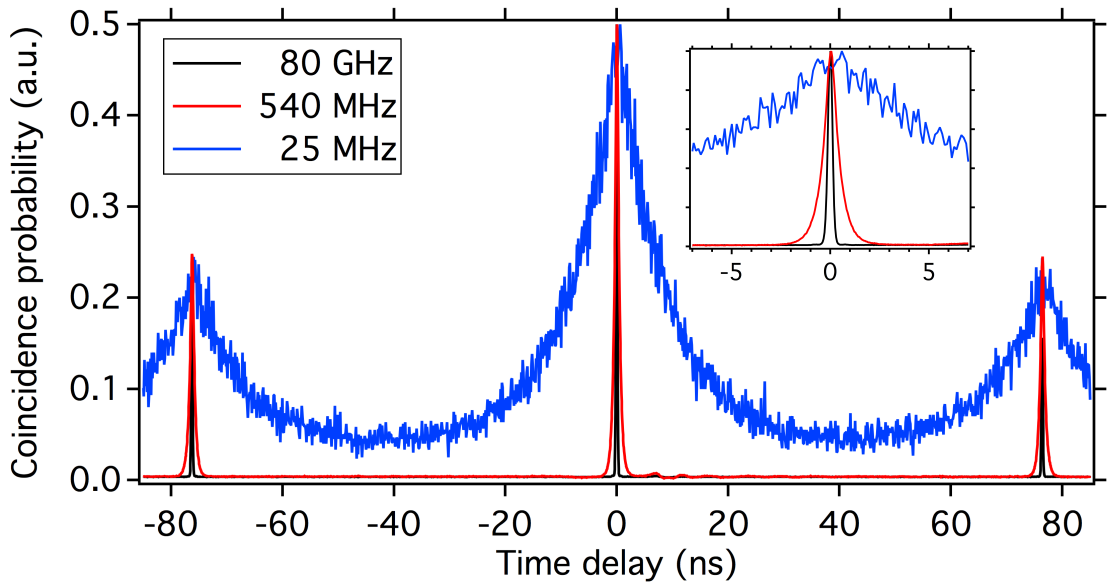

Figure 2.48.: Coincidences after the entanglement transcriber. Three separated peaks are obtained for single photon bandwidths of 25 MHz, 540 MHz and 80 GHz. The peaks are well separated in all cases, meaning that the 18 m path length difference is long enough for proper entanglement post-selection. To do so, only events in the central peak around zero relative delay are taken into account, where the contributions $|H\rangle|H\rangle$ and $|V\rangle|V\rangle$ are recorded. Side peak contributions, in which cross polarized paired photons are obtained, are electronically discarded. Note that the central to side peak ratio of two is a good indicator that the contributions $|H\rangle|H\rangle$ and $|V\rangle|V\rangle$ are generated with the same weights, which is a crucial requirement towards generating maximally polarization entangled bi-photon states. The inset graph is a zoom at zero relative delay.

has been properly adjusted towards obtaining $|H\rangle|H\rangle$ and $|V\rangle|V\rangle$ contributions with the same weights (α and β), which is necessary for creating maximally polarization entangled bi-photon states. For all three filters, a proper post-selection of events around zero relative time delay is possible. The respective peak widths are

- DWDM filter (80 GHz): 230±2 ps.
- AOS 540 MHz PS-FBG: 835±28 ps.
- Teraxion 25 MHz PS-FBG: 15.6±0.7 ns.

For the DWDM filter, a ~ 5 ps photon coherence time is expected, so that the observed coincidence peak width is almost solely determined by the APD timing jitter. Note that

in this case the peaks show a Gaussian shaped profile. The convolved timing resolution of a pair of detectors is then 230 ps, which results in a single APD timing jitter of $230\,\text{ps}/\sqrt{2} \approx 163\,\text{ps}$. The denominator of $\sqrt{2}$ takes into account the Gaussian shaped curve profile.

For the AOS 540 MHz filter, the photon coherence time becomes comparable to the APD timing jitter. For a Lorentzian shaped frequency transmission profile, the temporal coherence is an exponential decay function. As a consequence, the shape of the coincidence peak is determined by the convolution of the Gaussian shaped APD timing jitter combined with an exponential decay function. An appropriate fitting function delivers a width of 803±27 ps for the exponential decay function, corresponding to a 548±18 MHz bandwidth in the spectral domain. This result is in very good agreement with the specified PS-FBG filter bandwidth.

Eventually, for the Teraxion 25 MHz filter, the photon coherence time is much greater than the APD timing jitter, so that the peak width is dominated by the exponential decay function. The observed peak width of 15.6±0.7 ns corresponds to a frequency bandwidth of 28±2 MHz and is in good agreement with the filter specifications.

2.5.5. Entanglement quality

In this subsection, the generated entanglement quality is measured when combining the type-0 PPLN/W photon pair generator, one of the filtering stages, the entanglement transcriber and the photon pair post-selection procedure described in the subsections above. The full experimental setup is outlined in Figure 2.49. The experimental setup is essentially the same as shown in Figure 2.47, however, Alice and Bob employ in addition polarization state analysers made of a half-wave plate (HWP), polarizing beam-splitter (PBS) and a single photon APD[25]. Alice and Bob select only events within the full width at half maximum coincidence peak region at zero relative delay, to properly post-select entangled photon pairs.

Demonstration of phase tuning capability

As a first measurement, our capability of tuning and stabilizing the phase is demonstrated. As stated in subsection 1.2.5, the violation of the so-called Bell's inequalities in the standard settings requires generating one of the maximally entangled Bell states, which means in other words that $\phi = 0 \bmod 2\pi$ or $\phi = \pi \bmod 2\pi$. In addition, the phase needs to be stable over the full measurement time. Consequently, a good phase control is indispensable. The phase measurement is carried out using the following settings (see also Figure 2.50). Alice and Bob set both their analysers at 45°, *i.e.* their respective HWPs are fixed at 22.5°. This projects the entangled state into the phase-sensitive diagonal basis. A continuous voltage ramp is applied on the piezo-electric fibre stretcher

[25] Either Id Quantique id220 operated at 20% detection efficiency and 4-10 μs dead time.

placed in the long arm of the transcriber and permits scanning the phase of the entangled state. The coincidence rate between Alice and Bob is then detected as a function of the applied voltage. This procedure is repeated for the three above mentioned filters and the corresponding measurements are shown in Figure 2.51. For all three filter bandwidths, sinusoidal coincidence rate oscillations are obtained. At $\phi = 0$ ($\phi = \pi$) the maximally entangled Bell state $|\Phi^+\rangle$ ($|\Phi^-\rangle$) is generated. The high net visibilities of $99.9 \pm 1.2\%$, $99.4 \pm 1.5\%$ and $97 \pm 2\%$ for the 80 GHz DWDM, 540 MHz PS-FBG and 25 MHz PS-FBG filters, respectively, underline that also a high phase stability is obtained. The raw visibilities, *i.e.* without subtraction of the accidental events induced by the noise in the detectors, are $99.7 \pm 1.5\%$, $97 \pm 2\%$ and $88 \pm 2\%$, respectively. The raw visibility reduction for the 25 MHz PS-FBG is rather strong compared to the other filters. For such narrowband photons, the coherence time is strongly increased, such that coincidence detection requires substantially longer time windows for entanglement post-selection. This increases the probability of having a dark count (typical dark count probability $\sim 10^{-6}$/ns) and consequently reduces the signal to noise ratio. Nevertheless,

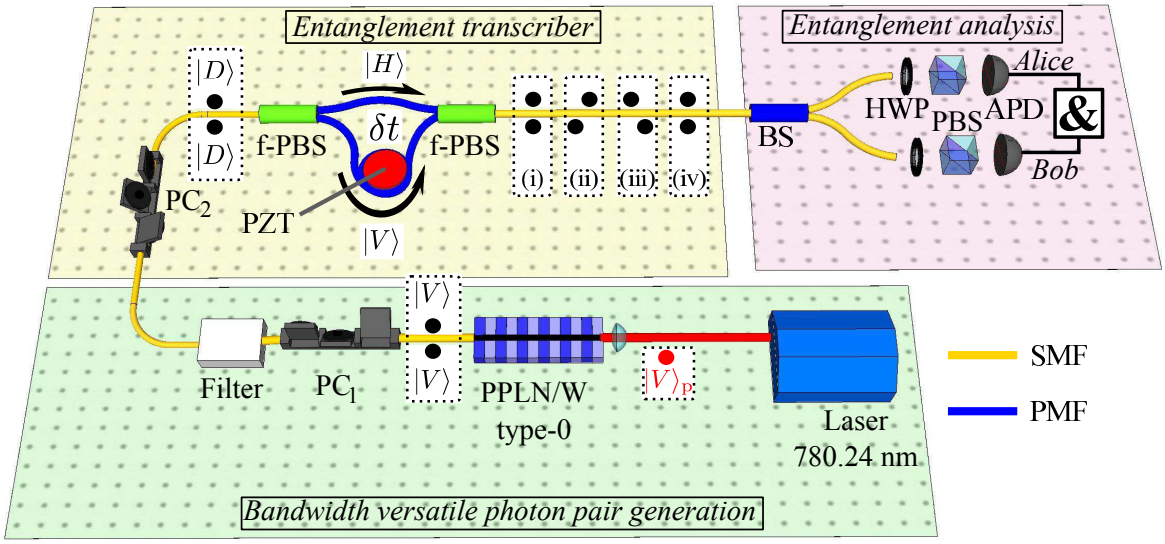

Figure 2.49.: Full experimental setup. A 780.24 nm laser generates vertically polarized photon pairs at 1560.48 nm thanks to a PPLN/W. The pairs are filtered down to spectral bandwidths ranging from 25 MHz to 80 GHz. An entanglement transcriber apparatus is used to generate polarization entanglement of the form $\frac{1}{\sqrt{2}}\left(|H\rangle|H\rangle + e^{i\phi}|V\rangle|V\rangle\right)$. Photon pairs are then separated at a BS and sent to Alice and Bob. Both of them comprise a standard polarization state analyser, comprising a half-wave plate (HWP), a polarizing beam-splitter (PBS) and an APD. The coincidence rates as a function of the HWP rotation angles are then measured using an AND-gate.

as the phase stability and tunability are photon pair bandwidth independent, the measurements for the 80 GHz DWDM and 540 MHz PS-FBG are sufficient to demonstrate the high degree of phase control obtained in this setup.

Violation of the Bell's inequalities

In the following, we set $\phi = \pi$ in order to produce the maximally polarization entangled Bell state $|\Phi^-\rangle$. Alice fixes her analyser consecutively to analyse horizontally ($|H\rangle$), vertically ($|V\rangle$), diagonally ($|D\rangle$) and anti-diagonally ($|A\rangle$) polarized photons. Bob's HWP is continuously rotated and the coincidence rate is measured as a function of Bob's HWP angle. For the measurements with 80 GHz and 540 MHz spectral bandwidth photons, Alice and Bob employ each a free running InGaAs APD[26]. In order to improve the signal to noise ratio for the measurements with the 25 MHz filter, the InGaAs detectors are replaced by superconducting detectors[27]. Although these devices show a reduced detection efficiency of $\sim 7\%$ at 1560 nm, they offer strongly reduced dark count probabilities of $\sim 10^{-8}$/ns, thus a much better signal to noise ratio is expected [154]. In Figure 2.52, the

[26]Id Quantique id220 operated at 20% detection efficiency and 4-10 μs dead time.
[27]Scontel TCOPRS-001.

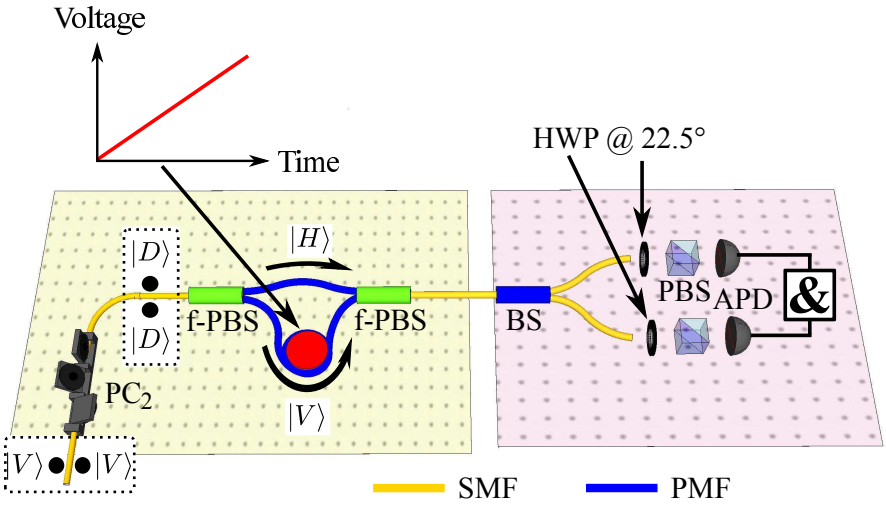

Figure 2.50.: Experimental setup towards measuring the phase ϕ introduced by the transcriber apparatus. Alice and Bob fix their respective half-wave plates at 22.5° to project the generated entangled state into the phase sensitive diagonal basis. In this case the coincidence rate is expected to show sinusoidal oscillations as the function of ϕ.The phase in the transcriber is scanned by applying a voltage ramp on the piezo-electric fibre stretcher, thus changing the optical path length difference and consequently the phase.

obtained experimental results are shown for the three employed filters. For all spectral bandwidths, high visibility sinusoidal oscillations are obtained for all settings at Alice's side. The obtained average raw visibilities, *i.e.* without subtraction of detector noise, are $99.6 \pm 1.3\%$, $97.1 \pm 0.9\%$ and $99 \pm 3\%$ for the 80 GHz DWDM, 540 MHz PS-FBG and 25 MHz PS-FBG filters, respectively. The Bell parameter S_{raw} is calculated to be 2.82 ± 0.01, 2.80 ± 0.02 and 2.82 ± 0.02, respectively. This represents a violation of the Bell's inequalities of at least 40 standard deviations without any noise subtraction and underlines both the excellent entanglement generation quality using the transcriber apparatus, and the high phase stability achieved in the transcriber apparatus.

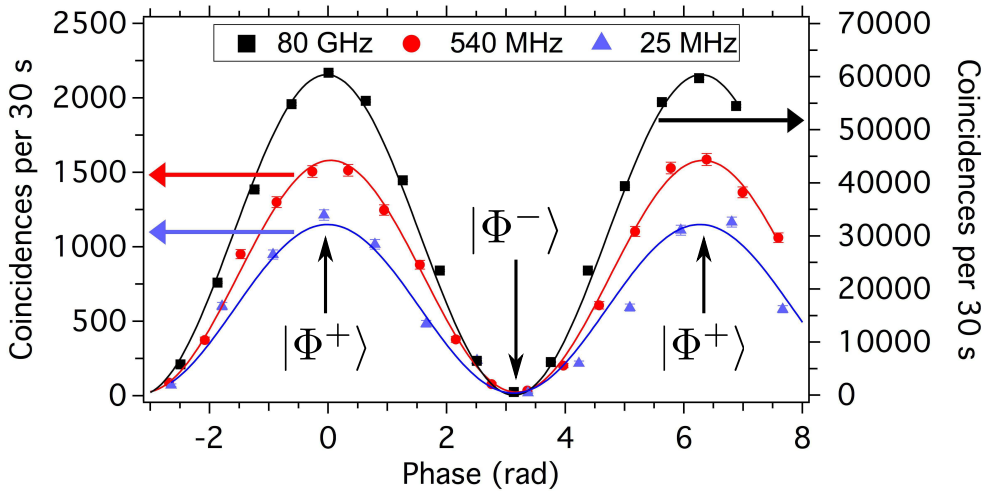

Figure 2.51.: Demonstration of phase tuning capability. When Alice and Bob fix both their analysers in the diagonal basis, the obtained coincidence rate is phase dependent. For all the three filters, *i.e.*, 80 GHz DWDM, 540 MHz and 25 MHz PS-FBG, high visibility coincidence rate oscillations are obtained as a function of the phase. This underlines both our capability of tuning and stabilizing the phase of the 18 m unbalanced transcriber apparatus. Note that for this graph, the noise contributions for the three respective measurements has been subtracted. As indicated in the graph, at $\phi = 0 \bmod 2\pi$ and $\phi = \pi \bmod 2\pi$ the maximally polarization entangled Bell states $|\Phi^+\rangle$ and $|\Phi^-\rangle$ are created.

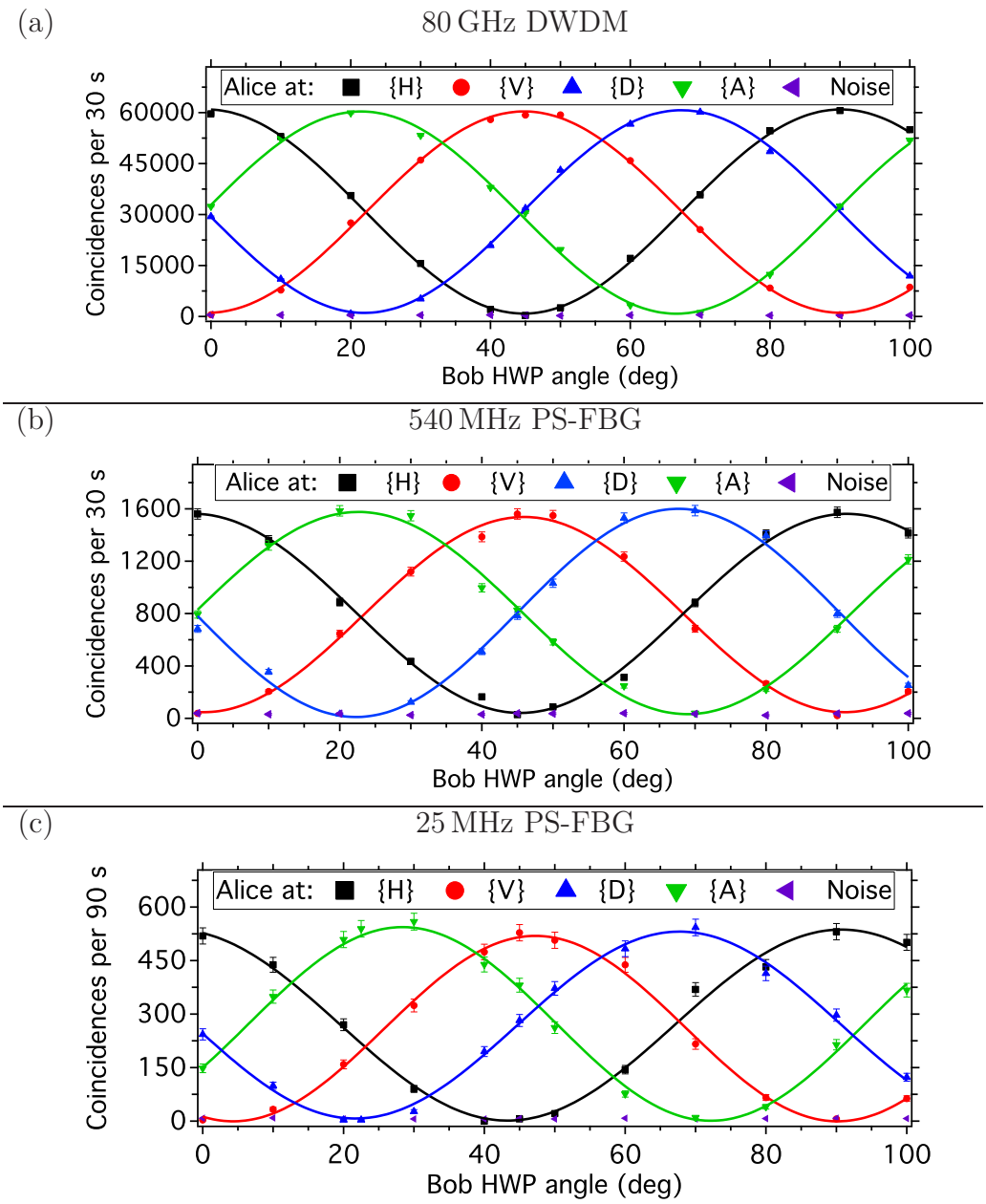

Figure 2.52.: Violation of the Bell's inequalities for the three employed filters. For all the tested bandwidths, high visibility sinusoidal oscillations are obtained for all settings at Alice's side. The Bell's inequalities are violated by at least 40 standard deviations for all measurements, even without subtraction of noise. While for measurements (a) and (b) InGaAs APDs are used, for measurement (c) superconducting detectors are employed to improve the signal to noise ratio.

2.5.6. Performance analysis and possible improvements

Performance analysis

A general performance summary of the results obtained with this source is given in Table 2.3. The following criteria are considered:

- Specified photon pair spectral bandwidth.
- Observed photon coherence time, τ_s.
- Waveguide coupled pump power at 780.24 nm.
- Mean number of generated photon pairs per coherence time, $\frac{\bar{n}}{\tau_s}$.
- Actual detected coincidence rate.
- Photon heralding efficiency, *i.e.* the probability that Bob's gets a photon in his analyser given the fact that Alice has detected her photon.
- Brightness measured as number of available photon pairs per second, mW of pump power, MHz of spectral bandwidth after the transcriber, B.
- Raw visibility for the violation of the Bell's inequalities, V_{raw}.
- Fidelity to the closest maximally entangled Bell state, $\mathcal{F}_{\text{raw}}^{|\Phi^-\rangle}$.
- Obtained Bell parameter, S_{raw}.

In Table 2.4, the obtained results are compared to other narrow spectral bandwidth photon pair entanglement sources. Note that this table does not claim completeness. The results obtained in this thesis represent one of the highest brightnesses ever reported combined with high quality entanglement. In addition, photon pairs are generated at a favourable wavelength of 1560.48 nm which is optimal for long distance photon distribution using fibre networks. Moreover, one of the key features of this source is its spectral bandwidth versatility, which is difficult to achieve for photonic entanglement sources based on optical parametric amplifiers or atoms. For this source, the bandwidth is adapted to the desired application by simply changing a filter. This source therefore stands for an ideal candidate for long distance entanglement distribution using various strategies such as DWDM-QKD, quantum relay, teleportation or quantum memories protocols.

Bandwidth [MHz]	$80{\cdot}10^3$	540	25
τ_s [ns]	$4.4{\cdot}10^{-3}$	0.803	15.6
Waveguide coupled pump power [mW]	0.009	0.2	3.5
$\frac{\bar{n}}{\tau_s}$ [ns^{-1}]	$5{\cdot}10^{-5}$	$2{\cdot}10^{-3}$	$2{\cdot}10^{-2}$
Detected pair rate [s^{-1}]	2000†	50†	6‡
Photon heralding efficiency [%]	13	4	5
B [(s·mW·MHz)$^{-1}$]	960	300	380
V_{raw} (%)	99.6 ±1.3	97.1 ±0.9	99 ±3
$\mathcal{F}_{\text{raw}}^{\lvert\Phi^-\rangle}$	0.998	0.985	0.995
S_{raw}	2.82±0.01	2.80±0.02	2.82±0.02

Table 2.3.: Summary of the obtained results for the three employed filters. † For these measurements, InGaAs APDs are used with 20% detection efficiency. ‡ For this measurement superconducting single photon detectors are used with 7% efficiency. The difference in heralding efficiency and brightness is due the different losses and transmission profiles of the three employed filters.

Group	Generator	Observable	Bandwidth (MHz)	λ (nm)	B^*	V_{net}
[211] Cambridge (2006)	KTP OPO	polar.	22	795	0.7	77%
[58] Geneva (2008)	PPLN/W	time-bin	1200	1560	446	NA$^\times$
[212] Hefei (2008)	PPKTP OPO	polar.	9.6	780	6	97%
[52] Barcelona (2009)	PPKTP	polar.	22	854	3	98%
[213] Geneva (2009)	PPLN/W OPO	time-bin	117	1560	17	94%
[246] Hong Kong	Rb atoms	polar.	6	780	0.5	90%
This thesis, 540 MHz	PPLN/W	polar.	540	1560	306	99%
This thesis, 25 MHz	PPLN/W	polar.	25	1560	380	99%

Table 2.4.: Comparison of several narrow bandwidth photon pair entanglement sources. They are sorted by group, photon pair generator, entanglement observable, spectral emission bandwidth in MHz, central emission wavelength in nm, spectral brightness measured after successful pair separation, and the obtained visibility in the violation of the Bell's inequalities. * The brightness is defined as available photon pairs per second, mW of pump power and MHz of spectral bandwidth. $^\times$ NA does not mean that no entanglement was observed, but rather that this experiment was used for entanglement swapping, such that the standard Bell's inequality test was not performed.

Possible improvements

One of the main criteria for long distance entanglement distribution is the photon heralding efficiency. This quantity depends essentially on the losses that the photons experience from the point of creation in the PPLN/W until successful photon pair separation. In an ideal scenario, every created photon pair is deterministically split up between Alice and Bob and experiences no losses. This way, if Alice detects a single photon, she is sure that Bob has also one photon in his analyser.

For the source presented here, there are three main strategies to improve the photon heralding efficiency.

- A segmented tapered waveguide structure would allow reducing the coupling losses from the PPLN/W to the optical fibre. Currently, the single photon coupling efficiency is $\sim 70\%$ and such segmented waveguide structures would permit reaching efficiencies up to 90%, *i.e.* a 1.3 times improvement [227, 228].

- Photon pairs in this realization are separated probabilistically at a BS. Consequently, half of the pairs are not separated and considered as lost. Using a deterministic photon pair separation strategy, as used for the source presented in section 2.3, would improve the photon heralding efficiency by a factor of two [59].

- As narrowband filters, PS-FBGs with a Lorentzian shaped transmission profile are used. However this is not favourable. If Alice's photon is transmitted, Bob is not sure that his photon has also been transmitted through the filter. Employing a PS-FBG with a rectangular shaped transmission profile, that have become commercially available only recently, would solve this problem. In this case, if Alice's photon is transmitted, Bob's photon is also. The heralding efficiency would also be increased by another factor of two.

All in all, the heralding efficiency for this source could be improved by ~ 5.2 times for the PS-FBG configuration, and $2.6\times$ for the DWDM configuration, when applying all the above mentioned improvements. Note that the maximum heralding efficiency for this source is limited to 50% as the transcriber apparatus projects only half of the photon pairs onto an entangled state.

2.5.7. Conclusion

In this section we have demonstrated a highly efficient and versatile telecom photon polarization entanglement source. The versatility concerns both the created entangled state and the photon spectral properties. Taking advantage of an advanced fibre-optical entanglement transcriber, connected to a high efficiency type-0 PPLN/W, any pure polarization entangled bi-photon state can be conveniently generated. The single photon emission wavelength can be tuned over more than 100 nm via PPLN/W temperature control. The photon pair spectral bandwidth can be chosen at will over more than five

orders of magnitude (25 MHz - 4 THz) via simple filter replacement. This way, the source can be simply adapted to various applications. In addition, for all demonstrated spectral bandwidths (25 MHz, 540 MHz and 80 GHz), Bell's inequalities have been violated by more than 40 standard deviations without subtraction of detector noise, so that near perfect entanglement quality is demonstrated. Such a source could be advantageously used for various quantum networking scenarios, ranging from DWDM-QKD (50 GHz - 200 GHz) to quantum relay and teleportation schemes (100 MHz - 1 GHz) and finally to optical quantum memories (10 MHz - 5 GHz). In the latter framework, note that wavelength adaptation, in and out of the memories, between telecom photons and atom or ion based quantum storage devices, can be addressed by means of coherence non-linear optical frequency conversion approaches, which is outlined in chapter 3.

The work of this section is found summarized in reference [64].

Chapter 3.

A photonic quantum interface

The experiments carried out in this chapter pave the way towards realizing a polarization entanglement preserving wavelength conversion interface based on the sum frequency generation process in type-0 PPLN/Ws. Such a device is of high interest for enabling future development of light-matter interaction, where telecom photons are used for entanglement distribution, and quantum memories (typically operating below 1000 nm) for entanglement storage.

This chapter is organized as follows: first, the need for such an interface is outlined and current approaches are listed. Then, considerations on several experimental configurations are made towards finding an efficient and reliable solution. Thereafter, preliminary optical characterization experiments are shown underlining the high efficiency of the chosen approach. However, in its present configuration, the Raman scattering background noise rate is too high, such that single photon applications are currently prohibited. A simple and reliable approach is outlined towards elimination of background noise in the near future, which will render this device suitable for single photon applications. The realization of an astute active phase stabilization system enables wavelength conversion of polarization entangled photons, and underlines the relevance of our approach. This chapter ends with a conclusion and an outlook.

3.1. Why wavelength converters?

In chapter 2, three sources of photonic entanglement have been demonstrated. All sources were designed for operation at a favourable telecom wavelength (1540 nm and 1560 nm), permitting long distance entanglement distribution using fibre networks.

Despite this advantage, there are several problems when working with telecom wavelength single photons. Single photon detectors in this wavelength range show typically reduced figures of merit compared to their counterparts operating in the visible range. This concerns mainly three parameters, the single photon detection efficiency, the timing resolution, and the maximum single photon counting rate. All of them limit (strongly) the maximum achievable bit rate of quantum networks. Such problems are overcome when using so-called up-conversion detectors. Here, the telecom wavelength photons of interest are distributed in fibre networks and finally wavelength converted from the tele-

com to the visible regime. This permits exploiting the advantages of high performance visible light single photon detectors [247, 248, 249, 250, 251, 252, 253].

As stated in subsection 1.5.3, there is a high interest in exploiting the advantages of (telecom) photons as flying qubit carriers and quantum memories as stationary qubit carriers for increasing the speed of quantum communication. A problem here is that most of the currently developed quantum information storage devices operate typically at wavelengths below 1000 nm. Consequently, a network comprising telecom wavelength photons to distribute, and quantum memories to store qubits, requires wavelength adaptation devices. A crucial point for such devices is that they need to perform a *coherent* wavelength conversion in order to preserve the qubit state (and thus the information comprised on the qubit) [254, 255, 256, 62, 257]. In the following, this point is stressed.

Today's classical communication networks typically exploit light pulses at wavelengths of about 1550 nm for information distribution. When wanting to convert the wavelength of these light pulses, probably the most intuitive manner is to first measure the light pulse using a suitable detector and then generate a new light pulse using a suitable laser at the desired wavelength (see Figure 3.1). However, such a procedure is not possible in the quantum domain. The no-cloning theorem forbids this task (see reference [87] and subsection 1.2.3). A single quantum (in an unknown initial state) cannot be cloned. To make this point clear, assume an incoming photon in the state $|\psi\rangle = \alpha\,|H\rangle + \beta\,|V\rangle$ with $|\alpha|^2 + |\beta|^2 = 1$ and $\alpha, \beta \in \mathbb{C}$. The wavelength conversion interface is now going to measure the polarization state of the incoming photon, say by using a polarizer oriented in the $\{H, V\}$-basis. Obviously, if a $|H\rangle$ ($|V\rangle$) photon is incident, the interface gets the right measurement outcome and can re-produce a new photon having another

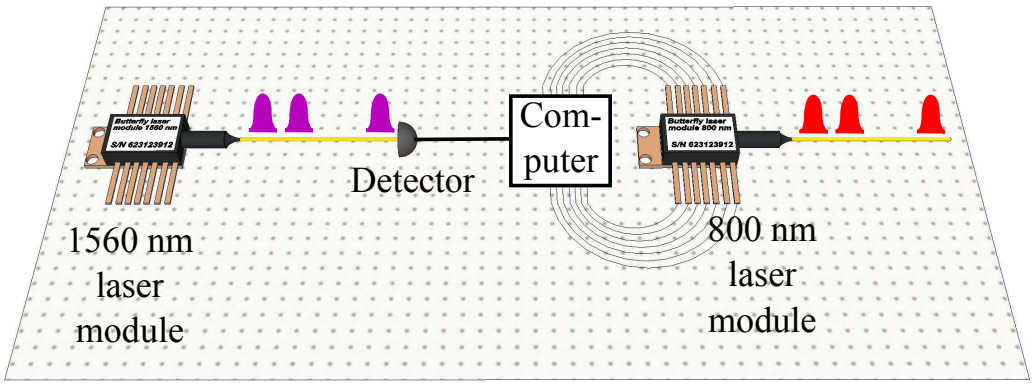

Figure 3.1.: Working princinple of a classical wavelength conversion interface. The light pulses from a 1560 nm laser are measured using a suitable detector. The signal is treated on a computer and forwarded to another laser, operating at a different wavelength and repeating the light pulses. Note that such a scheme does not work for wavelength conversion of entangled photons.

wavelength but the same polarization. This corresponds to the special cases $\alpha = 1 \,\&\, \beta = 0$ respectively $\alpha = 0 \,\&\, \beta = 1$. However, in all other cases, this wavelength conversion device introduces errors. As an example, consider the case $\alpha = \beta = \frac{1}{\sqrt{2}}$, corresponding to a diagonally polarized photon $|D\rangle$. In this case, the device measures randomly either $|H\rangle$ or $|V\rangle$, but never $|D\rangle$. The interface will then send randomly polarized photons (either $|H\rangle$ or $|V\rangle$, but never $|D\rangle$) at the new wavelength. We have lost the coherence between the contributions $|H\rangle$ and $|V\rangle$. Therefore, this interface is not capable of wavelength converting arbitrary polarized photons without having some information about the initial polarization state. However, when dealing with entangled photons, such information does not exist (see subsection 1.2.5 and chapter 4) and the proposed interface is useless in this case.

Nevertheless, wavelength conversion is still possible, however one has to get sure that any kind of measurement on the desired entanglement observable is avoided. The coherence has to be preserved.

3.1.1. Single photon wavelength conversion via SFG

The first wavelength conversion interface, that preserved (energy-time) entanglement was demonstrated in 2005 by S. Tanzilli and collaborators [62]. They exploited the non-linear process of sum frequency generation (SFG) in a type-0 PPLN/W. The SFG interaction is described by the following equation:

$$|V\rangle_{\omega_1} |V\rangle_{\omega_2} \overset{\text{SFG}}{\mapsto} |V\rangle_{\omega_3=\omega_1+\omega_2} \,. \tag{3.1}$$

Two vertically polarized photons, one having the angular frequency ω_1 and the other ω_2, are mixed in the PPLN/W and generate a new vertically polarized photon having the angular frequency $\omega_3 = \omega_1 + \omega_2$. Note that the probability for this process on the single photon level is relatively weak, on the order of 10^{-8} in a type-0 PPLN/W having a length of a few centimetres. However, it is possible to increase the efficiency up to unity by increasing the intensity of one of the two light fields. For example, sending a single photon at ω_1 and, at the same time, $\sim 10^8$ photons at ω_2 allows (in principle) to increase the efficiency for the process described in equation 3.1 up to unity.

A schematic of the first entanglement preserving wavelength conversion experiment is shown in Figure 3.2. Pairs of energy-time entangled photons were generated in a type-0 PPLN/W. The QPM was chosen for generating one photon at 1555 nm and the other at 1312 nm. In a first experiment, they demonstrated high quality energy-time entanglement between these two photons. Then the 1312 nm photon was sent to another type-0 PPLN/W and mixed with a 700 mW pump laser operating at 1560 nm. Via the non-linear process of sum frequency generation (SFG) the photons at 1312 nm were converted to the wavelength of 712 nm with an internal conversion efficiency of more than 50%. Finally, energy-time entanglement was measured between the 1555 nm and the 712 nm photons and essentially no degradation of entanglement was observed.

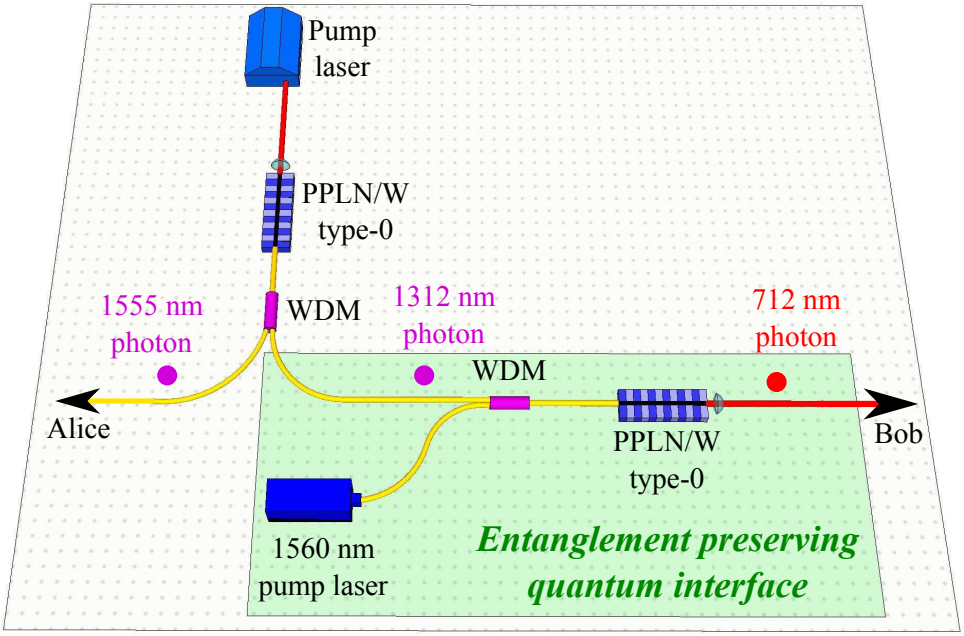

Figure 3.2.: Working principle of the first entanglement preserving wavelength conversion interface. A pump laser generates energy-time entangled photon pairs in a type-0 PPLN/W. The QPM is chosen such that there is always one photon at 1555 nm and the other at 1312 nm. These photons are then separated using a WDM. The 1312 nm photon is sent to the interface and mixed with a 1560 nm pump laser using another WDM. The two light fields are coupled into a type-0 PPLN/W in which the QPM is optimized for SFG, thus achieving a 56% probability of converting the 1312 nm photon to the wavelength of 712 nm. After the interface, high quality entanglement between the 1555 nm and 712 nm photons is preserved. This is because the coherence time of both pump lasers is much greater than the time-bin separation of the employed energy-time analysis interferometers (not represented in this figure).

This milestone experiment demonstrated clearly the suitability of SFG for wavelength conversion of entangled photons.

3.1.2. Why SFG is a powerful approach

As outlined before, exploiting SFG in a crystal offers coherent wavelength conversion with a relatively simple experimental apparatus. Note that SFG is not the only way of wavelength conversion. Recently, an experiment based on the non-linear process of four wave mixing in a cloud of cold rubidium atoms has also shown wavelength conversion between telecom photons at 1367 nm and 795 nm with high efficiencies [255]. A relatively complex experimental apparatus was used for this experiment and in addition, such

atom based approaches do not offer a great conversion wavelength versatility, as the wavelength is fixed by the available atomic transitions.

On the other side, the conversion wavelength of SFG is widely adjustable by simply tuning the QPM and pump laser wavelength. As stated in section 3.1, a quantum interface needs to preserve the coherence, implying that any kind of projective measurement on the quantum state has to be avoided. Why did this work in the experiment of Tanzilli and collaborators [62]? Energy-time entanglement relies on the fact that we are unable to tell the time at which a photon pair has been generated. As soon as this information is revealed, entanglement is destroyed. One might think that the process of SFG reveals this information, because the wavelength conversion of a single photon implies that one pump laser photon is missing. Consequently, when measuring the pump laser power after the PPLN/W, one should observe that the light intensity drops at the time a photon is converted, which would allow inferring the photon creation time and thus destroy entanglement. But in reality, such a measurement cannot be performed for two reasons. First of all, measuring light intensities of several 100 mW with a precision of a single photon is generally not possible due to Heisenberg's uncertainty principle. But even if this would be possible, the coherence of entanglement is protected by another circumstance, namely the pump laser coherence time. The photons emitted by the pump laser show a coherence time of $\sim 1\,\mu$s. This means that we can measure the time of a missing photon at most with a precision of $\sim 1\,\mu$s. But, as discussed in subsection 2.4.3, in order to reveal the photon pair generation time, one needs a timing resolution of less than the time-bin separation of the employed entanglement analysis interferometers, in this case about 1 ns. Therefore, energy-time entanglement is actually protected by the long coherence time of the employed pump laser.

The relevance of SFG as efficient and practical single photon wavelength conversion process is demonstrated in many experiments carried out in the last decade [247, 248, 249, 250, 251, 252, 253, 254, 255, 256, 62, 257] and research is still going on.

Among all the above mentioned wavelength conversion experiments, most of them were meant for application in up-conversion detection devices [247, 248, 249, 250, 251, 253] where no efforts are required to preserve the coherence of the photons to be converted. One of them comprised a system to preserve the coherence, however tests were only performed for classical light fields [252]. A few of them dealt with the wavelength conversion of energy-time entangled photons [254, 62, 257], but only two of them showed wavelength conversion of polarization entangled photons [255, 256]. The lack of wavelength conversion devices for polarization entangled photons lies in the fact that this task is unequally more difficult than for the energy-time observable. In the following, a short list is given why this is:

- Most wavelength converters are either birefringent or only capable of converting one polarization mode. This leads to a distinguishability between the conversion of horizontally and vertically polarized converted photons, which degrades or completely destroys polarization entanglement.

- If considering a solution in which two conversion devices are used, one for vertical and one for horizontal modes, then it is crucial that the conversion efficiencies of both devices are precisely matched. Otherwise the quality of the entangled state is degraded.

- The phase relation between the two components $|H\rangle$ and $|V\rangle$ needs to be stable (or at least known at any time). For instance, if a diagonally polarized photon $|D\rangle = \frac{1}{\sqrt{2}}(|H\rangle + |V\rangle)$ is incident on the conversion apparatus, the phase relation between the two components is zero. However, if the conversion interface introduces a phase shift of θ between the two components, then the converted state is $\frac{1}{\sqrt{2}}\left(|H\rangle + e^{i\,\theta}\,|V\rangle\right)$. As long as θ is stable or known at all times, we can always find an experimental procedure to compensate it. However, if θ fluctuates randomly, entanglement cannot be analysed anymore. Guaranteeing a stable (or at all times known) θ is not evident, especially for solutions comprising two conversion interfaces.

Note that wavelength converters for energy-time and time-bin entanglement conveniently circumvent these problems as typically only a single polarization mode is present, such that only one conversion device is required, making the issues of balanced conversion efficiencies and phase stability irrelevant.

However, developing and improving polarization entanglement wavelength converters is of major interest for future applications. For instance, heralded quantum memories following the DLCZ protocol are naturally designed for the polarization observable [205, 46]. Thus, when wanting to distribute polarization entanglement using telecom photons and then store these photons in quantum memories, a suitable polarization entanglement wavelength conversion interface is required. In addition, such a device could then also be used as polarization insensitive up-conversion detector.

In the following, some considerations are given on how to design such a polarization entanglement preserving wavelength conversion interface.

3.2. Considerations on the experimental apparatus

In this section, three examples are given how to outline the quantum interface apparatus for wavelength conversion of polarization entangled photons. So far, only two polarization entanglement wavelength conversion interfaces have been demonstrated, one of them relying on rubidium atoms [255] and the other on SFG in a bulk crystal [256]. In the following, this solid state interface is briefly outlined, its advantages and disadvantages are listed, and then two other solid state approaches are considered.

3.2.1. Two cascaded crystals

So far the only solid state quantum interface has been demonstrated by Ramelow and collaborators [256], using two orthogonally oriented periodically poled potassium titanyl phosphate (PPKTP) crystals. A schematic of their quantum interface is shown in Figure 3.3. They mix a single photon, belonging to a polarization entangled pair at 810 nm,

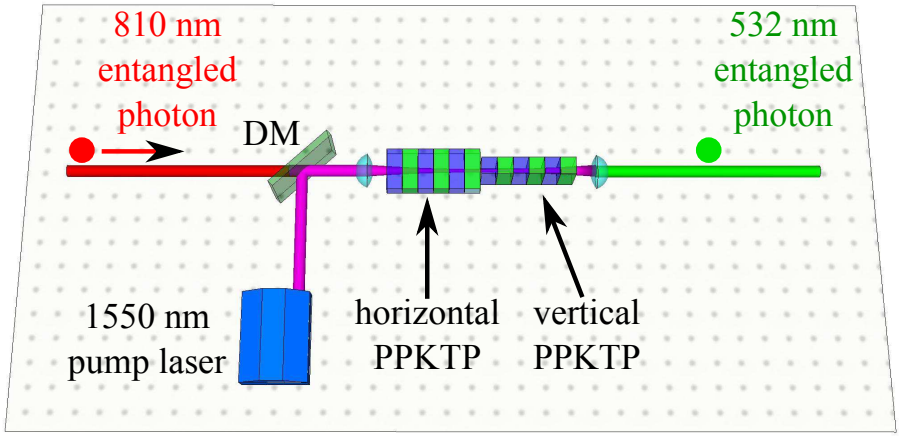

Figure 3.3.: Polarization entanglement wavelength conversion interface based on bulk crystals. An incoming 810 nm photon, belonging to a polarization entangled state, is mixed with a strong 1550 nm pump laser using a dichroic mirror (DM). Both fields are coupled into an arrangement of two orthogonally oriented PPKTP crystals for conversion of the two polarization modes $|H\rangle$ and $|V\rangle$ via SFG. The converted photons are obtained at a wavelength of 532 nm and are sent to a polarization entanglement analyser.

with a strong ($\sim$ 1 W) diagonally polarized pump laser at 1550 nm using a dichroic mirror. The two light fields are then focussed using a lens and sent through an arrangement of two PPKTP crystals. They use the type-I QPM in each crystal permitting only wavelength converting one polarization mode. To convert polarization entangled photons, both crystals are oriented orthogonally with respect to each other such that the first crystal converts the $|H\rangle$ component, and the second the $|V\rangle$ component. After the second PPKTP, light is collected using a lens and sent to an entanglement analysis setup. After properly adjusting the conversion efficiencies and losses in both crystals, the polarization state of the converted photon is preserved with a fidelity of 98%. The internal conversion efficiency of this interface is reported to be 0.04 %. In this experiment, relatively short PPKTP crystals are used and the rest of the setup is based on free-space optics. As the crystals are short, temperature dependent birefringence (and consequently phase) fluctuations are reduced to a minimum. In addition, the birefringence fluctuations of free-space and the corresponding optics are negligible, which makes

this approach relevant as a polarization entanglement quantum interface.

Advantages

The main advantages of this interface scheme are:

- A high phase stability.
- A relatively simple and reliable experimental apparatus.

Disadvantages

The following drawback is encountered:

- A relatively low conversion efficiency.

The low conversion efficiency is mainly explained by the use of bulk instead of waveguide crystals. Although the light confinement was optimized by properly choosing an appropriate focusing lens, the light was confined only in a cross section area of 2000 μm^2 (810 nm) respectively 4000 μm^2 (1550 nm) over a short crystal length ($\sim$mm). Waveguide structures permit much higher conversion efficiencies thanks to longer light field interaction lengths (a few cm) in combination with tight light confinement on the order of 10 μm^2. However, it seems difficult to combine two orthogonally oriented waveguides in a real experiment. Typically, surface waveguide structures and confined light modes are not symmetric, which results in high losses when coupling light between two orthogonally oriented waveguides. Moreover, the waveguides should guide both polarization modes, which is not the case for the widely used PPLN/W structures based on proton exchange[1]. As type-I crystals are used for wavelength conversion, this interface performs actually the tasks $|V\rangle_1 \mapsto |H\rangle_3$ and $|H\rangle_1 \mapsto |V\rangle_3$. Obtaining the correct polarization settings is then easily achieved using a half-wave plate after the interface to rotate the photon polarizations. In the next subsection, a new solution is proposed based on a single crystal as a conversion device. This solution is also intrinsically phase stable.

3.2.2. Sagnac configuration

The Sagnac configuration for SFG is shown in Figure 3.4. The entangled photon to be converted and the diagonally polarized pump laser (operating at angular frequency ω_2) are mixed using a dichroic mirror (DM) and sent to a Sagnac loop apparatus. This apparatus is made of a PBS at the input sending the vertically polarized photon contribution $|V\rangle_1$ in the clockwise sense and the horizontally polarized counterpart $|H\rangle_1$ anti-clockwise. The same is true for the pump laser. Following the path of the $|V\rangle_1$ contribution, it enters then a type-0 PPLN/W and is wavelength converted following

[1] PPLN/Ws based on Ti in-diffusion are capable of guiding both modes.

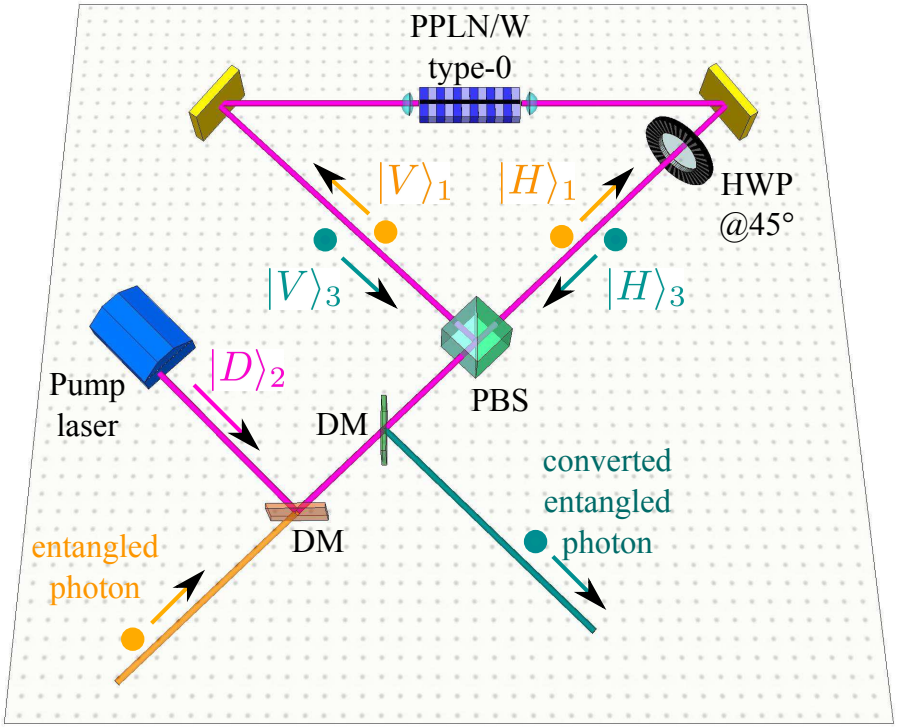

Figure 3.4.: Sagnac configuration for a quantum interface. The entangled photon is mixed with the pump laser using a dichroic mirror (DM). The light contributions $|H\rangle$ and $|V\rangle$ are separated on a PBS. The vertically (horizontally) polarized contribution travels clockwise (anti-clockwise) and is converted in a high efficiency type-0 PPLN/W. A half-wave plate (HWP) in one arm ensures that only vertically polarized light enters the PPLN/W. This is necessary as the type-0 interaction works only for vertically polarized light. The wavelength converted contributions are recombined at the PBS and separated from the pump laser using a dichroic mirror (DM).

equation 3.1. At the PPLN/W output, a vertically polarized contribution at angular frequency ω_3 is obtained, $|V\rangle_3$. This contribution is sent through a half-wave plate (HWP) rotating the polarization state by 90°, thus one obtains $|H\rangle_3$, which is further transmitted on the PBS (towards the bottom left output) and separated from the pump laser using a DM.
Following the $|H\rangle_1$ contribution, it is first rotated by the HWP to be vertical and then converted in the PPLN/W to generate $|V\rangle_3$. This contribution is further reflected on the PBS (towards exiting through the bottom left output port), and also separated from the pump laser using a DM. In this configuration, the HWP and PBS need to be achromatic, meaning that they work properly at all three wavelengths. Such an interface would perform the tasks $|V\rangle_1 \mapsto |H\rangle_3$ and $|H\rangle_1 \mapsto |V\rangle_3$. Obtaining the correct

polarization settings is then easily achieved using another HWP after the interface.

Advantages

The Sagnac configuration offers three main advantages:

- Sagnac loop experimental configurations are widely used for photon pair generation, in fibre [188, 258, 259] as well as in bulk crystal configurations [260, 261, 262, 187], such that there is some knowledge available on building up and aligning such setups.
- This configuration permits using a single non-linear crystal for the conversion task. It is used in both directions simultaneously and only one polarization mode is present inside the crystal.
- The Sagnac configuration is intrinsically phase stable as the optical paths in clockwise and anti-clockwise directions are always identically long.

Disadvantages

The encountered drawbacks of the Sagnac configuration are:

- High performance optics components are required, for instance, a broadband PBS and a HWP working for all three wavelengths simultaneously. As such components are non-standard, their realization is technically very challenging.
- A major issue is that waveguide structures cannot be used without serious drawbacks. As the waveguide is not symmetric and birefringent, different wavelengths are coupled in and out of the waveguide in different positions and directions. Thus it is almost impossible to properly overlap the three light fields in this configuration. This causes additional losses and difficulties to align the experiment, such that this configuration is generally restricted to the use of bulk crystals.

In the following, a solution is proposed that overcomes the problems introduced by the non symmetric waveguides.

3.2.3. Mach-Zehnder configuration

A solution towards overcoming the problems introduced by the non symmetric waveguide structure, is shown in Figure 3.5. A diagonally polarized pump laser and the entangled photon are mixed using a wavelength division multiplexer (WDM) and sent to a polarizing beam-splitter (PBS). A PBS reflects the vertical and transmits the horizontal polarization components. The vertical components are directly sent to a type-0 PPLN/W where the entangled photon component is wavelength converted. The converted photon,

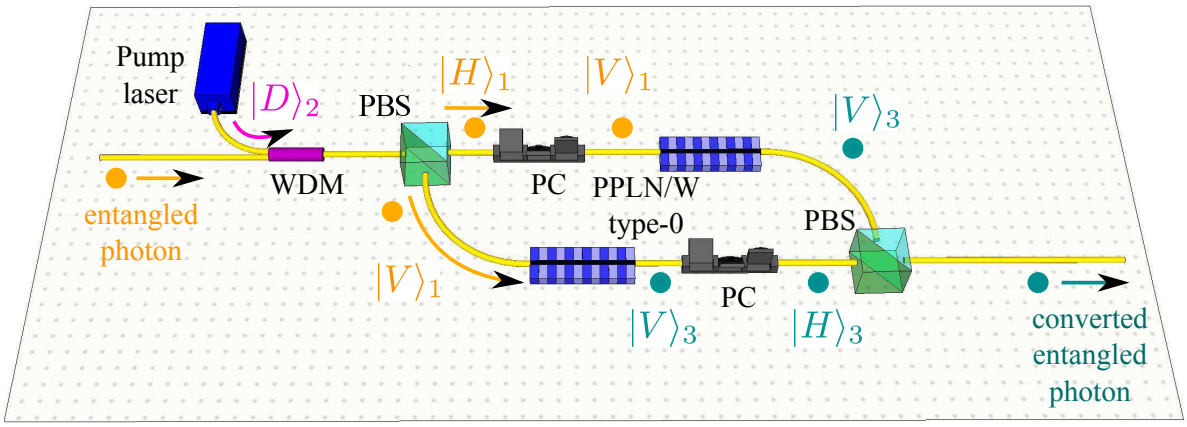

Figure 3.5.: Interface based on a Mach-Zehnder interferometer like configuration. The entangled photon and the diagonally polarized pump laser are mixed using a WDM. After the first PBS, the horizontal (vertical) components travel along the upper (lower) interferometer arm. The upper contribution is first rotated using a PC and converted in a PPLN/W. The vertical component is directly sent to the second PPLN/W, and rotated after conversion. Both arms are recombined using a PBS. Note that in order to simplify the experimental setup, one might consider employing polarization maintaining fibres inside the interferometer. By rotating these fibres appropriately, one could avoid using polarization controllers.

$|V\rangle_3$, is then rotated using a polarization controller (PC) to be horizontal, $|H\rangle_3$, and sent to another PBS where it is transmitted towards the interface output. Concerning the horizontal component of the initial entangled state, $|H\rangle_1$, after the input PBS, it is rotated using a PC to be vertical, $|V\rangle_1$, and wavelength converted in a second PPLN/W. The converted light, $|V\rangle_3$, is sent to the output PBS where it is reflected and exits at the same output like the other component. Note that this device performs, as the Sagnac solution, the transformation $|V\rangle_1 \mapsto |H\rangle_3$ and $|H\rangle_1 \mapsto |V\rangle_3$, such that an additional HWP is needed at the interface output.

Advantages

The main advantages of the Mach-Zehnder interferometer configuration are:

- It can be realized in a fully guided wave fashion compared to the previously mentioned approaches. The pump laser and entangled photon fields are mixed using a WDM and the $|H\rangle$ and $|V\rangle$ modes are separated on a fibred PBS (or fibre-PBS).

- The light fields are coupled to a PPLN/W sample via an optical fibre. In many applications the entangled photon and pump laser wavelengths are reasonably close

such that both are guided in a single mode fashion in the optical fibre and a good fibre to waveguide coupling can be achieved at both wavelengths.

- At the waveguide outputs, the converted light is collected using optical fibres. A good light collection efficiency is achieved, as at this stage, the coupling needs to be optimized for only one wavelength of interest. Recombination of the two paths is then made using a fibre coupled PBS.

- This setup permits using a type-0 PPLN/Ws for SFG of polarization entangled photons with very high efficiency.

Disadvantages

The Mach-Zehnder interferometer configuration has several drawbacks, but all of them are solvable with reasonable efforts:

- As for the other two schemes, one needs to take care that the conversion efficiencies for the two polarization modes are matched. Regarding that point, proper pump laser power adjustment in both waveguides solves this problem conveniently.

- The path length difference of the two interferometer arms needs to be matched to better than the photon coherence length, which typically ranges from 1 mm to several metres[2]. This problem is also conveniently solved by carefully aligning the experimental apparatus and a potential walk-off compensation stage.

- The biggest challenge concerns the stabilization of the phase between the two (fibred) interferometer arms, especially on a long time-scale. Solving this problem is not evident, but in section 3.4 an astute phase stabilization system is demonstrated.

The Mach-Zehnder interferometer configuration seems to be the only feasible solution towards achieving polarization entanglement wavelength conversion with a high efficiency. Consequently, this is the chosen strategy. In the following, we first show optical characterization experiments on the two used PPLN/W, and introduce then the phase stabilization system.

[2]The shortest coherence length of about 1 mm is mainly given by the SFG spectral acceptance bandwidth of the employed PPLN/W. This typically on the order of a few tens of GHz, which corresponds to a ~ 1 mm photon coherence length.

3.3. Optical sample characterization

Following the design of the Mach-Zehnder interferometer interface configuration, two type-0 PPLN/Ws are needed. The employed samples have both a length of 3.8 cm and have been fabricated by HC Photonics corporation[3].

The PPLN/W samples are optically characterized with the goal being to find the desired QPM

$$|V\rangle_{1560.48}\,|V\rangle_{1620.58} \mapsto |V\rangle_{794.98}\,, \tag{3.2}$$

where the subscripts denote the desired wavelengths of interest in nm. This particular wavelength combination is chosen as 1560.48 nm corresponds to the wavelength of the polarization entangled photon pairs emitted by the source described in section 2.5. On the other hand, 794.98 nm corresponds to the D_2 absorption line wavelength of rubidium atoms, one of the most promising quantum memory species. Conservation of energy for the SFG process dictates then the pump laser wavelength, that needs to be at 1620.58 nm. Note that the SFG process is widely wavelength tunable via QPM adjustment. For example, employing a 1614 nm pump laser and changing the PPLN/W temperature by ~ 20 K results in a QPM optimized for converting photons to the wavelength of 793.4 nm, which corresponds to the absorption wavelength of Tm^{3+}:YAG crystal based quantum memories [263].

The following of this section is organized as follows. First, the desired QPM is searched and found via tuning the temperature of the PPLN/Ws. Then, the wavelength conversion efficiencies of the two PPLN/Ws are measured in the classical regime as a function of the pump laser power. When passing to the single photon regime, strong Raman scattering noise is observed, strongly limiting the applicability of this approach for coherent polarization entanglement conversion. A solution for noise suppression is therefore proposed, that will be realized in the near future.

3.3.1. Finding the good QPM

The experimental setup for finding the desired QPM $|V\rangle_{1560.48}\,|V\rangle_{1620.58} \mapsto |V\rangle_{794.98}$ is shown in Figure 3.6. A 1620.58 nm laser is amplified using an erbium doped fibre amplifier (EDFA)[4], sent through a polarization controller (PC), and a wavelength division multiplexer (WDM), and coupled into a type-0 PPLN/W. The single photons at 1560.48 nm are simulated by a wavelength tunable laser, which is also sent through a PC, and a WDM, and coupled into the PPLN/W. The PCs permit aligning the two laser light polarization states such that they are vertical at the PPLN/W input. The 794.98 nm SFG signal at the PPLN/W output is collected using a lens and sent to a visible light power meter. The coupled power of the tunable laser is adjusted to ~ 3 mW and the coupled power of the 1620.58 nm laser is about 100 mW. The great difference of

[3] HC Photonics corporation, chip IDs: AS-Y100301-09-C07 and AS-Y100301-09-C08.
[4] The output power is adjustable up to 2 W.

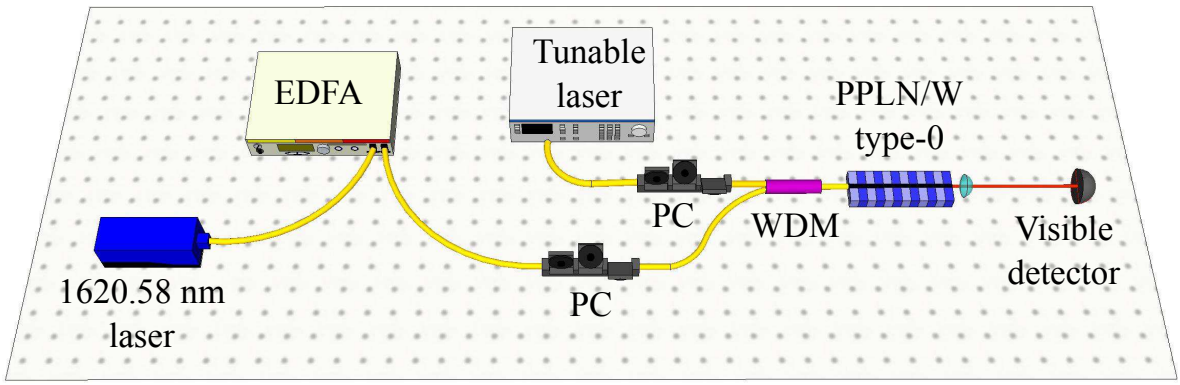

Figure 3.6.: Experimental setup towards finding the good QPM condition and SFG efficiency. A 1620.58 nm laser is amplified using an EDFA and mixed with a wavelength tunable laser simulating the single photons at around 1560.48 nm. Two polarization controllers (PC) permit aligning the light fields to be vertically polarized at the PPLN/W input. A visible light power meter at the PPLN/W output records the optical power of the SFG signal at around 794.98 nm.

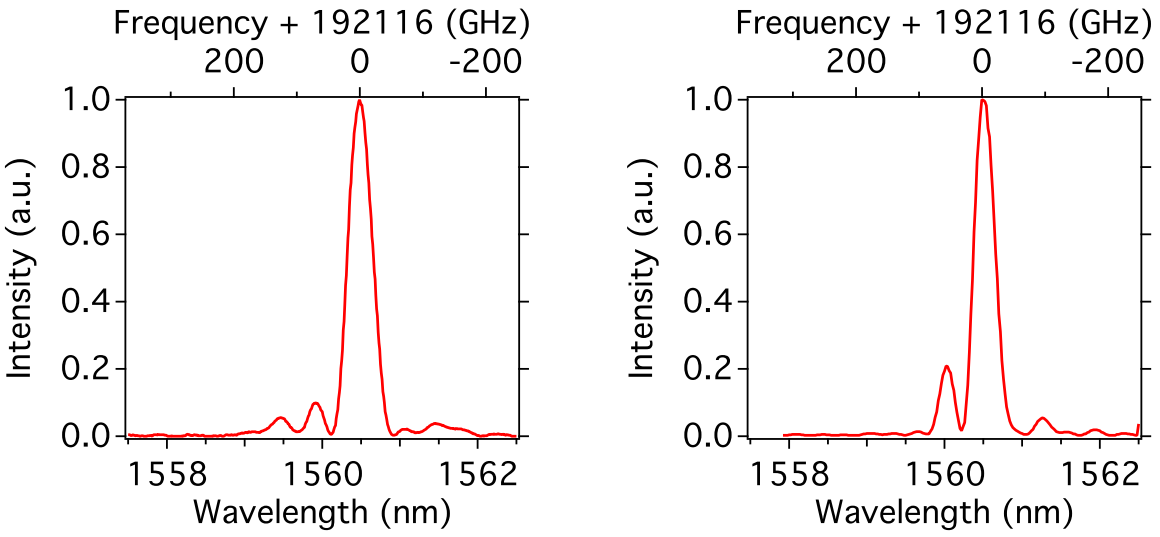

Figure 3.7.: Intensity of the wavelength converted light as a function of the wavelength of the tunable laser for (a) PPLN/W_1 and (b) PPLN/W_2. For PPLN/W_1 the desired QPM is obtained at a temperature of 75°C and for PPLN/W_2 at 69°C. The spectral acceptance bandwidths are 0.35 nm (44 GHz) and 0.32 nm (40 GHz), respectively.

pump powers ensures that one works always in the low pump depletion regime, thus the experimental results are not biased. The obtained signals, when the wavelength of the tunable laser is scanned, are shown in Figure 3.7. The sample PPLN/W$_1$ (PPLN/W$_2$) shows a maximum SFG efficiency at the desired wavelengths for a temperature of 75°C (69°C). The spectral acceptance bandwidths (full width at half maximum) of the two samples are 0.35 nm and 0.32 nm, corresponding to 44 GHz and 40 GHz, respectively. In the next subsection the conversion efficiency of these samples is analysed.

3.3.2. SFG efficiency

To measure the internal wavelength conversion efficiency, the same experimental setup as the one shown in Figure 3.6 is employed. This time, however, the laser wavelengths are fixed at 1620.58 nm and 1560.48 nm respectively, so as to operate always at the optimal QPM condition. The 1560.48 nm (λ_1) laser is waveguide coupled with a pump power of $P_1 = 3$ mW and the 1620.58 nm (λ_2) pump laser power, P_2, is varied from zero to around 500 mW. The intensity of the 794.98 nm (λ_3) SFG light, P_3, is then measured as a function of the pump laser power. In this operation regime, the optical powers for the light fields involved in the SFG process follow the following equation [247]:

$$\frac{\lambda_3 P_3}{\lambda_1 P_1} = \sin^2\left(\sqrt{\eta P_2}\right). \tag{3.3}$$

Here, η is the efficiency parameter, typically given in %/W. The experimental results are shown in Figure 3.8.
The results show that for a waveguide coupled pump power of 434 mW (450 mW) the conversion efficiencies reach their maximum. Further increasing the pump power results in reduced conversion efficiencies, as the SFG light experiences the process of difference frequency generation, *i.e* it is converted back to the initial wavelength of 1560.48 nm [247]. The maximum is relatively flat, such that matching the conversion efficiencies of both crystals (by properly adjusting the pump power in each of them) is conveniently achievable.

3.3.3. Background noise contributions

The PPLN/W characterizations described above are made using strong light fields with optical powers on the order of a few mW to several hundreds of mW. In this subsection, it is shown that passing from classical (high power) to quantum (low power) light fields is not evident and causes stringent noise problems due to Raman scattering.

SHG noise contribution

For the first measurement, consider the experimental apparatus shown in Figure 3.9. The 1620.58 nm pump laser is amplified using an EDFA and sent to a PPLN/W with

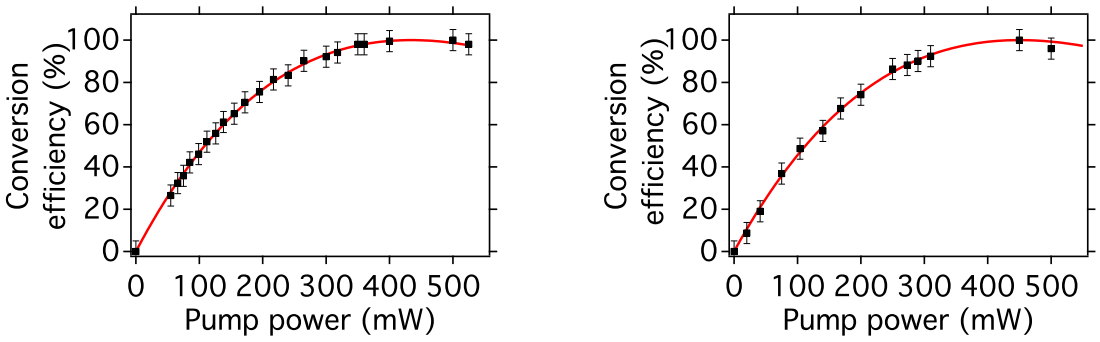

Figure 3.8.: Conversion efficiency for the light at 1560.48 nm as a function of the waveguide coupled pump power at 1620.58 nm for (a) PPLN/W_1, and (b) PPLN/W_2. Maximum conversion efficiency is achieved at a waveguide coupled power of 434 mW, corresponding to a SFG efficiency of η =569%/W (a), respectively at 450 mW, corresponding to η =548%/W (b). Solid lines are fits following the law given in equation 3.3 and error bars give ±5% error.

a waveguide coupled optical power of about 50 mW. At the same time, the 1560.48 nm laser is sent to the PPLN/W, however at a strongly attenuated optical power of about 1 nW. Light at the PPLN/W output is collected using a 10 m long single mode fibre designed for the wavelength of 800 nm, such that essentially no telecom laser light is guided. In order to record an optical spectrum, the light is then sent to a monochromator (rotatable grating)[5] having a single photon photo multiplier tube (PMT) at its output. The resolution of the monochormator is $\sim$ 0.2 nm at 800 nm. In Figure 3.10 the measured spectrum at around 800 nm is shown. As expected, there is one peak at the SFG wavelength of 794.98 nm. However, in addition a strong line at 810.29 nm is observed. This peak is attributed to the second harmonic generation of the pump laser. Although the QPM is not optimized for this process, this (well known) peak is often observed and is generally removed using suitable filters[6]. As shown later, this residual 810.29 nm is advantageously *recycled* for stabilizing the phase in the interferometer.

[5]Horiba Jobin Yvon S.A.S., model: MicroHR.

[6]By performing this experiment using appropriate filters, we convinced ourselves that this peak does not come from a second order reflection of the 1620.58 nm in the monochromator.

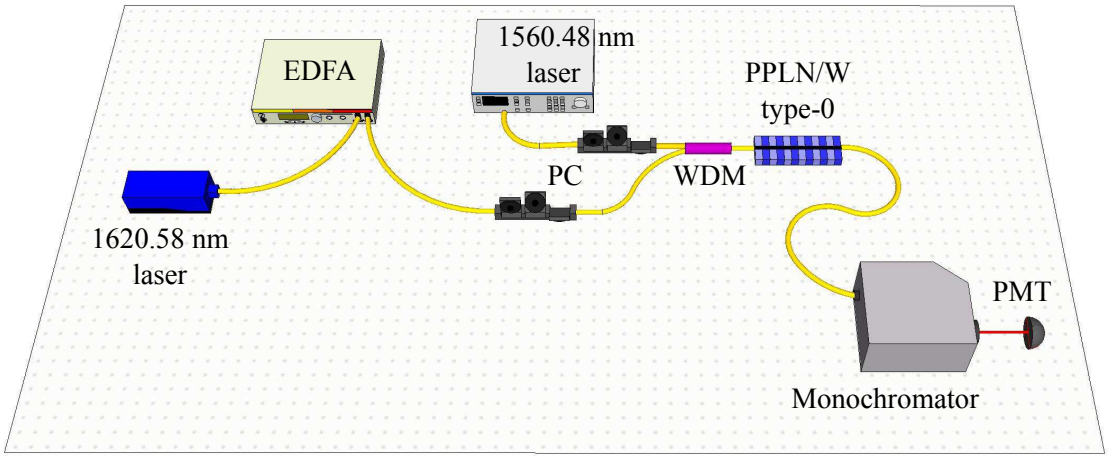

Figure 3.9.: Setup for measuring the noise contributions on the single photon level. The 1620.58 nm laser is amplified to 50 mW using an EDFA and further coupled to the PPLN/W. The 1560.48 nm laser is attenuated to approximately 1 nW and also waveguide coupled. Light at the PPLN/W is collected using a single mode fibre designed for 800 nm. This fibre directs to its cladding essentially all infrared light. The light is then sent to a monochromator (rotatable grating) having a resolution of about 0.2 nm. At its output a photomultiplier tube (PMT) is used to count single photons.

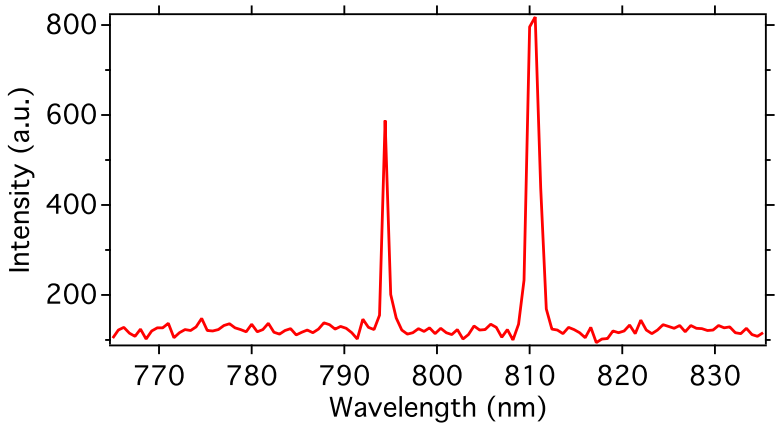

Figure 3.10.: Recorded optical spectrum when both, the 1620.58 nm and 1560.48 nm laser are coupled to the PPLN/W. Two peaks are obtained. The peak at around 795 nm is the SFG signal (1620.58 nm + 1560.48 nm). The peak at 810 nm is due to residual SHG of the strong pump laser at 1620.58 nm.

Raman scattering noise contribution

For the following experiment, the 1560.48 nm is switched off, such that when performing the measurements described before, no signal at 794.98 nm is expected. The obtained results are shown in Figure 3.11.

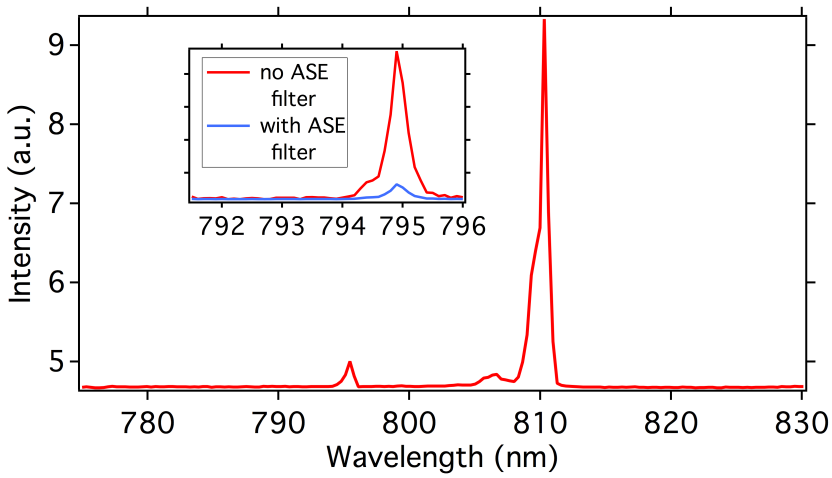

Figure 3.11.: Recorded optical spectrum when the 1560.48 nm laser is switched off. Note that there is still a peak at 795 nm which means that, due to some processes, photons at 1560.48 nm are present and converted inside the PPLN/W. As shown in the inset, when using appropriate filters towards removing laser ASE, the peak height is strongly reduced, however the peak at 795 nm does not completely vanish. This means that aside from ASE, there is another process generating light at 1560.48 nm.

The SHG peak at 810.29 nm is still present, however the one at 794.98 nm is not vanished. When carefully observing this peak, it is seen that not a narrow line is obtained but rather the QPM curve of Figure 3.7(a) is (approximately) reproduced. This means that there is a broadband noise contribution around 1560.48 nm which is sent to, or generated inside, the PPLN/W and further wavelength converted. To exclude noise coming from both the pump laser and EDFA (typically this would be amplified spontaneous emission (ASE)), bulk optical long-pass filters are employed. These filters show a rejection level of -40 dB (0.01% transmission) in the wavelength range $1260 - 1605$ nm, and, at the same time a transmission of more than 95% at $1615 - 1642$ nm[7]. When placing one filter after the EDFA and then measuring the optical spectrum after the PPLN/W, the 794.98 nm light is strongly attenuated, meaning that employing these filters reduces the ASE noise contribution at 1560.48 nm. However, the 794.98 nm peak does not completely vanish. Adding additional long-pass filters on the laser side does not improve the situation

[7]Iridian Spectral Technologies Ltd. Long Pass Filter 1610 LPP.

anymore. This means that there must be another source (after the filters) that generates broadband noise around 1560.48 nm.

The additional noise is ascribed to Raman scattering in both the optical fibres and the PPLN/W, which is demonstrated in the following.

Raman scattering in optical fibres

Consider the experimental apparatus shown in Figure 3.12. The 1620.58 nm pump laser is sent through two long-pass filters and a C/L band WDM[8] for removing any residual light at 1560.48 nm. The light is sent to the EDFA and amplified to 200 mW of optical power. After the amplifier, three more long-pass filters are employed to reject potential ASE at 1560.48 nm. Thereafter, the laser light travels along 20 m of optical fibre and is attenuated by $\sim$ 150 dB using five L/C band WDMs[9]. Finally, the light is sent to the monochromator, this time equipped with a free running InGaAs single photon detector

[8] C/L band WDMs transmit wavelengths above 1575 nm and reflect wavelengths below 1570 nm. The transmission rejection ratio is typically of −30 dB.

[9] L/C band WDMs are the counterpart of their C/L band devices. They transmit wavelengths below 1570 nm and reflect wavelengths above 1575 nm. The transmission rejection ratio is of −30 dB.

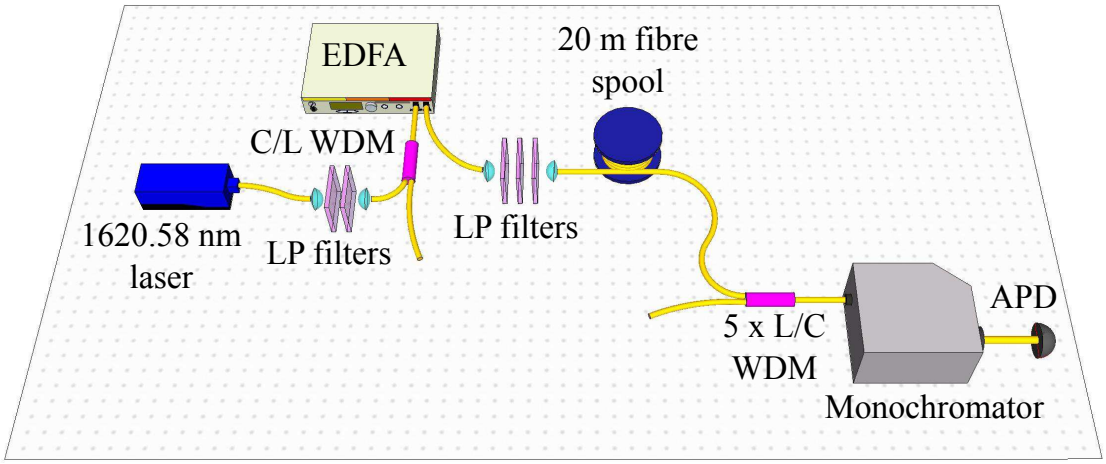

Figure 3.12.: Experimental setup towards measuring Raman scattering noise in a 20 m optical fibre. The pump laser at 1620.58 nm is amplified in an EDFA to a power of 200 mW. A C/L band WDM and several long-pass filters before and after the EDFA ensure that no residual ASE light at wavelengths below 1570 nm is present. The light then passes a 20 m fibre spool which is long enough to obtain sufficiently high Raman scattering intensities. Then the 1620.58 nm pump laser is rejected with an extinction ratio of more than 150 dB by 5 L/C band WDMs. Finally a spectrum from 1415 − 1575 nm is obtained using a monochromator followed by an InGaAs APD.

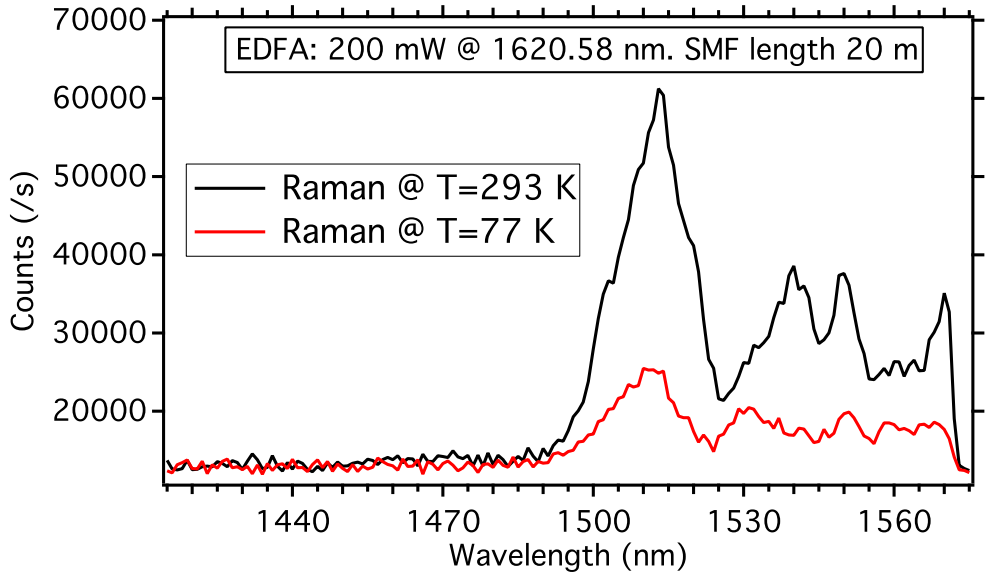

Figure 3.13.: Generated spectrum inside a 20 m singlemode fibre spool for a 1620.58 nm pump laser and 200 mW of optical power. One spectrum is taken at room temperature (T=293 K) and another spectrum when $\sim$ 10 m of this fibre are placed in a liquid nitrogen bath (T=77 K). The shape of the spectrum does almost not change, however the intensity at the lower temperature is strongly reduced. This is a clear signature that the spectrum is generated via Raman scattering inside the fibre. The strong intensity decrease at around 1570 nm is due to the filtering stage.

(APD)[10] at its output. The recorded spectrum between 1415 nm and 1575 nm is shown in Figure 3.13. A broadband spectrum ranging from 1490 nm to 1570 nm is obtained. The drop at 1570 nm is due to the employed L/C band WDMs. Adding additional long-pass filters directly after the EDFA does not change anything in the recorded spectrum. We conclude that the obtained broadband noise is generated after these filters. For Raman induced noise, a strong temperature dependence on the obtained intensity is expected, but the shape of the spectrum should not be changed. The recorded spectrum, when $\sim$ 10 m of optical fibre are put into liquid nitrogen is shown in Figure 3.13. Compared to the measurements performed at room temperature, the intensity of the signal is strongly reduced but the shape is not, which underlines the assertion that this noise is induced by Raman scattering. A simple theoretical model for calculating the Raman scattering in fused silica for a 1620.58 nm pump laser is given in Figure 3.14 and shows a good qualitative agreement with the experimental observations [264].

[10]Id Quantique id220 operating at 20% efficiency and 7 μs dead time.

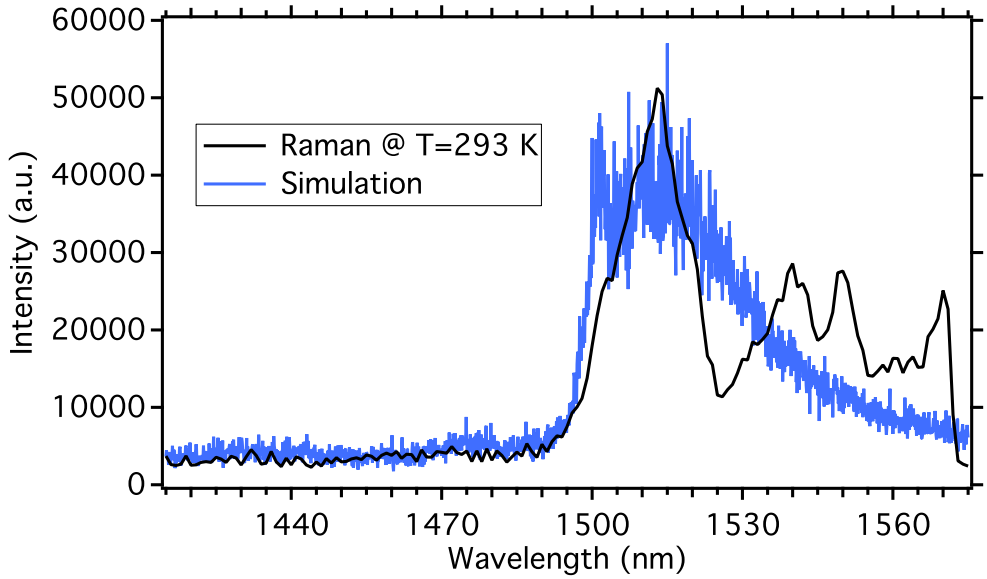

Figure 3.14.: Measured (black curve) and simulated (blue curve) Raman spectrum for a pump laser operating at 1620.58 nm and an incident power of 200 mW. The two curves are in good qualitative agreement.

Raman scattering in the PPLN/W

Consider the following experimental setup shown in Figure 3.15. The ASE-cleaned pump laser at 1620.58 nm is sent, via a free space channel (to avoid Raman scattering contributions from the optical fibres), to the PPLN/W. At the PPLN/W output, light is collected using free space optics and the pump laser light is rejected with > 120 dB by a set of three short-pass filters (cut-off at around 1570 nm). The light is further sent to a monochromator and the Raman induced noise spectrum is analysed using the same strategy as explained above. Figure 3.16 shows the obtained noise spectrum for a PPLN/w coupled pump power of 400 mW and 100 mW. These results are in very good agreement with the data obtained in reference [265] for a similar analysis. We observe a linear noise rate dependence as a function of the pump power. For better comparability, this graph shows also the results obtained when replacing the PPLN/W by a 2 m optical fibre at room temperature. It is found that the noise contribution at 1560 nm of the 3.8 cm long PPLN/W is roughly four times higher than the Raman noise originating from the 2 m long optical fibre, meaning that the Raman scattering inside the PPLN/W has to be considered as the main noise contribution.

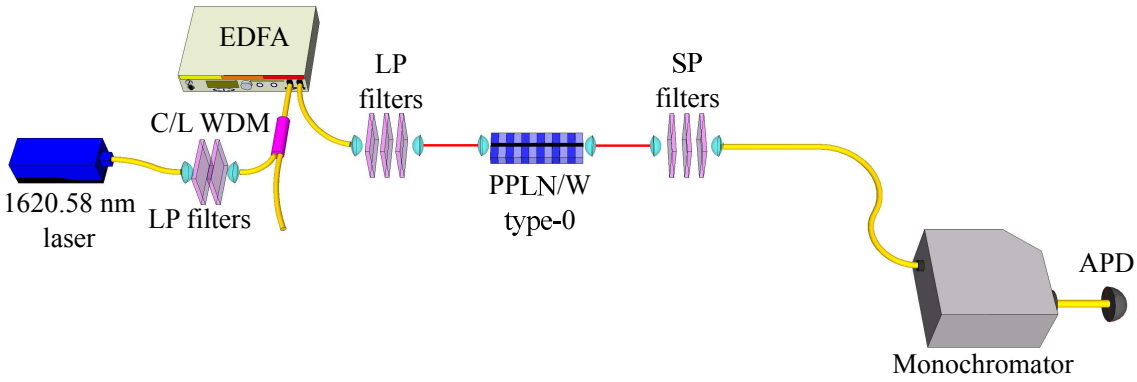

Figure 3.15.: Experimental setup for estimating the Raman scattering noise introduced by the PPLN/W sample. An ASE-cleaned pump laser at 1620.58 nm is coupled, via a free space channel, inside the PPLN/W and induces Raman scattering. At the waveguide output, the light is collected using free space optics and the pump laser is rejected by a set of 1570 nm short-pass filters (SP filters). The Raman spectrum is analysed using a monochomator followed by a single photon detector.

Raman scattering induced noise level

What is the level of noise introduced by Raman scattering in a realistic experimental configuration? This is estimated using the experimental setup outlined in Figure 3.17. The 1620.58 nm laser is filtered using long-pass filters and a C/L band WDM, and then amplified using an EDFA to around 1 W of optical power. After additional long-pass filters, the light is sent through another WDM (called recombination WDM), which is later employed to mix the 1560.48 nm single photons and the pump laser. Then a 2 m polarization maintaining (PM) fibre is employed. This corresponds to the length of the fibre employed in the final interface configuration. Thereafter, the light enters the PPLN/W with a waveguide coupled pump power of about 400 mW. With this power, almost 100% SFG efficiency is expected (see Figure 3.8). At the waveguide output, the light is collected using a 1 m PM fibre designed for the wavelength of 800 nm. Then, several bulk optics bandpass filters[11] are employed towards completely rejecting the SHG light at 810.29 nm. This way, only light at $\sim$ 795 nm is transmitted and sent to a fibre coupled Silicon avalanche photodiode (Si-APD)[12] having a single photon detection efficiency of $\sim$ 40% at this wavelength. In this particular configuration, the noise probability was measured to be $\sim 10^{-4}\,\mathrm{ns}^{-1}$. This noise probability is comparable to previous works where telecom photons have been wavelength converted in up-conversion detector schemes [247, 248, 249, 250, 251, 253, 252]. However, the noise probability is too

[11]Model: Semrock FF01-786-22-25 (three filters) and Thorlabs FB800-40 (one filter).
[12]Perkin Elmer SPCM-AQR-16.

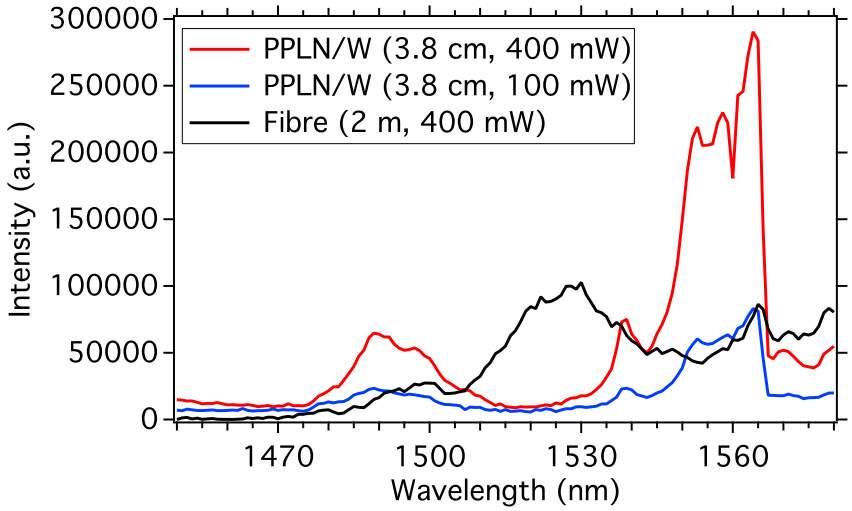

Figure 3.16.: Raman scattering noise obtained in the PPLN/W for 400 mW and 100 mW of waveguide coupled pump power. The shape of the noise spectrum does essentially not change, and a linear noise rate increase is obtained as a function of the pump power. For comparison, the Raman noise spectrum for a 2 m long optical fibre is shown at a fibre coupled pump power of 400 mW. The noise contribution of the 3.8 cm PPLN/W is roughly four times higher than the noise induced by the 2 m optical fibre.

high for realistic single photon applications. A comparison is given: The experimental results obtained in subsection 2.5.5 show a good violation of the Bell's inequalities for photons having 80 GHz and 540 MHz spectral bandwidth, using InGaAs APDs having a noise probability of $\sim 10^{-6}\,\mathrm{ns}^{-1}$. But for 25 MHz photons, where, due to the photons' long coherence times, long integration times are required, the raw entanglement quality was already degraded by $\sim 10\%$ due to detector noise. Consequently, an up-conversion detector having a noise probability of $10^{-4}\,\mathrm{ns}^{-1}$ cannot be applied to such narrowband photons.

A compromise may be obtained when reducing the pump power. As shown in Figure 3.18, the noise probability depends quadratically on the pump power, whereas the conversion efficiency for low pump powers can be roughly approximated by a linear function of the pump power. This means, that reducing the pump power by ten times reduces the noise rate by 100 times. Note that this reduces also the photon conversion efficiency by ten times, however, effectively the signal to noise ratio (SNR) is increased by a factor of ten using this strategy.

But reducing the pump power until a good SNR is achieved is not considered as an option in this work, as this means that very low conversion efficiencies are obtained, comparable to bulk crystal solutions which would then strongly reduce the applicability

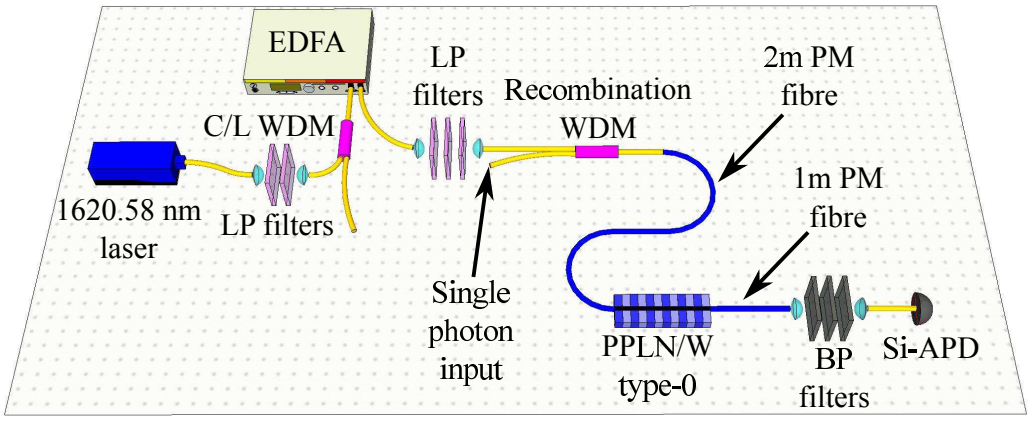

Figure 3.17.: Experimental setup for estimating the noise rate induced by Raman scattering in the fibres and PPLN/W. The 1620.58 nm pump laser is sent through several filters for removing ASE at around 1560 nm. An EDFA is used to increase the optical output power up to 1 W. After passing through additional long-pass filters, the light is sent through a recombination WDM, which is later used for mixing the single photons at 1560.48 nm and the pump laser. Thereafter 2 m of polarization maintaining (PM) fibre are employed, just like it would be in the final experimental setup. Then the PPLN/W is employed and the light at the output is collected using a PM fibre designed for the wavelength of 800 nm. Several band-pass filters are employed towards rejecting residual SHG light at 810.29 nm. The light is finally sent to a single photon Silicon avalanche photodiode (APD) that measures the residual noise.

of this interface scheme for real applications.

3.3.4. Proposed solution for reducing the Raman scattering induced noise

As shown in subsection 3.3.3, the Raman noise contributions are distributed over the full spectral acceptance bandwidth of the employed PPLN/Ws, ~ 40 GHz. For many experiments, wavelength conversion over this acceptance bandwidth is not required. For example, when applying this interface to the polarization entangled photon pair source described in section 2.5, depending on the employed filter, wavelength conversion is only needed over a bandwidth of 540 MHz (25 MHz). This permits using a noise reduction strategy based on spectral filtering after wavelength conversion, for example using a home-made optical cavity.

What are the requirements for such a cavity? First of all, the free spectral range (FSR) of the cavity should exceed the spectral acceptance bandwidth of the PPLN/W for proper noise filtering, see also Figure 3.19. For a plano-convex cavity design at a

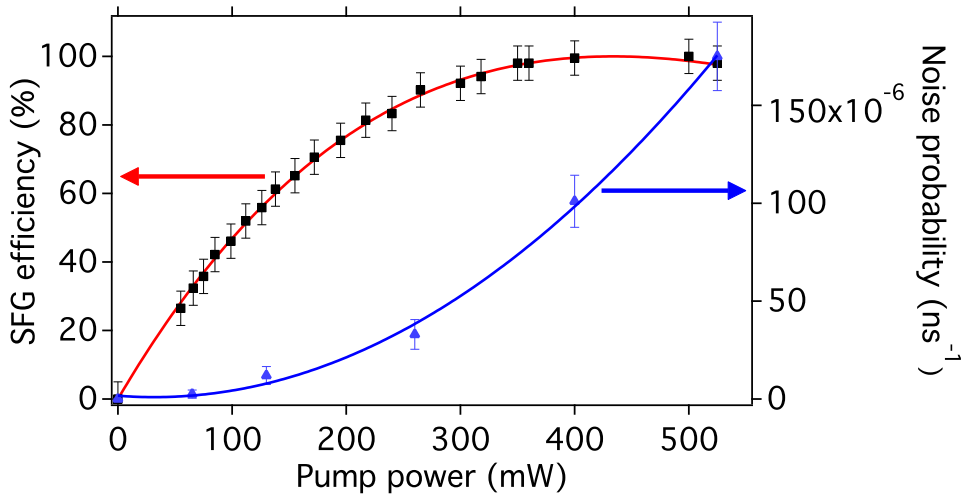

Figure 3.18.: SFG conversion efficiency and noise probability as a function of the pump power. The noise increases quadratically with the pump power and at 100% conversion efficiency, a noise probability of $\sim 10^{-4}\,\mathrm{ns}^{-1}$ is obtained, which is too high for most single photon applications.

light incident angle of 0°, we have

$$\mathrm{FSR} = \frac{c}{2\,L}, \tag{3.4}$$

where $c = 299\,792\,458\,\frac{\mathrm{m}}{\mathrm{s}}$ is the speed of light in vacuum and L is the optical length of the plano-convex cavity. As shown in Figure 3.19, a FSR of 300 GHz would be optimal for filtering. At ±300 GHz the QPM curve is essentially zero. This means that a cavity length of 0.5 mm is required.

Furthermore, a cavity transmission window of $\Delta\nu = 500\,\mathrm{MHz}$ is desired for several reasons. First, this corresponds to the spectral acceptance bandwidth of some solid state and hot atomic vapour quantum memories (and to the spectral emission bandwidth of the source described in section 2.5 when using the AOS GmbH filter). Second, this reduces the PPLN/W SFG acceptance bandwidth (and thus the Raman scattering noise) by almost two orders of magnitude, which results in a background noise level low enough for single photon applications. Third, as we shall see later in the text, a basic temperature stabilization system allows for stabilizing the transmission wavelength of the cavity with a precision of about 50 MHz. As this is much smaller than the transmission window, only small transmission intensity fluctuations at the desired wavelength are expected.

The FSR and $\Delta\nu$ are related through the finesse $\mathcal{F}$ defined as

$$\mathcal{F} = \frac{\mathrm{FSR}}{\Delta\nu}. \tag{3.5}$$

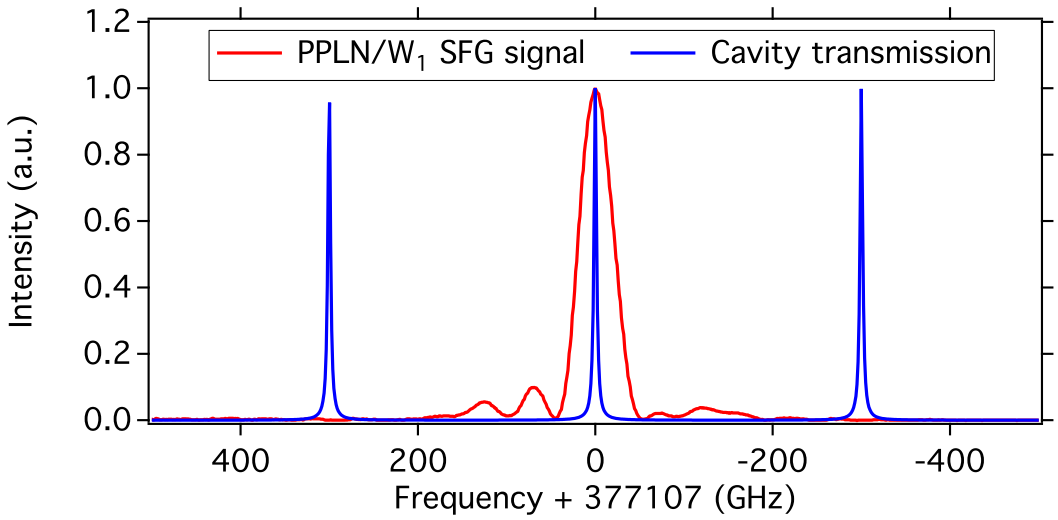

Figure 3.19.: Cavity solution for reducing Raman scattering induced background noise. The spectral SFG acceptance bandwidth of PPLN/W_1 is 44 GHz and the Raman scattering noise is distributed over the full acceptance window (see red curve). However, for the desired wavelength conversion application, light conversion is only demanded in a $\sim$ 500 MHz window inside the acceptance window. To reduce the Raman noise, light after the PPLN/W is sent through an optical cavity having a FSR of 300 GHz and a transmission window of 500 MHz (the transmission profile of the cavity is plotted in blue). The FSR is large enough to reject side peak contributions. As the cavity transmission window is almost two orders of magnitude smaller than the natural acceptance bandwidth, the Raman noise probability after the passing through the cavity is reduced by almost 100 times. This would permit using this interface at the single photon wavelength conversion level. Note that the cavity transmission profile (blue curve) plotted here has a transmission window of $\sim$ 3.5 GHz for better visibility.

The desired cavity needs therefore to have $\mathcal{F} = 600$. The finesse depends on the mirror reflectivity R and for $R > 0.5$ it is generally approximated by

$$\mathcal{F} \approx \frac{\pi\sqrt{R}}{1-R}. \tag{3.6}$$

To achieve a finesse of $\mathcal{F} = 600$, the mirror reflectivities need to be $R = 99.5\%$. Such a finesse implies that the light in the cavity experiences in average 600 round trips. This is a reasonably low number, such that absorption losses of high quality mirrors (typical losses of $\ll 0.01\%$) introduce only a maximum loss figure of about 11%, which is also reasonably low. Note that for $\mathcal{F} \gg 1000$ one needs also to take into account additionally the absorption of air which might require a vacuum system for reducing losses.

At the time this manuscript is written, such plan and convex cavity mirrors showing $R = 99.5\%$ and ultra low losses at the desired wavelength of 795 nm have been ordered. For the convex mirror, a curvature radius of 1 m is chosen which avoids that the two mirrors (one plan and one convex), positioned at a distance of 0.5 mm, touch each other.

Considering the long term frequency stability of the cavity system, one of the main limiting factors is thermal expansion of the material that is used as mirror holders. Note that the transmission frequency of the cavity is shifted by one FSR each time the cavity length is changed by $\lambda/2$, where λ is the wavelength of the light inside the cavity. Therefore, we have

$$\Delta f = \frac{2 \cdot \mathrm{FSR} \cdot \Delta L}{\lambda}. \tag{3.7}$$

Here, Δf is the transmission frequency drift and ΔL the drift of the cavity optical length. First order thermal expansion dictates

$$\Delta L = \alpha \cdot L \cdot \Delta T, \tag{3.8}$$

where ΔT is the temperature drift in Kelvin and α is the thermal expansion coefficient of the used mirror mount material. Combining equations 3.4, 3.7 and 3.8 leads to

$$\Delta f = \frac{\alpha \cdot c \cdot \Delta T}{\lambda}. \tag{3.9}$$

Remarkably, this equation is independent of the cavity length. In Table 3.1 the corresponding cavity frequency drifts are given for several (practical) cavity mirror mount materials. A basic cavity temperature stabilization system reaches a long term stability of $\lesssim 0.1$ K, meaning that a frequency stability of 45.3 MHz (0.75 MHz) for a low thermal expansion material such as Invar (Zerodur®) is achieved. This is small compared to the expected cavity transmission bandwidth $\Delta\nu = 500$ MHz. Thus, when using the corresponding materials for mounting the cavity, a basic temperature stabilization might be sufficient for appropriate frequency stabilization. In reality, also the thermal expansion of the mirror substrates has to be taken into account (typical material is fused silica), which might limit the capabilities of a temperature stabilization system and require the use of a stabilization system based on a reference laser as shown in subsection F.4 or reference [49]. Which stabilization system is required, will be evaluated in the near future.

	Aluminium	Titanium	Invar (FeNi36)	Zerodur®
α at 300 K [K^{-1}]	$23.1 \cdot 10^{-6}$	$8.6 \cdot 10^{-6}$	$1.2 \cdot 10^{-6}$	$0.02 \cdot 10^{-6}$
Δf at $\lambda = 795$ nm and $\Delta T = 1$ K [MHz]	8711	3243	453	7.5

Table 3.1.: Thermal expansion coefficient and resulting cavity frequency drifts for several practical cavity mirror mount materials.

3.4. Phase stabilization

As stated in subsection 3.1.2, the Mach-Zehnder interferometer configuration of a quantum interface results in general in a non-zero phase shift θ between the converted $|H\rangle$ and $|V\rangle$ contributions. This is due to non-identical optical path lengths for the two contributions. A constant non-zero phase is conveniently compensated using birefringent optics, such as a Soleil Babinet phase compensator. The major issue for this fully fibred interface design comes from the fact that θ is not stable due to small (uncontrollable) temperature fluctuations in the optical fibres employed between the input and output PBS. In the following, a brief estimation is given on the required temperature stability for an appropriate phase stabilization. Here the term appropriate means $\Delta\theta < \frac{2\pi}{50}$, the phase drift at which a $\sim 1\%$ degradation of the visibility for the standard Bell's inequalities test is obtained [225].

3.4.1. Phase drift estimation

The typical fibre length between the input PBS and the PPLN/W is $L_{\text{in}} = 2$ m. The fibre length from the PPLN/W to the output PBS is $L_{\text{out}} = 1$ m. We neglect the 0.038 m long PPLN/W for these calculations as this is small compared to the fibre lengths. The phase accumulated in one interferometer arm is then

$$\theta = 2\pi L_{\text{in}} \left(\frac{n_{1560.48}}{1560.48\,\text{nm}} + \frac{n_{1620.58}}{1620.58\,\text{nm}} \right) + 2\pi L_{\text{out}} \frac{n_{794.98}}{794.98\,\text{nm}}. \tag{3.10}$$

Here, n denotes the fibre refractive index at the wavelength (in nm) given by the corresponding subscripts. Taking into account the temperature dependent Sellmeier equations for fused silica given in Appendix E, as well as the fibre thermal expansion, the first order temperature dependent phase drift for this SFG process $\Delta\theta_{\text{SFG}}$ at a temperature of 300 K is given by

$$\Delta\theta_{\text{SFG}} = 198.8\,\text{K}^{-1} \cdot \Delta T. \tag{3.11}$$

Here, ΔT symbolizes the temperature drift in Kelvin. Consequently, a sub-mK fibre temperature stability is required to achieve the desired phase stability of $\Delta\theta < \frac{2\pi}{50}$, which is technically very challenging.

In order to stabilize the phase of the Mach-Zehnder interferometer, we employ an astute stabilization system. The 1620.58 nm pump laser light experiences (although not with a good efficiency) frequency doubling (process of second harmonic generation - SHG) as outlined in subsection 3.3.3. The generated light at 810.29 nm has a typical optical power of a few μW, thus being measurable using a standard photo detector. For this SHG process, the temperature dependent phase drift is calculated according to equation 3.10 at a temperature of 300 K:

$$\Delta\theta_{\mathrm{SHG}} = 195.0\,\mathrm{K}^{-1} \cdot \Delta T. \tag{3.12}$$

The interferometer is now phase stabilized with respect to the phase accumulated by the SHG process (details on the stabilization scheme are given later in the text). This effectively results in

$$\Delta\theta_{\mathrm{SHG}} = 0. \tag{3.13}$$

In this case the phase drift for the SFG process is reduced and it is

$$\Delta\theta_{\mathrm{SFG}} = (198.8 - 195.0)\,\mathrm{K}^{-1} \cdot \Delta T = 3.8\,\mathrm{K}^{-1} \cdot \Delta T. \tag{3.14}$$

Now, in order to achieve the desired phase stability of $\Delta\theta_{\mathrm{SFG}} < \frac{2\pi}{50}$, only a moderate fibre temperature stability of only 33 mK is required, which is achievable when the experimental apparatus is properly designed.

3.4.2. Phase stabilization scheme

A picture of the experimental setup is shown in Figure 3.20. In order to obtain a good temperature stability, the full experimental setup, including the two PPLN/Ws, is enclosed in a temperature stabilized box made of ~ 5 cm thick polystyrene. On one side of the box, two plexiglass windows are attached to access the optical components for alignment. Inside the box, four low rotation speed computer fans are employed, that guarantee a descent air flow inside the box. The fans are mounted on temperature controlled radiators. This system provides a good temperature stability inside the box ($\Delta T < 50$ mK[13]), thus permitting to use the above mentioned phase stabilization scheme.

The basic idea of the SHG phase stabilization scheme is outlined in Figure 3.21. The 1620.58 nm pump laser generates in both PPLN/Ws light at 810.29 nm. Note that light coming from the upper (lower) PPLN/W exits the interferometer vertically (horizontally) polarized, having accumulated a phase θ_V (θ_H). Via a dichroic mirror the 810.29 nm and 794.98 nm light fields are separated. The 810.29 nm light is sent through an electro-optic phase modulator (EOM) that adds a controllable phase shift to the vertically polarized light, $\theta_V \mapsto \theta_V + \theta_{\mathrm{EOM}}$. Thereafter, the light is sent to a

[13]This measurement is limited by the resolution of the employed temperature sensor, which is 50 mK.

polarizing beam-splitter (PBS) oriented at 45° compared to the natural $\{H, V\}$ basis. The transmitted light intensity I_t then follows

$$I_t \propto \cos^2\left(\frac{\theta_V - \theta_H + \theta_{\mathrm{EOM}}}{2}\right). \tag{3.15}$$

To stabilize the phase difference $\theta_V - \theta_H$, a standard feedback-loop system is used. The modulation output of a commercial Lock-In amplifier is sent to the EOM, thus a periodic modulation of θ_{EOM} around zero is obtained. The modulated intensity I_t is measured using a standard photodiode[14], the obtained signal is mixed with the modulation signal inside the Lock-In amplifier and low-pass filtered. The obtained error signal is integrated using a home-made electronic circuit and forwarded to a piezo-electric fibre stretcher (PZT). The PZT tracts on one of the input fibres towards changing its optical length, such that the phase difference between the two interferometer arms is always kept at zero. Note that by adjusting the phase accumulated in the EOM, it is also possible to precisely tune the phase difference accumulated in the interface.

[14]Thorlabs DET10A.

Figure 3.20.: Picture of the experimental setup for wavelength conversion. The two PPLN/Ws are enclosed in temperature stabilized ovens made of Bakelite (brown material). The waveguide in the front is free-space coupled at the in and output using aspheric lenses. The waveguide in the background is in the final configuration being fibre coupled at the input and output. In the top left corner of the picture, the piezo fibre stretcher is seen (two metallic half circles mounted on a translation stage). On top of the picture the beginning of the polystyrene box is seen (yellow).

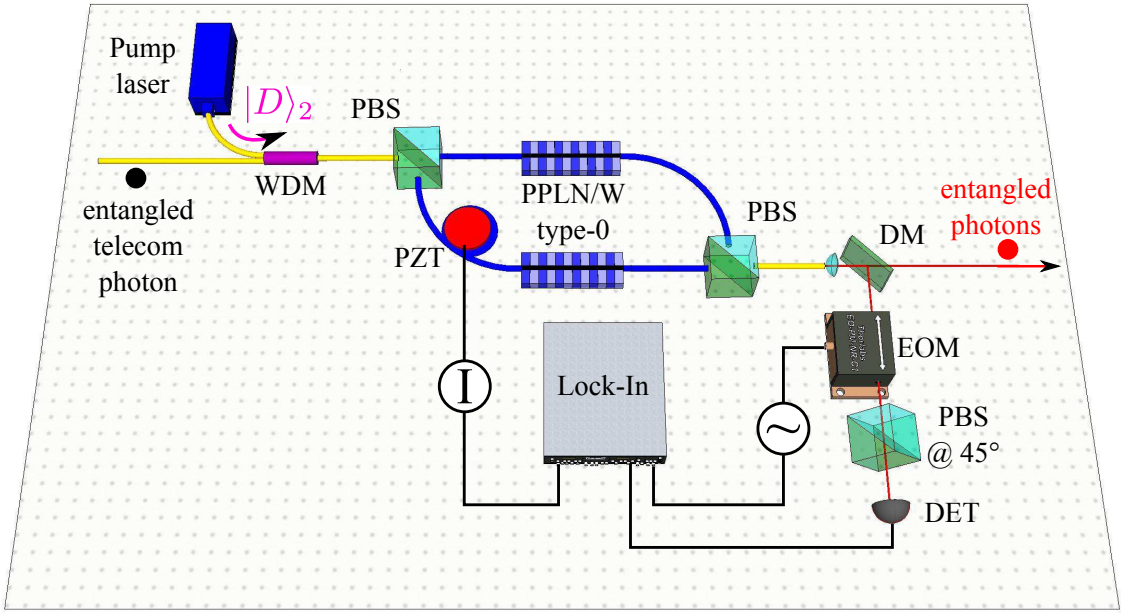

Figure 3.21.: Phase stabilization system for the Mach-Zehnder interferometer interface. The 1620.58 nm pump laser is sent to the interferometer and in each PPLN/W it is (although only with a small amount) frequency doubled. The optical power obtained at 810.29 nm is of about 1 μW at the output of each PPLN/W. Compared to the scheme shown in Figure 3.5, no polarization controllers are employed. The optical paths are made of polarization maintaining fibres (blue lines) which are rotated such that the proper light polarizations are obtained in front of each PPLN/W and the polarizing beam-splitter (PBS) at the interferometer output. After the interferometer, the 810.29 nm (SHG) and the 794.98 nm (SFG) lights are separated using a dichroic mirror (DM). The 810.29 nm light passes an electro-optic phase modulator (EOM) and a PBS oriented at 45° compared to the natural $\{H, V\}$ basis. The intensity measured on a photodiode (DET) depends on the phase accumulated in the interferometer. A Lock-In amplifier modulates the phase accumulated in the EOM, measures the signal obtained on the DET, and derives the error signal. This signal is integrated (I) and forwarded to a piezo-electric fibre stretcher (PZT) that tracts on one of the input fibres towards stabilizing the optical phase.

This stabilization system is tested in a long run of five hours, a time sufficiently long for performing Bell inequality tests. After this time, the interferometer phase is still locked with respect to the phase accumulated by the SHG process. The system does not jump between different intensity oscillation fringes, as no fast voltage jumps in the signal sent to the PZT are observed.

As a conclusion, this astute interferometer phase stabilization system has proven the

suitability of a Mach-Zehnder interferometer configuration for high efficiency wavelength conversion of polarization entangled photons.

3.5. Conclusion and outlook

The chapter paves the way towards the realization of a high efficiency wavelength conversion interface suitable for polarization entangled photons. In the beginning the need for such an interface was outlined, especially for realizing future quantum networks where telecom photons are used for distribution and quantum memories for storage of entanglement. It was shown that the non-linear process of sum frequency generation is a good candidate for performing such a task. It was shown further that the realization of such an interface applicable to polarization entangled photons is not a straight forward task and three experimental schemes have been considered. The only scheme permitting to achieve high conversion efficiencies was found to be based on a Mach-Zehnder configuration where two PPLN/Ws are employed, one for each polarization mode, $|H\rangle$ and $|V\rangle$. The PPLN/Ws have been optically characterized in terms of QPM, efficiency and noise contributions. It was found that the Raman scattering background noise level in both fibres and PPLN/W is currently too high for allowing single photon applications. A noise reduction solution was shown based on an optical cavity. The design parameters for such a cavity have been evaluated and the corresponding optical components have been ordered at the time this manuscript is written. In order to preserve the polarization entangled state after wavelength conversion, the interferometer phase needs to be stabilized. An astute phase stabilization scheme was shown which is based a small residual SHG signal induced by the strong pump laser. The suitability of this stabilization scheme was evaluated in a long-time measurement of five hours. The work for the near future is to built up the optical cavity, evaluate if a temperature stabilization system is good enough for stabilizing the position of the cavtiy transmission fringes, and finally employ it after the PPLN/Ws for Raman noise reduction. The quality of the phase stabilization system has then to be further tested via the violation of the Bell's inequalities.

Chapter 4.

An entanglement-enabled quantum delayed choice experiment

In this chapter, an entanglement-enabled quantum delayed choice experiment is demonstrated. This experiment underlines, in a striking way, the inadequacy of using classical pictures for describing the behaviour of quanta, namely whether they behave either as waves or particles. Although abandoning classical pictures requires enormous changes in our ways of thinking, this experiment, among others [266, 267, 268, 269, 270, 271, 272, 273, 167, 274, 41, 216][1], shows dramatically that there is no other choice.

In the following, we first give a brief description on the interpretation problem of quantum physics. Then, we proceed to the realization of the quantum delayed choice experiment and we recall why classical models are unsuitable for describing this experiment. In order to not overcharge the experimental part, all relevant experimental details are given only at the end of the experimental section. This chapter ends with a conclusion and a discussion on the obtained experimental results.

4.1. On the complementary behaviour of quanta

One of the main questions that people have asked since the birth of quantum physics is whether (light) quanta behave as waves or particles [10]. Many experiments have been carried out to underline either one of these two assumptions. Concerning the behaviour of true single photons, it was not until 1974 that Clauser demonstrated that photons (can) behave as particles in an unambiguous way [266]. To do so, he used a single photon source based on mercury atoms, excited by electron bombardment. The emitted photons were then sent to a setup similar to that of Hanbury Brown and Twiss (HBT) [275, 276] to measure coincidences (see Figure 4.1). As no coincidences between the two employed detectors were observed, these results showed that the light field of single

[1] Note that this list is far from being exhaustive.

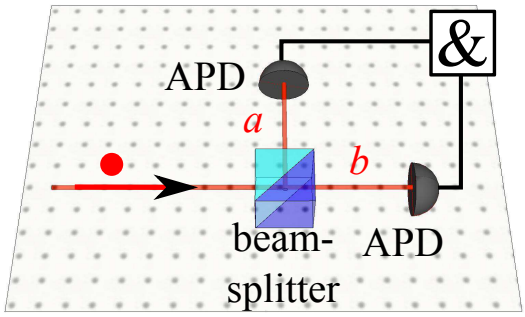

Figure 4.1.: Hanbury Brown and Twiss (HB-T) setup. An incoming photon is sent to a beam-splitter followed by two single photon detectors (APD), one placed in each path, a and b. The detectors are connected by a coincidence counting device (&). When single photons are incident on such a setup, no coincidences are observed, thus underlining the particle nature of photons, that (apparently) do not split up at a beam-splitter.

photons needs to be quantized, as if photons would behave as indivisible particles[2]. In 1986, the results of Clauser have been re-investigated in a very nice manner by Grangier and collaborators [267]. Using their famous calcium cascade bi-photon source (see also Figure 2.1 in section 2.1), they used one photon out of an emitted pair to herald the presence of the second (single) photon. The second photon was then sent to a HB-T setup to measure whether the single photon can split up at a beam-splitter, and generate coincidences between the two employed detectors. The obtained results showed again that this never happens. The particle-like behaviour was confirmed. Having (apparently) proven that a single photon never splits up at a beam-splitter, they slightly modified the experimental apparatus (see also Figure 4.2(a) in the closed configuration). As before, the single photon was sent to a first beam-splitter, BS_1, and, with the results obtained in the HB-T experiment, we might want to conclude that the single photon chooses one out of the two beam-splitter output paths, here denoted by a and b. The two paths were then recombined at BS_2, thus forming a Mach-Zehnder interferometer. The path length difference (and consequently the phase relation θ) between the two interferometer arms could be precisely tuned by moving one mirror. Note that in Figure 4.2(a)) we prefer to

[2]The HB-T apparatus measures the second order intensity autocorrelation function $g^{(2)}(t)$, where t is the time delay between the clicks on the two detectors. For a single photon source we expect $g^{(2)}(0) = 0$, meaning that the detectors never click at the same time (a single photon cannot be split up). A laser source gives $g^{(2)}(0) = 1$, which means that the probability of detecting two photons simultaneously ($t = 0$), one at each detector, is equal to the probability of detecting two photons with an arbitrary time delay t. Finally, an uncorrelated classical source, *e.g.* a light bulb, gives $g^{(2)}(0) = 2$, which is often interpreted as photons bunching. In this case, the probability of having two photons at $t = 0$ is two times higher than for $t \neq 0$. A light source is said to show quantum behaviour for $g^{(2)}(0) < 1$.

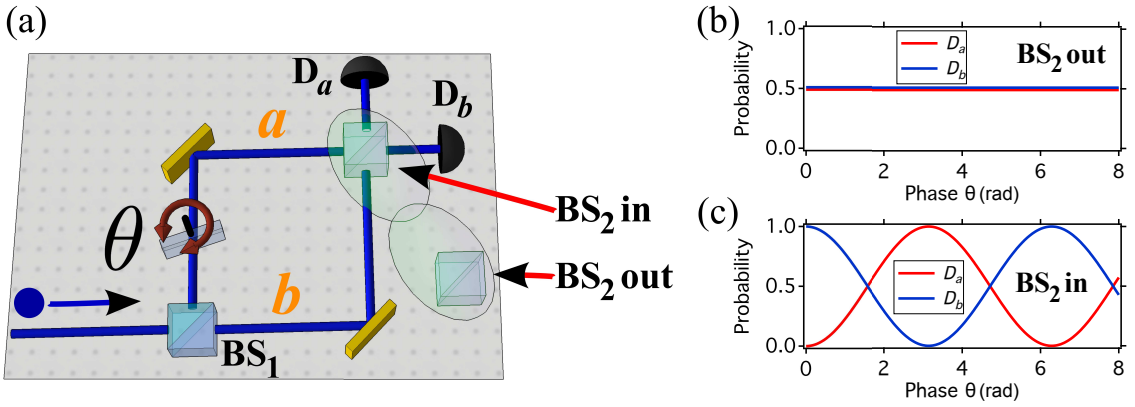

Figure 4.2.: Complementary behaviour of single photons incident on a closed (open) Mach-Zehnder interferometer as shown in (a). When the interferometer is open, *i.e.* BS_2 is out, then a click on detector D_a, respectively D_b, reveals that the photon has travelled along path b respectively a. As coincidences between both detectors are never observed, one concludes that a single photon never splits up at BS_1. Moreover, the click probabilities on the two detectors are independent of the phase θ, as shown in (b). When putting BS_2 in, the situation changes completely. The probability of a click at detector D_a, respectively D_b, depends now on the phase difference θ as shown in (c). Note that for each case (BS_2 in or out), there is a classical model describing the phenomenon, however both models exclude each other. This underlines the inadequacy of classical models for describing the behaviour of quantum systems. Bohr explained these observations by stating, that a photon behaves, accordingly to the measurement apparatus, either as a particle or as a wave.

symbolize the phase tuning capability by a rotatable glass plate. The obtained counting rates on detectors D_a and D_b were surprising as they depended on the phase difference as shown in Figure 4.2(c). This behaviour is simply explained in classical (wave) physics. For example the same interference results are obtained when using macroscopic water waves [277][3]. For obtaining interference using this classical model, one thing is crucial: the interfering object needs to propagate along *both paths simultaneously*. But in the HB-T experiment, outlined just before, it was shown that a photon never splits up at a beam-splitter. Consequently, classical theories impose serious contradictions of what happens in a quantum experiment in which only single quanta are used. Remarkably, the obtained results are perfectly predicted by quantum theory. Note that V. Zwiller and collaborators performed a very similar experiment using quantum dots as single photon emitters, however their experiment was used for spectroscopy reasons and they did not claim wave-particle complementarity [278]. In their work, wave-particle duality

[3]The configuration in this experiment was not a Mach-Zehnder interferometer, but a double-slit experiment. However these two apparatus are very similar regarding the observation of interference.

is exploited as a tool!

Although these experiments have been performed only in the last few decades, the *strange* predictions of quantum physics have been the subject of major discussions in the 1920s between famous physicists, such as Bohr, Einstein, Schrödinger, Heisenberg, Planck, Dirac, Pauli, and many more. But even today, the interpretation of quantum physics is still under debate [279, 280, 66].

In 1927, at a conference in Como (Italy), Bohr introduced for the first time his notion of 'wave-particle-duality' [281]. With the help of Pauli, he presented an improved version of his talk at the 1927 Solvay conference in Brussels (Belgium) [7, 282]. Bohr managed to convince the majority of physicists about his interpretation of the complementary behaviours of quanta. Bohr stated that quanta behave according to the measurement apparatus they are subjected to. When single photons are sent to an ordinary HBT setup (which is essentially the same as an open Mach-Zehnder interferometer), the user reveals their particle-like behaviour of the photon and the fact that the individual photons are not split up. Sending single photons to a Mach-Zehnder interferometer, in which the two paths remain indistinguishable, *i.e.* if we cannot obtain the which-path information, lets the photons behave as waves. This is often referred to be Bohr's notion of wave-particle-duality. The observed photon behaviour is either wave-like, or particle-like, depending on the measurement apparatus. In 1978, J. A. Wheeler proposed a new experiment trying to fool the photons in the Mach-Zehnder interferometer. To do so, one sends single photons to a Mach-Zehnder interferometer where the output beam-splitter, BS_2, can be removed or inserted at the choice of the user. However, this choice is only made *after* the photons have already passed the first beam-splitter, BS_1 [283, 9]. Interpreting Bohr's wave-particle-duality notion in a classical way imposes that the photons need to decide at BS_1 whether they will lead to the observation of wave or particle behaviour. But as the experimental configuration is not yet chosen at this particular moment, this leads to another contradiction, because "how should the photon decide?". In 2007, Wheeler's experiment was performed in an ideal configuration using single photons emitted from a nitrogen-vacancy defect center in diamond [270]. The experimental results agreed perfectly with quantum physics, which predicts in this case timing order independent behaviours. Depending on the *final* configuration of the measurement apparatus, the photons behaved accordingly, and Bohr's wave-particle-duality notion was obeyed. We cannot fool the photon! The results could not be interpreted using classical models without introducing serious problems of causality.

Finally, intermediate cases, in which BS_2 is only partially present[4], have been considered in theory and led to a more general description of Bohr's wave-particle-duality notion, expressed by an inequality limiting the simultaneously available amount of interference (signature of wave-like behaviour) and of the which-path information (particle-like behaviour) [271, 284, 285]. This inequality is often referred to be Bohr's complementar-

[4]Essentially this means that a beam-splitter is used whose reflectivity/transmissivity can be continuously adjusted.

ity notion, and it has been confirmed experimentally [286, 287] also in delayed choice configurations [272, 273]. We shall outline this inequality later, in subsection 4.3.4, in more details.

In the following, we take Wheeler's delayed choice idea one step further to emphasize even more the inadequacy of classical models for describing the phenomena of quantum mechanics.

4.2. Wheeler's idea pushed one step further

4.2.1. General idea

In the new version of Wheeler's experiment, the output beam-splitter, BS_2, is replaced by a 'quantum beam-splitter' (QBS), as recently proposed theoretically [65, 66]. The basic ideas of this experiment are summarized in the following:

- The output beam-splitter of a Mach-Zehnder interferometer is put in a coherent superposition of being present and absent described by the state

$$\frac{1}{\sqrt{2}}\left(|\text{BS in}\rangle + |\text{BS out}\rangle\right).$$

  Obviously, achieving such a state for a true (macroscopic) beam-splitter is quite impossible to achieve. But we shall see later a way to establish this.

- Sending a single photon to such an interferometer leads to

$$\frac{1}{\sqrt{2}}\left(|\text{BS in}\rangle\,|\text{wave}\rangle + |\text{BS out}\rangle\,|\text{particle}\rangle\right). \tag{4.1}$$

  Here, $|\text{wave}\rangle$ and $|\text{particle}\rangle$ describe the wave and particle like behaviour of the photon, which is correlated to the presence or absence of the output beam-splitter, respectively.

- An interesting feature of equation 4.1 is that the test photon can now be detected *before* the state of the output beam-splitter is determined. Consequently, the photon does not know whether it would behave as a wave or particle even after it is detected and destroyed. We call this the advanced version of Wheeler's experiment. In previous experiments, the photon behaviour was always determined before detection of the photon [270, 272]. In this new configuration, the user is free to choose to delay this (in principle) infinitely long after the photon has been destroyed in a detector. Trying to explain such an experiment in classical terms leads to serious causality problems.

- Finally, it is also possible to measure the presence or absence of the output beam-splitter in a non-natural analysis basis, *i.e.* to project the beam-splitter state on superpositions such as $\alpha\,|\text{BS in}\rangle + \beta\,|\text{BS out}\rangle$, with the normalization being $|\alpha|^2 + |\beta|^2 = 1$. This then projects the single photon under test into wave-particle superpositions $\alpha\,|\text{wave}\rangle + \beta\,|\text{particle}\rangle$, a purely quantum object that has no classical counterpart.

Consequently, such an experiment tries fooling the photon under test by detecting and destroying it even before it *could have known* how to behave.

In the following, the experimental implementation of this experiment is outlined schematically.

4.2.2. Experimental configuration: basic idea

For the experimental realization, it is essential to generate the state described by equation 4.1. As this state is actually an entangled state, it can be simulated using a two-photon polarization entangled state. This is why we choose the following implementation (see Figure 4.3):

- We start from a pair of polarization entangled photons in the state $|\Phi^+\rangle = \frac{1}{\sqrt{2}}\left(|V\rangle_c\,|V\rangle_t + |H\rangle_c\,|H\rangle_t\right)$. The subscripts t and c denote a photon travelling to the *test* and *corroborative*[5] photon apparatus, respectively. This state is emitted by the photon pair source described in section 2.5 and reference [64].

- The test photon apparatus, as shown in the right hand side of Figure 4.3, is a Mach-Zehnder interferometer that is open (closed) for the $|H\rangle_t$ ($|V\rangle_t$) component, thus revealing particle (wave) behaviour for the related photon polarization components. Experimentally, this is done by having as an output beam-splitter a polarization dependent beam-splitter (PDBS) showing ordinary 50/50 splitting for vertically polarized photons and 100% reflection for horizontally polarized photons. More details on the experimental realization of the PDBS are given in subsection 4.3.1.

- The presence of entanglement ensures that the polarization state, and thus the behaviour of the test photon is completely random. It is even undefined until projective measurements are performed. No information pre-exists in nature [16].

- After the interferometer, polarization state quantum erasers (in this case diagonally oriented polarizing beam-splitters PBS_1 and PBS_2) are used, which ensure that a measurement on the test photon does not reveal any information about which behaviour has been observed.

[5] Note that the term *corroborative photon* is used instead of *witness photon* to avoid confusion with the wording 'entanglement witness', commonly used to quantify the amount of entanglement shared by a bi-partite state. The reader finds more information about entanglement witnesses in the following reference [288].

- At this stage, the only way of knowing the behaviour is to measure the polarization state of the corroborative photon. The corroborative photon now plays the role of determining the presence/absence of the output beam-splitter. The corroborative photon apparatus is shown in the left hand side of Figure 4.3. It comprises an electro-optic modulator (EOM) to rotate the photon's polarization state, and a polarizing beam-splitter, PBS_3, followed by two single photon detectors. This apparatus allows manipulating, and analysing the corroborative photon's polarization state.

- When the corroborative photon is not rotated and measured to be horizontal (vertical), this projects the test photon to be horizontal (vertical) and consequently the particle (wave) behaviour of the test photon has been observed.

- When the corroborative photon is rotated before projection on PBS_3, the output beam-splitter is projected onto a superposition state and, consequently, wave particle interference is observed.

In the following, we state once more the subtleness' of this experiment which render explanations based on classical theories absurd.

Summarizing the subtleness of the quantum delayed choice experiment

- Nothing prevents us from measuring the corroborative photon *after* the test photon has been detected. This however implies that the test photon, even after it is detected, does not *know* how it actually behaved.

- Via manipulation of the corroborative photon, we can choose on which kind of superpositions the state of the QBS is projected (it can be either present or absent, but we might also project the QBS state onto a superposition of being present and absent). Especially, this can be done even *after* the test photon has been detected and consequently already passed the QBS.

- By carefully designing the experimental apparatus, the corroborative and test photons are separated in a space-like fashion, such that classical information exchange at the speed of light (or less) between the two photons is prohibited. Consequently, each photon of the entangled state cannot know or influence what the other photon does [167, 231]. Classical explanations would then need to assume that the two photons communicate with each other faster than the speed of light, meaning that the theory of special relativity would be violated.

In the following, the experimental apparatus is detailed more precisely, along with the corresponding calculations.

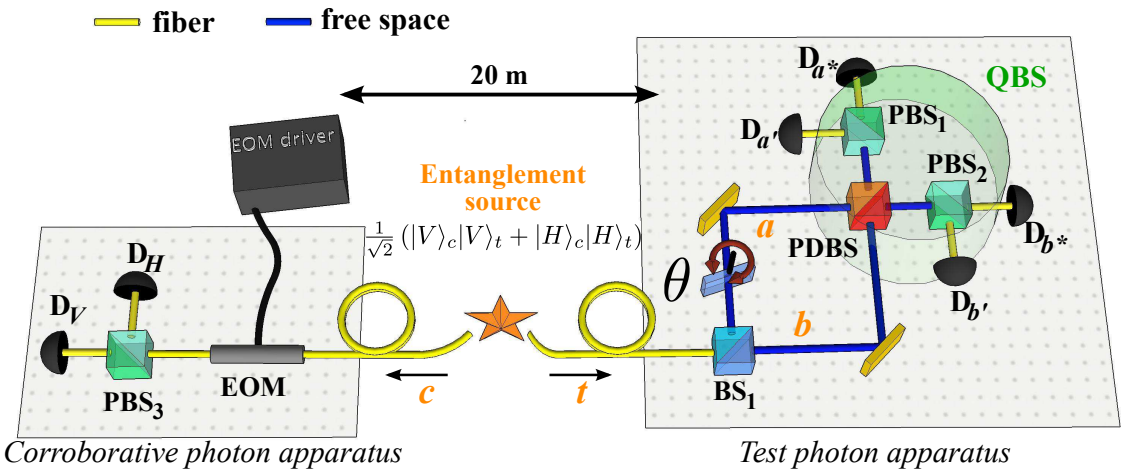

Figure 4.3.: Experimental setup. A source of polarization entangled photons emitted at $\lambda = 1560.48\,\text{nm}$ (see section 2.5 and reference [64] for more details) sends, through a single mode optical fiber, one test photon (t) to a quantum beam-splitter (QBS) apparatus, being an open (closed) Mach-Zehnder interferometer for horizontally (vertically) polarized photons. This is realized using a polarization dependent beam-splitter (PDBS), showing a 50/50 splitting ratio for vertical, and 100% reflection for the horizontal, components, respectively. The polarization state information of this photon is erased thanks to polarizing beam-splitters (PBS$_{1,2}$) oriented at 45° compared to the PDBS basis. The second photon (c) of the entangled state is sent to another laboratory 20 m away, and used as a 'corroborative' photon and allows determining whether wave or particle-like behaviour was observed. The space-like distant corroborative photon apparatus is used for rotating the polarization state of this photon using an electro-optical modulator (EOM). The photon then goes through PBS$_3$, followed by two detectors (D_H and D_V). The paths are denoted as follows: photons going to the corroborative apparatus are said to propagate along path c. A photon going towards the test apparatus travels along path t. In the test photon apparatus, the upper paths are denoted by a, while the lower paths are denoted by b. Finally, after PBS$_{1,2}$, the paths towards detectors D_{a^*}, $D_{a'}$, D_{b^*} and $D_{b'}$ are denoted by a^*, a', b^* and b', respectively.

4.2.3. Experimental configuration: detailed description

As outlined above, the QBS realization is based on the idea that when a test photon in an arbitrary polarization state enters an interferometer that is open for $|H\rangle_t$ (horizontally polarized) and closed for $|V\rangle_t$ (vertically polarized), the states of the interferometer and the test photon become entangled [289]. This apparatus, shown in the right hand side of Figure 4.3 and detailed in subsection 4.3.1, therefore reveals a particle behaviour for the $|H\rangle_t$ component of the test photon, and a wave behaviour for the $|V\rangle_t$ component. Note that such an experiment has been realized using single photons prepared in a coherent superposition of $|H\rangle$ and $|V\rangle$ [273]. However, as similar results would be obtained using an ordinary laser, we take this idea one step further by achieving a genuine quantum behaviour for the output beam-splitter by exploiting an intrinsically quantum resource, namely entanglement.

At this stage, we change the representation of quantum states, by introducing photon creation operators. This simplifies the reading of the following equations. The quantum state initially emitted by the photon pair source is then:

$$|\Phi^+\rangle = \frac{1}{\sqrt{2}}\left(c_H^\dagger t_H^\dagger + c_V^\dagger t_V^\dagger\right)|vac\rangle\,. \tag{4.2}$$

Here, using the notation of Figure 4.3, $c_H^\dagger$ ($t_H^\dagger$) and $c_V^\dagger$ ($t_V^\dagger$) represent creation operators for horizontally and vertically polarized photons, respectively, propagating towards the corroborative (test) photon apparatus. Moreover, $|vac\rangle$ represents the vacuum state.

The test photon is then sent to a Mach-Zehnder interferometer where the upper (lower) paths inside and outside the interferometer are always denoted a (b). The state in front of the output of the Mach-Zehnder is then given by

$$|\Psi\rangle = \frac{1}{2}\left(c_H^\dagger(ie^{i\,\theta}a_H^\dagger + b_H^\dagger) + c_V^\dagger(ie^{i\,\theta}a_V^\dagger + b_V^\dagger)\right)|vac\rangle\,. \tag{4.3}$$

Here, θ is the phase shift introduced by the glass plate in the upper arm. In addition, the components that are reflected at BS_1 experience a phase shift of i. $a_H^\dagger$, $a_V^\dagger$, $b_H^\dagger$ and $b_V^\dagger$ symbolize creation operators for test photons propagating in the upper and lower interferometer arm, respectively. At the Mach-Zehnder output, we employ the QBS device, that is made of two components. The first is a polarization dependent beam-splitter (PDBS) that shows 100% reflection for horizontally polarized photons and provides ordinary 50/50 splitting ratio for the vertically polarized photons[6]. The whole state after the PDBS reads

$$|\Psi\rangle = \frac{1}{2}\left(c_H^\dagger\,\left(-e^{i\,\theta}a_H^\dagger + ib_H^\dagger\right) + \frac{1}{\sqrt{2}}c_V^\dagger\,\left(b_V^\dagger(i + i\,e^{i\,\theta}) + a_V^\dagger(1 - e^{i\,\theta})\right)\right)|vac\rangle\,. \tag{4.4}$$

[6]The PDBS is actually realized using a combination of standard bulk optical components as explained in subsection 4.3.1.

Here, $a_H^\dagger$, $a_V^\dagger$, $b_H^\dagger$ and $b_V^\dagger$ symbolize creation operators for test photons propagating towards PBS_1 and PBS_2, respectively.

At this point (see equation 4.4), each polarization state of the test photon, vertical and horizontal, is associated with one of the two complementary types of behaviours, wave and particle.

The second QBS stage consists of polarizing beam-splitters (PBS_1 and PBS_2) oriented at 45° to the $\{H, V\}$ basis, that erase all polarization information that existed at the PDBS output [268, 269, 274]. The state of equation 4.4 is now described by the following equation

$$|\Psi\rangle = \frac{1}{\sqrt{2}}\left(c_H^\dagger[\text{particle}] + c_V^\dagger[\text{wave}]\right)|vac\rangle\,, \tag{4.5}$$

with

$$[\text{particle}] = \frac{1}{2}\left(-e^{i\,\theta}(a^{*\dagger} + a'^{\dagger}) + i(b^{*\dagger} + b'^{\dagger})\right),$$

and

$$[\text{wave}] = \frac{1}{2\sqrt{2}}\left((1 - e^{i\,\theta})(-a^{*\dagger} + a'^{\dagger}) + (i\,e^{i\,\theta} + i)(-b^{*\dagger} + b'^{\dagger})\right),$$

where the creation operators $a^{*\dagger}$, $a'^{\dagger}$, $b^{*\dagger}$ and $b'^{\dagger}$ denote photons propagating towards detectors D_{a^*}, $D_{a'}$, D_{b^*} and $D_{b'}$, respectively. At this stage, the polarization modes are dropped as they are no longer associated with wave or particle behaviours. Consequently, the only way of knowing which behaviour was observed is to examine the corroborative photon. The result on a measurement on this photon plays the role of determining the presence or absence of the output beam-splitter.

The corroborative photon measurement apparatus is shown on the left-hand side of Figure 4.3. An electro-optic phase modulator (EOM) allows rotating the polarization state of the corroborative photon by an angle α. The operation performed on the corroborative photon is then:

$$c_H^\dagger \;\rightarrow\; \cos\alpha\, c_H^\dagger + \sin\alpha\, c_V^\dagger \tag{4.6}$$

$$c_V^\dagger \;\rightarrow\; \cos\alpha\, c_V^\dagger - \sin\alpha\, c_H^\dagger. \tag{4.7}$$

Inserting this in equation 4.5 results in

$$|\Psi\rangle = \frac{1}{\sqrt{2}}\left(c_H^\dagger\,(\cos\alpha[\text{particle}] - \sin\alpha[\text{wave}]) + c_V^\dagger\,(\cos\alpha[\text{wave}] + \sin\alpha[\text{particle}])\right)|vac\rangle\,. \tag{4.8}$$

After passing PBS_3, that is oriented on the $\{H, V\}$ axis, the corroborative photon is reflected ($c_H^\dagger$) or transmitted ($c_V^\dagger$). This projects the test photon into a state defined by the terms in the parentheses of equation 4.8. Therefore, the firing of detector D_H indicates that the test photon is in the state $\cos\alpha[\text{particle}] - \sin\alpha[\text{wave}]$, while the firing of D_V that it is in the state $\cos\alpha[\text{wave}] + \sin\alpha[\text{particle}]$. By choosing $0 < \alpha < 90°$, a continuous morphing between wave and particle behaviour can be obtained. The expected

intensity correlations, given by the coincidence count probability between detectors D_H (corroborative) and $[D_{b^*} \oplus D_{b'}]$ (test), where $\oplus$ denotes an exclusive OR (XOR) gate, are [65].

$$I_{H,b}(\theta, \alpha) = \cos^2 \frac{\theta}{2} \sin^2 \alpha + \frac{1}{2} \cos^2 \alpha. \tag{4.9}$$

Note that the correlations between detectors D_V and $[D_{a^*} \oplus D_{a'}]$ follow the same function. On the contrary, the complementary intensity correlations, *i.e.* between detectors D_V and $[D_{b^*} \oplus D_{b'}]$ or between D_H and $[D_{a^*} \oplus D_{a'}]$, are given by $1 - I_{H,b}(\theta, \alpha)$. The use of XOR gates permits counting the photons from both outputs of each quantum eraser (PBS_1 or PBS_2), and reaching an average coincidence rate of 70/s for each of them. In addition, such XOR gates help to improve the signal to noise ratio by rejecting events in which both detectors click simultaneously, *e.g.* when obtaining a dark count at one detector and a single photon on the other. Note that equation 4.9 does not depend on the relative detection times of the two photons. In the experiment reported here, the detection of the corroborative photon is delayed until after the detection of the test photon. This is ensured by inserting an extra 5 m length of optical fiber in the path of the corroborative photon (c). In this case, for all the four intensity correlation functions mentioned above, the configuration of the interferometer remains undetermined even after the test photon has been detected. In other words, there is no information available yet from the corroborative photon that could influence the behaviour of the test photon. Furthermore, a space-time analysis shows that no classical communication can be established between the photon detection events, as they are space-like separated (see Figure 4.4). While the test photon travels in 50 m of optical fibre and is measured at a physical distance of 3 m away from the place where the paired photons are separated, the corroborative photon travels in 55 m of optical fibre and is measured in another laboratory, located 20 m away from the test photon apparatus. Thus the photons are measured with a timing difference of ~ 20 ns at positions that are space-time separated by 60 ns. This means that the measurement outcomes on the test and corroborative photon cannot influence each other in a classical manner.

We now measure the correlations between detectors D_H and $[D_{b^*} \oplus D_{b'}]$ via counting coincidence events on the corresponding single photon detectors (InGaAs avalanche photodiodes[7]). As shown in Figure 4.5(a), the experimentally measured results are in near perfect agreement with the theoretical expectations of equation 4.9. For the angle $\alpha = 0°$, $I_{H,b}(\theta, 0)$ is independent of the phase θ as predicted for particle-like behaviour. Setting $\alpha = 90°$ results in sinusoidal intensity oscillations as a function of θ, which corresponds to wave-like behaviour. For $0° < \alpha < 90°$, a continuous transition from wave to particle behaviour is observed, expressed by the continually reducing fringe visibility. As outlined in references [271, 284, 285, 289, 287, 272, 273] and at the end of section 4.1, a generalization of Bohr's wave-particle-duality notion implies the fringe visibility V and

[7] Id Quantique id220 operated at 20% detection efficiency and 10 μs dead time.

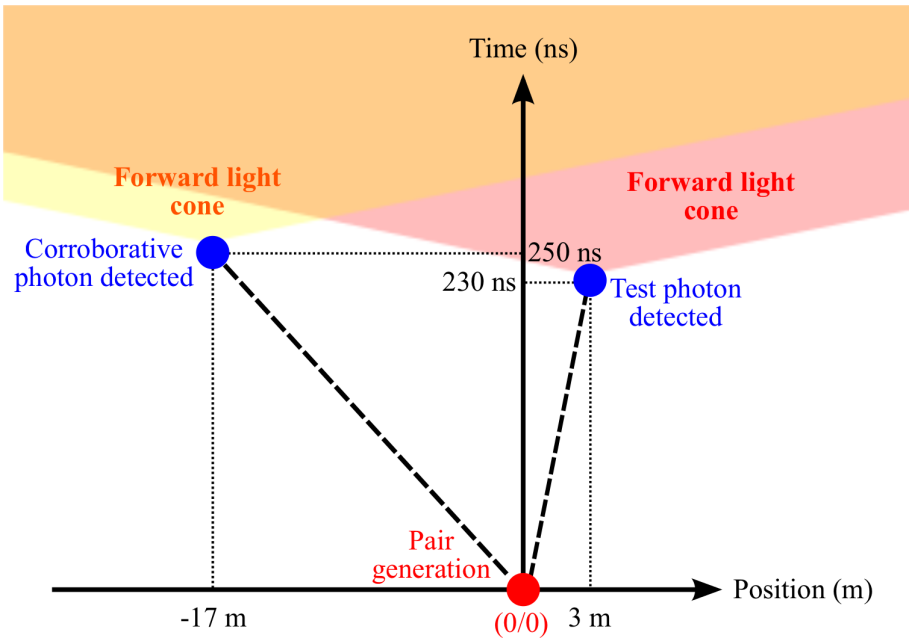

Figure 4.4.: Space-time diagram of the experiment. The paired photons are said to be generated and separated at the origin (0/0). The test photon travels about 50 m in an optical fiber before entering the QBS apparatus, that is located in the same laboratory as the entangled photon pair source. The corroborative photon is sent through a 55 m fiber to another laboratory. The corroborative and test photon apparatus are physically separated by 20 m. Note that the corroborative photon is measured 20 ns after the test photon was detected, thus determining the Mach-Zehnder interferometer configuration in a delayed fashion. The forward light cones from both photon detection events do not overlap with the detection event of the respective other photon, demonstrating that space-like separation is achieved. In other words, no causal connection between these events can be established. Correlations cannot be explained by means of classical physics.

the path distinguishability D to be limited by the following inequality

$$V^2 + D^2 \leq 1. \tag{4.10}$$

In subsection 4.3.4, the experimental measure of these two quantities, V and D, is outlined. Figure 4.5(b) shows the obtained results for V^2, D^2 and $V^2 + D^2$ as a function of the angle α. Equation 4.10 is confirmed for all angles of α, underlining the validity of Bohr's complementarity notion.

To prove the existence of a coherent quantum superposition of wave and particle behaviour of the test photon created by the detection of the corroborative photon, the

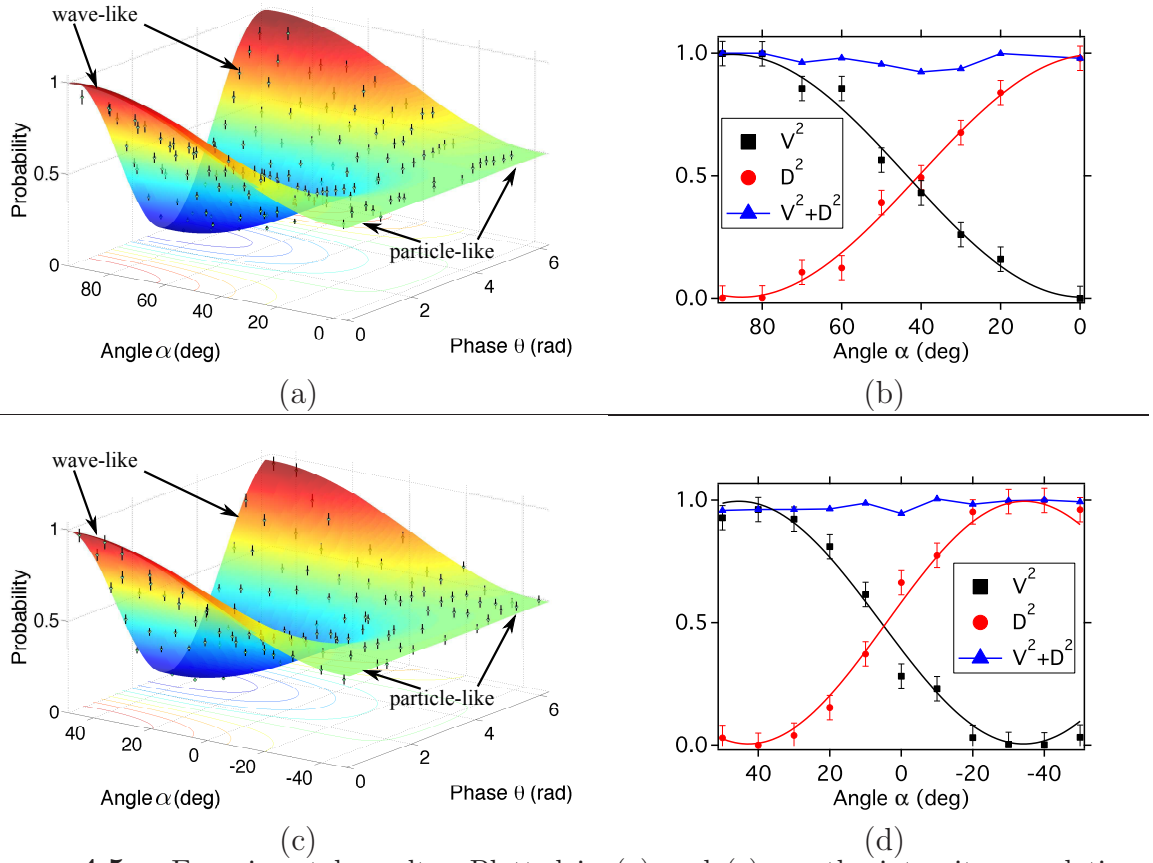

Figure 4.5.: Experimental results. Plotted in (a) and (c) are the intensity correlations, $I_{H,b}(\theta, \alpha)$ as defined by Eq. 4, expressed as the probability of a coincidence event between detectors D_H and $(D_{b^*} \oplus D_{b'})$ as a function of α and θ. Dots and associated vertical lines represent experimental data points and their corresponding standard deviations. Wave-particle morphing behaviour is observed for the natural $\{H, V\}$ basis (a), as well as for the complementary $\{D, A\}$ basis (c). The coloured surfaces in these graphs are fits to the experimental data using equation 4.9. The result obtained for the $\{D, A\}$ basis is essential since it represents the signature of the entangled state, proving the correct implementation of the desired QBS. Figures (b) and (d) represent plots of the fringe visibility V and path distinguishability D as a function of α. In all cases it is $V^2 + D^2 \leq 1$, which underlines the validity of the generalization of Bohr's wave-particle-duality notion for wave-particle superpositions. The solid lines for the curves V^2 and D^2 represent sinusoidal fits. For the curve $V^2 + D^2$, the solid line represents a connection between the data points and gives a guide to the eye. Experimentally, we obtain average coincidence rates of 350 events/5 s. The noise contribution, on the order of 3 events/5 s, has not been subtracted. The same experimental results would be obtained when inverting the timing order of the measurements of the test and corroborative photons, similar as in reference [41].

presence of entanglement needs to be verified [8, 16, 17, 64]. Several recent realizations ignored this and therefore the presence of a QBS has not been proven unambiguously [268, 290, 291]. In our realization, entanglement is proven by performing the same experiment as before, but using the complementary analysis basis, namely the diagonal basis $\{D, A\}$. Now, the initial quantum state is rotated by 45°, *i.e.* $\frac{1}{\sqrt{2}}\left(c_H^\dagger t_H^\dagger + c_V^\dagger t_V^\dagger\right)|vac\rangle \rightarrow \frac{1}{\sqrt{2}}\left(c_D^\dagger t_D^\dagger + c_A^\dagger t_A^\dagger\right)|vac\rangle$, where the subscripts D and A symbolize diagonally and anti-diagonally polarized photon polarizations, respectively. In this configuration, even if the polarization of the test photons would be known, every single photon is unpredictably subjected to a closed or open Mach-Zehnder configuration by the PDBS. In this case, as opposed to the experiment in the $\{H, V\}$ basis, if a statistical mixture was analysed instead of an entangled state, no correlations should be observed when measuring $I_{H,b}(\theta, \alpha)$. However, the strong correlations shown in Figure 4.5(c) exclude a statistical mixture and are in good agreement with the theoretical expectation of equation 4.9. This underlines that wave and particle behaviour coexist simultaneously for the entire range $0° < \alpha < 90°$ in the $\{H, V\}$ basis, and for $-45° < \alpha < 45°$ in the $\{D, A\}$ basis. Figure 4.5(d) shows the measurements for V^2, D^2 and $V^2 + D^2$ as a function of α and confirms the upper limits imposed by equation 4.10. The quality of the entangled state is measured via the Bell parameter S, which is deduced from the phase oscillation visibilities at $\alpha = 90°$ in the $\{H, V\}$ basis, and $\alpha = 45°$ in the $\{D, A\}$ basis. We obtain $S = 2.77 \pm 0.07$, which is very close to the optimal value of $2\sqrt{2}$ attained with maximally entangled states, and 11 standard deviations above the classical/quantum boundary $S = 2$ [8, 16, 17, 64].

We note that the 'detection loophole' remains open in our experiment, since some of the initial entangled photons are lost during their propagation in the fiber or bulk channels, or are not detected by the single photon detectors that show non-unit quantum detection efficiencies [292, 293]. One has therefore to make the reasonable assumption that undetected photons behave identically to the detected ones [167, 294].

In the following, some of the experimental details are outlined.

4.3. Considerations on the experimental apparatus

In this section, the experimental details for the quantum delayed choice experiment are summarized. They comprise the realization of the employed polarization dependent beam-splitter, considerations on the Mach-Zehnder interferometer and the procedure towards measuring the fringe visibilities and path distinguishabilities required for testing equation 4.10.

4.3.1. Realization of a polarization dependent beam-splitter

The above introduced polarization dependent beam-splitter (PDBS) is actually not a single device. In the above text we have used this description for the ease of reading.

In reality, the behaviour of the PDBS is mimicked using a set of standard bulk optical components towards achieving high quality experimental results. The schematic and explanation is shown in Figure 4.6 and the corresponding caption.

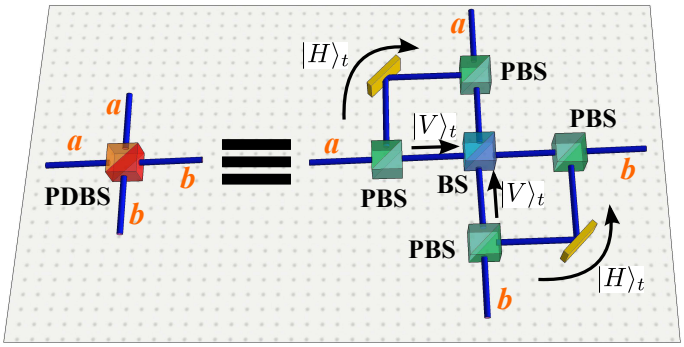

Figure 4.6.: In this realization, the polarization dependent beam-splitters (PDBS), yielding the desired 100/0 reflection/transmission ratio for $|H\rangle$ and 50/50 reflection/-transmission ratio for $|V\rangle$ was built using the bulk configuration shown. We used four polarizing beam-splitters (PBS) oriented in the $\{H, V\}$ basis. While $|H\rangle$ photons are reflected on each PBS and bypass the beam-splitter (BS), $|V\rangle$ photons are transmitted to an ordinary 50/50 BS. Commercially available PDBS devices show seriously reduced performance and would have significantly reduced the measured visibilities.

4.3.2. Phase tuning

In order to observe interference, the phase difference θ accumulated in the Mach-Zehnder interferometer needs to be tuned. Many realization rely therefore on piezoelectric systems moving or tilting one mirror (or beam-splitter), or on electro-optic phase modulators. In this realization, a cheap and simple method is used for phase tuning, namely a glass plate in one of the interferometer arms, that can be turned using a stepper motor with a resolution of $< 0.1°$. When the glass plate is rotated, its effective thickness is changed, thus the optical path length of the corresponding interferometer arm is modified, which corresponds to a tuning of the phase θ. As a glass plate, we use a standard microscopy glass slide having a thickness of 1 mm. Turning the glass plate by an angle of about 2-3° leads to a phase shift of $2\,\pi$, which is enough for observing one interference fringe. Note that for such small rotation angles, the absence of a glass plate anti-reflection coating is unimportant. Also, for such small angles, the rotation angle dependent transmission/reflection and beam displacement are negligible and interference visibilities are essentially not degraded.

4.3.3. Phase stability

Similarly to the experiments carried out in section 2.5, the phase of the interferometer needs to be stable during the measurement for obtaining good experimental results. However, in this configuration the interferometer is made of bulk optical components, such that a much better passive phase stability is achieved compared to a fibre-optical interferometer. To improve the stability, the interferometer is enclosed in a plexiglass box that avoids temperature fluctuations due to air flow. The phase stability was then measured using a diagonally polarized continuous wave laser and monitoring the optical output power after the quantum erasers PBS_1 and PBS_2. A phase drift of $2\,\pi$ was found every ~ 15 minutes, which means that the passive interferometer stability is not enough for performing all the measures shown in Figure 4.5. But the phase drifts are slow enough for employing a user controlled phase stabilization system.

The idea is the following: the uncorrelated single photon detection rate R_b on detectors $\mathrm{D}_{b^*} \oplus \mathrm{D}_{b'}$ is phase dependent (confirm equation 4.9, where integration over all angles α needs to be performed for obtaining the uncorrelated intensities) and follows

$$R_b = \frac{2\,C_{\max}}{3} \cdot \left(\cos^2\frac{\theta}{2} + \frac{1}{2}\right). \tag{4.11}$$

Here, $C_{\max}$ is the maximum count rate (observed at $\theta = 0$). Via continuously measuring R_b, information about θ is available. After having acquired 5 s of data, the rotation angle of the glass plate was then adjusted in order to keep R_b, and consequently θ, constant at the desired value.

4.3.4. Fringe visibility and path distinguishability

As stated before, the simultaneously available path distinguishability D and fringe visibility V of the above explained experiment are limited. Theoretically, this has been considered in the following references [271, 284, 285]. In reference [272], an equation has been derived, connecting the interference fringe visibility V and the output beam-splitter reflectivity R, for an experiment similar to ours.

$$V = 2\,\sqrt{R\,(1-R)}. \tag{4.12}$$

The same analysis has been performed for the path distinguishability D, which was found to be:

$$D = |1 - 2\,R|\,. \tag{4.13}$$

Now, how do we use these equations for our particular quantum delayed choice experiment? We need to give the quantity R a meaning. In our experiment, R is the probability that a test photon is reflected at the PDBS, given the fact that detector D_H fired. This probability depends only on the rotation angle α, introduced by the EOM

in the corroborative photon apparatus. Similarly to reference [272], we have:

$$R = \cos^2\left(\frac{\pi\,\alpha}{360}\right). \tag{4.14}$$

Here, α is the rotation angle in degrees. This equation holds only for experiments performed in the $\{H, V\}$ basis (see Figure 4.5(a,b)). In the diagonal basis $\{D, A\}$ (see Figure 4.5(c,d)), we need to replace

$$\alpha \rightarrow \alpha + 45^\circ. \tag{4.15}$$

Inserting equation 4.14 in equation 4.12, respectively equation 4.13 delivers then (in the $\{H, V\}$ basis)

$$V^2 = \sin^2\left(\frac{2\,\pi\,\alpha}{360}\right), \qquad D^2 = \cos^2\left(\frac{2\,\pi\,\alpha}{360}\right), \tag{4.16}$$

$$\longrightarrow V^2 + D^2 = 1. \tag{4.17}$$

We have obtained here the ideal result of $V^2 + D^2 = 1$. A more general analysis is performed in references [271, 284, 285] and it is found that $V^2 + D^2 \leq 1$.

How to measure V and D?

The interference fringe visibility V shown in Figure 4.5(b,d) is measured as follows. The angle α is fixed and the maximum ($p_{\max}$) and minimum ($p_{\min}$) fitted coincidence probabilities are determined as a function of θ. We then compute $V = (p_{\max} - p_{\min})/(p_{\max} + p_{\min})$.

D is measured for fixed angles α using the following procedure. First, the interferometer path a is blocked and the coincidence probabilities p_{aa} between detectors D_H and $(\mathrm{D}_{a'} \oplus \mathrm{D}_{a^*})$ and p_{ab} between detectors D_H and $(\mathrm{D}_{b'} \oplus \mathrm{D}_{b^*})$ are recorded. Here, the first subscript denotes the blocked interferometer arm and the second which detector combination is used. We then compute $D_a = (|p_{aa} - p_{ab}|)/(p_{aa} + p_{ab})$. Note that complete path distinguishability leads to $p_{aa} = 0$ and $p_{ab} = 1$, resulting in $D_a = 1$. The same measurement is repeated when interferometer path b is blocked, giving the probabilities p_{ba}, p_{bb}, and consequently $D_b = (|p_{ba} - p_{bb}|)/(p_{ba} + p_{bb})$. We finally calculate the average $D = (D_a + D_b)/2$, which drops to zero for wave-like behaviour and is unity for particle-like behaviour.

4.4. Conclusion and discussion

We have carried out a quantum delayed choice experiment, enabled by polarization entangled photons and the associated property of non-locality. We used a Mach-Zehnder interferometer where the output beam-splitter has been replaced by its quantum analogue, *i.e.* a beam-splitter in a coherent superposition of being present and absent. In this configuration, we observed that the single photons under test can indeed behave as waves and particles in the same experiment. This indicates that a too naive view, stating that photons behave either as waves or particles, depending on the measurement apparatus, has to be refuted. We experimentally excluded interpretations based on local hidden variables and/or information exchange between the photon and the quantum beam-splitter. This was done by determining the state of the quantum beam-splitter only after the detection of the corroborative photon. We have, therefore, demonstrated delayed interference between wave and particle behaviour, which underlines the subtleness of Bohr's complementarity notion. Although a classical interpretation of this experiment would cause many contradictions, quantum physics always predicts correctly the measurement outcomes. The way how quantum physics avoids contradictions is by not making any statements about what happens in the interferometer. We are only left with timing-order independent[8] measurement outcome probabilities. Although it requires enormous changes in our ways of thinking, probably we have to accept the fact that quantum physics allows us predicting measurement outcomes with an unprecedented precision, however, at the price of a lack of knowledge of what happens inside the measurement apparatus. If we still want to give a model of what happens to the photons inside a Mach-Zehnder interferometer, probably the most adequate (yet hand-waving argument) picture was given by Wheeler, who often stated that photons can behave as great smoky dragons, covering all interferometer paths simultaneously, and suddenly bend forward to bite the detector [10].

The work of this chapter is found summarized in reference [43]. We note that, parallel to this work, Peruzzo *et al.* realized another version of a quantum delayed choice experiment based on entangled photons [216].

[8] Note that none of the equations in this chapter shows a time dependence.

Chapter 5.

General summary

Since the beginning of the 1980s, the field of quantum information experiences continuous and tremendous advances. In 1981, Alain Aspect and collaborators demonstrated unambiguously the existence of entanglement between two photons. In 1984, Charles H. Bennett and Gilles Brassard introduced the first quantum communication protocol based on single photons. Compared to all other classical protocols, this one offers to implement, at least in principle, absolute secure communication. 25 years after this proposal, this protocol it is already commercialized and enables secure communication over distances of about 100 km. In order to increase the communication distance, and bit rate, many new theoretical solutions have been proposed, *e.g.* the Ekert protocol, teleportation, and entanglement swapping. All of them have already been experimentally realized in research laboratories all over the world, and it seems only to be a question of time until they reach a commercial level.

In the late 1980s, the creation of photonic entanglement experienced a paradigm shift which led to enormous advances. The first bulk crystal entanglement sources were introduced, offering an unprecedented ease of use compared to previous experiments. Ever since then, such crystal sources have become more and more efficient, practical, and reliable. Such technological advances allow us to study and understand physics in its very deepest details, for example in this thesis, we revisited Bohr's complementarity principle in a completely new way by employing a beam-splitter in a superposition of being present and absent. Thanks to the improved entanglement sources, we find now a variety of light-matter interaction experiments, operating at the single photon level. In addition, new high efficiency sources allow distributing entanglement over longer and longer distances at increased rates.

The work in this thesis takes part in this race towards demonstrating more efficient, reliable and versatile photonic entanglement sources, for various applications.

To this end, three different photonic entanglement sources have been developed, all of them operating at favourable telecom wavelengths, where a large variety of high-performance guided-wave optics components is commercially available.
The first source generates polarization entanglement using a type-II PPLN/W crystal and we used two astute fully guided-wave techniques for solving two of the main problems of such sources, namely birefringence compensation, and deterministic photon pair

separation into standard telecommunication channels. Thanks to the careful design of this source, it can be directly applied to quantum key distribution applications using the Ekert protocol.
The second source generates a new time-bin entangled bi-photon state, which is enabled by a fully guided-wave approach of transcribing polarization to energy-time entanglement. This source solves (partially) one of the problems of energy-time entanglement distribution protocols where only 50% of the detected photon pairs are useful. Our approach improves this figure of merit by an additional 25%.
The third entanglement source demonstrates several advances at a time. It is very efficient and reliable thanks to the extensive use of telecom guided-wave optics. In addition, it allows, at the will of the user, generating entanglement over a five orders of magnitude spectral bandwidth range and it is capable of generating any desired pure bi-photon state. Such a versatility and efficiency makes this source an ideal candidate for various applications, such as quantum key distribution in current telecom networks, quantum relay, teleportation, and entanglement swapping protocols.
With these experiments, we have underlined the suitability of telecom guided-wave technologies for generation and manipulation of photonic entanglement.

Current quantum communication protocols for ultra-long distances require the use of quantum memories at several stations between the communication parties. To enable such communication protocols in which photons are used to distribute, and quantum memories to store entanglement, light-matter interaction at the single photon level has to be studied. To do so, the different qubit supports need to be adapted, *i.e.* their operation wavelengths need to be matched in a coherent manner. Unfortunately, most of the current quantum memory devices operate at wavelengths below 1000 nm, at which losses in optical fibres are too high for long distance distribution. To overcome this problem, we outline a coherent wavelength conversion interface that is made for polarization entangled photons. This allows benefiting from both telecom photons for long distance distribution of photonic entanglement, and high efficiency, possibly heralded, quantum memories operating below 1000 nm.

Although at present it seems exaggerated to think about a world-wide quantum key distribution network, since many technological steps have still to be taken, we conclude with a positive feeling. In the last two decades, engineering of photonic entanglement has experienced tremendous advances and quantum memory devices were not even considered in theory 20 years ago. It has been shown that quantum networks can be improved from various sides by improving technology, but also by developing new communication protocols. Our current classical high-speed communication networks have been brought to near perfection over many decades, requiring many important milestone experiments and paradigm shifts in the time from the first telegraph cable to current fibre optical networks. First quantum communication systems became commercially available already 25 years after the first proposal! But we must accept the fact that quantum information science is still in a very early stage of development, comparable to the first telegraph systems in the middle of the 19^{th} century. However, if our developments go on at this

speed, large scale quantum networks are very likely to be realized within the century of the photon.

Appendix

A. Spontaneous parametric down conversion in PPLN/W crystals

Generating photon pairs via spontaneous parametric down conversion (SPDC) in lithium niobate crystals is at the heart of the work in this thesis. In this section this three photon interaction is described in detail. The waveguide structure and the periodic poling of the susceptibility constant are also taken into account.

A.1. Light field propagation in a non-linear crystal

We use the same notation as in the chapters before, a pump field (p) generates signal (s) and idler (i) fields inside a suitable crystal. In a dielectric material, the pump field, oscillating at an angular frequency of ω_p, deforms the charge distribution inside the crystal. This deformation is characterized by the so-called polarization density $\vec{P}$. For weak electric fields $\vec{E}$ of the pump field, the polarization density is a linear function of $\vec{E}$:

$$\vec{P} = \epsilon_0 \chi_e \vec{E}. \tag{A.1}$$

Here, ϵ_0 is the electric permittivity of free space and χ_e the susceptibility, a material constant. In other words, equation A.1 dictates that the charge distribution inside the crystal oscillates at the same frequency as the electric field of the pump. But $\vec{P}$ is not always a linear function of $\vec{E}$. For strong pump fields and special crystal symmetries (such as non-centrosymmetric, or in other words crystals without an inversion center), the polarization density depends also on higher order terms of $\vec{E}$ and is

$$\vec{P}(\vec{E}) = \epsilon_0 \overleftrightarrow{\chi}^{(1)} \vec{E} + \epsilon_0 \overleftrightarrow{\chi}^{(2)} \vec{E}\vec{E} + \epsilon_0 \overleftrightarrow{\chi}^{(3)} \vec{E}\vec{E}\vec{E} + \ldots = \epsilon_0 \overleftrightarrow{\chi}^{(1)} \vec{E} + \vec{P}^{NL}(\vec{E}). \tag{A.2}$$

Here, $\overleftrightarrow{\chi}^{(n)}$ is the non-linear susceptibility tensor of the order n. This non-linear form of $\vec{P}(\vec{E})$ allows the charge distribution to oscillate not only at the frequency of the pump field, but also at linear combinations of this frequency [14, 295, 296, 297, 298].

The propagation of a light field is described by the Helmholtz equation

$$\vec{\nabla}^2 \vec{E} - \vec{\nabla}(\vec{\nabla} \cdot \vec{E}) - \frac{1}{c^2} \frac{\partial^2 \vec{E}}{\partial t^2} = \mu_0 \frac{\partial^2 \vec{P}(\vec{E})}{\partial t^2}. \tag{A.3}$$

For obtaining this equation we assume that the crystal is charge neutral ($\rho = 0$) and there is no displacement current ($\vec{j} = 0$). Inserting equation A.2 delivers

$$\vec{\nabla}^2\vec{E} - \vec{\nabla}(\vec{\nabla}\cdot\vec{E}) - \frac{1+\overleftrightarrow{\chi}^{(1)}}{c^2}\cdot\frac{\partial^2\vec{E}}{\partial t^2} = \mu_0\frac{\partial^2\vec{P}^{NL}}{\partial t^2}. \tag{A.4}$$

In this case, we define

$$1+\overleftrightarrow{\chi}^{(1)} = \overleftrightarrow{\epsilon_r} = \begin{pmatrix} n_x^2 & 0 & 0 \\ 0 & n_y^2 & 0 \\ 0 & 0 & n_z^2 \end{pmatrix}, \tag{A.5}$$

where n_x, n_y and n_z the refractive index of the material along the three axes x, y and z, respectively.

A.2. Waveguide configuration

In this thesis, the crystals used for photon pair generation exhibit a light guiding structure (waveguide) along the z-axis. Concerning the type-0 PPLN/W crystals, that are made using a proton exchange technique [220, 299, 221], only the electric field component along the x direction (vertically polarized) is guided (see Figure A.1). This reduces the electric field vector to $\vec{E} = (E_x, 0, E_z)$ and simplifies equation A.4:

$$\vec{\nabla}^2 E_x - \vec{\nabla}(\vec{\nabla}\cdot E_x) - \frac{\epsilon_r}{c^2}\frac{\partial^2 E_x}{\partial t^2} = \mu_0\frac{\partial^2 P_x^{NL}}{\partial t^2}, \tag{A.6}$$

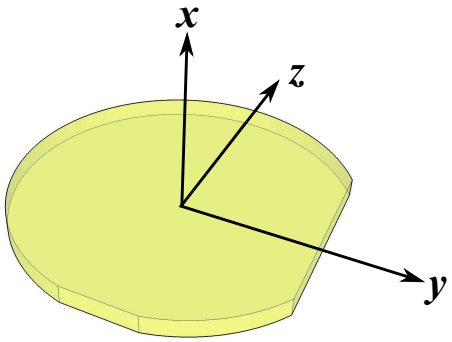

Figure A.1.: Typical shape of a commercial Z-cut lithium niobate waver. Note that the crystalline Z-axis corresponds to the optical x-axis shown in the graph. All the axis notations shown here correspond to the optical axes, where z denotes the direction of the waveguide structure. The waveguides fabricated in our laboratory are made using the soft proton exchange technique and guide only light fields having the electric field component along the x-axis (vertically polarized light).

where

$$P_x^{NL}(\omega_p) = \epsilon_0 \chi_{xxx} E_x(\omega_i) E_x(\omega_s). \tag{A.7}$$

Here, ω_p, ω_s and ω_i represent the angular frequencies of the pump, signal and idler electric fields, respectively. χ_{xxx} is the susceptibility relating the three light fields along the x-axis[1].

Equation A.6 is generally solved using the following ansatz:

$$E_x(\omega_j) = \sum_m A^{m,j}(z) \varepsilon_x^{m,j}(x,y) e^{i(\omega_j t - \beta^{m,j} z)}, \tag{A.8}$$

where $A^{m,j}(z)$ is the amplitude of each mode of the electric field defined by $\varepsilon_x^{m,j}(x,y)$ and $\beta^{m,j} = \frac{n_\mathrm{eff}^m \omega_j}{c}$ is the propagation constant. n_eff^m is the effective refractive index of the mth mode.

Taking into account the law of conservation of energy between the three fields, expressed as

$$\omega_\mathrm{p} = \omega_\mathrm{s} + \omega_\mathrm{i}, \tag{A.9}$$

and considering only the fundamental light propagation mode ($m = 0$)[2] and making the reasonable assumption that the mode shape develops slowly along the propagation axis, leads to the following equation system

$$\begin{cases} \dfrac{dA^\mathrm{p}(z)}{dz} &= -\alpha^\mathrm{p} A^\mathrm{p}(z) - i\chi_{33}\omega^\mathrm{p} I^\mathrm{p} A^\mathrm{s}(z) A^\mathrm{i}(z) e^{i\delta\beta z} \\ \dfrac{dA^\mathrm{s}(z)}{dz} &= -\alpha^\mathrm{s} A^\mathrm{s}(z) - i\chi_{33}\omega^\mathrm{s} I^\mathrm{s} A^\mathrm{p}(z) (A^\mathrm{i})^*(z) e^{i\delta\beta z} \\ \dfrac{dA^\mathrm{i}(z)}{dz} &= -\alpha^\mathrm{i} A^\mathrm{i}(z) - i\chi_{33}\omega^\mathrm{i} I^\mathrm{i} A^\mathrm{p}(z) (A^\mathrm{s})^*(z) e^{i\delta\beta z}, \end{cases} \tag{A.10}$$

relating the pump, signal and idler field amplitudes. Here it is $\delta\beta = \beta^\mathrm{p} - \beta^\mathrm{s} - \beta^\mathrm{i}$ and the losses are given by $-\alpha^j A^j(z)$. We have also inserted χ_{33}, the susceptibility constant used for the type-0 process in PPLN crystals. This constant is related to the non-linear coefficient d_{33} via the relation $\chi_{33} = 2\, d_{33} = 2 \cdot 30\,\mathrm{pm/V}$. For the type-II process, the non-linear coefficient $d_{24} \approx 10\,\mathrm{pm/V}$ is used.

A.3. Quasi phase matching - periodic poling

The system of equations A.10 comprises phase terms $e^{i\delta\beta z}$ which are in general not zero. Thus a dephasing between the three light fields is introduced leading to destructive interference after a characteristic distance of $L_\mathrm{ch} = \frac{\pi}{\delta\beta}$. At a distance of $2\, L_\mathrm{ch}$ the intensities of signal and idler field are zero. There are essentially two ways for achieving

[1] Note that the highest reported value for χ_{xxx} is obtained for lithium niobate, and thus the strongest coupling between the three light fields is expected.

[2] This assumption is justified as the waveguide widths are chosen appropriately small to guide only the fundamental mode.

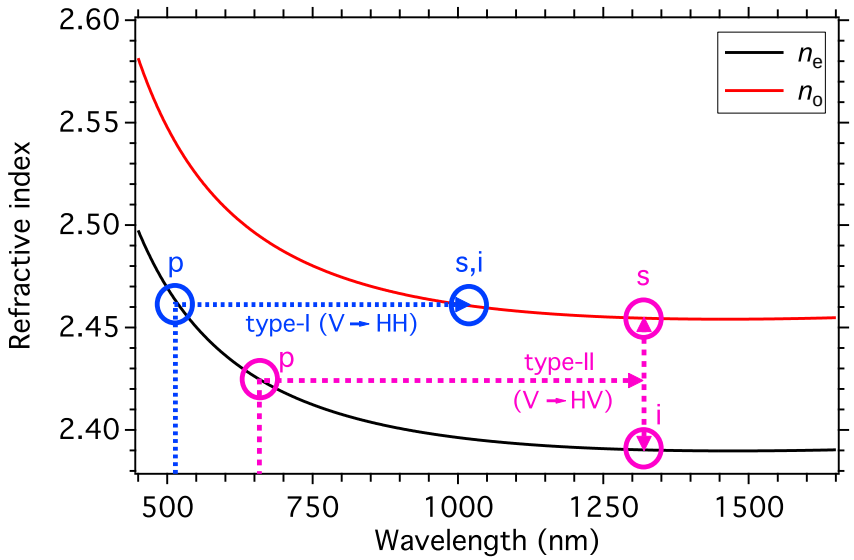

Figure A.2.: Refractive index of lithium niobate for ordinary and extraordinary polarizations of light at a crystal temperature of 373 K. Two possibilities are encountered towards obtaining $\delta\beta = 0$. Namely having an extraordinary polarized pump field at ~ 510 nm generating ordinarily polarized signal and idler fields at ~ 1020 nm (type-I process). Another possibility is found when using an extraordinarily polarized pump at ~ 660 nm giving birth to cross polarized signal and idler fields at ~ 1320 nm.

$\delta\beta = 0$. One is to exploit the fact that each, β^{p}, β^{s} and β^{i} are wavelength and polarization dependent. As shown in Figure A.2, the different polarization modes $|H\rangle$ (ordinary) and $|V\rangle$ (extraordinary) show generally different refractive indices in lithium niobate crystals (see also Appendix D). In this graph it is shown that there are two possible combinations of achieving $\delta\beta = 0$. One is by having a vertically polarized pump at ~ 510 nm generating horizontally polarized photon pairs at ~ 1020 nm. For this particular configuration it is

$$n_{\mathrm{p}} = n_{\mathrm{s}} = n_{\mathrm{i}}, \tag{A.11}$$

which leads to

$$\beta^{\mathrm{p}} = 2\beta^{\mathrm{s}} = 2\beta^{\mathrm{i}} \qquad \rightarrow \qquad \delta\beta = 0. \tag{A.12}$$

This process is generally referred to as the type-I interaction, the efficiency of this process being related by the non-linear coefficient d_{31}.
Another possibility to reach $\delta\beta = 0$ is also shown in Figure A.2, namely the so-called type-II interaction. Here, a vertically polarized pump photon at ~ 660 nm generates a cross polarized photon pair at ~ 1320 nm. For this particular configuration we have

$$n_{\mathrm{p}} = (n_{\mathrm{s}} + n_{\mathrm{i}})/2, \tag{A.13}$$

which leads directly to

$$\beta^{\mathrm{p}} = \beta^{\mathrm{s}} + \beta^{\mathrm{i}} \qquad \rightarrow \qquad \delta\beta = 0. \tag{A.14}$$

This process is called the type-II interaction and it's efficiency is given by the coefficient d_{31}. This way of finding $\delta\beta = 0$ is called birefringent phase matching. Other phase matching combinations are possible by using a slightly different pump laser wavelength combined with non-degenerate photon pair generation.

Three problems are encountered at this stage. First of all, the wave guiding structure needs to support both polarization modes, which is not the case for waveguides based on proton exchange. However, waveguides based on titanium indiffusion processes are capable of guiding the corresponding polarization modes. Second, non-linear coefficients d_{24} and d_{31}, which are related to the efficiency of the corresponding processes, are relatively low. Much higher efficiencies would be obtained, when exploiting the coefficient d_{33}. But this relates three vertically polarized modes, for which no birefringent phase matching is possible. Third, this way of birefringent phase matching in a bulk crystal is essentially limited to the two pump laser wavelengths described above. A relatively small wavelength tunability might be achieved via temperature control. Higher tunability is achieved by allowing the pump, signal and idler fields to propagate in different directions in and out of the crystal, however this requires abandoning the waveguide strategy, which will strongly reduce the efficiency as a tight light field confinement cannot be obtained for long interaction distances.
In order to circumvent all these drawbacks of birefringent phase matching, we introduce now a new strategy, namely the so-called quasi phase matching strategy. In this case a periodic poling of the susceptibility constant in the non-linear material is employed [14].

We assume that the sign of the susceptibility is periodically inverted along the light propagation axis (z). The periodic inversion is abrupt as shown in Figure A.3. Thus the susceptibility can be written as

$$\chi(z) = \sum_{n \in \mathbb{N}_0} \chi_n e^{-inKz}, \tag{A.15}$$

where $\chi_n = \frac{\chi_{33}}{n\,\pi}$, $\chi_0 = \chi_{33}$ and $K = \frac{2\pi}{\Lambda}$. Here, Λ is the poling period. By imposing

$$n\,K = \delta\beta \tag{A.16}$$

we can convince ourselves that the phase terms in the equation system A.10 are vanishing. For example, when first order quasi phase matching is achieved ($n = 1$), this system of equations reads then

$$\begin{cases} \dfrac{dA^{\mathrm{p}}(z)}{dz} &= -\alpha^{\mathrm{p}} A^{\mathrm{p}}(z) - i\chi_{33}\omega^{\mathrm{p}} I^{\mathrm{p}} A^{\mathrm{s}}(z) A^{\mathrm{i}}(z)/\pi \\ \dfrac{dA^{\mathrm{s}}(z)}{dz} &= -\alpha^{\mathrm{s}} A^{\mathrm{s}}(z) - i\chi_{33}\omega^{\mathrm{s}} I^{\mathrm{s}} A^{\mathrm{p}}(z)(A^{\mathrm{i}})^*(z)/\pi \\ \dfrac{dA^{\mathrm{i}}(z)}{dz} &= -\alpha^{\mathrm{i}} A^{\mathrm{i}}(z) - i\chi_{33}\omega^{\mathrm{i}} I^{\mathrm{i}} A^{\mathrm{p}}(z)(A^{\mathrm{s}})^*(z)/\pi. \end{cases} \tag{A.17}$$

Obviously, achieving quasi phase matching results in lower efficiencies than it is the case for perfect phase matching (essentially for obtaining equations A.17, the phase term in equations A.10 has been replaced by a factor $1/\pi$). However, the efficiencies are still better than for the case where no phase matching is achieved. Note that the efficiency of the QPM procedure is inversely proportional to the order n as it is $\chi_n = \frac{\chi_{33}}{n\,\pi}$. Summarizing the necessary conditions for observation of SPDC (conservation of energy and momentum), it is

$$\begin{cases} \dfrac{1}{\lambda_\mathrm{p}} &= \dfrac{1}{\lambda_\mathrm{s}} + \dfrac{1}{\lambda_\mathrm{i}} \\ \dfrac{n^\mathrm{p}_\mathrm{eff}}{\lambda_\mathrm{p}} &= \dfrac{n^\mathrm{s}_\mathrm{eff}}{\lambda_\mathrm{s}} + \dfrac{n^\mathrm{i}_\mathrm{eff}}{\lambda_\mathrm{i}} + \dfrac{1}{\Lambda}. \end{cases} \tag{A.18}$$

In Figure A.4, the conservation of momentum is depicted for the QPM process. As the user is free to chose the poling period and the order of QPM, it is in principle possible to design any wavelength combination between the pump, signal and idler fields while keeping the waveguide structure, which imposes fixed propagation directions for the three fields. For practical applications, one is limited to wavelengths within the transparency window of the used crystal (lithium niobate: $350 - 5200\,\mathrm{nm}$). Note that also the geometrical properties of the waveguide structure have an influence on the

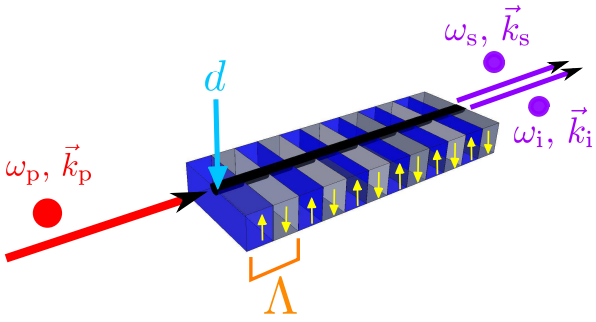

Figure A.3.: Lithium niobate waveguide structure with periodic poling of the susceptibility constant. The propagation direction of pump signal and idler fields are fixed by the waveguide structure having a width of d. High intensities for the signal and idler fields are obtained when applying a QPM strategy where the sign of the susceptibility is periodically inverted along the propagation axis. The poling period Λ is chosen to achieve the desired QPM.

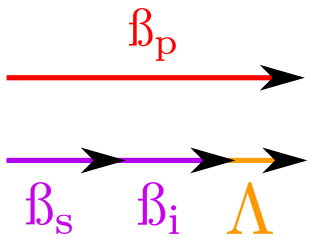

Figure A.4.: Schematic of the conservation of momentum for quasi phase matched SPDC. The propagation constants of pump, signal and idler fields are given by β_p, β_s and β_i, respectively. The poling period of the susceptibility is given by Λ. The equation $\beta_\mathrm{p} = \beta_\mathrm{s} + \beta_\mathrm{i} + \Lambda$ must be fulfilled to guarantee conservation of momentum. Note that the vector signs are removed here as the waveguide structure allows only one direction of propagation.

QPM via modification of n_{eff}. Furthermore the refractive index of most materials is temperature dependent, such that unavoidable fabrication errors can be conveniently compensated via temperature control [300].

The type-0 PPLN/Ws used in this thesis are generally meant to convert pump photons at 770-780 nm to signal and idler photons at 1540-1560 nm. The parameters of the home-made PPLN/Ws based on soft proton exchange have typical parameters of $d \approx 6\,\mu$m and $\Lambda \approx 16\,\mu$m corresponding to first order QPM ($n = 1$).

B. Single photon detectors and coincidence detection

Detecting single photons is essential for the work carried out in this thesis. The typical wavelength of the photons to be detected is about $1.55\,\mu$m which corresponds to a single photon energy of $\sim 1.3 \cdot 10^{-19}\,$J ($\sim 0.8\,$eV). This is relatively high compared to the thermal radiation background energy at room temperature of $\sim 0.026\,$eV. Thus, single photon detection at room temperature is possible when carefully designing the detection device. In the following, two single photon detection strategies are briefly outlined.

One is based on a charge avalanche effect that is triggered by the absorption of a single photon (avalanche photodiode - APD). Detection of a charge avalanche announces therefore the detection of a photon. The advantage of this device is that it is simple, reliable and cheap to implement in experimental setups.

The other strategy is based on a nano-wire that is cooled down until it becomes superconducting. Absorption of a single photon heats up the wire above the critical temperature, such that the resistance increases to a finite value. Measuring a non-zero resistance corresponds to the detection of a photon. This approach offers sometimes better figures of merit than detectors based on charge avalanches, however the resource overhead is seriously increased as liquid Helium is required for detector operation.

The reader finds a general summary on photon detectors for the visible and near-infrared regime of wavelengths in reference [154].

B.1. InGaAs avalanche photodiode

Typically, avalanche photodiodes are based on a so-called p-n junction in a semiconductor. InGaAs APDs are typically based on a separate absorption and multiplication (SAM) structure as outlined in Figure B.1. In the n-doped InGaAs region, photons are absorbed and create electron-hole pairs. Via a reverse biassed electric field, the generated holes are then injected into an InP zone where a charge avalanche is generated. Typically, InP is the preferred material as its higher bandgap of 1.27 eV offers a smaller dark current compared to InGaAs. In addition, the multiplication effect (avalanche) in InP is generally less noisy than in InGaAs structures. The charge avalanche is then measured using suitable electronics components. After detection of the signal, the avalanche

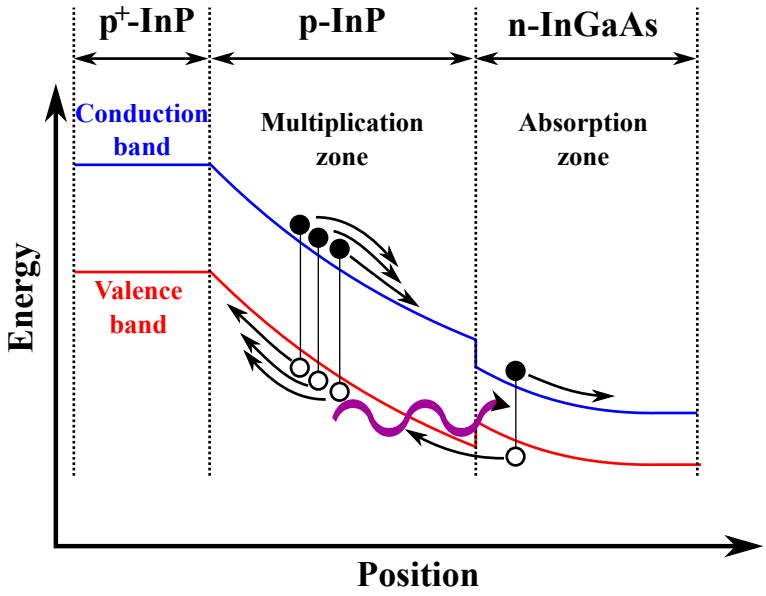

Figure B.1.: SAM structure for single photon detection via an avalanche effect. In the n-doped InGaAs region, a single photon is absorbed and generates an electron-hole pair. The hole is injected into the p-doped InP zone where a charge avalanche is generated and detected in the p^+-doped InP region. Due to non-identical band gaps of InGaAs and InP, the band gap shows a jump at the interface between the two materials. Improved APDs implement an InGaAsP gradding layer in-between the absorption and multiplication zones to avoid charge accumulation.

is actively stopped using suitable and fast electronics. This makes the detector ready for detecting the next incoming photon. The time required for stopping the avalanche is called *dead time* as the detector cannot detect photons during this interval. Note that the dark count rate of such detectors can be generally reduced by cooling the device to temperatures of $\sim 200\,\mathrm{K}$, which is conveniently achieved using Peltier elements, but this temperature reduction implies typically longer dead times in order to reduce the after-pulsing probability.

The figures of merit for the InGaAs devices used in this thesis are summarized in Table B.1.

Detector	Id Quantique id201	Id Quantique id220	Scontel TCOPRS-001
Efficiency at 1550 nm	$10-25\%$	$10-20\%$	$1-7\%$
Operation mode	gated	free running	free running
Typical dead time	$40-100\,\mu$s	$4-10\,\mu$s	10 ns
Maximum count rate	$10-25$ kHz	$100-250$ kHz	100 MHz
Timing jitter at maximum efficiency	116 ps (1^{st} gen.) 150 ps (2^{nd} gen.)	163 ps	< 50 ps
Dark count probability at maximum efficiency	$\sim 10^{-5}$/ns at $\geq 60\,\mu$s dead time	$\sim 10^{-6}$/ns $\geq 10\,\mu$s dead time	$\sim 10^{-8}$/ns
Wavelength range	$1300-1600$ nm	$1300-1600$ nm	visible - near-infrared

Table B.1.: Figures of merit for the used single photon detectors.

B.2. Superconducting nano-wire single photon detector

Superconducting nano-wire single photon detectors come with several advantages compared to InGaAs based APDs. They offer single photon sensitivity from the visible to the near-infrared regime of wavelengths. In addition, high count rates up to several MHz can be achieved, combined with low dark count probabilities ($\sim 10^{-8}$/ns) and low timing jitters on the order of a few tens of picoseconds. The working principle is sketched in Figure B.2. The detector is typically a 100 nm wide Niobium Nitride meander nano-wire covering an area of several μm^2. It is cooled down to the temperature of liquid Helium (≤ 4.2 K). At this temperature the nano-wire is superconducting, meaning that the electric resistance is zero. The nano-wire is operated just below its critical current at which it becomes resistive. When an incoming photon is absorbed by the wire, it creates a local hotspot. This perturbs the current distribution in the nano-wire such that its resistance is non-zero for a short time period which is measured by the observation of a fast voltage-pulse and consequently a photon has been detected. The figures of merit for the devices used in this thesis are summarized in Table B.1.

B.3. Coincidence detection

Analysing coincidence events is important for most of the experiments shown in this thesis. Due to propagation losses and non-unit detection efficiencies, revealing entanglement requires to restrict ourselves to cases in which each Alice and Bob detect simultaneously one out of the two entangled photons. Due to the character of spontaneous parametric down-conversion, the photons of a pair are always generated simultaneously in the PPLN/W. Thus a detected photon on Alice's side fixes the arrival time of Bob's photon. With the exception of one measurement[3], all the experiments

[3]The only exception is the measurement leading to the violation of the Bell's inequalities for the 25 MHz filter. Here, two free running superconducting detectors are used.

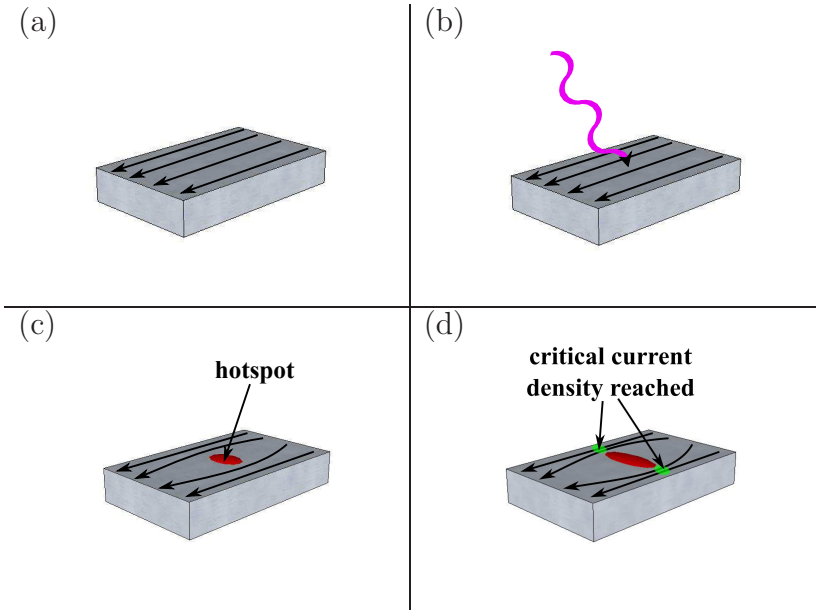

Figure B.2.: Working principle of a superconducting single photon detector. The temporal development is shown from (a) to (d). (a) a superconducting nano-wire of about 100 nm width is operated just below its critical current. The current is unperturbed as indicated by the straight lines. (b) A photon incident on the nano-wire is absorbed. (c) The absorbed photon generates an hotspot which disturbs the current distribution. (d) The current has been disturbed so much that the critical current density is reached. At this point, the nano-wire is not superconducting any more and a fast voltage-pulse is observed.

carried out in this thesis have in common that on Alice's side a free-running InGaAs APD is employed[4]. Every time this detector measures a photon, it triggers a start-event on a time-to-amplitude converter (TAC). The second photon, going to Bob is typically delayed by around 100 ns in a 20 m fibre line. Then this photon is either detected using
(a) another free running InGaAs detector (id220),
(b) or a gated InGaAs detector (id201).

In both cases, a detection event on Bob's detector triggers a stop-event on the TAC. Thus strong correlations between Alice's and Bob's detectors are expected at around 100 ns delay.

Note that the 100 ns delay is necessary as the TAC apparatus can only analyse positive delays. In addition the 100 ns delay is long enough for electronic gating of the id201 detector, *i.e.* a detection event on Alice's sides is used to open a detection window on

[4]Id Quantique id220.

Bob's detector.

In Figure B.3, a typical coincidence peak measurement is shown. At a delay of 100 ns, a strong temporal correlation is found, which indicates that coincidence events are recorded. The coincidence rate is then typically obtained by integrating the photon detection events in the coincidence peak region. The noise contributions can also be obtained from this graph, when considering the false events obtained in a region far away from the coincidence peak.

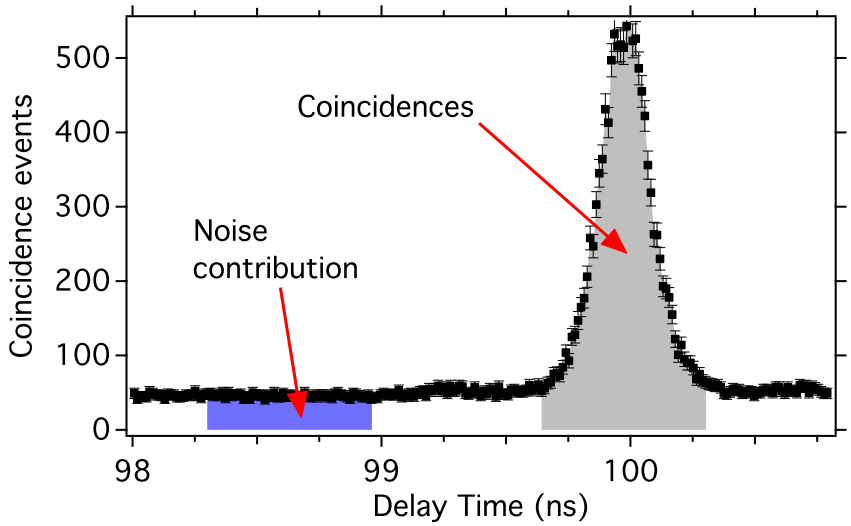

Figure B.3.: Typical coincidence histogram when Alice's detector is used to trigger a start-event and Bob's detectors to trigger a stop event on a time-to-amplitude converter. Coincidence events are observed at around 100 ns delay as Bob's photon is optically delayed in a 20 m fibre. The coincidence rate is obtained when integrating the events in the coincidence peak region (grey area), while the detector noise contribution is obtained when considering the events far away from the coincidence peak (blue area).

C. Photon pair filtering stages at a telecom wavelength

This section is outlined to show how three particularly interesting photon pair bandwidths are obtained for the photon pair source described in section 2.5. The initial spectral emission bandwidth is about 4 THz and the chosen filtering bandwidths are:

- 80 GHz, for telecommunication network compatibility using the commonly used 100 GHz ITU grid;
- 540 MHz, for continuous wave quantum relay and teleporation based entanglement distribution, as well as light matter interaction between entangled photons and solid state or hot atomic vapour quantum memories;
- 25 MHz, for light matter interaction between entangled photons and cold atom or ion quantum memories.

C.1. 80 GHz ↔ 0.64 nm filtering stage

Obtaining a photon pair spectral bandwidth of 80 GHz at a wavelength of 1560.48 nm is very conveniently achieved using standard telecommunication optics components. A standard dense wavelength division multiplexer (DWDM) shows the desired properties as shown in Figure 2.40. Typically, such DWDMs show rejection ratios of at least 30 dB (99.9%) in combination with a good transmission ($\sim$ 95%). In addition, they typically feature a (near) rectangular shaped transmission profile, which is advantageous for photon pair transmission. If Alice's photon is transmitted, Bob's photon is also with a chance of 95%. DWDMs are inherently wavelength stable, show low polarization dependent loss and can be considered as low-cost components[5].

C.2. Phase shifted fibre Bragg gratings

Spectral bandwidths down to $\sim$ 10 GHz are achieved using a fibre Bragg grating (FBG). As shown in Figure C.1, such FBGs are created when inscribing a refractive index modulation into an optical fibre. Appropriate choice on the modulation results in a narrowband reflection spectrum, which can be recovered using an optical circulator or a beam-splitter. Achieving even narrower filtering bandwidths at a telecom wavelength is established using phase shifted fibre Bragg gratings (PS-FBG), that can in principle be considered as the fibre equivalent of bulk optical cavities. As shown in Figure C.2, such PS-FBGs are fabricated by inserting a π phase-shift defect in the middle of an ordinary FBG, thus forming a two mirror system, just like it is used for bulk optical cavities. This results in a very narrow transmission feature within the normal reflection

[5]Typical pricing 100-200 US$.

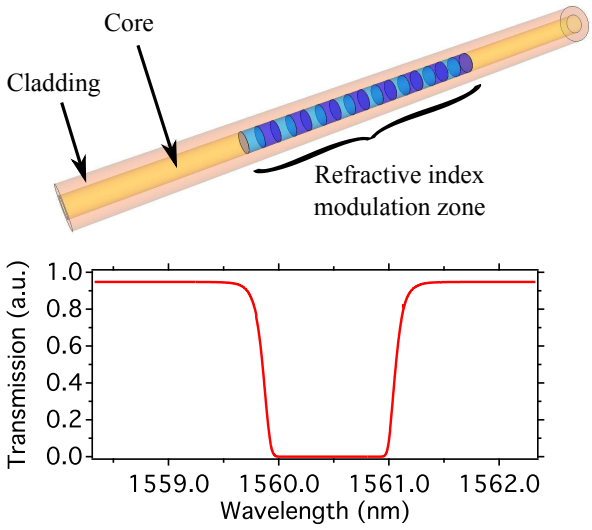

Figure C.1.: Schematics of a standard fibre Bragg grating (FBG). A refractive index modulation zone is inscribed into an optical fibre, resulting in a *hole* in the transmission spectrum. The non-transmitted wavelengths are reflected. This way, filters down to $\sim 10\,\mathrm{GHz}$ bandwidth can be achieved. Note that the reflected signal is the filtered one, so that an optical circulator or beam-splitter is required to recover the signal.

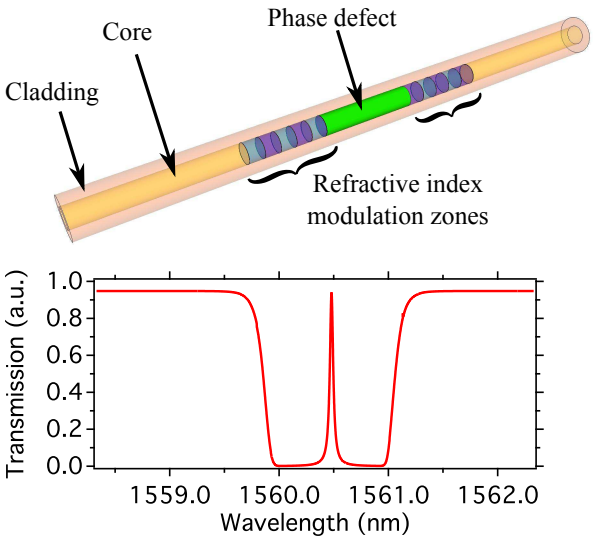

Figure C.2.: Schematics of a phase shifted FBG. A π phase defect in-between two FBGs results in a cavity like transmission behaviour. Within the reflection band of a normal FBG, a narrow transmission peak is obtained. Peak widths down to a few MHz can be achieved. The filter is used in transmission, which is advantageous for many applications. Note that an additional filter needs to be added to remove the transmission in the side-bands, *e.g.* a DWDM or FBG filter.

bandwidth of the FBG. In general, an additional DWDM or FBG filter is required to reject the transmitted side-bands of the PS-FBG.

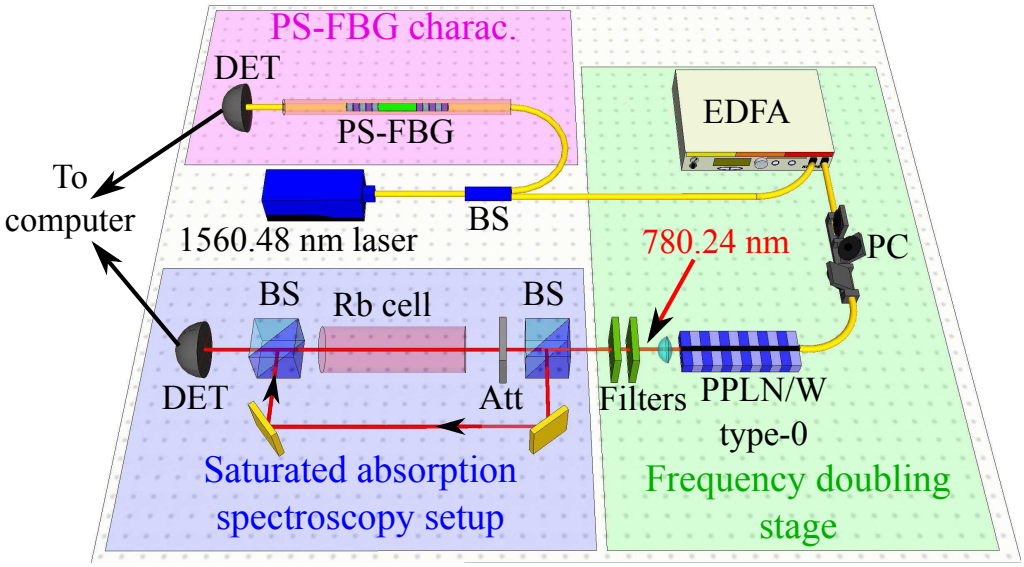

Figure C.3.: Experimental setup for characterizing the employed PS-FBG filters. A wavelength tunable telecom laser operating at around 1560.48 nm is split up at a beam-splitter (BS). Half of the laser light is sent through the PS-FBG and the transmission is measured using a fast photodiode. A wavelength reference is obtained using the following strategy: the other half of the laser light is amplified using an EDFA and frequency doubled in a PPLN/W. The obtained 780.24 nm light is sent to a standard rubidium saturated absorption spectroscopy setup, where the hyperfine structure is used for wavelength referencing.

C.3. 540 MHz ↔ 4.3 pm filtering stage

The employed 540 MHz PS-FBG is fabricated by AOS GmbH in Germany. Due to a relatively strong temperature dependence of the transmission wavelength (~ 1 GHz/K), the device is enclosed in a Peltier element controlled temperature stabilized box[6]. Figure C.3 shows the experimental setup towards characterizing the PS-FBG. A 1560.48 nm tunable telecom laser[7] is split up at a beam-splitter. Half of the light goes through a polarization controller and then to the PSFBG, while the other half is sent to an erbium doped fibre amplifier (EDFA). After the amplifier, the light is frequency doubled in a PPLN/W and the obtained 780.24 nm light is sent to a rubidium standard saturated absorption spectroscopy setup. The spectroscopy setup is employed for two crucial reasons. First, it allows a precise PS-FBG bandwidth characterization via comparison with the rubidium hyperfine structure lines. In addition, it permits precise temperature tuning of the filter towards placing the transmission window at exactly the photon pair degeneracy

[6] AOS GmbH UltraBox.
[7] Toptica DL pro design.

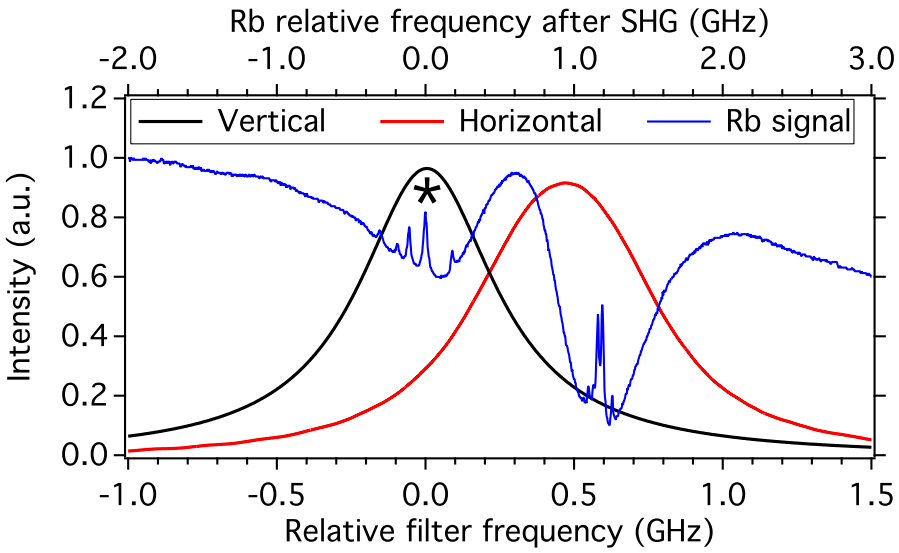

Figure C.4.: Characterization of the 540 MHz PS-FBG from AOS GmbH. Two polarization dependent transmission peaks are obtained. The peaks are separated by $\sim$ 480 MHz due to a residual fibre birefringence. The peak widths are 540 MHz and 580 MHz for vertically and horizontally polarized photons, respectively. Via temperature control, the transmission peak for vertically polarized light is positioned at two times the wavelength of the $F = 2 \rightarrow F' = 2 \times 3$ crossover transition in the D_2 line of ^{87}Rb (indicated by the asterisk).

wavelength (which is two times the wavelength of the $F = 2 \rightarrow F' = 2 \times 3$ crossover transition in the D_2 line of ^{87}Rb). The polarization dependent transmission spectrum of the 540 MHz PS-FBG is shown in Figure C.4. The spectrum is obtained when the laser frequency is scanned and the PS-FBG transmission is recorded on a fast photodiode[8]. Two distinct transmission peaks are observed for horizontal and vertically polarized photons. This is explained by a small residual birefringence in the PS-FBG, causing different effective cavity lengths for the two polarization modes. The peak width for vertically (horizontally) polarized light is 540 MHz (580 MHz), Lorentzian shaped. The maximum transmission reaches 58% (52%). This transmission figure of merit comprises already the secondary filtering stage for removing the PS-FBG side-band transmission features. Via temperature control, the narrower transmission peak is positioned to be at the photon pair wavelength degeneracy for optimum transmission. Note that actually the observed birefringence is a major problem, when wanting to apply this PS-FBG to polarization entangled photons. The filter labels the polarization modes with a wavelength, such that entanglement is degraded. To avoid this problem, the PS-FBG is applied directly at the type-0 PPLN/W output and consequently before the entanglement transcriber (see sec-

[8]Thorlabs DET10C.

tion 2.5). Here, both photons of each pair are still vertically polarized and experience the same filtering behaviour in the PS-FBG.

C.4. 25 MHz ↔ 0.2 pm filtering stage

The 25 MHz PS-FBG is produced by Teraxion corporation in Canada. The temperature dependence of the transmission wavelength of this filter is somewhat less than for the 540 MHz PS-FBG, in this case ∼ 200 MHz/K, such that the temperature stabilization system is home-made using selfadhesive heatermats and a standard temperature controller[9]. The 25 MHz PS-FBG is characterized using the same procedure as out-

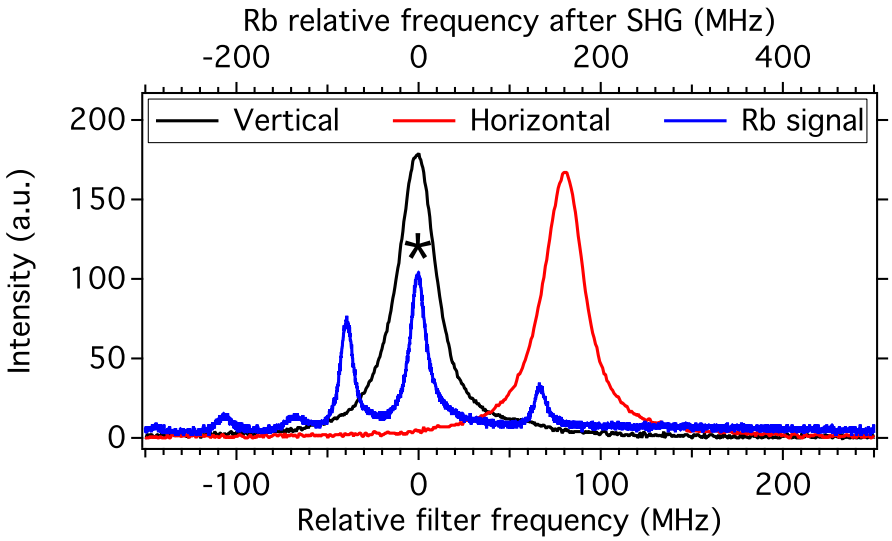

Figure C.5.: Characterization of the 25 MHz PS-FBG from Teraxion corporation. Two polarization dependent transmission peaks are obtained. The peaks are separated by ∼ 80 MHz due to a residual fibre birefringence. The peak widths are 25 MHz and 28 MHz for vertically and horizontally polarized photons, respectively. Via temperature control, the transmission peak for vertically polarized light is positioned at two times the wavelength of the $F = 2 \rightarrow F' = 2 \times 3$ crossover transition in the D_2 line of ^{87}Rb (indicated by the asterisk).

lined above and the experimental results are shown in Figure C.5. Again, two distinct transmission peaks are obtained for vertically and horizontally polarized photons. Consequently, birefringence is also present in this device and the PS-FBG cannot be applied to polarization entangled photons. The transmission bandwidth for vertically (horizontally) polarized light is 25 MHz (28 MHz), with maximum transmission of 71% (63%), including side-band rejection using a 100 GHz DWDM. The transmission profiles for this

[9] Thorlabs TED 8020.

	n_e	n_o
A_1	4.582	4.9048
A_2	9.921E4	1.1775E5
A_3	2.109E2	2.1802E2
A_4	2.194E-8	2.7153E-8
B_1	5.2716E-2	2.2314E-2
B_2	-4.9143E-5	-2.9671E-5
B_3	2.2971E-7	2.1429E-8

Table D.1.: Coefficients for the temperature dependent Sellmeier equation for lithium niobate.

filter are also Lorentzian shaped, as it is expected for cavity like filters. At a temperature of $\sim 331\,\mathrm{K}$, the transmission peak for vertically polarized light is at the desired wavelength of1560.48 nm.

D. Sellmeier equations for lithium niobate

The temperature and wavelength dependent refractive index of a given material is typically described by the so-called Sellmeier equation. These empirical equations are available for many materials.

The refractive index of lithium niobate as a function of the crystal temperature and light wavelength and polarization is given in this section. This is a necessary information for calculating both, the temporal walk-off induced by the waveguide birefringence for the photon pair source described in section 2.3, but also when engineering a desired three photon interaction using the QPM technique. The chosen ansatz is the following:

$$n_i = \sqrt{1 + A_{i1} + \frac{A_{i2} + B_{i1} f(T)}{\lambda^2 - (A_{i3} + B_{i2} f(T))^2} + B_{i3} f(T) + A_{i4}\lambda^2}, \tag{D.1}$$

with

$$f(T) = (T - 248,7)(T + 843.7). \tag{D.2}$$

The subscript i denotes the light polarization, either being extraordinary (e), or ordinary (o). The temperature is denoted by the symbol T. The parameters given in Table D.1 describe the refractive index for wavelengths of 400 nm to 2000 nm and temperatures from 298 K to 573 K [301, 302]:

E. Sellmeier equations for fused silica

In this section, the Sellmeier equation for fused silica[10] is given. This information is necessary for estimating the phase stability in the entanglement transcriber apparatus used in section 2.5. The data are taken over from reference [303]. The formulae are valid for temperatures ranging from 30 to 310 K at wavelengths from 0.4 to 2.6 microns. The temperature and wavelength dependent refractive index $n(\lambda, T)$ is given by

$$n(\lambda, T) = \sqrt{\sum_{i=1}^{3} \frac{S_i(T) \cdot \lambda^2}{\lambda^2 - \lambda_i^2(T)} + 1}, \tag{E.1}$$

where

$$S_i(T) = \sum_{j=0}^{4} S_{ij} \cdot T^j \tag{E.2}$$

$$\lambda_i(T) = \sum_{j=0}^{4} \lambda_{ij} \cdot T^j. \tag{E.3}$$

S_i is called the strength of the resonance features at wavelengths λ_i over the full temperature and wavelength range. The coefficients S_{ij} and λ_{ij} are given in the following table.

In Figure E.1 the temperature dependent refractive index of fused silica at a wavelength of 1560 nm is shown as an example. On the other side, Figure E.2 shows the wavelength dependent refractive index at a temperature of 300 K.

[10] Corning 7980 fused silica.

term	S_1	S_2	S_3	λ_1	λ_2	λ_3
T^0	1.10127	1.78752E-5	7.93552E-1	−8.90600E-2	2.97562E-1	9.24454
T^1	-4.94251E-5	4.76391E-5	-1.27815E-3	9.08730E-6	-8.59578E-4	-7.09788E-3
T^2	5.27414E-7	-4.49019E-7	1.84595E-5	-6.53638E-8	6.59069E-6	1.01968E-4
T^3	-1.59700E-9	1.44546E-9	-9.20275E-8	7.77072E-11	-1.09482E-8	-5.07660E-7
T^4	1.75949E-12	-1.57223E-12	1.48829E-10	6.84605E-14	7.85145E-13	8.21348E-10

Table E.1.: Coefficients for the three term Sellmeier model with fourth order temperature dependence for fused silica.

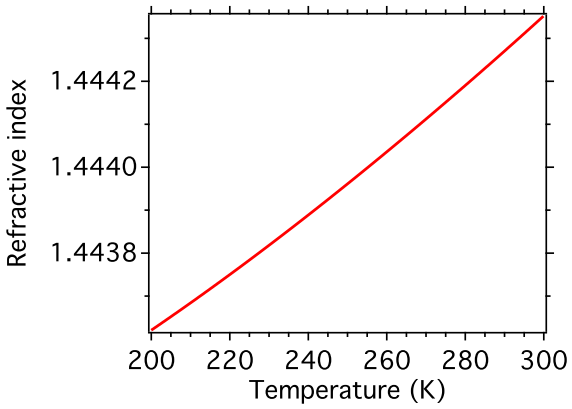

Figure E.1.: Temperature dependent refractive index of fused silica at a wavelength of 1560 nm.

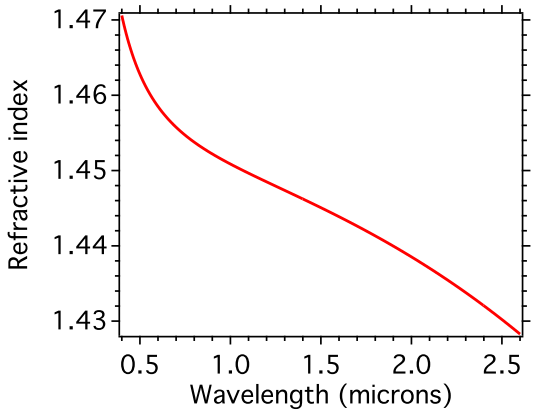

Figure E.2.: Wavelength dependence of the refractive index of fused silica at a temperature of 300 K.

F. Stabilization of the entanglement transcriber phase relation

In order to demonstrate high quality polarization entanglement via the violation of the Bell's inequalities, the phase relation ϕ between the two contributions leading to the entangled state $|\Phi(\phi)\rangle = \frac{1}{\sqrt{2}}\left(|H\rangle_a |H\rangle_b + e^{i\,\phi}\,|V\rangle_a |V\rangle_b\right)$ needs to be kept constant [225]. Phase fluctuations on the order of $\Delta\phi \approx \frac{2\,\pi}{50}$ cause entanglement visibility degradations of about 1% for the standard Bell inequality test. In this section, the advanced phase stabilization scheme for the experiment carried out in section 2.5 is outlined.

F.1. Ab initio considerations

In this particular realization, the phase relation is imposed by the path length difference L of the entanglement transcriber apparatus and it is

$$\phi = 2\,\pi\,L\left(\frac{n_1}{\lambda_1} + \frac{n_2}{\lambda_2}\right). \tag{F.1}$$

Here, λ_1 and λ_2 are the wavelengths of the two photons. The experienced refractive indices for these two photons are given by n_1 and n_2, respectively. For reasons of simplicity, it is now considered that

$$\lambda_1 = \lambda_2 \qquad \leftrightarrow \qquad n_1 = n_2. \tag{F.2}$$

This means that the photon pairs are wavelength degenerate and the phase relation is then given by

$$\phi = 4\,\pi\,L\frac{n}{\lambda}. \tag{F.3}$$

As the photon wavelength λ is considered to be constant, phase drifts are only caused by path length difference drifts ΔL and fluctuations of the refractive index Δn. In this particular realization, the two paths are made of standard telecom polarization maintaining fibres (PMF), which means, that ΔL and Δn are mainly temperature dependent. In the following, this dependency is outlined.

Optical fibres are made of fused silica. In the literature [304] one finds that the thermal expansion for this material (at room temperature) is

$$\frac{\Delta L}{L} \approx 0.55 \cdot 10^{-6}\,\mathrm{K}^{-1} \cdot \Delta T. \tag{F.4}$$

Here, ΔT is the temperature shift in K. The temperature dependence of the refractive index can be obtained from the so-called Sellmeier equations, see also Appendix E. The temperature dependent refractive index of fused silica for a wavelength of 1560 nm is shown in Figure F.1.

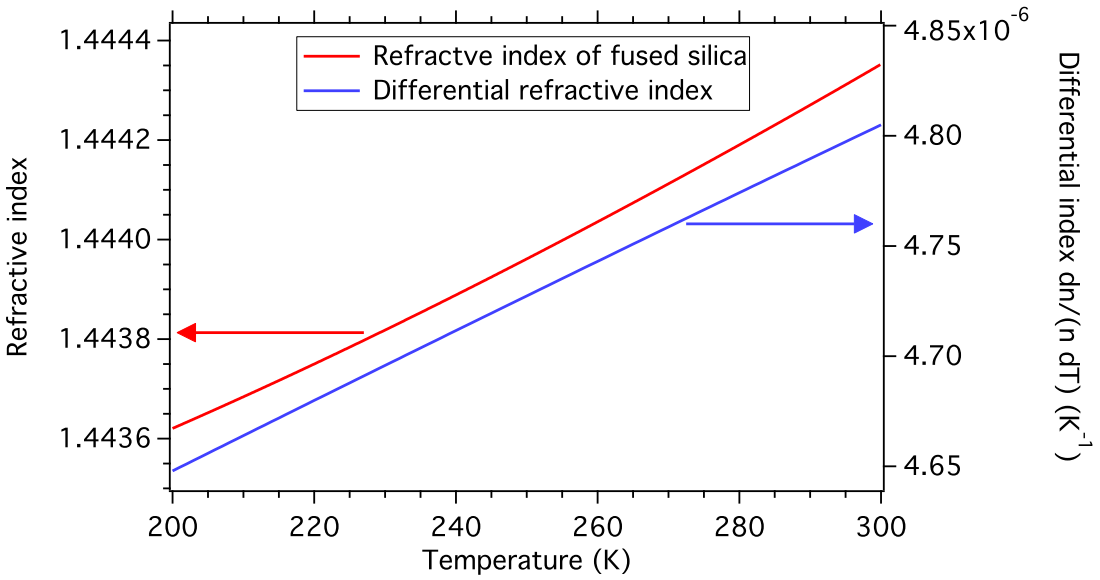

Figure F.1.: Temperature dependent refractive index of fused silica at a wavelength of 1560 nm. The left y-axis gives the absolute refractive index and the right hand side y-axis represents the temperature dependent refractive index variation $\frac{dn}{n\,dT}$.

From the graph it is seen that, at room temperature ($T = 300\,\mathrm{K}$), it is

$$\frac{\Delta n}{n} \approx 4.8 \cdot 10^{-6}\,\mathrm{K}^{-1} \cdot \Delta T. \tag{F.5}$$

The refractive index temperature dependence is almost ten times stronger than thermal expansion. The phase relation is therefore mainly dominated by equation F.5.

Combining thermal expansion and temperature dependent refractive index delivers then (in a first order approximation)

$$\phi \approx \underbrace{\frac{4\,\pi\,L\,n}{\lambda}}_{\phi_0} + \underbrace{\frac{4\,\pi\,L\,n}{\lambda}\,\Delta T \cdot 5.35 \cdot 10^{-6}\mathrm{K}^{-1}}_{\Delta\phi}. \tag{F.6}$$

Note that the term ϕ_0 is in principle irrelevant, it is only the phase drift $\Delta\phi$, that leads to possible degradation of entanglement. If the entanglement degradation should be kept below 1%, a good approximation is

$$\Delta\phi \overset{!}{<} \frac{2\,\pi}{50}. \tag{F.7}$$

Inserting this in equation F.6, results in

$$\Delta T \overset{!}{<} \frac{4 \cdot 10^{-3}\,\mathrm{K} \cdot \mathrm{m}}{L}. \tag{F.8}$$

Note that here $n = 1.4443$ has been inserted. In practice, standard temperature stabilization systems reach an absolute stability of about 10 mK[11]. This means, that path length differences of $L = 0.4\,\mathrm{m}$ can be achieved while still keeping a good entanglement quality.

However, the experiments in this thesis require a much longer path length difference in order to fulfil equation 2.80 even for ultra long coherence time photons. To properly post-select entangled photon pairs down to an atom or ion absorption compatible bandwidth of $\sim 20\,\mathrm{MHz}$ ($\leftrightarrow \tau_\mathrm{s} = 22\,\mathrm{ns}$), the path length difference is required to be $L = 18\,\mathrm{m}$ ($\delta t = 76\,\mathrm{ns}$). Such a path length difference implies sub-mK temperature stability, which is technically very challenging, especially for long term measurements. To still guarantee a good phase stability, an advanced phase stabilization system is employed.

F.2. Basic idea of the active phase stabilization system

The general idea of the phase stabilization system is the following. A telecom reference laser is injected into the transcriber interferometer and measures constantly the phase fluctuations. Via a piezoelectric transducer fibre stretcher, the optical length of the fibre is constantly corrected so as to reduce temperature induced phase fluctuations to a minimum. To avoid noise background due to scattering in the fibres and fibre connectors, the telecom reference laser is operated at a different wavelength compared to the photon pair wavelength of 1560.48 nm and at low optical power ($\leq 100\,\mathrm{nW}$).

The general working principle of the employed phase stabilization system is outlined in Figure F.2. A frequency stabilized telecom reference laser is diagonally polarized and injected, via a dense wavelength division multiplexer (DWDM), in the backward direction in the transcriber interferometer. More details on the laser stabilization system are given later in this subsection. After the transcriber, the laser light photons' quantum state is described by

$$|\psi\rangle_\mathrm{r} = \frac{1}{\sqrt{2}}\left(|H\rangle_\mathrm{r} + e^{i\,\phi_\mathrm{r}}\,|V\rangle_\mathrm{r}\right). \tag{F.9}$$

The subscript r denotes the reference laser. The light paths of the reference laser and the single photons are separated using another DWDM. Thereafter the laser light passes an electro-optic modulator (EOM), that introduces an additional, yet precisely controllable, phase ϕ_E to the $|V\rangle_r$ contribution. For reasons of simplicity this EOM is not shown in Figure F.2. After the EOM it is

$$|\psi\rangle_\mathrm{E} = \frac{1}{\sqrt{2}}\left(|H\rangle_\mathrm{r} + e^{i\,(\phi_\mathrm{r}+\phi_\mathrm{E})}\,|V\rangle_\mathrm{r}\right). \tag{F.10}$$

Note that at this stage, measuring the phase ϕ_r and it's fluctuations is difficult. In general, one prefers to measure light intensities. In the following, it is shown how the phase information is transformed to an optical intensity.

[11] Thorlabs TED200C, Thorlabs TED8020.

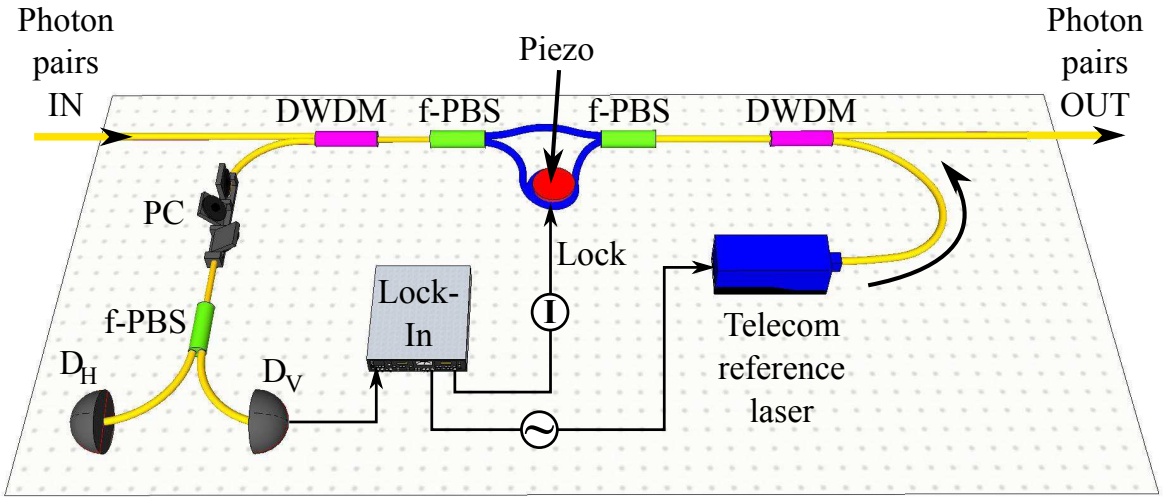

Figure F.2.: Phase stabilization setup. A diagonally polarized telecom reference laser is coupled via a DWDM in the backward sense into the interferometer. Another DWDM is used to separate the reference laser and the photon pairs. Via a polarization controller (PC), the laser light polarization is turned by 45° and sent to a fibre polarizing beam-splitter (f-PBS). Two fast photodiodes are used to measure the phase dependent intensities I_H and I_V. A Lock-In amplifier wavelength modulates the reference laser, measures the signal I_V and gives the error signal. The error signal is integrated and sent to a piezo-electric fibre stretcher to compensate phase fluctuations.

After a polarization controller (PC), the light is rotated by 45°, meaning that the quantum state develops

$$|\psi\rangle_{\mathrm{PC}} = \frac{1}{2}\left(|H\rangle_{\mathrm{r}} + |V\rangle_{\mathrm{r}} + e^{i(\phi_{\mathrm{r}}+\phi_{\mathrm{E}})}|V\rangle_{\mathrm{r}} - e^{i(\phi_{\mathrm{r}}+\phi_{\mathrm{E}})}|H\rangle_{\mathrm{r}}\right) \tag{F.11}$$

$$= \frac{1-e^{i(\phi_{\mathrm{r}}+\phi_{\mathrm{E}})}}{2}|H\rangle_{\mathrm{r}} + \frac{1+e^{i(\phi_{\mathrm{r}}+\phi_{\mathrm{E}})}}{2}|V\rangle_{\mathrm{r}}\,. \tag{F.12}$$

Eventually, a fibre polarizing beam-splitter (f-PBS) is used to separate the $|H\rangle_{\mathrm{r}}$ and $|V\rangle_{\mathrm{r}}$ modes. The intensities I_H and I_V on the detectors D_H and D_V, respectively, read

$$I_H \propto \sin^2\frac{\phi_{\mathrm{r}}+\phi_{\mathrm{E}}}{2} \tag{F.13}$$

$$I_V \propto \cos^2\frac{\phi_{\mathrm{r}}+\phi_{\mathrm{E}}}{2}. \tag{F.14}$$

Consequently, it is possible to measure $\phi_{\mathrm{r}}+\phi_{\mathrm{E}}$ in a convenient way, via the light intensity on a detector. As ϕ_{E} is controllable and adjustable, this results in an effective measurement of ϕ_{r}.

The stabilization system works then as follows (see also Figure F.2). The modulation output of a commercial Lock-In amplifier is connected to the current modulation input of the reference laser diode[12]. This results in a periodic laser wavelength modulation. As the accumulated phase $\phi_\mathrm{r}+\phi_\mathrm{e}$ is wavelength dependent, oscillations in the intensities I_H and I_V are observed. I_V is measured using a fast photodiode[13], and the voltage output signal is sent to the Lock-In amplifier, where it is multiplied with the 32 kHz modulation signal and thereafter low-pass filtered. The outcome is a signal that is proportional to the first derivative of I_V and referred to be the error signal. The aim is now to keep the error signal always at zero, so as to stabilize I_V on the top (or the bottom) of an intensity oscillation fringe. This is achieved by sending the error signal to a home-made integrator circuit and then to the piezo-electric fibre stretcher. The piezo corrects the length of the fibre so as to keep $\phi_\mathrm{r}+\phi_\mathrm{e}=0$. As the sum of phases is always kept at zero, tuning of the phase in the electro-optical modulator, ϕ_e, results in tuning of ϕ_r in a very convenient manner. Thus this system does not only permit stabilizing ϕ_r, but also precise tuning.

It is important to remark that in general $\phi_\mathrm{r}\neq\phi_\mathrm{pair}$. The transcriber interferometer is stabilized with respect to the phase accumulated reference laser, ϕ_r, which does not necessarily imply that the phase accumulated by the photon pairs, ϕ_pair, is stabilized. The reason for that is the wavelength dependence of the fibre refractive index. In addition, the differential refractive index $\frac{dn}{n\,dT}$ shows also a wavelength dependence. Consequently, if the wavelengths of the photons and reference laser differ too much, or if too high temperature fluctuations occur, a proper phase stabilization is impossible. In the following, the upper limits for the wavelength difference and temperature fluctuations are calculated.

F.3. Limitations of the stabilization system

In order avoid overcharging this part, the calculations are not fully detailed, however all necessary steps are elucidated. The phase ϕ_r accumulated by the reference laser can be calculated using the Sellmeier equations given in Appendix E and it is a function of the starting temperature T_0 and the drift ΔT

$$\phi_\mathrm{r}=\phi_\mathrm{r}(T_0,\Delta T)=\phi_\mathrm{r}(T_0+\Delta T). \tag{F.15}$$

The phase drift $\Delta\phi_\mathrm{r}$ depends also on these two variables

$$\Delta\phi_\mathrm{r}=\Delta\phi_\mathrm{r}(T_0,\Delta T). \tag{F.16}$$

[12]Toptica DLpro design.
[13]Thorlabs DET10C.

The active phase stabilization system is used to eliminate phase drifts, via fine adjustment of the fibre length

$$\underbrace{\Delta\phi_{\mathrm{r}}(T_0, \Delta T)}_{\text{unwanted drift}} + \underbrace{\frac{2\,\pi\,L_{\mathrm{corr}}\,n_{\mathrm{r}}(T_0, \Delta T)}{\lambda_r}}_{\text{correction}} \stackrel{!}{=} 0. \tag{F.17}$$

Here, L_{corr} is the correction of the fibre length. Solving this equation delivers the function

$$L_{\mathrm{corr}} = L_{\mathrm{corr}}(T_0, \Delta T). \tag{F.18}$$

This fibre length correction does not necessarily compensate the phase fluctuations at the photon pair wavelength $\Delta\phi_{\mathrm{pair}}$. The mismatch $\Delta\left(\Delta\phi_{\mathrm{pair}}\right)$ is given by

$$\begin{aligned} \Delta\left(\Delta\phi_{\mathrm{pair}}\right) &= \Delta\left(\Delta\phi_{\mathrm{pair}}\right)(T_0, \Delta T) \\ &= \Delta\phi_{\mathrm{pair}}(T_0, \Delta T) + 2\,\frac{2\,\pi\,n_{\mathrm{pair}}(T_0, \Delta T)\,L_{\mathrm{corr}}(T_0, \Delta T)}{\lambda_{\mathrm{pair}}}. \end{aligned} \tag{F.19}$$

The factor two in front of the fraction comes from the fact, that the two photons of the pair have to be considered (instead of single photons coming from the reference laser). In Figure F.3, the photon pair phase mismatch $\Delta\left(\Delta\phi_{\mathrm{pair}}\right)$ is shown as a function of the reference laser wavelength λ_{r}. The following parameters (that show a good agreement with the actual experiment) are used: path length difference $L = 18\,\mathrm{m}$, start temperature $T_0 = 298\,\mathrm{K}$, entangled photon pair wavelength $\lambda_{\mathrm{pair}} = 1560\,\mathrm{nm}$ and a temperature shift of $\Delta T = 0.1\,\mathrm{K}$. From the graph it is seen that a broad range of reference lasers can be used for efficient phase stabilization without serious entanglement degradation. The window of suitable lasers is particularly interesting as it covers the telecommunication bands, for which high performance lasers are available. In addition the window covers nearly the full range of wavelengths that are single mode guided in standard telecommunication fibres. Figure F.4 shows the unwanted phase drift $\Delta\left(\Delta\phi_{\mathrm{pair}}\right)$ as a function of the temperature drift for two fixed reference laser wavelengths $\lambda_{\mathrm{r}} = 1559\,\mathrm{nm}$ and $\lambda_{\mathrm{r}} = 1590\,\mathrm{nm}$, respectively. The choice for these two particular wavelengths is motivated by the fact that they are used in the actual experiment. In the graph it is seen that a smaller wavelength mismatch between reference laser and entangled photon pairs results in a better stability. Ideally, a 1560 nm reference laser should be used, however for better noise suppression, the reference laser wavelength should differ from the photon pair wavelength. From the graph it is also seen that even for our non-optimized temperature stabilization system, showing a stability of $|\Delta T| < 0.1\,\mathrm{K}$, a reference laser at 1590 nm can be used. With some additional efforts, a stability of 0.01 K should be attainable, thus permitting even greater wavelength mismatches.

In Figure F.5 a photograph of the actual experimental realization of the transcriber apparatus is shown. The inside walls of a plastic box are covered with polyurethane plates for better temperature isolation. The fibre interferometer is fixed on a 1 cm

thick Aluminium plate under which selfadhesive heatermats are used for temperature stabilization. A standard temperature controller[14] is used to regulate the current in the heatermats, so as to achieve a constant temperature of $\sim 298\,\mathrm{K}$. The piezoelectric fibre stretcher is made of two metal half circles around which the 18 m fibre is wound a few times. The displacement between these two metal pieces can be fine adjusted with a precision of $\sim 1\,\mathrm{nm}$ using a piezoelectric transducer. This way, the path length difference can be precisely tuned and the phase stabilized.

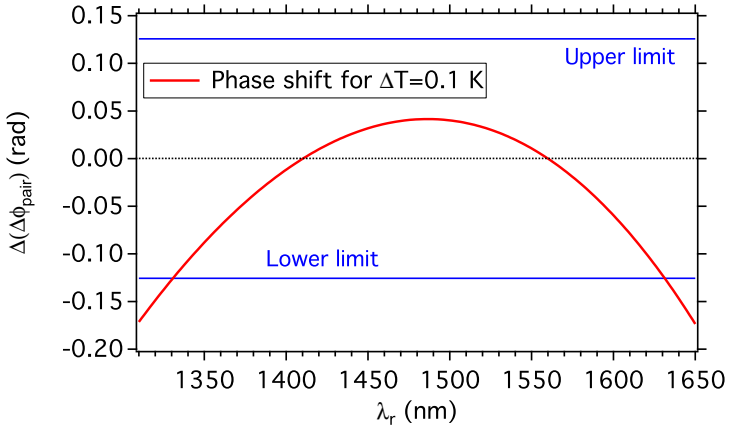

Figure F.3.: Entangled photon pair phase mismatch $\Delta\left(\Delta\phi_{\mathrm{pair}}\right)$ as a function of the wavelength of the reference laser, λ_{r}. The following parameters are used: $L = 18\,\mathrm{m}$, $T_0 = 298\,\mathrm{K}$, $\lambda_{\mathrm{pair}} = 1560\,\mathrm{nm}$ and $\Delta T = 0.1\,\mathrm{K}$. The upper and lower limit lines represent an unwanted phase shift of $\pm\frac{2\pi}{50}$, at which entanglement degradation of 1% is observed. A broad range of reference laser wavelengths can be used for efficient phase stabilization.

[14] Thorlabs TED 200C.

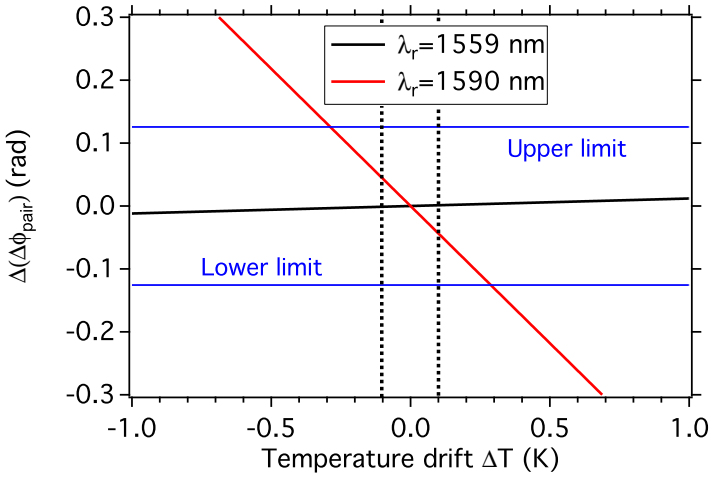

Figure F.4.: Entangled photon pair phase mismatch $\Delta\left(\Delta\phi_{\text{pair}}\right)$ as a function of the temperature drift ΔT. The following parameters are used: $L = 18\,\text{m}$, $T_0 = 298\,\text{K}$, $\lambda_\text{r} = 1559\,\text{nm}$ respectively $\lambda_\text{r} = 1590\,\text{nm}$. The upper and lower limit lines represent an unwanted phase shift of $\pm\frac{2\pi}{50}$, at which entanglement degradation of 1% is observed. Note that our non-optimized home-made temperature stabilization system reaches $|\Delta T| < 0.1\,\text{K}$, as indicated by the vertical dashed lines.

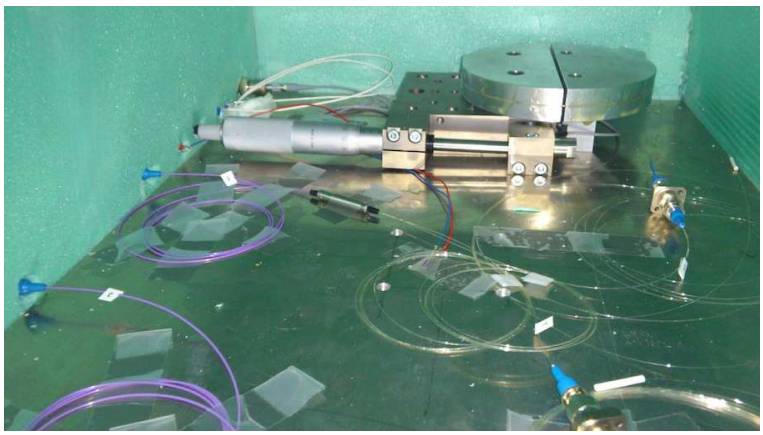

Figure F.5.: Actual experimental realization of the transcriber apparatus. On the left hand side, the input and output fibres are seen. The home-made piezo fibre stretcher is located in the picture background. The fibre of the long transcriber arm is wound around two metal half circles. The distance between the circles can be adjusted using a piezo-electric transducer. The whole setup is enclosed in a temperature stabilized box for better stability.

F.4. Reference laser stabilization scheme

In order to guarantee a good phase stability, the reference laser needs to be frequency stabilized. Note that a 18 m unbalanced fibre interferometer implies a phase shift of $\Delta\phi_r = 2\,\pi$ for a reference laser frequency shift of 11.5 MHz. Commercially available, passively stabilized telecom lasers achieve long term frequency stabilities of a few MHz, which is not good enough for stabilizing a 18 m unbalanced interferometer. Consequently, an active stabilization system is required.

In the following, two strategies are shown towards laser frequency stabilization at 1590 nm and 1559 nm.

Reference laser stabilization scheme at 1590 nm

To actively frequency stabilize a telecom wavelength laser[15] at 1590 nm, the experimental setup outlined in Figure F.6 is employed. The laser light at 1590 nm is split up at a 98/2 fibre coupler. 2% of the light is sent to the entanglement transcriber apparatus for phase stabilization. The rest of the light is amplified to around 1 W of optical power, using an erbium doped fibre amplifier (EDFA). The light is sent to a PPLN/W, whose quasi phase matching is optimized for frequency doubling, *i.e.* the 1590 nm laser light is converted to 795 nm. At this wavelength an optical power of about 10 mW is obtained after the PPLN/W. Several bulk optics filters are used to reject the remaining 1590 nm light. Then the 795 nm light is sent to a standard rubidium saturated absorption spectroscopy setup. This setup permits observing the hyperfine structure of the rubidium D_1 line. In Figure F.7, the observed optical hyperfine (and crossover) transitions are shown, when the laser frequency is scanned. Note that each line shows a width of about 5.75 MHz and serves as absolute frequency reference. The same procedure as described above for phase stabilization is also used for laser frequency stabilization. The laser current is modulated so as to modulate the laser wavelength. The Doppler free saturated absorption spectroscopy signal is mixed with the modulation signal using a commercial Lock-In amplifier. After an electronic low-pass filter, the obtained error signal is integrated and forwarded to the laser current, so as to stabilize the laser wavelength to be always on top one of the hyperfine structure peaks. As the reference laser is now absolutely frequency stabilized with respect to the hyperfine structure of rubidium, the phase of the interferometer is also considered to be absolutely stable. Although this stabilization system is used for the first experiments, several inconveniences are observed. The saturated absorption spectroscopy signal in this realization is relatively weak, so that a somewhat noisy error signal is obtained. In addition, the signal is strongly intensity dependent. The intensity fluctuations after the frequency doubling stage are on the order of $\pm 20\%$ due to non-perfect PPLN/W temperature stability. This causes the laser wavelength stabilization scheme to occasionally jump between two hyperfine structure

[15] Toptica TApro design.

peaks. Although the time scale of unwanted jumps is on the order of 1-2 hours, this represents anyway a major inconvenience, as the jumps cannot be predicted.

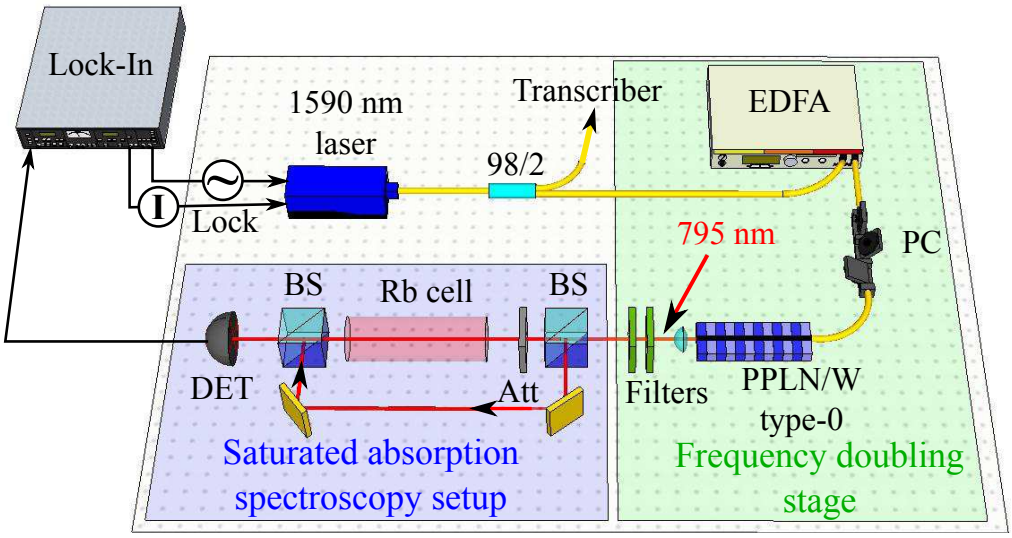

Figure F.6.: Wavelength stabilization of the reference laser at 1590 nm. A 98/2 coupler sends 2% of the light to the transcriber stabilization system. The rest goes to an erbium doped fibre amplifier (EDFA) and passes a polarization controller towards obtaining vertically polarized 1590 nm light in front of a PPLN/W. The PPLN/W is used for frequency doubling, consequently light at 795 nm is obtained. Several bulk filters are used at the PPLN/W output to reject the residual 1590 nm light. A standard rubidium saturated absorption spectroscopy setup is used to resolve the hyperfine structure of atomic rubidium. Used elements: beam-splitter (BS), optical attenuator (Att) and a fast photodiode (DET). A Lock-In amplifier applies a modulation on the laser diode current to obtain a wavelength modulation. The saturation absorption spectroscopy signal is mixed with the modulation signal. The resulting error signal is integrated and forwarded to the laser diode current for wavelength stabilization.

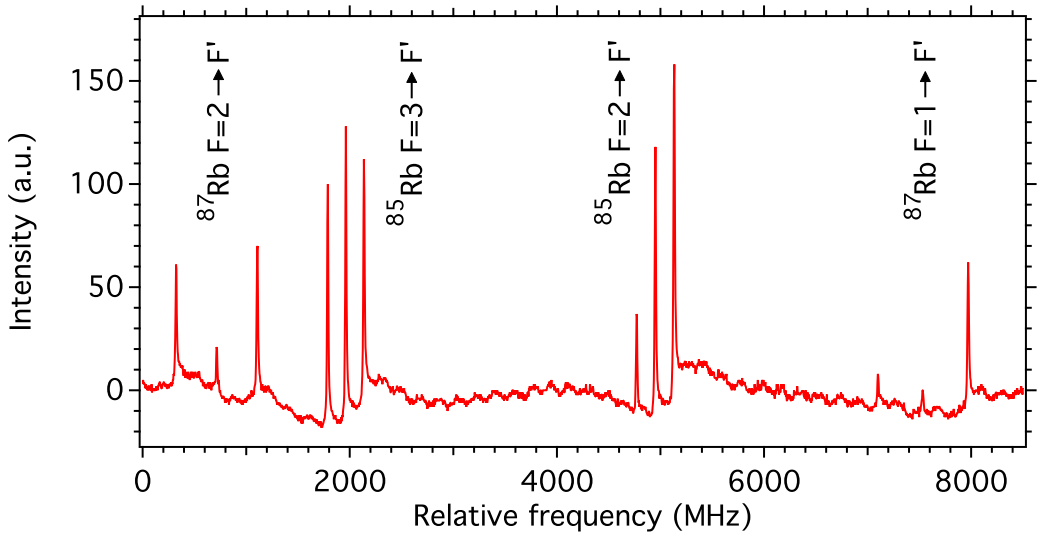

Figure F.7.: Doppler free saturated absorption spectroscopy signal for the D_1 line ($\sim$ 795 nm) in atomic rubidium. Twelve spectroscopy lines are obtained, eight of them being direct optical hyperfine transitions, and four being cross-over transitions. Typically, the reference laser is locked to one of the optical transitions in the ^{87}Rb F=2→F' manifold. Each peak has a width of 5.75 MHz.

Reference laser stabilization scheme at 1559 nm

A more reliable laser wavelength stabilization scheme is outlined in Figure F.8. At first glance, this scheme might seem to be more complicated, but it is found that in a real experiment, it offers an unprecedented ease of use. A fraction of the wavelength stabilized 780.24 nm pump laser (which is required to pump the type-0 PPLN/W used in section 2.5) is sent to an optical cavity having a free spectral range of 1 GHz and a finesse of 400, thus leading to transmission line widths of 2.5 MHz[16]. The cavity length is stabilized with respect to the 780.24 nm laser using the following strategy. The length of the cavity is tuned, using a piezo-electric transducer mounted on one of the mirrors, until a peak of transmission is observed. In order to obtain an error signal, the length of the cavity is modulated. To obtain a high modulation frequency, a mechanical resonance is searched and found at 11.6 kHz. The modulated cavity transmission signal is sent to a commercial Lock-In amplifier where it is mixed with the 11.6 kHz modulation signal. A low-pass filter is used to give the error signal. The integrated error signal is

[16]Toptica FPI100.

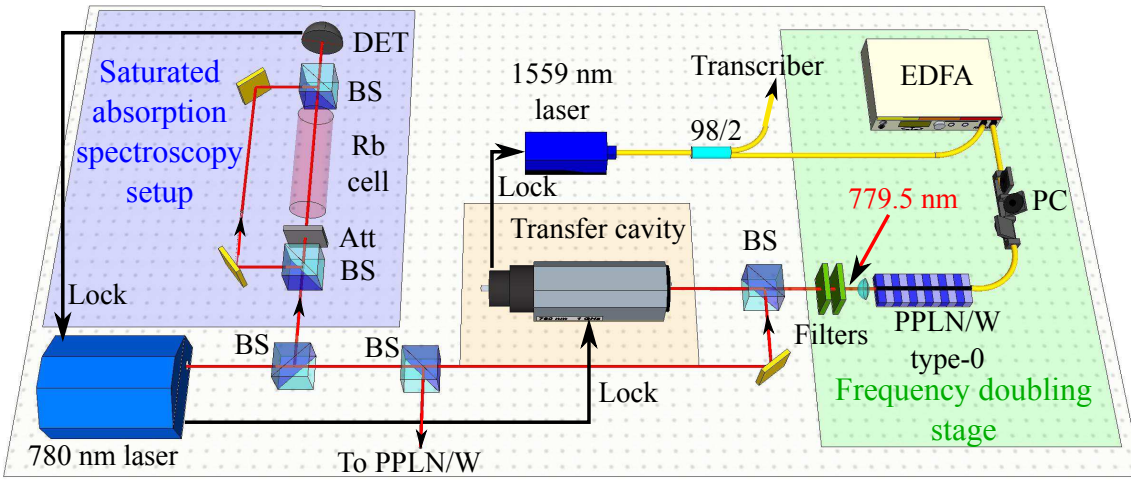

Figure F.8.: Telecom reference laser stabilization scheme using a transfer cavity lock. A 780.24 nm laser is stabilized against a hyperfine transition in atomic rubidium using a standard saturated absorption spectroscopy setup. A portion of this laser is coupled to an optical cavity. The cavity length is stabilized with respect to this laser. The 1559 nm telecom laser is stabilized on a transmission peak of the stabilized cavity after being amplified in an erbium doped fibre amplifier (EDFA) and frequency doubled in a PPLN/W. Although this system looks relatively complicated, unprecedented long term stabilities are achieved. Note that the corresponding Lock-In amplifiers are not shown in this graph. The black arrows indicate, however, the direction of the stabilization systems.

forwarded to the piezo and consequently stabilizes the cavity length on a transmission peak. For better stability, the cavity is additionally enclosed in a temperature stabilized box that avoids also air pressure fluctuations inside the cavity. As the cavity length is stabilized with respect to the absolutely wavelength stabilized 780.24 nm laser, all the other cavity transmission peaks (occurring every 1 GHz $\leftrightarrow$ 0.002 nm) are also considered to serve as absolute frequency reference. This circumstance is advantageously exploited. The telecom reference laser is now operated at 1559 nm, 2% of the light is sent to the entanglement transcriber interferometer, 98% are sent to an erbium doped fibre amplifier, and thereafter frequency doubled in a PPLN/W towards achieving 15 mW optical power at 779.5 nm. The light at the PPLN/W output is coupled to an optical fibre to obtain a good Gaussian shaped mode. The 779.5 nm laser light is sent to the stabilized cavity. As the cavity offers absolute frequency stable transmission peaks every 1 GHz ($\leftrightarrow$ 0.002 nm), it is possible to stabilize the 779.5 nm on one of the peaks (see Figure F.9). To avoid crosstalk between the signals at 780.24 nm and 779.5 nm, the modulation speeds of the two signals are chosen far away from each other, *i.e.* the cavity is stabilized at 780.24 nm using a 11.6 kHz modulation, while the telecom reference laser is stabilized using the 779.5 nm signal, being modulated at 32 kHz. This way any unwanted cross-talk or interference effects between the two signals in the cavity are avoided. The advantages of this transfer cavity system are that the error signal is less sensitive to intensity fluctuations and that the spacing between the cavity peaks is large enough (1 GHz) to avoid wavelength jumping between different transmission peaks. Via long term measurements, it is found that this combined system stabilizes lasers and transcriber interferometer for more than two days without unwanted jumps or drifts[17].

Combining these two systems (laser stabilization and phase stabilization), an absolute phase stability of $\Delta\phi < \frac{2\pi}{200}$ is achieved over more than two days of measurement. The value of $\frac{2\pi}{200}$ is deduced from short term error signal fluctuations and the obtained temperature stability in the entanglement transcriber box.

To conclude this section, it is shown how to phase stabilize the entanglement transcriber interferometer, which is a necessary requirement towards observation of high quality entanglement. The general phase stabilization and tuning procedure are shown using a piezo-electric fibre stretcher and an electro-optic modulator. For proper phase stabilization, a wavelength stabilized reference laser is required. Two telecom laser wavelength stabilization schemes are outlined, working at 1590 nm and 1559 nm. Stabilization of a laser at 1590 nm is achieved using a frequency doubling stage and a rubidium saturated absorption spectroscopy setup. However, limited stabilities are obtained using this strategy. The stability is strongly improved using a transfer cavity locking scheme, where an actively stabilized laser at 780.24 nm serves as reference for cavity stabilization. The 1559 nm is frequency doubled and injected into the cavity, leading to an actively stabilized laser at 1559 nm. Note that this wavelength is very close to the photon pair

[17]Note that longer stability test have not been performed, however it is expected that this laser wavelength stabilization system works reliable for much more than two days.

wavelength, which results in much lower interferometer phase sensitivity due temperature fluctuations.

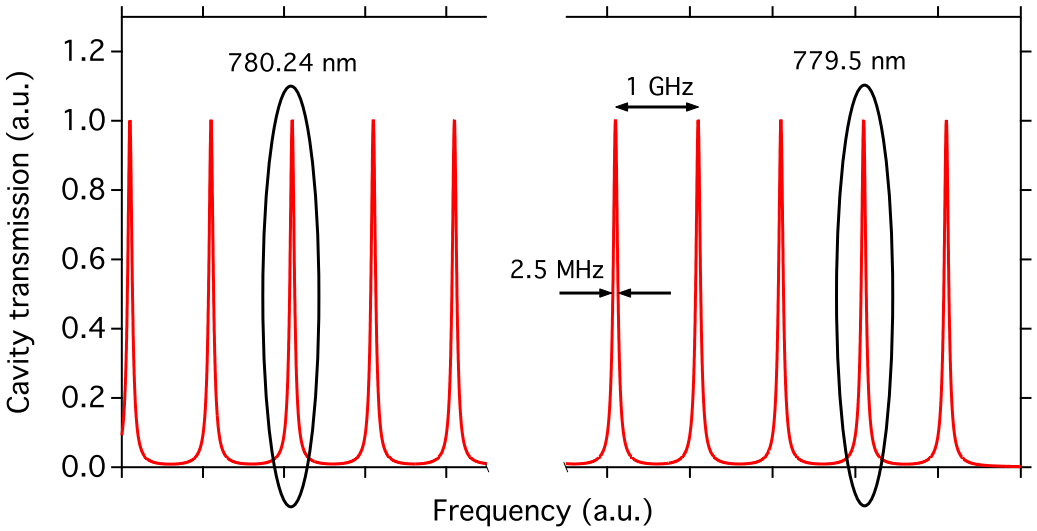

Figure F.9.: Cavity transmission signal (the graph represents a theoretical plot). Every 1 GHz, a transmission peak is obtained. The cavity length is stabilized using the frequency stabilized 780.24 nm pump laser. This results in absolutely frequency stable cavity transmission peaks. The telecom reference laser at 1559 nm is frequency doubled towards obtaining 779.5 nm light. This laser is then stabilized with respect to one of the cavity transmission peaks.

F.5. Post-selection fidelity for the entanglement transcriber

From Figure 2.48, it is obvious that the central peak for the DWDM and 540 MHz filters can be properly post-selected. Considering the Teraxion 25 MHz filter, the post-selection fidelity is quickly calculated in the following. The shape of the central coincidence peak for this filter is mathematically described by

$$I(t) \propto e^{-2\ln 2 \frac{|t|}{\mathrm{FWHM}}}. \tag{F.20}$$

Here, $I(t)$ is the delay time dependent intensity, and FWHM is the full peak width at half the maximum intensity. In this case we take the experimentally measured value of FWHM=15.6 ns. The full coincidence peak figure, comprising the three peaks, is given by

$$I(t) + I(t+\delta t)/2 + I(t-\delta t)/2, \tag{F.21}$$

where δt is the temporal peak separation, in this case $\delta t = 76\,\text{ns}$. In order to estimate the post-selection fidelity, the probability p_g of having a *good* coincidence and the probability p_w of having a *wrong* coincidence need to be compared. It is

$$p_g = \int_{-\Delta t/2}^{\Delta t/2} I(t)\,dt \tag{F.22}$$

$$p_w = \int_{-\Delta t/2}^{\Delta t/2} I(+\delta t)/2 + I(t-\delta t)/2\,dt. \tag{F.23}$$

Here, Δt is the integration time. The coincidence post-selection fidelity $\mathcal{F}_\text{c}$ is then given by

$$\mathcal{F}_\text{c} = \frac{p_g}{p_g + p_w}. \tag{F.24}$$

In Figure F.10, the obtained fidelity as a function of the integration time is shown. The parameters FWHM=15.6 ns and $\delta t = 76\,\text{ns}$ are used as fixed parameters. At higher integration times, the fidelity drops down due to selection of side-peak contributions. However, for reasonable integration times of 5-20 ns, still high post-selection fidelities of $\mathcal{F}_\text{c} > 0.998$ are obtained. Consequently, the peak separation is sufficiently long for this experiment. Note moreover that a post-selection fidelity $\mathcal{F}_\text{c} > 0.99$ can be obtained down to a photon pair spectral bandwidth of 19 MHz (coherence time of 23 ns).

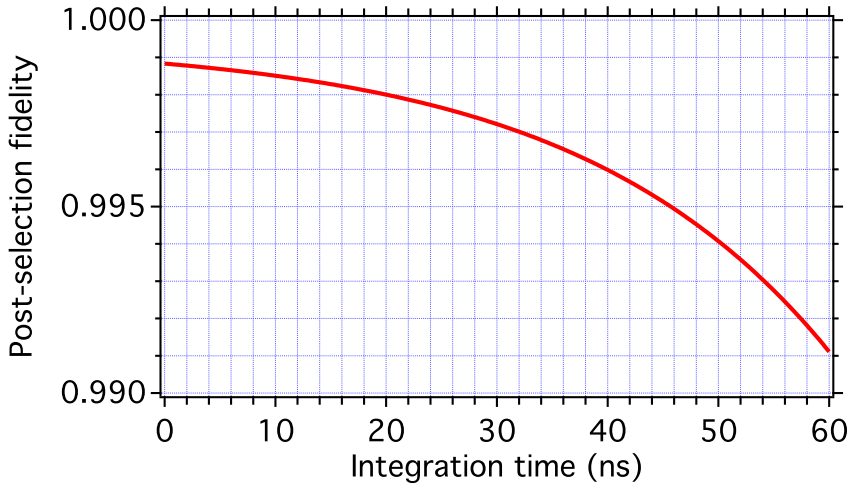

Figure F.10.: Post-selection fidelity for the Teraxion 25 MHz filter as a function of the integration time. For longer integration times, the side-peak contributions are taken more into account, thus reducing the fidelity. Typical integration times are 5-20 ns, for which fidelities above 0.998 are expected.

Bibliography

[1] C. Huygens, *Traité de la lumiere*, Pieter van der Aa, 1690.

[2] I. Newton, "New theory about light and colors", *Philos. Trans. R. Soc. London*, vol. 80, pp. 3075–3087, 1671/1672.

[3] J. C. Maxwell, "A dynamical theory of the electromagnetic field", *Phil. Trans. R. Soc. Lond.*, vol. 155, pp. 459–512, 1865.

[4] M. Planck, "Über eine Verbesserung der Wienschen Spektralgleichung", *Verhandlungen der Deutschen Physikalischen Gesellschaft*, vol. 2, pp. 202–204, 1900.

[5] P. A. M. Dirac, "The quantum theory of the emission and absorption of radiation", *Proc. R. Soc. Lond. A*, vol. 114, pp. 243–265, 1927.

[6] A. Einstein, "Über einen die Erzeugung und Verwandlung des Lichtes betreffenden heuristischen Gesichtspunkt", *Annalen der Physik*, vol. 322, pp. 132–148, 1905.

[7] "The fifth Solvay conference: Electrons and photons, Brussels (Belgium)", 1927.

[8] A. Einstein, B. Podolsky, and N. Rosen, "Can Quantum-Mechanical description of physical reality be considered complete?", *Phys. Rev.*, vol. 47, pp. 777–780, 1935.

[9] J. A. Wheeler and W. H. Zurek, *Quantum Theory and Measurement*, Eds. (Princeton Univ. Press, Princeton, NJ), 1984.

[10] G. Greenstein and A. Zajonc, *The Quantum Challenge: Modern Research On The Foundations Of Quantum Mechanics*, Jones and Bertlett Publishers, Sudbury, 2006.

[11] R. J. Glauber, "The quantum theory of optical coherence", *Phys. Rev.*, vol. 130, pp. 2529–2539, 1963.

[12] L. Mandel and E. Wolf, "Coherence properties of optical fields", *Rev. Mod. Phys.*, vol. 37, pp. 231–287, 1965.

[13] L. Mandel and E. Wolf, *Optical coherence and quantum optics*, Cambridge University Press, 1995.

[14] J. A. Armstrong, N. Bloembergen, J. Ducuing, and P. S. Pershan, "Interactions between light waves in a nonlinear dielectric", *Phys. Rev.*, vol. 127, no. 6, pp. 1918, 1962.

[15] T. H. Maiman, "Stimulated optical radiation in ruby", *Nature*, vol. 187, pp. 493–494, 1960.

[16] J. S. Bell, "On the Einstein-Podolsky-Rosen paradox", *Physics (Long Island City, N.Y.)*, vol. 1, pp. 195–200, 1964.

[17] J. F. Clauser, M. A. Horne, A. Shimony, and R. A. Holt, "Proposed experiment to test local Hidden-Variable theories", *Phys. Rev. Lett.*, vol. 23, no. 15, pp. 880–884, 1969.

[18] S. J. Freedman and J. F. Clauser, "Experimental test of local Hidden-Variable theories", *Phys. Rev. Lett.*, vol. 28, no. 14, pp. 938, 1972.

[19] A. Aspect, P. Grangier, and G. Roger, "Experimental tests of realistic local theories via Bell's theorem", *Phys. Rev. Lett.*, vol. 47, no. 7, pp. 460–463, 1981.

[20] R. Feynman, "Simulating physics with computers", *International Journal of Theoretical Physics*, vol. 21, pp. 467–488, 1982.

[21] D. Deutsch, "The Church-Turing principle and the universal quantum computer", *Proceedings of the Royal Society of London A.*, vol. 400, pp. 97, 1985.

[22] P. Shor, "Polynomial-time algorithms for prime factorization and discrete logarithms on a quantum computer", *Proc. 35^{th} IEEE Symp. on Foundations of Computer Science*, vol. Santa Fe, ed S. Goldwasser, pp. 124, 1994.

[23] L. K. Grover, "A fast quantum mechanical algorithm for database search", in *Proceedings of the twenty-eighth annual ACM symposium on Theory of computing*, New York, NY, USA, 1996, STOC '96, pp. 212–219, ACM.

[24] B. Schumacher, "Quantum coding", *Phys. Rev. A*, vol. 51, no. 4, pp. 2738, 1995.

[25] C. H. Bennett and G. Brassard, "Quantum cryptography: Public key distribution and coin tossing", *Proceedings of the IEEE International Conference on Computers, Systems and Signal Processing, Bangalore, India*, vol. , pp. 175, 1984.

[26] A. K. Ekert, "Quantum cryptography based on Bell's theorem", *Phys. Rev. Lett.*, vol. 67, no. 6, pp. 661–663, 1991.

[27] N. Gisin, G. Ribordy, W. Tittel, and H. Zbinden, "Quantum cryptography", *Rev. Mod. Phys.*, vol. 74, no. 1, pp. 145–195, 2002.

[28] M. Dušek, N. Lütkenhaus, and M. Hendrych, "Quantum cryptography", *Prog. Opt.*, vol. 49, pp. 381–454, 2006.

[29] V. Scarani, H. Bechmann-Pasquinucci, N. J. Cerf, M. Duscaronek, N. Lütkenhaus, and M. Peev, "The security of practical quantum key distribution", *Rev. Mod. Phys.*, vol. 81, no. 3, pp. 1301, 2009.

[30] "ID Quantique (Switzerland)", `http://idquantique.com/`.

[31] "MagiQ Technology (USA)", `http://www.magiqtech.com/`.

[32] "SeQureNet (France)", `http://www.sequrenet.fr/`.

[33] "Auréa Technologie (France)", `http://aureatechnology.fr/`.

[34] "NuCrypt (USA)", `http://www.nucrypt.net/`.

[35] "QuTools (Germany)", `http://www.qutools.com/`.

[36] "QuintessenceLabs (Australia)", `http://qlabsusa.com/`.

[37] C. H. Bennett, G. Brassard, C. Crépeau, R. Jozsa, A. Peres, and W. K. Wootters, "Teleporting an unknown quantum state via dual classical and Einstein-Podolsky-Rosen channels", *Phys. Rev. Lett.*, vol. 70, no. 13, pp. 1895–1899, 1993.

[38] J. W. Pan, D. Bouwmeester, H. Weinfurter, and A. Zeilinger, "Experimental entanglement swapping: Entangling photons that never interacted", *Phys. Rev. Lett.*, vol. 80, no. 18, pp. 3891, 1998.

[39] E. Knill, R. Laflamme, and G. J. Milburn, "A scheme for efficient quantum computation with linear optics", *Nature*, vol. 409, pp. 46–52, 2001.

[40] A. Aspect, J. Dalibard, and G. Roger, "Experimental test of Bell's inequalities using taime-varying analyzers", *Phys. Rev. Lett*, vol. 49, pp. 1804–1807, 1982.

[41] X. Ma, S. Zotter, J. Kofler, R. Ursin, T. Jennewein, C. Brukner, and A. Zeilinger, "Experimental delayed-choice entanglement swapping", *Nature Phys.*, vol. 8, pp. 480–485, 2012.

[42] X. Ma, J. Kofler, A. Qarry, N. Tetik, T. Scheidl, R. Ursin, S. Ramelow, T. Herbst, L. Ratschbacher, A. Fedrizzi, T. Jennewein, and A. Zeilinger, "A non-local quantum eraser", *arXiv:1206.6578*, 2012.

[43] F. Kaiser, T. Coudreau, P. Milman, D. B. Ostrowsky, and S. Tanzilli, "Entanglement-enabled delayed choice experiment", *Science*, vol. 338, pp. 637, 2012.

[44] C. Simon, H. de Riedmatten, M. Afzelius, N. Sangouard, H. Zbinden, and N. Gisin, "Quantum repeaters with photon pair sources and multimode memories", *Phys. Rev. Lett.*, vol. 98, no. 19, pp. 190503, 2007.

[45] M. D. Eisaman, J. Fan, A. Migdall, and S. V. Polyakov, "Invited review article: Single-photon sources and detectors", *Rev. Sci. Instrum.*, vol. 82, pp. 071101, 2011, and references therein.

[46] C. Simon, M. Afzelius, J. Appel, A. Boyer de la Giroday, S. J. Dewhurst, N. Gisin, C. Y. Hu, F. Jelezko, S. Kröll, J. H. Müller, J. Nunn, E. S. Polzik, J. G. Rarity, H. De Riedmatten, W. Rosenfeld, A. J. Shields, N. Sköld, R. M. Stevenson, R. Thew, I. A. Walmsley, M. C. Weber, H. Weinfurter, J. Wrachtrup, and R. J. Young, "Quantum memories", *Eur. Phys. J. D*, vol. 58, no. 1, pp. 1–22, 2010.

[47] D. Stucki, N. Walenta, F. Vannel, R. Thew, N. Gisin, H. Zbinden, S. Gray, C. R. Towery, and S. Ten, "High rate, long-distance quantum key distribution over 250 km of ultra low loss fibres", *New J. Phys.*, vol. 11, pp. 075003, 2009.

[48] S. Tanzilli, A. Martin, F. Kaiser, M. P. De Micheli, O. Alibart, and D. B. Ostrowsky, "On the genesis and evolution of integrated quantum optics", *Laser & Photon. Rev.*, vol. 6, pp. 115–143, 2012.

[49] N. Piro, *Controlled absorption of heralded single photons by a single atom: Towards entanglement distribution in quantum networks*, PhD thesis, Universitat Politècnica de Catalunya, 2010.

[50] N. Piro, F. Rohde, C. Schuck, M. Almendros, J. Huwer, J. Ghosh, A. Haase, M. Hennrich, F. Dubin, and J. Eschner, "Heralded single-photon absorption by a single atom", *Nature Phys.*, vol. 7, pp. 17–20, 2011.

[51] M. Lettner, M. Mücke, S. Riedl, C. Vo, C. Hahn, S. Baur, J. Bochmann, S. Ritter, S. Dürr, and G. Rempe, "Remote entanglement between a single atom and a Bose-Einstein condensate", *Phys. Rev. Lett.*, vol. 106, pp. 210503, 2011.

[52] N. Piro, A. Haase, M. W. Mitchell, and J. Eschner, "An entangled photon source for resonant single-photon-single-atom interaction", *J. Phys. B: At. Mol. Opt. Phys.*, vol. 42, pp. 114002, June 2009.

[53] C. Clausen, I. Usmani, F. Bussieres, N. Sangouard, M. Afzelius, H. de Riedmatten, and N. Gisin, "Quantum storage of photonic entanglement in a crystal", *Nature*, vol. 469, no. 7331, pp. 508–511, 2011.

[54] E. Saglamyurek, N. Sinclair, J. Jin, J. A. Slater, D. Oblak, F. Bussieres, M. George, R. Ricken, W. Sohler, and W. Tittel, "Broadband waveguide quantum memory for entangled photons", *Nature*, vol. 469, no. 7331, pp. 512–515, 2011.

[55] S. Tanzilli, H. de Riedmatten, W. Tittel, H. Zbinden, P. Baldi, M. P. De Micheli, D. B. Ostrowsky, and N. Gisin, "Highly efficient photon-pair source using a periodically poled lithium niobate waveguide", *Electron. Lett.*, vol. 37, pp. 26–28, 2001.

[56] K. Sanaka, K. Kawahara, and T. Kuga, "New High-Efficiency source of photon pairs for engineering quantum entanglement", *Phys. Rev. Lett.*, vol. 86, no. 24, pp. 5620, 2001.

[57] S. Tanzilli, W. Tittel, H. De Riedmatten, H. Zbinden, P. Baldi, M. De Micheli, D.B. Ostrowsky, and N. Gisin, "PPLN waveguide for quantum communication", *Eur. Phys. J. D*, vol. 18, no. 2, pp. 155–160, 2002.

[58] M. Halder, A. Beveratos, N. Gisin, V. Scarani, C. Simon, and H. Zbinden, "Entangling independent photons by time measurement", *Nature Phys.*, vol. 3, no. 10, pp. 692–695, 2007.

[59] F. Kaiser, A. Issautier, L. A. Ngah, O. Danila, H. Herrmann, W. Sohler, A. Martin, and S. Tanzilli, "High-quality polarization entanglement state preparation and manipulation in standard telecommunication channels", *New J. Phys.*, vol. 14, pp. 085015, 2012.

[60] A. Martin, F. Kaiser, A. Vernier, A. Beveratos, V. Scarani, and S. Tanzilli, "Cross time-bin photonic entanglement for quantum key distribution", *arXiv:1207.6586*, 2012, Accepted in Phys. Rev. A for publication (2013).

[61] K.-I. Yoshino, M. Fujiwara, A. Tanaka, S. Takahashi, Y. Nambu, A. Tomita, S. Miki, T. Yamashita, Z. Wang, M. Sasaki, and A. Tajima, "High-speed wavelength-division multiplexing quantum key distribution system", *Opt. Lett.*, vol. 37, pp. 223–225, 2012.

[62] S. Tanzilli, W. Tittel, M. Halder, O. Alibart, P. Baldi, N. Gisin, and H. Zbinden, "A photonic quantum information interface", *Nature*, vol. 437, no. 7055, pp. 116–120, 2005.

[63] R. Lauro, T. Chanelière, and J. L. Le Gouët, "Slow light using spectral hole burning in a Tm^{3+}-doped yttrium-aluminum-garnet crystal", *Phys. Rev. A*, vol. 79, pp. 063844, 2009.

[64] F. Kaiser, A. Issautier, L. A. Ngah, O. Alibart, A. Martin, and S. Tanzilli, "A versatile source of polarisation entangled photons for quantum network applications", *arXiv:1111:5683*, 2011, Accepted for publication in Laser Phys. Lett. (2013).

[65] R. Ionicioiu and D. R. Terno, "Proposal for a quantum delayed-choice experiment", *Phys. Rev. Lett.*, vol. 107, pp. 230406, 2011.

[66] M. Schirber, "Another step back for wave-particle duality", *Physics*, vol. 4, pp. 102, 2011.

[67] H. Buhrman, R. Cleve, and R. Van Dam, "Quantum entanglement and communication complexity", *Siam J. Comput*, vol. 30, no. 6, pp. 1829–1841, 1998, Albert Einstein in a letter to Niels Bohr.

[68] C. Herrmann and M. Armbruster, "Geschichte der Kommunikation", 2004, Universität Potsdam (Leitung: Klaus Rebensburg).

[69] "Milestones: The first submarine transatlantic telephone cable system (TAT-1), 1956", *http* : *//www.ieeeghn.org*, 2012.

[70] M. A. Nielsen and I. L. Chuang, *Quantum computation and quantum information*, Cambridge Univ. Press, Cambridge, 2000.

[71] S. Singh, *The Code Book: The Science of Secrecy from Ancient Egypt to Quantum Cryptography*, Anchor, 2000, available in French under the title "Histoire des codes secrets : de l'Égypte des Pharaons à l'ordinateur quantique".

[72] A. Kerckhoffs, "La cryptographie militaire", *Journal des sciences militaires*, vol. 9, no. 1, pp. 5–38, 1883.

[73] G. S. Vernam, "Secret signaling system", 1919, US Patent 1,310,719.

[74] C. E. Shannon, "Communication theory of secrecy systems", *Bell Syst. Tech. J.*, vol. 28, no. 4, pp. 656–715, 1949.

[75] D. R. Stinson, *Cryptography: Theory and Practice*, CRC Press, 1995.

[76] R. S. Maddocks, S. Matthews, E. W. Walker, and C. H. Vincent, "A compact and accurate generator for truly random binary digits", *J. Phys. E: Sci. Instrum.*, vol. 5, pp. 542, 1972.

[77] A. Stefanov, N. Gisin, O. Guinnard, L. Guinnard, and H. Zbinden, "Optical quantum random number generator", *J. Mod. Optic.*, vol. 47, no. 4, pp. 595, 2000.

[78] T. Jennewein, U. Achleitner, G. Weihs, H. Weinfurter, and A. Zeilinger, "A fast and compact quantum random number generator", *Rev. Sci. Instrum.*, vol. 71, pp. 1675, 2000.

[79] A. Uchiada, K. Amano, M. Inoue, K. Hoirano, S. Naito, H. Someya, I. Oowada, T. Kurashige, M. Shiki, S. Yoshimori, K. Yoshimura, and P. Davis, "Fast physical random bit generation with chaotic semiconductor lasers", *Nature Photon.*, vol. 2, pp. 728–732, 2008.

[80] T. E. Murphy and R. Rajarshi, "Chaotic lasers: The world's fastest dice", *Nature Photon.*, vol. 2, pp. 714–715, 2008.

[81] I. Reidler, Y. Aviad, M. Rosenbluh, and I. Kanter, "Ultrahigh-speed random number generation based on a chaotic semiconductor laser", *Phys. Rev. Lett.*, vol. 103, pp. 024102, 2009.

[82] I. Kanter, Y. Aviad, I. Reidler, E. Cohen, and M. Rosenbluh, "An optical ultrafast random bit generator", *Nature Photon.*, vol. 4, pp. 58, 2010.

[83] R. L. Rivest, A. Shamir, and L. Adleman, "A method for obtaining digital signatures and public-key cryptosystems", *Com. of the ACM*, vol. 21, no. 2, pp. 120–126, 1978.

[84] T. Kleinjung, K. Aoki, J. Franke, A. Lenstra, E. Thomé, J. Bos, P. Gaudry, A. Kruppa, P. Montgomery, D. A. Osvik, H. te Riele, A. Timofeev, and P. Zimmermann, "Factorization of a 768-bit rsa modulus", *Cryptology ePrint Archive*, 2010, `http://eprint.iacr.org/`.

[85] T. Kleinjung, J. W. Bos, A. K. Lenstra, D. A. Osvik, K. Aoki, S. Contini, J. Franke, E. Thomé, P. Jermini, M. Thiémard, P. Leyland, P. L. Montgomery, A. Timofeev, and H. Stockinger, "A heterogeneous computing environment to solve the 768-bit RSA challenge", *Cluster Computing*, vol. , pp. 1–16, 2010.

[86] "NIST recommendation for RSA key lengths.", 2007, `http://csrc.nist.gov/publications/nistpubs/800-57/sp800-57-Part1-revised2_Mar08-2007.pdf` , page 66.

[87] W. K. Wootters and W. H. Zurek, "A single quantum cannot be cloned", *Nature*, vol. 299, pp. 802–803, 1982.

[88] S. Wiesner, "Conjugate coding", *Sigact News*, vol. 15, no. 1, pp. 78–88, 1983.

[89] V. Scarani, S. Iblisdir, N. Gisin, and A. Acín, "Quantum cloning", *Rev. Mod. Phys.*, vol. 77, no. 4, pp. 1225, 2005.

[90] V. Scarani, L. Chua, and S. Y. Liu, *Six Quantum Pieces: A First Course in Quantum Physics*, World Scientific Publishing Company, 2010.

[91] W. Tittel and G. Weihs, "Photonic entanglement for fundamental tests and quantum communication", *Quant. Inf. Comp.*, vol. 1, pp. 3–56, 2001.

[92] Y. Makhlin, G. Scohn, and A. Shnirman, "Josephson-junction qubits with controlled couplings", *Nature*, vol. 398, no. 6725, pp. 305–307, 1999.

[93] Y. Kubo, F. R. Ong, P. Bertet, D. Vion, V. Jacques, D. Zheng, A. Dréau, J.-F. Roch, A. Auffeves, F. Jelezko, J. Wrachtrup, M. F. Barthe, P. Bergonzo, and D. Esteve, "Strong coupling of a spin ensemble to a superconducting resonator", *Phys. Rev. Lett.*, vol. 105, pp. 140502, 2010.

[94] C. Monroe, D. M. Meekhof, B. E. King, W. M. Itano, and D. J. Wineland, "Demonstration of a fundamental quantum logic gate", *Phys. Rev. Lett.*, vol. 75, pp. 4714–4717, 1995.

[95] F. Schmidt-Kaler, H. Häffner, M. Riebe, S. Gulde, G. P. T. Lancaster, T. Deuschle, C. Becher, C. F. Roos, J. Eschner, and R. Blatt, "Realization of the Cirac-Zoller controlled-NOT gate", *Nature*, vol. 422, pp. 408–411, 2003.

[96] D. Leibfried, B. DeMarco, V. Meyer, D. Lucas, M. Barrett, J. Britton, W. M. Itano, B. Jelenkovic, C. Langer, T. Rosenband, and D. J. Wineland, "Experimental demonstration of a robust, high-fidelity geometric two ion-qubit phase gate", *Nature*, vol. 422, pp. 412–415, 2003.

[97] M. Barrett, J. Chiaverini, T. Schaetz, J. Britton, W. M. Itano, J. D. Jost, E. Knill, C. Langer, D. Leibfried, R. Ozeri, and D. J. Wineland, "Deterministic quantum teleportation of atomic qubits", *Nature*, vol. 429, pp. 737–739, 2004.

[98] D. Leibfried, E. Knill, S. Seidelin, J. Britton, R. B. Blakestad, J. Chiaverini, D. B. Hume, W. M. Itano, J. D. Jost, C. Langer, R. Ozeri, R. Reichle, and D. J. Wineland, "Creation of a six-atom 'Schrödinger cat' state", *Nature*, vol. 438, pp. 639–642, 2005.

[99] J. Beugnon, M. P. A. Jones, J. Dingjan, B. Darquie, G. Messin, A. Browaeys, and P. Grangier, "Quantum interference between two single photons emitted by independently trapped atoms", *Nature*, vol. 440, pp. 779–782, 2006.

[100] T. Wilk, A. Gaëtan, C. Evellin, J. Wolters, Y. Miroshnychenko, P. Grangier, and A. Browaeys, "Entanglement of two individual neutral atoms using Rydberg blockade", *Phys. Rev. Lett.*, vol. 104, pp. 010502, 2010.

[101] L. Isenhower, E. Urban, X. L. Zhang, A. T. Gill, T. Henage, T. A. Johnson, T. G. Walker, and M. Saffman, "Demonstration of a neutral atom controlled-not quantum gate", *Phys. Rev. Lett.*, vol. 104, pp. 010503, 2010.

[102] S. Ritter, C. Nölleke, C. Hahn, A. Reiserer, A. Neuzner, M. Uphoff, M. Mücke, E. Figueroa, J. Bochmann, and G. Rempe, "An elementary quantum network of single atoms in optical cavities", *Nature*, vol. 484, pp. 195–200, 2012.

[103] P. Neumann, N. Mizuochi, F. Rempp, P. Hemmer, H. Watanabe, S. Yamasaki, V. Jacques, T. Gaebel, F. Jelezko, and J. Wrachtrup, "Multipartite entanglement among single spins in diamond", *Science*, vol. 320, pp. 1326–1329, 2008.

[104] H. de Riedmatten, M. Afzelius, M. U. Staudt, C. Simon, and N. Gisin, "A solid-state light-matter interface at the single-photon level", *Nature*, vol. 456, no. 7223, pp. 773–777, 2008.

[105] N. Akopian, L. Wang, A. Rastelli, O. G. Schmidt, and V. Zwiller, "Hybrid semiconductor-atomic interface: slowing down single photons from a quantum dot", *Nature Photon.*, vol. 5, no. 4, pp. 230–233, 2011.

[106] Y.-W. Cho and Y.-H. Kim, "Atomic vapor quantum memory for a photonic polarization qubit", *Opt. Express*, vol. 18, no. 25, pp. 25786–25793, 2010.

[107] D. G. England, P. S. Michelberger, T. F. M. Champion, K. F. Reim, K. C. Lee, M. R. Sprague, X.-M. Jin, N. K. Langford, W. S. Kolthammer, J. Nunn, and I. A. Walmsley, "High-fidelity polarization storage in a gigahertz bandwidth quantum memory", *J. Phys. B: At., Mol. Opt. Phys.*, vol. 45, no. 12, pp. 124008, June 2012.

[108] K. F. Reim, J. Nunn, V. O. Lorenz, B. J. Sussman, K. C. Lee, N. K. Langford, D. Jaksch, and I. A. Walmsley, "Towards high-speed optical quantum memories", *Nature Photon.*, vol. 4, no. 4, pp. 218–221, 2010.

[109] K. S. Choi, H. Deng, J. Laurat, and H. J. Kimble, "Mapping photonic entanglement into and out of a quantum memory", *Nature*, vol. 452, no. 7183, pp. 67–71, 2008.

[110] H. P. Specht, C. Nolleke, A. Reiserer, M. Uphoff, E. Figueroa, S. Ritter, and G. Rempe, "A single-atom quantum memory", *Nature*, vol. 473, no. 7346, pp. 190–193, 2011.

[111] X.-H. Bao, A. Reingruber, P. Dietrich, J. Rui, A. Dück, T. Strassel, L. Li, N.-L. Liu, B. Zhao, and J.-W. Pan, "Efficient and long-lived quantum memory with cold atoms inside a ring cavity", *Nature Phys.*, 2012.

[112] A. T. Black, J. K. Thompson, and V. Vuletic, "On-demand superradiant conversion of atomic spin gratings into single photons with high efficiency", *Phys. Rev. Lett.*, vol. 95, no. 13, pp. 133601, 2005.

[113] T. Chanelière, D. N. Matsukevich, S. D. Jenkins, S.-Y. Lan, T. A. B. Kennedy, and A. Kuzmich, "Storage and retrieval of single photons transmitted between remote quantum memories", *Nature*, vol. 438, no. 7069, pp. 833–836, 2005.

[114] Y.-A. Chen, S. Chen, Z.-S. Yuan, B. Zhao, C.-S. Chuu, J. Schmiedmayer, and J.-W. Pan, "Memory-built-in quantum teleportation with photonic and atomic qubits", *Nature Phys.*, vol. 4, no. 2, pp. 103–107, 2008.

[115] K. S. Choi, A. Goban, S. B. Papp, S. J. van Enk, and H. J. Kimble, "Entanglement of spin waves among four quantum memories", *Nature*, vol. 468, no. 7322, pp. 412–416, 2010.

[116] C. W. Chou, H. de Riedmatten, D. Felinto, S. V. Polyakov, S. J. van Enk, and H. J. Kimble, "Measurement-induced entanglement for excitation stored in remote atomic ensembles", *Nature*, vol. 438, no. 7069, pp. 828–832, 2005.

[117] C.-W. Chou, J. Laurat, H. Deng, K. S. Choi, H. de Riedmatten, D. Felinto, and H. J. Kimble, "Functional quantum nodes for entanglement distribution over scalable quantum networks", *Science*, vol. 316, no. 5829, pp. 1316 –1320, 2007.

[118] J. Laurat, "Heralding the storage of light", *Physics*, vol. 2, pp. 62, 2009.

[119] D. Moretti, D. Felinto, and J. W. R. Tabosa, "Pulse pair generation from coherently prepared atomic ensembles", *Eur. Phys. J. D*, vol. 60, no. 2, pp. 373–382, 2010.

[120] A. G. Radnaev, Y. O. Dudin, R. Zhao, H. H. Jen, S. D. Jenkins, A. Kuzmich, and T. A. B. Kennedy, "A quantum memory with telecom-wavelength conversion", *Nature Phys.*, vol. 6, no. 11, pp. 894–899, November 2010.

[121] J. Simon, H. Tanji, J. K. Thompson, and V. Vuletic, "Interfacing collective atomic excitations and single photons", *Phys. Rev. Lett.*, vol. 98, no. 18, pp. 183601, 2007.

[122] H. Wang, S. Li, Z. Xu, X. Zhao, L. Zhang, J. Li, Y. Wu, C. Xie, K. Peng, and M. Xiao, "Quantum interference of stored dual-channel spin-wave excitations in a single tripod system", *Phys. Rev. A*, vol. 83, no. 4, pp. 043815, 2011.

[123] H. Zhang, X.-M. Jin, J. Yang, H.-N. Dai, S.-J. Yang, T.-M. Zhao, J. Rui, Y. He, X. Jiang, F. Yang, G.-S. Pan, Z.-S. Yuan, Y. Deng, Z.-B. Chen, X.-H. Bao, S. Chen, B. Zhao, and J.-W. Pan, "Preparation and storage of frequency-uncorrelated entangled photons from cavity-enhanced spontaneous parametric downconversion", *Nature Photon.*, vol. 5, no. 10, pp. 628–632, 2011.

[124] B. Zhao, Y.-A. Chen, X.-H. Bao, T. Strassel, C.-S. Chuu, X.-M. Jin, J. Schmiedmayer, Z.-S. Yuan, S. Chen, and J.-W. Pan, "A millisecond quantum memory for scalable quantum networks", *Nature Phys.*, vol. 5, no. 2, pp. 95–99, 2009.

[125] R. Zhao, Y. O. Dudin, S. D. Jenkins, C. J. Campbell, D. N. Matsukevich, T. A. B. Kennedy, and A. Kuzmich, "Long-lived quantum memory", *Nature Phys.*, vol. 5, no. 2, pp. 100–104, 2009.

[126] A. I. Lvovsky, B. C. Sanders, and W. Tittel, "Optical quantum memory", *Nature Photon.*, vol. 3, no. 12, pp. 706–714, 2009.

[127] N. Sangouard, C. Simon, H. de Riedmatten, and N. Gisin, "Quantum repeaters based on atomic ensembles and linear optics", *Rev. Mod. Phys.*, vol. 83, pp. 33–80, 2011.

[128] N. G Walker and G. R. Walker, "Polarization control for coherent communications", *J. Lightwave Technol.*, vol. 8, no. 3, pp. 438–458, 1990.

[129] C. Z. Peng, J. Zhang, D. Yang, W. B. Gao, H. X. Ma, H. Yin, H. P. Zeng, T. Yang, X. B. Wang, and J. W. Pan, "Experimental Long-Distance Decoy-State quantum key distribution based on polarization encoding", *Phys. Rev. Lett.*, vol. 98, no. 1, pp. 010505, 2007.

[130] J. Chen, G. Wu, Y. Li, E. Wu, and H. Zeng, "Active polarization stabilization in optical fibers suitable for quantum keydistribution", *Opt. Express*, vol. 15, no. 26, pp. 17928–17936, 2007.

[131] G. B. Xavier, N. Walenta, G. Vilela de Faria, G. P. Temporão, N. Gisin, H. Zbinden, and J. P. von der Weid, "Experimental polarization encoded quantum key distribution over optical fibres with real-time continuous birefringence compensation", *New J. Phys.*, vol. 11, no. 4, pp. 045015, 2009.

[132] J. D. Franson, "Bell inequality for position and time", *Phys. Rev. Lett.*, vol. 62, no. 19, pp. 2205–2208, 1989.

[133] J. Brendel, E. Mohler, and W. Martienssen, "Experimental test of Bell's inequality for energy and time", *Europhys. Lett.*, vol. 20, pp. 575, 1992.

[134] J. Brendel, N. Gisin, W. Tittel, and H. Zbinden, "Pulsed Energy-Time entangled Twin-Photon source for quantum communication", *Phys. Rev. Lett.*, vol. 82, no. 12, pp. 2594, 1999.

[135] D. Boschi, S. Branca, F. De Martini, L. Hardy, and S. Popescu, "Experimental realization of teleporting an unknown pure quantum state via dual classical and Einstein-Podolsky-Rosen channels", *Phys. Rev. Lett.*, vol. 80, pp. 1121–1125, 1998.

[136] S. Ramelow, L. Ratschbacher, A. Fedrizzi, N. K. Langford, and A. Zeilinger, "Discrete tunable color entanglement", *Phys. Rev. A*, vol. 103, no. 25, pp. 253601, 2009.

[137] L. Olislager, J. Cussey, A. T. Nguyen, P. Emplit, S. Massar, J.-M. Merolla, and K. P. Huy, "Frequency-bin entangled photons", *Phys. Rev. A*, vol. 82, no. 1, pp. 013804, 2010.

[138] L. Olislager, J. Cussey, A. T. Nguyen, P. Emplit, S. Massar, J.-M. Merolla, and K. P. Huy, *Manipulating Frequency Entangled Photons*, vol. 36, Springer Berlin Heidelberg, Berlin, Heidelberg, 2010.

[139] L. Olislager, I. Mbodji, E. Woodhead, J. Cussey, L. Furfaro, P. Emplit, S. Massar, K. P. Huy, and J.-M. Merolla, "Reliable and efficient control of two-photon interference in the frequency domain", *arXiv:1107.5519*, 2011.

[140] A. Mair, A. Vaziri, G. Weihs, and A. Zeilinger, "Entanglement of the orbital angular momentum states of photons", *Nature*, vol. 412, no. 6844, pp. 313–316, 2001.

[141] Y.-H. Kim, "Single-photon two-qubit entangled states: Preparation and measurement", *Phys. Rev. A*, vol. 67, no. 4, pp. 040301, 2003.

[142] M. N. O'Sullivan-Hale, I. Ali Khan, R. W. Boyd, and J. C. Howell, "Pixel entanglement: Experimental realization of optically entangled d=3 and d=6 qudits", *Phys. Rev. Lett.*, vol. 94, no. 22, pp. 220501, 2005.

[143] Y. I. Bogdanov, E. V. Moreva, G. A. Maslennikov, R. F. Galeev, S. S. Straupe, and S. P. Kulik, "Polarization states of four-dimensional systems based on biphotons", *Phys. Rev. A*, vol. 73, no. 6, pp. 063810, 2006.

[144] G. Vallone, E. Pomarico, P. Mataloni, F. De Martini, and V. Berardi, "Realization and characterization of a Two-Photon Four-Qubit linear cluster state", *Phys. Rev. Lett.*, vol. 98, no. 18, pp. 180502, 2007.

[145] S.-Y. Baek and Y.-H. Kim, "Generating entangled states of two ququarts using linear optical elements", *Phys. Rev. A*, vol. 75, no. 3, pp. 034309, 2007.

[146] G. Vallone, R. Ceccarelli, F. De Martini, and P. Mataloni, "Hyperentanglement of two photons in three degrees of freedom", *Phys. Rev. A*, vol. 79, no. 3, pp. 030301, 2009.

[147] N. Lütkenhaus, "Security against individual attacks for realistic quantum key distribution", *Phys. Rev. A*, vol. 61, no. 5, pp. 052304, 2000.

[148] R. Renner, N. Gisin, and B. Kraus, "Information-theoretic security proof for quantum-key-distribution protocols", *Phys. Rev. A*, vol. 72, no. 1, pp. 012332, 2005.

[149] H. Inamori, N. Lütkenhaus, and D. Mayers, "Unconditional security of practical quantum key distribution", *Eur. Phys. J. D*, vol. 41, no. 3, pp. 599–627, 2007.

[150] A. Acín, N. Brunner, N. Gisin, S. Massar, S. Pironio, and V. Scarani, "Device-Independent security of quantum cryptography against collective attacks", *Phys. Rev. Lett.*, vol. 98, no. 23, pp. 230501, 2007.

[151] S. Pironio, A. Acín, N. Brunner, N. Gisin, S. Massar, and V. Scarani, "Device-independent quantum key distribution secure against collective attacks", *New J. Phys.*, vol. 11, no. 4, pp. 045021, 2009.

[152] C. H. Bennett, "Quantum cryptography using any two nonorthogonal states", *Phys. Rev. Lett.*, vol. 68, no. 21, pp. 3121, 1992.

[153] K. M. Rosfjord, J. K. W. Yang, E. A. Dauler, A. J. Kerman, V. Anant, B. M. Voronov, G. N. Gol'tsman, and K. K. Berggren, "Nanowire single-photon detector with an integrated optical cavity and anti-reflection coating", *Opt. Express*, vol. 14, pp. 527–534, 2006.

[154] R. H. Hadfield, "Single-photon detectors for optical quantum information applications", *Nature Photon.*, vol. 3, no. 12, pp. 696–705, 2009.

[155] A. Martin, *Puce photonique pour les communications quantiques longues distances*, PhD thesis, University of Nice - Sophia Antipolis (France), 2011.

[156] D. Bouwmeester, J. W. Pan, K. Mattle, M. Eibl, H. Weinfurter, and A. Zeilinger, "Experimental quantum teleportation", *Nature*, vol. 390, no. 6660, pp. 575–579, 1997.

[157] I. Marcikic, H. de Riedmatten, W. Tittel, H. Zbinden, and N. Gisin, "Long-distance teleportation of qubits at telecommunication wavelengths", *Nature (London)*, vol. 421, pp. 509–513, 2003.

[158] H. de Riedmatten, I. Marcikic, W. Tittel, H. Zbinden, D. Collins, and N. Gisin, "Long distance quantum teleportation in a quantum relay configuration", *Phys. Rev. Lett.*, vol. 92, no. 4, pp. 047904, 2004.

[159] J. A. W. van Houwelingen, N. Brunner, A. Beveratos, H. Zbinden, and N. Gisin, "Quantum teleportation with a three-Bell-state analyzer", *Phys. Rev. Lett.*, vol. 96, pp. 130502, 2006.

[160] X. Ma, T. Herbst, T. Scheidl, W. Daqing, S. Kropatschek, W. Naylor, B. Wittmann, A. Mech, J. Kofler, E. Anisimova, V. Makarov, T. Jennewein, R. Ursin, and A. Zeilinger, "Quantum teleportation over 143 kilometres using active feed-forward", *Nature*, vol. 489, pp. 269–273, 2012.

[161] D. Collins, N. Gisin, and H. de Riedmatten, "Quantum relays for long distance quantum cryptography", *J. Mod. Opt.*, vol. 52, pp. 735–753, 2005.

[162] H. de Riedmatten, I. Marcikic, J. A. W. van Houwelingen, W. Tittel, H. Zbinden, and N. Gisin, "Long-distance entanglement swapping with photons from separated sources", *Phys. Rev. A*, vol. 71, no. 5, pp. 050302, 2005.

[163] A. R. Wilson, J. Lowe, and D. K. Butt, "Measurement of the relative planes of polarization of annihilation quanta as a function of separation distance", *J. Phys. G*, vol. 2, no. 9, pp. 613, 1976.

[164] J. F. Clauser, "Experimental investigation of a polarization correlation anomaly", *Phys. Rev. Lett.*, vol. 36, pp. 1223–1226, 1976.

[165] E. S. Fry and R. C. Thompson, "Experimental test of local hidden-variable theories", *Phys. Rev. Lett.*, vol. 37, pp. 465–468, 1976.

[166] M. Lamehi-Rachti and W. Mittig, "Quantum mechanics and hidden variables: A test of Bell's inequality by the measurement of the spin correlation in low-energy proton-proton scattering", *Phys. Rev. D*, vol. 14, pp. 2543–2555, 1976.

[167] A. Aspect, P. Grangier, and G. Roger, "Experimental realization of Einstein-Podolsky-Rosen-Bohm Gedankenexperiment: A new violation of Bell's inequalities", *Phys. Rev. Lett.*, vol. 49, no. 2, pp. 91–94, 1982.

[168] P. G. Kwiat, K. Mattle, H. Weinfurter, A. Zeilinger, A. V. Sergienko, and Y. Shih, "New High-Intensity source of Polarization-Entangled photon pairs", *Phys. Rev. Lett.*, vol. 75, no. 24, pp. 4337–4341, 1995.

[169] P. G. Kwiat, E. Waks, A. G. White, I. Appelbaum, and P. H. Eberhard, "Ultrabright source of polarization-entangled photons", *Phys. Rev. A*, vol. 60, no. 2, pp. R773–R776, 1999.

[170] Y. H. Shih and C. O. Alley, "New type of Einstein-Podolsky-Rosen-Bohm experiment using pairs of light quanta produced by optical parametric down conversion", *Phys. Rev. Lett.*, vol. 61, pp. 2921–2924, 1988.

[171] J. G. Rarity and P. R. Tapster, "Experimental violation of Bell's inequality based on phase and momentum", *Phys. Rev. Lett.*, vol. 64, pp. 2495–2498, 1990.

[172] J. Brendel, E. Mohler, and W. Martienssen, "Time-resolved dual-beam two-photon interferences with high visibility", *Phys. Rev. Lett.*, vol. 66, pp. 1142–1145, 1991.

[173] J. G. Rarity, J. Burnett, P. R. Tapster, and R. Paschotta, "High-visibility two-photon interference in a single-mode-fibre interferometer", *Europhys. Lett.*, vol. 22, pp. 95, 1993.

[174] P. G. Kwiat, A. M. Steinberg, and R. Y. Chiao, "High-visibility interference in a Bell-inequality experiment for energy and time", *Phys. Rev. A*, vol. 47, no. 4, pp. R2472–R2475, 1993.

[175] P. R. Tapster, J. G. Rarity, and P. C. M. Owens, "Violation of Bell's inequality over 4 km of optical fiber", *Phys. Rev. Lett.*, vol. 73, pp. 1923–1926, 1994.

[176] W. Tittel, J. Brendel, B. Gisin, T. Herzog, H. Zbinden, and N. Gisin, "Experimental demonstration of quantum correlations over more than 10 km", *Phys. Rev. A*, vol. 57, no. 5, pp. 3229, May 1998.

[177] W. Tittel, J. Brendel, H. Zbinden, and N. Gisin, "Violation of Bell inequalities by photons more than 10 km apart", *Phys. Rev. Lett.*, vol. 81, pp. 3563–3566, 1998.

[178] W. Tittel, J. Brendel, N. Gisin, and H. Zbinden, "Long-distance Bell-type tests using energy-time entangled photons", *Phys. Rev. A*, vol. 59, no. 6, pp. 4150–4163, 1999.

[179] A. Martin, V. Cristofori, P. Aboussouan, H. Herrmann, W. Sohler, D. B. Ostrowsky, O. Alibart, and S. Tanzilli, "Integrated optical source of polarization entangled photons at 1310 nm", *Opt. Express*, vol. 17, no. 2, pp. 1033–1041, 2009.

[180] T. Zhong, F. N. Wong, T. D. Roberts, and P. Battle, "High performance photon-pair source based on a fiber-coupled periodically poled $KTiOPO_4$ waveguide", *Opt. Express*, vol. 17, no. 14, pp. 12019–12030, 2009.

[181] A. Martin, A. Issautier, H. Herrmann, W. Sohler, D. B. Ostrowsky, O. Alibart, and S. Tanzilli, "A polarization entangled photon-pair source based on a type-II PPLN waveguide emitting at a telecom wavelength", *New J. Phys.*, vol. 12, no. 10, pp. 103005, 2010.

[182] T. Zhong, X. Hu, F. N. C. Wong, K. K. Berggren, T. D. Roberts, and P. Battle, "High-quality fiber-optic polarization entanglement distribution at 1.3 um telecom wavelengths", *Opt. Lett.*, vol. 35, no. 9, pp. 1392–1394, 2010.

[183] A. Yoshizawa, R. Kaji, and H. Tsuchida, "Generation of polarisation-entangled photon pairs at 1550 nm using two PPLN waveguides.", *Electron. Lett.*, vol. 39, no. 7, pp. 621, 2003.

[184] Y.-H. Kim, S. P. Kulik, and Y. Shih, "High-intensity pulsed source of space-time and polarization double-entangled photon pairs", *Phys. Rev. A*, vol. 62, no. 1, pp. 011802, 2000.

[185] H. Takesue, K. Inoue, O. Tadanaga, Y. Nishida, and M. Asobe, "Generation of pulsed polarization-entangled photon pairs in a 1.55-μm band with a periodically poled lithium niobate waveguide and anorthogonal polarization delay circuit", *Opt. Lett.*, vol. 30, no. 3, pp. 293–295, 2005.

[186] Y.-K. Jiang and A. Tomita, "The generation of polarization-entangled photon pairs using periodically poled lithium niobate waveguides in a fibre loop", *J. Phys. B: At. Mol. Opt. Phys.*, vol. 40, no. 2, pp. 437–443, 2007.

[187] M. Hentschel, H. Hübel, A. Poppe, and A. Zeilinger, "Three-color Sagnac source of polarization-entangled photon pairs", *Opt. Express*, vol. 17, no. 25, pp. 23153–23159, 2009.

[188] H. Takesue and K. Inoue, "Generation of polarization-entangled photon pairs and violation of Bell's inequality using spontaneous four-wave mixing in a fiber loop", *Phys. Rev. A*, vol. 70, no. 3, pp. 031802, 2004.

[189] X. Li, P. L. Voss, J. E. Sharping, and P. Kumar, "Optical-Fiber source of Polarization-Entangled photons in the 1550 nm telecom band", *Phys. Rev. Lett.*, vol. 94, no. 5, pp. 053601, 2005.

[190] K. F. Lee, J. Chen, C. Liang, X. Li, P. L. Voss, and P. Kumar, "Generation of high-purity telecom-band entangled photon pairs in dispersion-shifted fiber", *Opt. Lett.*, vol. 31, no. 12, pp. 1905–1907, 2006.

[191] X. Li, C. Liang, K. F. Lee, J. Chen, P. L. Voss, and P. Kumar, "Integrable optical-fiber source of polarization-entangled photon pairs in the telecom band", *Phys. Rev. A*, vol. 73, no. 5, pp. 052301–6, 2006.

[192] J. Fulconis, O. Alibart, J. L. O'Brien, W. J. Wadsworth, and J. G. Rarity, "Non-classical interference and entanglement generation using a photonic crystal fiber pair photon source", *Phys. Rev. Lett.*, vol. 99, no. 12, pp. 120501, 2007.

[193] O. Cohen, J. S. Lundeen, B. J. Smith, G. Puentes, P. J. Mosley, and I. A. Walmsley, "Tailored Photon-Pair generation in optical fibers", *Phys. Rev. Lett.*, vol. 102, no. 12, pp. 123603–4, 2009.

[194] M. Medic, J. B. Altepeter, M. A. Hall, M. Patel, and P. Kumar, "Fiber-based telecommunication-band source of degenerate entangled photons", *Opt. Lett.*, vol. 35, no. 6, pp. 802–804, 2010.

[195] H. Takesue and K. Inoue, "1.5-μm band quantum-correlated photon pair generation in dispersion-shifted fiber: suppression of noise photons by cooling fiber", *Opt. Express*, vol. 13, no. 20, pp. 7832–7839, 2005.

[196] S. D. Dyer, J. S. Martin, B. Baek, and S. W. Nam, "High-efficiency, ultra low-noise all-fiber photon-pair source", *Opt. Express*, vol. 16, no. 13, pp. 9966–9977, 2008.

[197] X. Caillet, A. Orieux, A. Lemaître, P. Filloux, I. Favero, G. Leo, and S. Ducci, "Two-photon interference with a semiconductor integrated source at room temperature", *Opt. Express*, vol. 18, no. 10, pp. 9967–9975, 2010.

[198] P. Maunz, D. L. Moehring, S. Olmschenk, K. C. Younge, D. N. Matsukevich, and C. Monroe, "Quantum interference of photon pairs from two remote trapped atomic ions", *Nature Phys.*, vol. 3, pp. 538–541, 2007.

[199] A. Sipahigil, M. L. Goldman, E. Togan, Y. Chu, M. Markham, D. J. Twitchen, A. S. Zibrov, A. Kubanek, and M. D. Lukin, "Quantum interference of single photons from remote nitrogen-vacancy centers in diamond", *Phys. Rev. Lett.*, vol. 108, pp. 143601, 2012.

[200] H. Bernien, L. Childress, L. Robledo, M. Markham, D. Twitchen, and R. Hanson, "Two-photon quantum interference from separate nitrogen vacancy centers in diamond", *Phys. Rev. Lett.*, vol. 108, pp. 043604, 2012.

[201] A. Muller, W. Fang, J. Lawall, and G. S. Solomon, "Creating Polarization-Entangled photon pairs from a semiconductor quantum dot using the optical stark effect", *Phys. Rev. Lett.*, vol. 103, no. 21, pp. 217402–4, 2009.

[202] A. Mohan, M. Felici, P. Gallo, B. Dwir, A. Rudra, J. Faist, and E. Kapon, "Polarization-entangled photons produced with high-symmetry site-controlled quantum dots", *Nature Photon.*, vol. 4, no. 5, pp. 302–306, 2010.

[203] A. Dousse, J. Suffczynski, A. Beveratos, O. Krebs, A. Lemaitre, I. Sagnes, J. Bloch, P. Voisin, and P. Senellart, "Ultrabright source of entangled photon pairs", *Nature*, vol. 466, no. 7303, pp. 217–220, 2010.

[204] S. Ates, I. Agha, A. Gulinatte, I. Rech, T. Rakher, A. Badolato, and K. Srinivasan, "Two-photon interference using background-free quantum frequency conversion of single photons from a semiconductor quantum dot", *arXiv:1207.4226v1*, 2012.

[205] L.-M. Duan, M. D. Lukin, J. I. Cirac, and P. Zoller, "Long-distance quantum communication with atomic ensembles and linear optics", *Nauture*, vol. 414, pp. 413–418, 2001.

[206] M. S. Shahriar, P. Kumar, and P. R. Hemmer, "Connecting processing-capable quantum memories over telecommunication links via quantum frequency conversion", *J. Phys. B: At. Mol. Opt. Phys.*, vol. 45, pp. 124018, 2012.

[207] I. Usmani, C. Clausen, F. Bussieres, N. Sangouard, M. Afzelius, and N. Gisin, "Heralded quantum entanglement between two crystals", *Nature Photon.*, vol. 6, pp. 234–237, 2012.

[208] J. K. Thompson, J. Simon, H. Loh, and V. Vuletić, "A High-Brightness source of narrowband, Identical-Photon pairs", *Science*, vol. 313, no. 5783, pp. 74 –77, 2006.

[209] Z.-S. Yuan, Y.-A. Chen, S. Chen, B. Zhao, M. Koch, T. Strassel, Y. Zhao, G.-J. Zhu, J. Schmiedmayer, and J.-W. Pan, "Synchronized independent Narrow-Band single photons and efficient generation of photonic entanglement", *Phys. Rev. Lett.*, vol. 98, no. 18, pp. 180503, 2007.

[210] H. Wang, T. Horikiri, and T. Kobayashi, "Polarization-entangled mode-locked photons from cavity-enhanced spontaneous parametric down-conversion", *Phys. Rev. A*, vol. 70, no. 4, pp. 043804, 2004.

[211] C. E. Kuklewicz, F. N. C. Wong, and J. H. Shapiro, "Time-bin-modulated biphotons from cavity-enhanced down-conversion", *Phys. Rev. Lett.*, vol. 97, no. 22, pp. 223601, 2006.

[212] X.-H. Bao, Y. Qian, J. Yang, H. Zhang, Z.-B. Chen, T. Yang, and J.-W. Pan, "Generation of Narrow-Band Polarization-Entangled photon pairs for atomic quantum memories", *Phys. Rev. Lett.*, vol. 101, no. 19, pp. 190501, 2008.

[213] E. Pomarico, B. Sanguinetti, N. Gisin, R. Thew, H. Zbinden, G. Schreiber, A. Thomas, and W. Sohler, "Waveguide-based OPO source of entangled photon pairs", *New J. Phys.*, vol. 11, pp. 113042, 2009.

[214] E. Pomarico, B. Sanguinetti, C.I. Osorio, H. Herrmann, and R. Thew, "Engineering integrated pure narrow-band photon sources", *arXiv:1108.5542*, 2011.

[215] M. Halder, A. Beveratos, R. T. Thew, C. Jorel, H. Zbinden, and N. Gisin, "High coherence photon pair source for quantum communication", *New J. Phys.*, vol. 10, no. 2, pp. 023027, 2008.

[216] A. Peruzzo, P. J. Shadbolt, N. Brunner, S. Popescu, and J. L. O'Brien, "A quantum delayed choice experiment", *Science*, vol. 338, pp. 634, 2012.

[217] S. Fouchet, A. Carenco, C. Daguet, R. Guglielmi, and L. Riviere, "Wavelength dispersion of ti induced refractive index change in $LiNbO_3$ as a function of diffusion parameters", *IEEE J. Light. Tech.*, vol. 5, no. 5, pp. 700–708, 1987.

[218] W. Sohler, "Integrated optics in $LiNbO_3$", *Thin Solid Films*, vol. 175, pp. 191–200, 1989.

[219] L. Chanvillard, P. Aschiéri, P. Baldi, D. B. Ostrowsky, M. de Micheli, L. Huang, and D. J. Bamford, "Soft proton exchange on periodically poled $linbo_3$: A simple waveguide fabrication process for highly efficient nonlinear interactions", *Appl. Phys. Lett.*, vol. 76, no. 9, pp. 1089–1091, 2000.

[220] L. Chanvillard, *Interactions paramétriques guidées de grandes efficacité : utilisation de l'échange protonique doux sur niobate de lithium polarisé périodiquement*, PhD thesis, Université de Nice - Sophia Antipolis (France), 1999.

[221] G. Bertocchi, *Circuit optique sur $LiNbO_3$ pour un relais quantique intégré*, PhD thesis, Université de Nice - Sophia Antipolis (France), 2006.

[222] H. Hu, R. Ricken, and W. Sohler, "Low-loss ridge waveguides on lithium niobate fabricated by local diffusion doping with titanium", *Appl. Phys. B*, vol. 98, pp. 677–679, 2010.

[223] C. K. Hong, Z. Y. Ou, and L. Mandel, "Measurement of subpicosecond time intervals between two photons by interference", *Phys. Rev. Lett.*, vol. 59, no. 18, pp. 2044–2046, 1987.

[224] R. Ludon, *The Quantum Theory of Light*, Oxford Science Publications, 2000.

[225] A. Martin, J.-L. Smirr, F. Kaiser, E. Diamanti, A. Issautier, O. Alibart, R. Frey, I. Zaquine, and S. Tanzilli, "Analysis of elliptically polarized maximally entangled states for Bell inequality tests", *Laser Physics*, vol. 22, pp. 1105–1112, 2012.

[226] T. Suhara, H. Okabe, and M. Fujimura, "Generation of polarization-entangled photons by Type-II quasi-phase-matched waveguide nonlinear-optic device", *IEEE Photon. Technol. Lett.*, vol. 19, no. 14, pp. 1093–1095, 2007.

[227] K. Thyagarajan, C. W. Chien, R. V. Ramaswamy, H. S. Kim, and H. C. Cheng, "Proton-exchanged periodically segmented waveguides in $LiNbO_3$", *Opt. Lett.*, vol. 19, no. 12, pp. 880–882, 1994.

[228] D. Castaldini, P. Bassi, P. Aschieri, S. Tascu, M. De Micheli, and P. Baldi, "High performance mode adapters based on segmented SPE:$LiNbO_3$ waveguides", *Opt. Express*, vol. 17, no. 20, pp. 17868–17873, 2009.

[229] M. Varnava, D. E. Browne, and T. Rudolph, "How good must single photon sources and detectors be for efficient linear optical quantum computation?", *Phys. Rev. Lett.*, vol. 100, pp. 060502, 2008.

[230] T. B. Pittman, D. V. Strekalov, A. Migdall, M. H. Rubin, A. V. Sergienko, and Y. H. Shih, "Can two-photon interference be considered the interference of two photons?", *Phys. Rev. Lett.*, vol. 77, pp. 1917–1920, 1996.

[231] G. Weihs, T. Jennewein, C. Simon, H. Weinfurter, and A. Zeilinger, "Violation of Bell's inequality under strict Einstein locality conditions", *Phys. Rev. Lett.*, vol. 81, pp. 5039–5043, 1998.

[232] T. Jennewein, C. Simon, G. Weihs, H. Weinfurter, and A. Zeilinger, "Quantum cryptography with entangled photons", *Phys. Rev. Lett.*, vol. 84, no. 20, pp. 4729–4732, 2000.

[233] G. Ribordy, J. Brendel, J.-D. Gautier, N. Gisin, and H. Zbinden, "Long-distance entanglement-based quantum key distribution", *Phys. Rev. A*, vol. 63, pp. 012309, 2000.

[234] A. Poppe, A. Fedrizzi, R. Ursin, H. Böhm, T. Lörunser, O. Maurhardt, M. Peev, M. Suda, C. Kurtsiefer, H. Weinfurter, T. Jennewein, and A. Zeilinger, "Practical quantum key distribution with polarization entangled photons", *Opt. Express*, vol. 12, pp. 3865–3871, 2004.

[235] I. Marcikic, H. de Riedmatten, W. Tittel, H. Zbinden, M. Legré, and N. Gisin, "Distribution of Time-Bin entangled qubits over 50 km of optical fiber", *Phys. Rev. Lett.*, vol. 93, no. 18, pp. 180502, 2004.

[236] A. Muller, T. Herzog, B. Huttner, W. Tittel, H. Zbinden, and N. Gisin, ""Plug and play" systems for quantum cryptography", *Appl. Phys. Lett.*, vol. 70, no. 7, pp. 793–795, 1997.

[237] W. Tittel, J. Brendel, T. Herzog, H. Zbinden, and N. Gisin, "Non-local two-photon correlations using interferometers physically separated by 35 meters", *Europhys. Lett.*, vol. 40, pp. 595, 1997.

[238] Z. Y. Ou, X. Y. Zou, L. J. Wang, and L. Mandel, "Observation of nonlocal interference in separated photon channels", *Phys. Rev. Lett.*, vol. 65, pp. 321–324, 1990.

[239] P. G. Kwiat, W. A. Vareka, C. K. Hong, H. Nathel, and R. Y. Chiao, "Correlated two-photon interference in a dual-beam Michelson interferometer", *Phys. Rev. A*, vol. 41, pp. 2910–2913, 1990.

[240] P. Oberson, B. Huttner, and N. Gisin, "Frequency modulation via the Doppler effect in optical fibers", *Opt. Lett.*, vol. 24, pp. 451–453, 1999.

[241] J. Liang, J. D. Franson, and T. B. Pittman, "Time-bin entangled photon holes", *arXiv:1208.4776*, 2012, Submitted to Phys. Rev. A.

[242] S. Fasel, N. Gisin, G. Ribordy, and H. Zbinden, "Quantum key distribution over 30 km of standard fiber using energy-time entangled photon pairs: a comparison of two chromatic dispersion reduction methods", *Eur. Phys. J. D*, vol. 30, no. 1, pp. 143–148, 2004.

[243] H. Tanji, S. Ghosh, J. Simon, B. Bloom, and V. Vuletić, "Heralded single-magnon quantum memory for photon polarization states", *Phys. Rev. Lett.*, vol. 103, pp. 043601, 2009.

[244] K. Sanaka, K. Kawahara, and T. Kuga, "Experimental probabilistic manipulation of down-converted photon pairs using unbalanced interferometers", *Phys. Rev. A*, vol. 66, pp. 040301, 2002.

[245] J. Ye, S. Swartz, P. Jungner, and J. L. Hall, "Hyperfine structure and absolute frequency of the 87Rb 5p3/2 states", *Opt. Lett.*, vol. 21, pp. 1280–1282, 1996.

[246] H. Yan, S. Zhang, J. F. Chen, M. M. T. Loy, G. K. L. Wong, and S. Du, "Generation of narrow-band hyperentangled nondegenerate paired photons", *Phys. Rev. Lett.*, vol. 106, pp. 033601, 2011.

[247] C. Langrock, E. Diamanti, R. V. Roussev, Y. Yamamoto, M. M. Fejer, and H. Takesue, "Highly efficient single-photon detection at communication wavelengths by use of upconversion in reverse-proton-exchanged periodically poled LiNbO3 waveguides", *Opt. Lett.*, vol. 30, pp. 1725–1727, 2005.

[248] H. Kamada, M. Asobe, T. Honjo, H. Takesue, Y. Tokura, Y. Nishida, O. Tadanaga, and H. Miyazawa, "Efficient and low-noise single-photon detection in 1550 nm communication band by frequency upconversion in periodically poled LiNbO3 waveguides", *Opt. Lett.*, vol. 33, pp. 639–641, 2008.

[249] H. Pan and H. Zeng, "Efficient and stable single-photon counting at 1.55 μm by intracavity frequency upconversion", *Opt. Lett.*, vol. 31, pp. 793–795, 2006.

[250] J. S. Pelc, Q. Zhang, C. R. Phillips, L. Yu, Y. Yamamoto, and M. M. Fejer, "Cascaded frequency upconversion for high-speed single-photon detection at 1550 nm", *Opt. Lett.*, vol. 37, pp. 476–478, 2012.

[251] H. Takesue, E. Diamanti, C. Langrock, M. M. Fejer, and Y. Yoshihisa, "1.5- μm single photon counting using polarization-independent up-conversion detector", *Opt. Express*, vol. 14, pp. 13067–13072, 2006.

[252] M. A. Albota, F. N. C. Wong, and J. H. Shapiro, "Polarization-independent frequency conversion for quantum optical communication", *J. Opt. Soc. Am. B*, vol. 23, pp. 918–924, 2006.

[253] M. A. Albota and F. N. C. Wong, "Efficient single-photon counting at 1.55 μm by means of frequency upconversion", *Opt. Lett.*, vol. 29, pp. 1449–1451, 2004.

[254] R. Thew, S. Tanzilli, L. Krainer, S. C. Zeller, A. Rochas, I. Rech, S. Cova, H. Zbinden, and N. Gisin, "Low jitter up-conversion detectors for telecom wavelength GHz QKD", *New J. Phys.*, vol. 8, pp. 32, 2006.

[255] Y. O. Dudin, A. G. Radnaev, R. Zhao, J. Z. Blumoff, T. A. B. Kennedy, and A. Kuzmich, "Entanglement of light-shift compensated atomic spin waves with telecom light", *Phys. Rev. Lett.*, vol. 105, pp. 260502, 2010.

[256] S. Ramelow, A. Fedrizzi, A. Poppe, N. K. Langford, and A. Zeilinger, "Polarization-entanglement-conserving frequency conversion of photons", *Phys. Rev. A*, vol. 85, pp. 013845, 2012.

[257] A. P. VanDevender and P. G. Kwiat, "Quantum transduction via frequency upconversion", *J. Opt. Soc. Am. B*, vol. 24, pp. 295–299, 2007.

[258] J. Chen, K. F. Lee, X. Li, P. L. Voss, and P. Kumar, "Schemes for fibre-based entanglement generation in the telecom band", *New J. Phys.*, vol. 9, pp. 289, 2007.

[259] J. Chen, J. B. Altepeter, and P. Kumar, "Quantum-state engineering using nonlinear optical Sagnac loops", *New J. Phys.*, vol. 10, pp. 123019, 2008.

[260] B.-S. Shi and A. Tomita, "Generation of a pulsed polarization entangled photon pair using a Sagnac interferometer", *Phys. Rev. A*, vol. 69, pp. 013803, 2004.

[261] T. Kim, M. Fiorentino, and F. N. C. Wong, "Phase-stable source of polarization-entangled photons using a polarization Sagnac interferometer", *Phys. Rev. A*, vol. 73, pp. 012316, 2006.

[262] S. Sauge, M. Swillo, M. Tengner, and A. Karlsson, "A single-crystal source of path-polarization entangled photons at non-degenerate wavelengths", *Opt. Express*, vol. 16, pp. 9701–9707, 2008.

[263] M. Bonarota, J.-L. Le Gouet, S. A. Moiseev, and T. Chanelière, "Atomic frequency comb storage as a slow-light effect", *J. Phys. B: At. Mol. Opt. Phys.*, vol. 45, pp. 124002, 2012.

[264] F. Doutre, *Sources d'impulsions brèves basées sur des procédés de découpe non linéaires au sein d'une fibre optiques*, PhD thesis, Université de Limoges, 2010.

[265] J. S. Pelc, L. Ma, C. R. Phillips, Q. Zhang, C. Langrock, O. Slattery, X. Tang, and M. M. Fejer, "Long-wavelength-pumped upconversion single-photon detector at 1550 nm: performance and noise analysis", *Optics Express*, vol. 19, pp. 21445–21456, 2011.

[266] J. F. Clauser, "Experimental distinction between the quantum and classical field-theoretic predictions for the photoelectric effect", *Phys. Rev. D*, vol. 9, pp. 853, 1974.

[267] P. Grangier, G. Roger, and A. Aspect, "Experimental evidence for a photon anti-correlation effect on a beam splitter: A new light on single-photon interferences", *Europhys. Lett.*, vol. 1, pp. 173, 1986.

[268] Y.-H. Kim, R. Yu, S. P. Kulik, Y. Shih, and M. O. Scully, "Delayed "choice" quantum eraser", *Phys. Rev. Lett.*, vol. 84, pp. 1–5, 2000.

[269] S. P. Walborn, M. O. Terra Cunha, S. Pádua, and C. H. Monken, "Double-slit quantum eraser", *Phys. Rev. A*, vol. 65, pp. 033818, 2002.

[270] V. Jacques, E. Wu, F. Grosshans, F. Treussart, P. Grangier, and A. Aspect, "Experimental realization of Wheeler's delayed-choice gedanken experiment", *Science*, vol. 315, pp. 966–968, 2007.

[271] W. K. Wootters and W. H. Zurek, "Complementarity in the double-slit experiment: Quantum nonseparability and a quantitative statement of Bohr's principle", *Phys. Rev. D*, vol. 19, pp. 473–484, 1979.

[272] V. Jacques, E. Wu, F. Grosshans, F. Treussart, P. Grangier, A. Aspect, and J.-F. Roch, "Delayed-choice test of quantum complementarity with interfering single photons", *Phys. Rev. Lett.*, vol. 100, pp. 220402, 2008.

[273] J.-S. Tang, Y.-L. Li, X.-Y. Xu, G.-Y. Xiang, C.-F. Li, and G.-C. Guo, "Realization of quantum Wheeler's delayed-choice experiments", *Nat. Photon*, 2012.

[274] T. J. Herzog, P. G. Kwiat, H. Weinfurter, and A. Zeilinger, "Complementarity and the quantum eraser", *Phys. Rev. Lett.*, vol. 75, pp. 3034–3037, 1995.

[275] R. Hanbury Brown and R. Q. Twiss, "Correlation between photons in two coherent beams of light", *Nature*, vol. 177, no. 4497, pp. 27–29, 1956.

[276] R. Hanbury Brown and R. Q. Twiss, "A test of a new type of stellar interferometer on Sirius", *Nature*, vol. 178, pp. 1046–1048, 1956.

[277] Y. Tang, Y. Shen, J. Yang, X. Liu, J. Zi, and B. Li, "Experimental evidence of wave chaos from a double slit experiment with water surface waves", *Phys. Rev. E*, vol. 78, pp. 047201, 2008.

[278] V. Zwiller, T. Aichele, and O. Benson, "Single-photon Fourier spectroscopy of excitons and biexcitons in single quantum dots", *Phys. Rev. B*, vol. 69, pp. 165307, 2004.

[279] Y. Aharonov, S. Popescu, and P. Skrzypczyk, "Quantum Cheshire cats", *arXiv:1202:0631*, 2012.

[280] I. Ibnouhsein and A. Grinbaum, "Twin quantum Cheshire cats", *arXiv:1202:4894*, 2012.

[281] N. Bohr, "Talk on complementarity", in *International Physical Congress, Volta Conference in Como (Italy)*, 1927.

[282] N. Bohr, "The quantum postulate and the recent development of atomic theory", *Nature*, vol. 121, pp. 580–590, 1928.

[283] A. R. Marlow, *J. A. Wheeler in Mathematical Foundations of Quantum Mechanics*, New York: Academic Press), 1978.

[284] G. Jaeger, A. Shimony, and L. Vaidman, "Two interferometric complementarities", *Phys. Rev. A*, vol. 51, pp. 54–67, 1995.

[285] Berthold-Georg Englert, "Fringe visibility and which-way information: An inequality", *Phys. Rev. Lett.*, vol. 77, pp. 2154–2157, 1996.

[286] S. Dürr, T. Nonn, and G. Rempe, "Fringe visibility and which-way information in an atom interferometer", *Phys. Rev. Lett.*, vol. 81, pp. 5705–5709, 1998.

[287] X. Peng, X. Zhu, X. Fang, M. Feng, M. Liu, and K. Gao, "An interferometric complementarity experiment in a bulk nuclear magnetic resonance ensembe", *J. Phys. A: Math. Gen*, vol. 36, pp. 2555, 2003.

[288] J. B. Altepeter, E. R. Jeffrey, P. G. Kwiat, S. Tanzilli, N. Gisin, and A. Acín, "Experimental methods for detecting entanglement", *Phys. Rev. Lett.*, vol. 95, no. 3, pp. 033601, 2005.

[289] M. Brune, E. Hagley, J. Dreyer, X. Maître, A. Maali, C. Wunderlich, J. M. Raimond, and S. Haroche, "Observing the progressive decoherence of the "meter" in a quantum measurement", *Phys. Rev. Lett.*, vol. 77, pp. 4887–4890, 1996.

[290] S. S. Roy, A. Shukla, and T. S. Mahesh, "NMR implementation of a quantum delayed-choice experiment", *Phys. Rev. A*, vol. 85, pp. 022109, 2012.

[291] R. Auccaise, R. M. Serra, J. G. Filgueiras, R. S. Sarthour, I. S. Oliveira, and L. C. Céleri, "Experimental analysis of the quantum complementarity principle", *Phys. Rev. A*, vol. 85, pp. 032121, 2012.

[292] P. M. Pearle, "Hidden-variable example based upon data rejection", *Phys. Rev. D*, vol. 2, pp. 1418–1425, 1970.

[293] J. F. Clauser and M. A. Horne, "Experimental consequences of objective local theories", *Phys. Rev. D*, vol. 10, pp. 526–535, 1974.

[294] J. R. Torgerson, D. Branning, C. H. Monken, and L. Mandel, "Reply to the comment by Cabello and Santos on "Experimental demonstration of the violation of local realism without Bell inequalities"", *Phys. Lett. A*, vol. 214, pp. 319–320, 1996.

[295] N. Blœmbergen and P. S. Pershan, "Light waves at the boundary of nonlinear media", *Phys. Rev.*, vol. 128, no. 2, pp. 606, 1962.

[296] C. Vassalo, *Électro-magnétisme classique dans la matière*, Dunod, Paris, 1980.

[297] Y. H. Shen, *Principles of nonlinear optics*, Wiley, New-York, 1984.

[298] A. Yariv, *Quantum electronics*, Wiley, New-York, 1989.

[299] K. Gallo, *Guides enterrés polarisé périodiquement et étude théorique d'un amplificateur paramétrique contrapropagatif*, PhD thesis, Université de Nice - Sophia Antipolis, 2001.

[300] G. Ghosh, *Handbook of optical constants of solids : Handbook of thermo-optic coefficients of optical material with applications*, Elsevier Science & Technology Books, 1998.

[301] D. H. Jundt, "Temperature-dependent Sellmeier equation for the index of refraction, ne, in congruent lithium niobate", *Opt. Lett.*, vol. 22, no. 20, pp. 1553–1555, 1997.

[302] French Wikipedia atricle about lithium niobate (12.09.2012), "Niobate de lithium", *http* : $//fr.wikipedia.org/wiki/Niobate\_de\_lithium$.

[303] D. B. Leviton and B. J. Frey, "Temperature-dependent absolute refractive index measurements of synthetic fused silica", *arXiv:0805.0091*, 2008.

[304] J. W. Berthold and S. F. Jacobs, "Ultraprecise thermal expansion measurements of seven low expansion materials", *Appl. Opt.*, vol. 15, pp. 2344–2347, 1976.

Abstract

The aim of this thesis is to develop sources of photonic entanglement to study both quantum networking tasks and some of the foundations of quantum physics. To this end, three high-performance sources are developed, each of them taking extensively advantage of standard telecom fibre optics components. The first source generates polarization entanglement via deterministic pair separation in two adjacent telecommunication channels. This source is naturally suitable for quantum cryptography in wavelength multiplexed network structures. The second source generates for the first time a cross time-bin entangled bi-photon state which allows for quantum key distribution tasks using only passive analyzers. The third source generates, with a record efficiency, polarization entanglement using an energy-time to polarization entanglement transcriber. The photon spectral bandwidth can be chosen over more than five orders of magnitude (25 MHz - 4 THz). This permits implementing the source into existing telecom networks, but also in advanced quantum relay and quantum memory applications. Moreover, this source is used to revisit Bohr's single-photon wave-particle complementarity notion via employing a Mach-Zehnder interferometer with an output quantum beam-splitter in a true superposition of being present and absent. Finally, to adapt the wavelength of the entangled telecom photon pairs to the absorption wavelength of current quantum memories, a coherent wavelength converter is presented and discussed.

Résumé

Le but de cette thèse est de développer des sources d'intrication photonique pour étudier les réseaux de communication quantique et l'optique quantique fondamentale. Trois sources très performantes sont construites uniquement autour de composants standards de l'optique intégrée et des télécommunications optiques. La première source génère de l'intrication en polarisation via une séparation déterministe des paires de photons dans deux canaux adjacents des télécommunications. Cette source est donc naturellement adaptée à la cryptographie quantique dans les réseaux à multiplexage en longueurs d'ondes. La seconde source génère, pour la première fois, de l'intrication en time-bins croisés, autorisant l'implémentation de crypto-systèmes quantiques à base d'analyseurs passifs uniquement. La troisième source génère, avec une efficacité record, de l'intrication en polarisation via un convertisseur d'observable temps/polarisation. La bande spectrale des photons peut être choisie sur plus de cinq ordres de grandeur (25 MHz - 4 THz), rendant la source compatible avec toute une variété d'applications avancées, telles que la cryptographie, les relais et les mémoires quantiques. Par ailleurs, cette source est utilisée pour revisiter la notion de Bohr sur la complémentarité des photons uniques en employant un interféromètre de Mach-Zehnder dont la lame séparatrice de sortie se trouve dans une superposition quantique d'être à la fois présente et absente. Enfin, pour adapter la longueur d'onde des paires des photons télécoms intriqués vers les longueurs d'ondes d'absorption des mémoires quantiques actuelles, un convertisseur cohérent de longueur d'onde est présenté et discuté.